68-9042

NEILL, DeWitt Talmage, 1932-
HEAT TRANSFER FROM UNCONTROLLED BUOYANT DIFFUSION FLAMES.

The University of Oklahoma, Ph.D., 1968
Engineering, chemical

University Microfilms, Inc., Ann Arbor, Michigan

Downloaded from SHAREOK. Persistent Handle URL: https://hdl.handle.net/11244/2334

THE UNIVERSITY OF OKLAHOMA

GRADUATE COLLEGE

HEAT TRANSFER FROM UNCONTROLLED BUOYANT DIFFUSION FLAMES

A DISSERTATION

SUBMITTED TO THE GRADUATE FACULTY

in partial fulfillment of the requirements for the

degree of

DOCTOR OF PHILOSOPHY

BY

DEWITT TALMAGE NEILL

Norman, Oklahoma

1968

HEAT TRANSFER FROM UNCONTROLLED BUOYANT

DIFFUSION FLAMES

APPROVED BY

C. M. Sliepcevich

D. J. Seo

O. A. Plumb

F. M. Townsend

J. Kudlaty

ABSTRACT

This study was initiated to add to the limited knowledge of heat transfer from uncontrolled, buoyant diffusion flames by obtaining total heat transfer data for flames from a variety of liquid fuels. A second objective was to develop the necessary equations and compare several techniques for calculating the radiant heat transfer from the flames. A third objective was to compare the convective heat transfer rates, determined as the difference between the measured total and the calculated radiant heat transfer rates, with the predicted convective heat transfer rates based on the available convective heat transfer coefficient correlations.

The total heat transfer rates were obtained from a heat balance around a boiler type heat transfer probe which was completely surrounded by the flames. Radiant heat transfer measurements were made external to the flame for use in evaluating the radiation calculation techniques. The flame dimensions were determined from photographs made during the tests. A constant-head siphon was used to supply fuel to the burners and maintain a constant flame size during the test.

The accumulation of soot on the test cylinder caused the total heat transfer rate to decrease exponentially with time. The coefficients for the equation depend on the fire size and the fuel. None of the radiation calculation techniques were found to provide significantly better answers over the others; the assumptions and difficulties associated with each technique are discussed. The convective heat transfer coefficient was found to be 2 to 3 times greater than the coefficient predicted by the available correlations. The physical size and characteristics of the flame were found to be more difficult to define than had been anticipated.

ACKNOWLEDGEMENTS

Many people have contributed to the completion of my graduate program and I wish to express my sincere appreciation to all of them.

Dr. C. M. Sliepcevich has applied, over the past 12 years, the steady confidence and gentle pressure which I have needed to accomplish my objectives. His efforts deserve a special measure of respect and gratitude.

Dr. J. R. Welker has listened with patience and concern to my day to day problems, and has earned my special thanks.

I appreciate the individual and collective contributions of the other members of my graduate committee, Dr. T. J. Love, Dr. F. M. Townsend, and Dr. C. P. Colver.

The efforts of Mr. R. J. Krause, who has been a willing and careful worker throughout the experimental program, Mrs. Joyce Meyer, who typed most of the manuscript, and the other members of the Flame Dynamics Laboratory staff are particularly appreciated.

I am grateful for the financial assistance furnished through the programs of the National Defense Education Act,

The U. S. Army Chemical Research and Development Laboratories at Edgewood Arsenal, and the University of Oklahoma Research Institute.

Finally, I must express my gratitude to my wife, Marjorie, who has lovingly indulged me these past three years.

DeWitt T. Neill

TABLE OF CONTENTS

		Page
LIST OF TABLES		ix
LIST OF ILLUSTRATIONS		xii
Chapter		
I.	INTRODUCTION	1
II.	REVIEW OF PREVIOUS WORK	7
	Total Heat Transfer from Fires Radiant Heat Transfer from Flames Convective Heat Transfer from Flames	
III.	THEORETICAL DEVELOPMENTS	34
	General Radiant Heating of Test Cylinder Surrounded by Flames Radiant Heating of a Target External to a Cylindrical Flame	
IV.	FACILITIES AND EQUIPMENT	52
	Test Cylinders Lead Tube Control Panels Support and Lifting Mechanism Burners and Fuel Supply System Instrumentation	
V.	EXPERIMENTAL PROCEDURE	84
VI.	RESULTS	93
	General Soot Accumulation Total Heat Transfer Rates	

Radiant Heat Transfer Rates
Convective Heat Transfer Rates
Flame Photographs and Test Discussions
Fuel Burning Rates
Flicker Factors

VII. CONCLUSIONS. 169

REFERENCES. 173

NOMENCLATURE. 177

APPENDICES

A. CALCULATION OF HEAT TRANSFER THROUGH TEST CYLINDER FROM EXPERIMENTAL DATA. 181

B. NOTES ON NUMERICAL AND ANALYTICAL INTEGRATIONS FOR CALCULATING RADIANT HEATING FROM FLAMES. 204

C. FORMAL DEVELOPMENT OF RADIATION HEATING EQUATIONS FOR AN ABSORBING-EMITTING MEDIUM . 220

D. TABULAR SUMMARIES OF EXPERIMENTAL DATA AND CALCULATED PARAMETERS. 228

E. DESIGN OF SUPPORT AND LIFTING MECHANISM. . . . 289

F. THERMISTOR ACTUATED LIQUID LEVEL MONITOR CIRCUIT. 295

G. CORRECTION FACTORS FOR RADIATION ABSORBED BY ATMOSPHERE AND RADIOMETER QUARTZ WINDOW 299

LIST OF TABLES

Table		Page
II-1.	Heat Absorption Rates from In-Fire Tests.	8
II-2.	Calculated Free and Forced Convection Coefficients	33
IV-1.	Instrument List.	81
VI-1.	Initial Total Heat Transfer.	116
VI-2.	Exponential Time Decay Constants	117
VI-3.	Coefficients for Calculating Total Flame Radiation Based on Channel Burner Data . .	121
VI-4.	Calculated Incident Radiant Heating Inside Methanol Flames	134
VI-5.	Calculated Incident Radiant Heating Inside Luminous Flames	135
VI-6.	Summary of Heat Transfer Rates Inside Methanol Flames.	138
VI-7.	Summary of Heat Transfer Rates Inside Luminous Flames.	139
VI-8.	Flicker Factors for Various Fuels and Flame Thicknesses.	167
VII-1.	Maximum Heat Transfer Rates from Optically Thick Flames from Single Burners	172
A-1.	Summary of Heat Gain Through Top and Bottom Insulators.	199
B-1.	Incident Radiant Heat from Flame Cylinders Calculated with 4- and 12-Point Gauss Quadratures.	205

Table Page

D-1. Experimental Data from Lead Tube Heat Loss Calibration Tests 229

D-2. Measured Radiation Intensity from Circular Burner Fires 230

D-3. Miscellaneous Temperatures, Soot Accumulation and Test Duration Data. . . . 231

D-4. Fire Size, Fuel Burning Rates and External Radiation Data. 233

D-5. Total Heat Transfer Data and Calculated Results for Methanol Fires 235

D-6. Total Heat Transfer Data and Calculated Results for Acetone Fires. 244

D-7. Total Heat Transfer Data and Calculated Results for Hexane Fires 254

D-8. Total Heat Transfer Data and Calculated Results for Cyclohexane Fires. 263

D-9. Total Heat Transfer Data and Calculated Results for JP-4 Fires 269

D-10. Total Heat Transfer Data and Calculated Results for Napalm Test Solvent Fires. . . 273

D-11. Total Heat Transfer Data and Calculated Results for Benzol Fires 274

D-12. Emission and Absorption Coefficients from Small Methanol Flames. 275

D-13. Emission and Absorption Coefficients from Small Acetone Flames 277

D-14. Emission and Absorption Coefficients from Small Hexane Flames. 280

D-15. Emission and Absorption Coefficients from Small Cyclohexane Flames 283

D-16. Measured Radiation from Various Merged Fires. 286

Table Page

D-17. Measured Radiation from Various Fires in Small Channel Burners 288

G-1. Atmospheric Absorption Coefficients and Quartz Window Transmissivities 301

LIST OF ILLUSTRATIONS

Figure		Page
III-1.	System Geometry for Cylindrical Target Surrounded by a Cylindrical Flame.	36
III-2.	System Geometry for Target External to a Cylindrical Flame.	43
III-3.	Simplified Geometry for Target External to a Cylindrical Flame	50
IV-1.	Thick-wall Test Cylinder	54
IV-2.	Thin-wall Test Cylinder.	55
IV-3.	Insulating End Pieces for Test Cylinder. . .	57
IV-4.	Miscellaneous Metal Pieces for Test Cylinder	58
IV-5.	Test Cylinder Top Cap.	59
IV-6.	Miscellaneous Metal Pieces for Lead Tube . .	61
IV-7.	Assembly Drawing for Test Cylinder and Lead Tube.	62
IV-8.	Location of Lead Tube Thermocouples.	64
IV-9.	Control Panel in Observation Room.	66
IV-10.	Control Panel in Test Room	67
IV-11.	Low Velocity Wind Tunnel	68
IV-12.	Schematic Flow Diagram for Experimental System	69
IV-13.	Schematic Flow Diagram for Lead Tube Assembly	70

Figure		Page
IV-14.	Lifting and Support Mechanism for Lead Tube Assembly.	75
IV-15.	Photograph of Experiment Assembly During Test 49.	78
IV-16.	Schematic Diagram of Fuel Level Control System	79
VI-1.	Typical Soot Deposit on Test Cylinder. . . .	95
VI-2.	Non-typical Soot Deposit on Test Cylinder. .	96
VI-3.	Typical Soot Deposit Removed from Test Cylinder	97
VI-4.	Total Heat Transfer Rates from 12- and 18-inch Diameter Single Burner Acetone Fires.	101
VI-5.	Total Heat Transfer Rates from 24-inch Diameter Single and 6-inch Diameter Cluster Burner Acetone Fires	102
VI-6.	Total Heat Transfer Rates from 12- and 18-inch Diameter Single Burner Hexane Fires.	103
VI-7.	Total Heat Transfer Rates from 6-inch Diameter Cluster Burner Hexane Fires . . .	104
VI-8.	Total Heat Transfer Rates from 12- and 18-inch Diameter Single Burner Cyclohexane Fires.	105
VI-9.	Total Heat Transfer Rates from 6-inch Diameter Cluster Burner Cyclohexane Fires.	106
VI-10.	Total Heat Transfer Rates from 12- and 18-inch Diameter Single Burner JP-4 Fires.	107
VI-11.	Total Heat Transfer Rates from 6-inch Diameter Cluster Burner JP-4 Fires	108
VI-12.	Total Heat Transfer Rates from 12-inch Diameter Single Burner Benzol Fires. . . .	109
VI-13.	Total Heat Transfer Rates from 12-inch Diameter Single Burner Napalm Test Solvent Fires.	109

Figure		Page
VI-14.	Linear Plot of Total Heat Transfer Rates from 12-, 18-, and 24-inch Diameter Single Burner Methanol Fires. . .	110
VI-15.	Linear Plot of Total Heat Transfer Rates from 24-inch Diameter Single Burner Acetone Fires	111
VI-16.	Linear Plot of Total Heat Transfer Rates from 6-inch Diameter Cluster Burner Hexane Fires	112
VI-17.	Linear Plot of Total Heat Transfer Rates from 6-inch Diameter Cluster Burner Cyclohexane Fires	113
VI-18.	Linear Plot of Total Heat Transfer Rates from 6-inch Diameter Cluster Burner JP-4 Fires.	114
VI-19.	Calculated Radiant Heating from Hemispherical Flames of Several Fuels, Based on Channel Burner Data	120
VI-20.	Calculated Radiant Heating from Hexane Flames Using Different Methods	124
VI-21.	Comparison of Calculated and Measured Radiant Heating External to Acetone Fires.	127
VI-22.	Comparison of Calculated and Measured Radiant Heating External to Acetone Fires.	128
VI-23.	Comparison of Calculated and Measured Radiant Heating External to Hexane Fires .	129
VI-24.	Comparison of Calculated and Measured Radiant Heating External to Cyclohexane Fires.	130
VI-25.	Comparison of Calculated and Measured Radiant Heating External to Benzol Fires .	131
VI-26.	Methanol Fires from 12-, 18-, and 24-inch Diameter Single Burners	144
VI-27.	Variations in Methanol Flame Shape	145

Figure		Page
VI-28.	Acetone Fires from 12-, 18-, and 24-inch Diameter Single Burners.	146
VI-29.	Acetone Fires from 6-inch Diameter Cluster Burners	147
VI-30.	Hexane Fires from 12- and 18-inch Diameter Single Burners.	148
VI-31.	Hexane Fires from 24-inch Diameter Single and 6-inch Diameter Cluster Burners.	149
VI-32.	Cyclohexane Fires from 12- and 18-inch Diameter Single and 6-inch Cluster Burners.	150
VI-33.	JP-4 Fires from 12- and 18-inch Diameter Single and 6-inch Diameter Cluster Burners.	151
VI-34.	Napalm Test Solvent Fire from 12-inch Diameter Single Burner	152
VI-35.	Fuel Burning Rates During Several Hexane Fire Tests.	157
VI-36.	Single 16 mm Movie Frames of Hexane Flames from 12-inch Diameter Single Burner (24 frames/sec)	161
VI-37.	Single 16 mm Movie Frames of Cyclohexane Flames from 12-inch Diameter Single Burner (24 frames/sec)	162
VI-38.	Single 16 mm Movie Frames of Cyclohexane Flames from 12-inch Diameter Single Burner (64 frames/sec)	163
VI-39.	Measured Radiation Intensity from Cylindrical Flames	165
A-1.	Schematic of Heat Gains and Losses by Primary Coolant.	182
A-2.	Heat Gain Through Bottom and Top Insulators Around Test Cylinder	193
A-3.	Conformal Mapping Sketch for Infinite Slab .	194

Figure Page

B-1. Angular Distribution of Radiant Heat from Flame Cylinder 206

B-2. Hemispherical Flame Sketch 212

B-3. Flattened Torus Flame Sketch 213

B-4. Torus Flame Sketch 214

B-5. Balloon Flame Sketch 216

B-6. Paraboloid Flame Sketch. 217

B-7. Ellipsoid Flame Sketch 219

C-1. Directional Intensity of Radiation 221

E-1. Load, Shear and Bending Moment Diagrams for Lead Tube Assembly 291

F-1. Thermistor Actuated Liquid Level Monitor Circuit. 297

G-1. Effects of Spectral Absorption Corrections on Calculated Radiant Heating from Acetone Flames 304

G-2. Effects of Spectral Absorption Corrections on Calculated Radiant Heating from Hexane Flames. 305

G-3. Effects of Spectral Absorption Corrections on Calculated Radiant Heating from Cyclohexane Flames 306

INTRODUCTION

Fires, one of man's oldest scourges, still threaten all levels of our civilization from the latest jet aircraft to our shrinking forests. The annual cost of direct physical damage from fires in the United States is estimated (Ref. 1) to be 1-1/2 billion dollars; the annual fire deaths number about 11,500.

Heat transfer from uncontrolled buoyant diffusion fires is of paramount importance in the design of fire protection systems. Continual improvement of the fire protection for passengers and equipment must be made in airplanes and other common carriers. The design of lightweight, economical fire barriers which will permit passenger escape and will protect valuable equipment until the fire can be extinguished is largely dependent on the heat transfer rate from the fire. The ignition of flammable materials, either desired or undesired, and the rate of fire spread is usually dependent on the heat transfer rate from an adjacent flame. Vessels and storage tanks containing volatile materials must be equipped with emergency venting systems to dispose of their contents safely in the event of fire. As individual tanks have become larger the cost

of overdesigned venting systems has become prohibitive. In fact, so little is known about the heat transfer rates from fires that the designer of fire protection systems can make only the crudest use of such specifics as the probable type of fuel, prevailing weather conditions, and physical locations.

Investigations and predictions of heat transfer rates from fires have usually been made from two approaches; the use of total heat transfer rates measured during large scale tests, or the use of measured or calculated average flame temperatures to calculate the heat transfer rates.

A number of large scale tests have been made on heat transfer rates from buoyant diffusion fires. Lott and Sliepcevich (Ref. 29) compared the results of these tests and the many design equations which have been proposed for calculating heat transfer rates from large fires. The test results varied considerably, a common occurrence in fire research, and were always reported as overall heat fluxes. The measured heat fluxes ranged from 5,400 Btu/hr-ft^2 to 32,000 Btu/hr-ft^2; the majority of the results were above 20,000 Btu/hr-ft^2. The design equations are all empirical modifications of the overall heat transfer rates since none of the investigators attempted to separate the heat transfer into radiant and convective components. The equations attempt to account for partially-filled tanks, the presence of insulation and an

exposure factor for different tank sizes as well as differences in the specific total heat transfer rate. Large scale tests are extremely difficult and expensive to carry out and the results are not necessarily applicable to other situations. Information is needed so that the contribution of both the radiant and convective heat transfer mechanisms can be determined for large scale fires. Even more important is the need for information which will aid in applying fire test results to conditions which are not identical to those of the tests. The total heat transfer rate approach is usually applied to the design of fire protection and safety systems where maximum heat transfer rates are used.

The several techniques for calculating the radiant heat transfer rate from fires use an average flame temperature and some modification of the Stefan-Boltzmann Law. The average flame temperature required for these equations is unusually difficult to determine accurately enough for reliable heat transfer calculations. A temperature variation of 10 to 20 percent is quite common and this inaccuracy results in large differences in the radiant heat flux calculated by the Stefan-Boltzmann equation. For example, the calculated heat flux from a black body at temperatures of 2000 and 1600°F are 62,800 and 31,000 Btu/hr-ft^2 respectively. To make matters worse, the problem is not limited to obtaining reproducible accuracy with a given temperature-measuring technique. Major

variations of measured flame temperature will occur between the several, theoretically-sound, measuring techniques and between different measuring-point locations within the flame.

The luminosity, composition and size of the flames are usually accounted for by varying the flame emissivity and sometimes the power to which the flame temperature is raised, viz. $T^{3.5}$ rather than T^4. (Ref. 38, p. 307, Ref. 27, p. 429, Ref. 32, p. 99 and Ref. 18 are just a few applicable sources). The convective heat transfer coefficient is usually determined from a correlation based on moderate temperature differences in a non-reacting gas. These techniques are usually applied to controlled, jet fires as well as uncontrolled, buoyant, diffusion fires.

The fires considered in this work are the uncontrolled, buoyant, diffusion type following the definitions and distinctions drawn by Welker (Ref. 48). A flame is described as "buoyant" when the forces causing it to rise are due to the buoyancy of the hot flame gases. "Jet" flames result when the fuel is injected so that its initial momentum is large compared to the buoyancy forces of the hot flame gases. In "uncontrolled" fires the fuel burning rate depends only on the fuel and environmental conditions. Gas fires are "controlled" and are frequently burned with "jet" flames. Fires from liquid pools and solid fuels are usually "uncontrolled." The fuel and

oxidizer are combined before the combustion zone is reached in "premixed" flames whereas "diffusion" flames depend on molecular and eddy diffusion to mix the fuel and oxidizer at the combustion zone.

Recent investigations by Hood (Ref. 17), Shahrokhi (Ref. 36) and Tsai (Ref. 40) at the University of Oklahoma Research Institute have produced data and calculation techniques which provided radiant heating results within ±5 percent of measured values for small laminar flames. The calculation technique utilizes measured energy emission and absorption spectra for a specific fuel. The radiant energy transport equations are integrated over the visible volume of the flame to obtain the radiant heat from the flame incident on a target. Since this technique produces only radiant heating results, convective heat transfer rates must be included when the fire comes in contact with the target.

This investigation was initiated to obtain experimental data on the total heat transferred to a cooled target surrounded by uncontrolled buoyant diffusion fires. A second objective was to develop the equations and techniques for calculating the radiant heat transfer to a target surrounded by an emitting-absorbing medium. A third objective was to check the results of the radiant heat transfer calculations using absorption and emission coefficients obtained from measurements on small, laminar flames.

The experimental fires were as large as the existing facilities could handle. The maximum flame sizes were approximately 10 feet high x 3 feet in diameter using a 2-foot diameter burner. The convective heating contribution was taken as the difference between the measured total and the calculated radiant heat transfer. The temperature of the cooled target was held constant so that the resulting constant temperature difference between the flame and target could be used to calculate a convective heat transfer coefficient.

CHAPTER II

REVIEW OF PREVIOUS WORK

Total Heat Transfer from Fires

Uncontrolled buoyant diffusion fires are most often associated with destructive fires. It is not surprising then that the major impetus for studying such fires comes from agencies and companies concerned with fire prevention and protection. Heat transfer tests run for safety purposes are usually large scale tests. The results are reported as total heat transfer rates without regard to the relative contributions from radiation and convection.

Lott and Sliepcevich (Ref. 29) surveyed the large scale fire tests run over the past 40 years in which heat transfer rates were measured to aid in establishing emergency venting requirements for storage tanks. Table II-1, reprinted from Ref. 29, summarizes the results of these tests. Although the results vary widely, the majority of the total heat transfer rates are above 20,000 Btu/hr-ft^2 with a maximum at 32,500 Btu/hr-ft^2. Generally the fuels burned in large scale tests vary from gasoline to fuel oil and frequently are unspecified mixtures of whatever is available.

TABLE II-1

HEAT ABSORPTION RATES FROM IN-FIRE TESTS[a]

Source	Wetted Area (A) Ft^2	Q/A Btu per hr per ft^2	Q Btu per hr
Hottel-avg of 36 tests	296	12,700	3,760,000
Hottel-avg of 13 tests	296	7,226	2,139,000
Std. of Calif.	26	16,000	416,000
Std. of Calif.	105	32,000	3,370,000
Underwriter's Lab Flat Plate	24	32,500	780,000
Rubber Reserve Corp. Test No. 17	400	23,200	9,280,000
Rubber Reserve Corp. Test No. 17	400	21,000	8,400,000
Rubber Reserve Corp. Test No. 17	9.0	30,400	274,000
API Project Test No. 1	6.1	15,700	95,800
API Project Test No. 2	6.1	16,800	102,500
48-Ft Butane Sphere	4363	5,400	23,560,000
Fetterly	56.82	23,300	1,350,000
Alum. Co. of Amer.	15	29,500	442,000
Union Carbide, avg. 3 tests	176	28,400	4,993,000
Union Carbide	132	17,400	2,300,000
Union Carbide, avg. 3 tests	14.3	24,370	348,000

[a] J. L. Lott and C. M. Sliepcevich, "A Investigation of the Emergency Venting Requirements for Cargo and Portable Tanks," unpublished, 1966.

The consensus derived from these test results is probably expressed by the current Compressed Gas Association design equation (Ref. 10) for the heat transferred to storage tanks immersed in fire

$$Q = 34{,}500\ A^{0.82} \qquad \text{(II-1)}$$

where Q = total heating rate, Btu/hr

A = total surface area of tank, ft^2

Equation (II-1) is intended for application to liquid full tanks with at least several square feet of surface area. Raising the surface area to the 0.82 power, which effectively decreases the applied heat flux with increasing surface area, is intended to compensate for the lack of complete fire coverage as the tank size increases. Applying Eq. (II-1) to tanks with total surface areas of 10 and 100 ft^2 is equivalent to applying heat fluxes of 22,800 and 13,000 Btu/hr-ft^2, respectively, to the total surface area of each tank.

Measurements of the heat transfer to targets immersed in uncontrolled, buoyant diffusion flames are very scarce. Most of the data which have been published concern heat transfer back to the fuel or direct impingement heat transfer from controlled, jet flames.

Copley (Ref. 12) exposed 11-inch and 4-inch diameter cylinders to a buoyant diffusion fire fueled with JP-4. An incident radiant heat flux of 31,400 Btu/hr-ft^2 was calculated using the following equation.

$$(Q/A)_R = \epsilon \sigma F T^4 \qquad \text{(II-2)}$$

where ϵ = emissivity of the radiating body

F = geometric view factor

σ = Stefan-Boltzmann constant (1.714 x 10^{-12} Btu/hr-ft^2 °R^4)

T = temperature of the radiating body, °R

The flame temperature was obtained by time averaging temperatures measured by several shielded iron-constantan thermocouples placed in the fire. The geometric view factor was equal to 1.0 since the flame completely surrounded the cylinders and the flame emissivity ϵ was assumed to be 1.0 as a starting point. The measured flame temperatures varied between 1500°F and 1700°F, the average value was 1610°F.

Copley solved the radial heat flow equations describing the temperatures inside the cylinders using a constant heat flux boundary condition, i.e. the convective heating from the flame was considered negligible. The time rate of change of the measured cylinder temperatures was used to determine a numerical value for the applied constant heat flux. This "experimental" heat flux, 30,400 Btu/hr-ft^2, agrees well with the radiant heat flux, 31,400 Btu/hr-ft^2, calculated with Eq. (II-2).

The JP-4 fuel was contained in a 10 x 18-foot rectangular fuel pan. Enough fuel was placed in the pan

for the fire to last about 150 seconds. The flame temperatures rose to their average value in about 25 seconds and the metal cylinder temperatures reached about 850°F for the small cylinder and 350°F for the large cylinder at the end of the tests.

The heat transferred from uncontrolled buoyant diffusion fires back to the fuel has been the subject of many investigations and some controversy exists over whether the dominant mechanism is radiant or convective heat transfer. Hottel (Ref. 18) proposed that the fuel vaporization rate would be proportional to a heat flux given by

$$q = \frac{4k\ (T_f - T_b)}{D} + U(T_f - T_b) + \sigma\ F\ (T_f^4 - T_b^4)\ (1-e^{-\eta D}) \qquad (II-3)$$

where q = heat flux transferred to the fuel

k = conduction coefficient

U = convection coefficient

σ = Stefan-Boltzmann constant

F = geometric view factor

η = flame opacity coefficient

D = burner or fuel pan diameter

T_f = absolute flame temperature

T_b = absolute fuel temperature

Equation (II-3) was designed to fit data taken by Blinov and Khudiakov (Ref. 5) using a wide variety of liquid

hydrocarbon fuels and burner sizes. Additional investigations by Emmons (Ref. 14), Rasbash, Ragowski, and Stark (Ref. 34), Burgess, Strasser, and Grumer (Ref. 7) and Akita and Yumoto (Ref. 2) have produced results which agree in principal with Eq. (11-3). The convective heat transfer to the fuel surface remains relatively constant. The radiant heat transfer continues to increase with fire size; however, the rate of increase is so low for large fires that the radiant heat transfer becomes effectively constant. The conduction term in Eq. (II-3) accounts for the influence of the rim of the burner pans on small fire sizes. The radiation contribution does not level off for luminous flames until burner diameters exceed about 4 feet. The convective contribution is relatively large, if not dominant, for non-luminous flames; measured burning rates for methanol are usually constant even for small burner sizes.

The heat transfer rates from uncontrolled buoyant diffusion fires burning gasoline and similar fuels are probably in the range of 25,000 to 40,000 Btu/hr-ft^2. If the target is very large with respect to the fire size, the correction for incomplete flame coverage becomes very important. The radiant contribution from luminous flames becomes constant for flame thicknesses on the order of 4 feet. Convection makes a significant contribution, at least to the heat transfer rate to the fuel.

Radiant Heat Transfer from Flames

Calculations of the rate of radiant heat transfer from flames have usually been separated into luminous and non-luminous techniques. These techniques are all oriented towards calculations for jet fires burning in furnace enclosures although McAdams (Ref. 32, p. 103) reports that at least one of the techniques has been used successfully on flames of less than 1/2-inch diameter.

Hsu (Ref. 22), Thring (Ref. 38), McAdams (Ref. 32) and every reference found all use the same approach for calculating the non-luminous radiation from flames. The techniques are based on data and correlations presented by Hottel and Egbert (Ref. 20) and Hottel and Manglesdorf (Ref. 21).

The basic idea behind the work of Hottel was to apply Beer's Law of exponential absorption to the radiation intensity emitted by a gas in its characteristic frequencies. The results were expressed as an effective emissivity for a specific gas. The effective emissivity was defined as the ratio of the radiant energy emitted by the gas to the radiation from a black body at the same temperature. The equation defining the non-luminous effective emissivity, E_n, is

$$E_n = \frac{\int_{\lambda_n} (1-e^{-\beta_n x}) \, f(\lambda,T) \, d\lambda}{\sigma T^4} \qquad \text{(II-4)}$$

where β_n = absorption coefficient for the non-luminous radiation

x = radiation path length

σ = Stefan-Boltzmann constant

T = absolute temperature of the emitting gas

λ = wavelength of emitted radiation

The integration is carried out over the characteristic wavelength bands of the non-luminous radiation. The function $f(\lambda,T)$ represents the energy emitted at a given wavelength λ by any substance in thermodynamic equilibrium at a given temperature T or simply Planck's Law.

Hottel and his associates integrated Eq. (II-4) using numerical techniques and presented graphs which give E_n as functions of gas concentration (usually expressed as partial pressure) and path length. The non-luminous absorption coefficient β_n is a function of wavelength and the particular gas; therefore, separate graphs are required for each emitting gas present in a flame.

The gases CO_2, CO, and H_2O are the only significant non-luminous emitters in flames from hydrocarbon fuels. McAdams is the only cited textbook reference which presents effective emissivities for gases other than CO_2 and H_2O. Apparently most authors feel there is so little CO in flames that it can be neglected or rather lumped in with the CO_2. This assumption may not be

good for uncontrolled, buoyant, diffusion flames.

The total non-luminous radiation is obtained by adding the contribution from the individual gases. Correction factors must be applied for different total pressures and for the case when the emission spectra of different gases overlap. A significant correction factor is required when CO_2 and H_2O are both present, as they are in a flame.

Thring (Ref. 38, p. 318) presents empirical equations for calculating the heat radiated from CO_2 and H_2O vapor. These equations were developed by Schack using data obtained by Eckert. The results of Hottel and Eckert differ by 20 to 30 percent. An interesting point about the equations developed by Schack is that the heat radiated from the CO_2 is proportional to the 3.5 power of the absolute temperature and the heat radiated from the CO is proportional to the 3.0 power of the absolute temperature.

Hsu presents a particularly clear discussion of the calculation of the non-luminous heat transfer by fires in furnaces and enclosures. Some reference texts are not careful in distinguishing between equations for calculating the heat transfer from enclosed and open fires.

The luminous radiation from a flame originates from the glowing soot particles at or very near the flame

gas temperature. These particles are so small (~1μ diameter) that they are not opaque and the transfer of radiation through a cloud of such particles is a very complicated process of emission, absorption and scattering. It has been generally accepted that the radiation from the luminous portion of a flame can be treated with an effective emissivity defined in the same manner as the effective emissivity of the non-luminous radiation. The equation defining the luminous effective emissivity is

$$E_L = \frac{\int_0^\infty (1-e^{-\varkappa s x})\ f(\lambda,T)\ d\lambda}{\sigma T^4} \qquad \text{(II-5)}$$

where $\varkappa$ = mass absorption coefficient for the soot

s = soot concentration

x = radiation path length

T = absolute temperature of the soot

The integration is carried out over all wavelengths since the spectrum of the radiation from the soot particles is continuous.

Hottel and Broughton (Ref. 19) determined that the absorption $\varkappa$ was proportional to $1/\lambda^n$ where n varies for different types of soot. They integrated Eq. (II-5) using their data on the absorption coefficients and presented nomograms which give E_L as functions of red (λ = 0.6651μ)

and green ($\lambda = 0.5553\mu$) brightness temperatures. A true temperature, determined from these nomograms, is used to calculate the radiant heating. The two-color pryometer of Hottel and Broughton is based on these developments.

Hsu presents several other techniques which have been developed for obtaining the effective emissivity of a flame. One method uses an optical temperature and a "true" temperature measured by a thermocouple. However, neither the reference wavelength of the optical measurement nor the details of the thermocouple measuring technique are given. Flame temperatures are too strong a function of the measuring technique to permit much latitude and still preserve accuracy and reproducibility. Thring also presents a thorough discussion of the various methods for measuring flame temperatures.

In most references the luminous and non-luminous radiation contributions are added to get the total radiation from a flame. This approach can lead to greater than black body radiation output since it neglects the fact that the soot radiates over the entire spectrum, including the emission band of the non-luminous gases. Following Thring, a technique which avoids this problem but requires a constant absorption coefficient $\varkappa$ is presented below. Thring suggests a constant value for the absorption coefficient $\varkappa$ of about 0.005 liters/mg-cm.

The total radiant energy from a luminous flame is given by

$$Q/A)_R = \int_{\lambda_L} (1-e^{-\kappa sx}) \; f(\lambda,T) \; d\lambda + \int_{\lambda_n} (1-e^{-x(\kappa s+\beta n)}) \; f(\lambda,T) \; d\lambda \qquad \text{(II-6)}$$

where λ_L denotes all wavelengths not covered by non-luminous gas emission and λ_n all wavelengths of the non-luminous gas emission. Rewriting Eq. (II-6) with different integration limits yields

$$Q/A)_R = \int_0^\infty (1-e^{-\kappa sx}) \; f(\lambda,T) \; d\lambda + \int_{\lambda_n} (-e^{-x(\kappa s+\beta_n)} + e^{-\kappa sx}) \; f(\lambda,T) \; d\lambda \qquad \text{(II-7)}$$

$$Q/A)_R = \int_0^\infty (1-e^{-\kappa sx}) \; f(\lambda,T) \; d\lambda + e^{-\kappa sx} \int_{\lambda_n} (1-e^{-\beta_n x}) \; f(\lambda,T) \; d\lambda \qquad \text{(II-8)}$$

The integral in the last term is part of the definition of the non-luminous effective emissivity from Eq. (II-4). Substituting Eq. (II-4) into Eq. (II-8) yields

$$Q/A)_R = \int_0^\infty (1-e^{-\kappa sx}) \; f(\lambda,T) \; d\lambda + e^{-\kappa sx} E_n \; \sigma \; T^4 \qquad \text{(II-9)}$$

It is not necessary to assume a constant soot absorption coefficient κ to integrate the first term on the right side

of Eq. (II-7) since the integral is part of the definition of the luminous effective emissivity from Eq. (II-5). Substituting both Eq. (II-4) and Eq. (II-5) into Eq. (II-8) yields

$$Q/A)_R = E_L \sigma T^4 + e^{-\kappa sx} E_n \sigma T^4 \qquad \text{(II-10)}$$

As the effective emissivity of the luminous contribution increases, the influence of the non-luminous contribution diminishes.

All the radiant heat transfer calculation methods presented so far are dominated by the value chosen for the flame temperature. Only the two-color pyrometer method provides any help in determining a true flame temperature for use in radiation calculations. As pointed out by Broida (Ref. 6), there is little doubt that methods have not yet (circa 1955) been developed which give practical measurements of flame temperature. This failure may be caused more by temperature gradients and non-equilibrium than by any fault of the temperature measuring methods. Vlasov (Ref. 41) presented an interesting analysis and developed corrections which yield a true average flame temperature from measured flame temperatures. Part of Vlasov's analysis indicated that poor mixing causes temperature fluctuations of 15 to 30 percent.

Two different methods for calculating the radiation contribution from the luminous portion of a flame have been presented. The two-color method requires actual measurements of the red and green brightness temperatures with special instruments and cannot be used a priori for predicting radiant heat transfer from flames. The second approach requires knowledge of the soot concentration in the flame and an average or true flame temperature. Thring presents a bit of data on the soot concentration in diffusion jet fires inside furnaces.

All these methods for calculating the radiant heat transfer in flames require knowledge of the concentrations of soot, CO, CO_2 and H_2O vapor inside the flame. In the absence of measured data for the particular fire system the best, indeed the only consistent, estimates can be obtained by assuming chemical equilibrium between a fuel-air mixture at the flame temperature. The resulting concentrations can be calculated with the well known equilibrium constant methods presented by Gaydon and Wolfhard (Ref. 16) or possibly the newer methods developed by White, Johnson, and Dantzig (Ref. 44). The equilibrium constant method requires not only knowledge of the chemical reactions involved, but also requires the solution of simultaneous, frequently non-linear, equations. Gaydon and Wolfhard present an approach which they recommend for occasional hand calculations. The method of White, Johnson

and Dantzig is based on the principle that the free energy of a mixture at equilibrium is at a minimum and the calculations require use of a digital computer.

The assumption of thermodynamic equilibrium is woven into every calculation technique presented so far. The development of Planck's Law is based on a system in thermodynamic equilibrium described by the Einstein-Bose statistical distribution. There can be little doubt that thermal equilibrium does not exist for the whole flame; however, if equilibrium is reached between the thermal and internal energy of the molecules Planck's Law can be applied.

Attaining equilibrium on a microscopic scale is discussed by Gaydon (Ref. 15 and Ref. 16) who presents arguments both ways. The radiative transition time is large relative to the frequency of molecular collisions so that a molecule experiences 10 to 1000 collisions, thereby quenching any chemical excitation, before the molecule radiates. However, there are abnormally large numbers of excited states in flames and some evidence to suggest that the Maxwell-Boltzmann energy distribution is not valid in flames.

Most of the discussions in the literature concern premixed, laminar flames where all the chemical reactions take place in the primary reaction zone. In diffusion flames the combustion cannot be completed in the primary reaction zone. Turbulent flames provide better mixing

with air but contact with the cooler air is believed to quench many of the reactions, causing incomplete combustion. This process may account for the variety of partial oxidation compounds which have been detected in turbulent diffusion flames. The combustion reactions release radiation (chemiluminescence) which has nothing to do with thermal radiation described by Planck's Law. The existence of thermodynamic equilibrium in a diffusion-flame, even on a microscopic scale is doubtful.

A flame radiation calculation method which does not require an equilibrium assumption has been developed by Shahrokhi (Ref. 36) and Hood (Ref. 17). The method is based on the differential equation describing the radiation intensity as a function of optical path length in an absorbing-emitting medium. This equation is

$$\frac{dI_\lambda}{dx} = -\beta_\lambda I_\lambda + J_\lambda \qquad \text{(II-11)}$$

where I_λ = the monochromatic intensity, watts/cm^2-μ-steradian

x = optical path length, cm

β_λ = monochromatic absorption coefficient, cm^{-1}

J_λ = monochromatic volume emission coefficient, watts/cm^3-μ-steradian

The symbol μ is an abbreviation for microns. If the absorption coefficient β_λ and the emission coefficient J_λ

are assumed to be constant along the optical path length, Eq. (II-11) can be readily integrated using an integrating factor of $e^{\beta_\lambda x}$. The final solution is

$$I_\lambda = \frac{J_\lambda}{\beta_\lambda} (1-e^{-\beta_\lambda x}) \qquad \text{(II-12)}$$

when the boundary condition $I_\lambda = 0$ at $x = 0$ is applied.

If suitable values of J_λ and β_λ can be obtained, the calculation of the monochromatic radiation flux from a flame becomes simply the geometrical problem of determining the optical path length and integrating the function over the "visible" flame volume. Of course the monochromatic radiation flux must be integrated over all wavelengths which contribute significantly to obtain the total radiant heat flux.

The spectrum of radiant energy released by the burning of various fuels in small buoyant diffusion flames has been measured by Hood (Ref. 17). The results were reported as volume emission coefficients, J_λ, and absorption coefficients, β_λ, as a function of wavelength. The measurements were made at several locations on small, 1/2- to 3/4-inch diameter, laminar flames, and the coefficients are average values through the flame thickness at each location. Shahrokhi (Ref. 36) and Tsai (Ref. 40), utilizing coefficients from the region three quarters up the flame cone height, compared calculated and measured radiant

heating rates for buoyant diffusion flames from burners up to 4 inches in diameter. The results agreed well for measurements made several burner diameters from the fire. As the radiometer was moved closer the measurements exceeded the calculated values, apparently due to the heating of the quartz window of the radiometer.

If the absorption and emission coefficient data are applicable to larger turbulent diffusion fires, radiation calculations based on them would provide considerable improvements over the techniques presently available.

Convective Heat Transfer from Flames

The published literature does not contain much information on convective heat transfer coefficients inside buoyant diffusion flames. Kilham (Ref. 26) investigated the radiant and convective heat transfer from CO gas flames to small diameter cylinders. These were forced convection experiments at flame temperatures of about 3400°F and cylinder surface temperatures of 1700 to 2400°F. Convective heating contributed approximately 85 percent of the energy transferred. The experimental convective transfer coefficients were about 18 Btu/hr-ft^2 °F and agreed very well with calculated values using the following equation from McAdams (Ref. 32, p. 268).

$$Nu = (Pr)^{0.3} \{0.35 + 0.56 \ (Re)^{0.52}\} \qquad (II-13)$$

The dimensionless groups used in Eq. (II-13) are

$$\text{Nusselt number (Nu)} = hD/k$$

$$\text{Prandtl number (Pr)} = \mu c_p/k$$

$$\text{Reynolds number (Re)} = Dv\rho/\mu$$

where h = convective heat transfer coefficient

D = diameter

k = thermal conductivity

μ = viscosity

C_p = heat capacity

v = velocity

ρ = density

The physical properties are usually evaluated at the arithmetic average film temperature. McAdams recommends Eq. (II-13) for the heating of single cylinders by liquids. The mixed gas velocities in Kilham's experiments were 2.38 ft/sec and 3.06 ft/sec.

Anderson and Stresino (Ref. 3) measured the heat transfer from oxygen-hydrogen, air-methane and several other similar combustion mixtures. Their study covered flame or jet velocities from 1 to 4600 ft/sec. In all their results radiation was reported to be negligible. For the low velocity tests using air-methane flames the heat transfer rates near the center of the jet ranged from 57,000 to 83,000 Btu/hr-ft^2. They apparently used the family of equations from McAdams (Ref. 32, p. 252-261) for air flow normal to a single

cylinder to calculate the convective heat transfer coefficient. Using coefficients from this equation, calculated theoretical flame temperatures, and a rather complex correction for the thermal conductivity of dissociated hydrogen, they calculated heat transfer rates within 25 percent of the measured values for the low velocity air-methane flames. There is some question whether the thermal conductivity correction was applied to the low velocity flames. There is no apparent reason why the radiation could be neglected by Anderson and Stresino but was found to account for at least 15 percent of the heat transfer in Kilham's work.

Zartman and Churchill (Ref. 47) measured the heat transfer from propane-air flames inside a 5-inch diameter burner tube. For their low velocity flames they reported peak heat transfer rates of 25,000 Btu/hr-ft^2. They calculated the radiant heat contribution, using techniques from McAdams, to be 10 to 20 percent of the total heat transferred to the burner tube. This percentage implies that the convective heating was 20,000 to 22,500 Btu/hr-ft^2.

Thomas, Baldwin, and Heselden (Ref. 37) measured the convective and radiant heat transfer from alcohol and wood crib fires. The measurements were made 1 to 2 cm above the surface of the fuel. They reported a total heat transfer rate of 13,800 Btu/hr-ft^2 for alcohol fires and

that convection accounted for 21 percent of the total. The wood fires had peak total heat transfer rates of 9,300 to 17,650 Btu/hr-ft^2 and convection accounted for 19 to 23 percent of the total.

Since there is so little published data on convective heating in flames it is not surprising that none of the available correlations for convective coefficients include any data from flames. Indeed, most of the natural convection coefficient correlations are based on experimental data where only moderate temperature differences were employed.

The results of many tests on the heating of gases by horizontal cylinders are reported by Bird (Ref. 4), Kays (Ref. 25) and McAdams (Ref. 32). The test data are correlated very well by log-log plots of the Nusselt number vs. the product of the Prandtl and Grashof number. The Grashof number is defined as

$$Gr = \frac{g \beta \ell^3 \theta \rho}{\mu}$$

where g = gravitational constant

β = volumetric expansion coefficient

ℓ = characteristic height

θ = temperature difference above ambient

Schlichting (Ref. 35, p. 336) reports results by Hermann where the mean convective heat transfer coefficients around a cylinder were correlated by

$$Nu = 0.372(Gr)^{0.25} \qquad \text{(II-14)}$$

This correlation is for cylinders being heated by gases.

Kutateladze (Ref. 27, p. 294) reports a number of results for free convection heat transfer correlations which resemble Eq. (II-14); however, for small (Gr Pr) products he reports a correlation of

$$Nu = 1.18\ (Gr\ Pr)^{1/8} \qquad \text{(II-15)}$$

Also, he points out that for (Gr Pr) $< 10^3$ the shape of the body has an appreciable effect.

In much of the above work the data were for relatively small bodies, i.e. wires, small diameter tubing, etc. The heat transfer to relatively large cylinders may resemble that of vertical surfaces rather than small diameter cylinders.

Hsu (Ref. 22, p. 375) reports a survey made by Zijnen covering much of the published data over a variety of conditions. These data were correlated by

$$Nu = 0.544\ (Gr\ Pr)^{1/4} \qquad \text{(II-16)}$$

where all gas properties were evaluated at the average film temperature.

Douglas and Churchil (Ref. 13) surveyed the available literature and recorrelated the data for high

temperature difference convective heat transfer for both heating and cooling. Since their results were intended to apply to forced flow systems, some of the data did not correlate well due to natural convection effects. Plots of the data as Nu number vs Re number were presented; both the heating and cooling data correlated better when all properties were evaluated at the arithmetic average film temperature. This means using $Re = Dv_\infty \rho_f / \mu_f$ rather than $Dv_\infty \rho_\infty / \mu_f$. This result is consistent with the observations of Kays (Ref. 25, p. 268) that the variation of the properties with temperature tend to cancel each other out.

The correlations and coefficients considered up to this point are for non-reacting systems at thermodynamic equilibrium where temperature difference is the only significant driving force for heat transfer. As discussed previously, these conditions may not apply to flames. Heat transfer inside flames is to some extent heat transfer in a reacting gas mixture where the temperature due to kinetic energy of the molecules may not be the dominant feature of non-radiant heat transfer.

The rate of heat transfer in reacting gas systems is frequently several times the maximum rate predicted using non-reacting convection coefficients and temperature difference, as reported by Woodruff and Giedt (Ref. 46). In reacting gas systems a significant heat transfer

contribution arises from the movement of activated species across the boundary layer. This movement may be Fickian diffusion where the activated species disappears at the cool surface or the result of random motion where the activated species simply gives up its activation energy at the cool surface.

Heat transfer in such mixtures has been the subject of many publications. One of the best discussions of this phenomenon is by D. B. Spalding and F. Bosnjakovic' in Ref. 24. Most of the investigations have been limited to systems where the activated enthalpy is dominated by the dissociation energy of O_2, H_2 and other simple molecules; however, dissociation of most chemical species is not appreciable below 2000-3000°K. Since flame temperatures will be below the equilibrium adiabatic temperature, 2000-2200°K (Ref. 33), of hydrocarbon-air reactions, it seems likely that dissociation energies will not contribute much to heat transfer in flames. However, since a turbulent flame is to some extent a reacting system throughout its volume, an object immersed in the flame will be occasionally wiped by a reaction interface and may receive considerable reaction or activation energy.

Considering the above discussion, it must be concluded that the convective heat transfer inside a flame should be higher than that predicted by correlations based on moderate temperature differences and non-

reacting systems. For comparison purposes, natural convection heat transfer coefficients have been calculated using the several correlations reported here.

Accurate knowledge of a diffusion flame composition and thermal transport properties seems hopeless, and results which incorporate involved calculations are not warranted unless they are accurate. Therefore, the physical properties of air were assumed for the flames. The air temperature was assumed to be 2200°F which corresponds to uncontrolled buoyant diffusion flame temperatures measured by Welker (Ref. 43). The air properties were evaluated at the arithmetic average film temperature except the volumetric expansion coefficient in the Grashof number which was evaluated at the air temperature. A small target with a characteristic length of 3 inches was assumed, and the target surface temperature was assumed to vary between 300°F and 1800°F. The Pr number varied from 0.62 to 0.755 and the (Gr Pr) product varied from 1.64×10^5 to 2.12×10^4 over the above temperature range.

Since the upward velocity of buoyant diffusion flame gases are on the order of several feet per second, some forced flow convective heat transfer coefficients were calculated using a gas velocity of 3 feet per second. Following the results of Douglas and Churchill the gas properties were evaluated at the average film temperature.

The resulting Re number varied from 589 to 418.

The calculated convective coefficients are presented in Table II-2. Across the large temperature difference (1900°F) the natural convective heating varies from 2,300 to 3,200 Btu/hr-ft^2.

Considering the convective heat transfer coefficients calculated for non-reacting systems and the possibility of additional reactive energy heat transfer by convection, the effective convective heat transfer coefficient for a buoyant diffusion fire should exceed 2.0 Btu/hr-ft^2°F.

TABLE II-2

CALCULATED FREE AND FORCED CONVECTION HEAT TRANSFER COEFFICIENTS

Correlation	Reference Source	Convection Heat Transfer Coefficient at Cool Surface Temperatures °F	
		300°F	1800°F
$Nu = 0.372\ (Gr)^{1/4}$	Reference 35 p. 336	1.21	0.76
$Nu = 0.544\ (Gr\ Pr)^{1/4}$	Reference 22 p. 375	1.56	1.02
$Nu = 0.59\ (Gr\ Pr)^{1/4}$	Reference 4 p. 413	1.72	1.12
$Nu = (Pr)^{0.3}\ [0.35 + 0.56\ (Re)^{0.52}]$	Reference 32 p. 268	1.95	1.91
Graphical Presentation	Reference 13	2.8	2.3

CHAPTER III

THEORETICAL DEVELOPMENTS

General

The use of absorption-emission coefficient data to calculate the radiant heat transferred to a particular target from a specified flame requires integration of Eq. (II-12) over the "visible" flame volume. The geometric relationships between the target and the flame must be developed and applied to Eq. (II-12). The development of the geometrical relationships and the numerical integration of the resulting equations for a target surrounded by flame and for a target located external to a flame are presented in this chapter. Shahrokhi (Ref. 36) has previously developed and solved the equations for the radiant heating of a target external to a cylindrical flame; however, the approach presented here is somewhat different.

Analytical integration of the radiant heating equations are possible for some hypothetical flame shapes which may have some interest and applicability. These special cases are presented in Appendix B.

Radiant Heating of Test Cylinder Surrounded by a Flame

The basic equations for the radiant heating of a target surrounded by a flame can be derived in several ways. In this development the flames will be assumed to have the shape of a right circular cylinder. The cylindrical target will be located at various heights in the flame; its axis concentric with that of the flame. The equations will be derived using horizontal and directional angles rather than the usual polar and azimuthal angles because the relationships between the angles and the flame depth are simpler for the integration over the various flame surfaces. Figure (III-1) shows the details of the system geometry. A more formal development of the equations describing the radiant heat transfer inside an absorbing-emitting medium is presented in Appendix C.

The angle ζ is the horizontal directional angle parallel to the base of the flame cylinder.

The angle ξ is the vertical directional angle always in a plane perpendicular to the base of the flame cylinder and containing the flame depth r.

The monochromatic radiant power incident on the target surface from a volume element along r is

$$- \Delta Q_\lambda = J_\lambda e^{-\beta_\lambda r} \; (t\Delta\zeta)(r\Delta\xi) \; \Delta r \; \Delta\Omega \qquad \text{(III-1)}$$

where $\Delta\Omega$ is the solid angle to the target surface and t is the projected flame depth. The radiant power term is

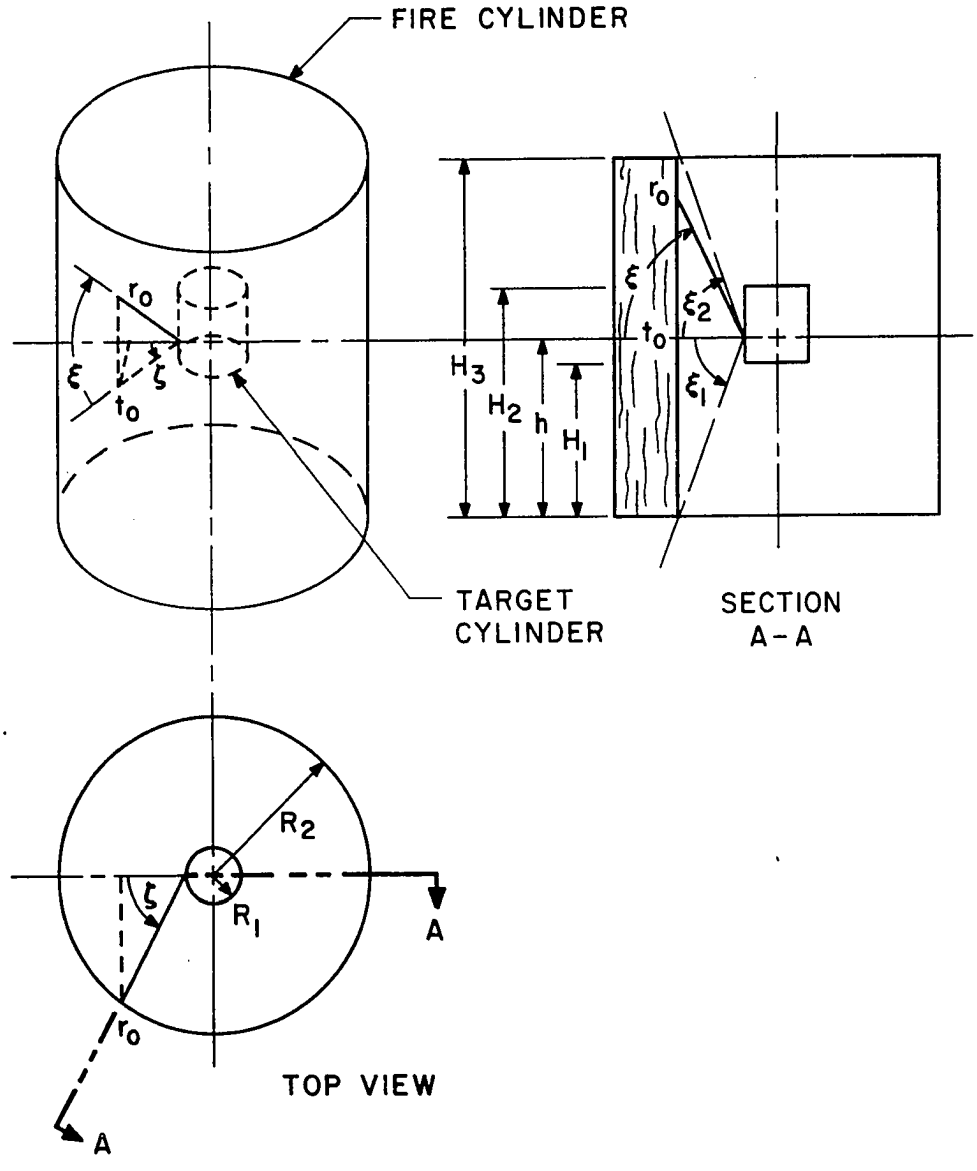

Figure III-1. System Geometry for Cylindrical Target Surrounded by a Cylindrical Flame.

negative with respect to the positive direction of r.

The point of reference of the radiant flux in Eq. (III-1) is different from that used in Eq. (II-11). The intensity used in Eq. (II-11) is at the particular location along the path length. The radiant flux used in Eq. (III-1) is the radiation arriving at the target after traveling the length of the optical path.

The flame depth, r, and the projected flame depth, t, are related by

$$r = t/\cos \xi \qquad \text{(III-2)}$$

Eliminating t from Eq. (III-1) yields

$$-\Delta Q_\lambda = J_\lambda e^{-\beta_\lambda r} (r^2 \cos \xi) \Delta\zeta \, \Delta\xi \, \Delta r \, \Delta\Omega \qquad \text{(III-3)}$$

The solid angle of the element of target surface perpendicular to r is

$$\Delta\Omega = \frac{A_T \cos\zeta \cos\xi}{r^2} \qquad \text{(III-4)}$$

where A_T is the area element on the target surface.

For most cases of interest the flame cylinder will not be so much larger than the target cylinder that the incident radiation can be considered constant over the target surface. Therefore, the target area is divided out and an expression for the incident power per unit target area from a differential flame element results after substituting Eq. (III-4) into Eq. (III-3).

$$-\frac{\Delta Q_\lambda}{A_T} = J_\lambda e^{-\beta_\lambda r} \cos^2\xi \cos\zeta \, \Delta\zeta \, \Delta\xi \, \Delta r \qquad \text{(III-5)}$$

The total power per unit target area is given by the integral of Eq. (III-5)

$$-\frac{dQ_\lambda}{A_T} = \int_{\zeta=-\frac{\pi}{2}}^{\zeta=\frac{\pi}{2}} \int_{\xi=-\frac{\pi}{2}}^{\xi=\frac{\pi}{2}} \int_{r=0}^{r=r_o(\xi,\zeta)} J_\lambda e^{-\beta_\lambda r} \cos^2\xi \cos\zeta \, d\zeta \, d\xi \, dr \qquad \text{(III-6)}$$

Since ξ and ζ are constant along any given optical path the first integration can be carried out and the boundary condition that $Q_\lambda=0$ at $r=r_o$ applied to obtain

$$-\frac{Q_\lambda}{A_T}\Bigg]_{Q_\lambda}^{0} = \int_{-\frac{\pi}{2}}^{\frac{\pi}{2}} \int_{-\frac{\pi}{2}}^{\frac{\pi}{2}} -\frac{J_\lambda}{\beta_\lambda} e^{-\beta_\lambda r} \cos^2\xi \cos\zeta \, d\zeta \, d\xi \Bigg]_0^{r_o(\xi,\zeta)} \qquad \text{(III-7)}$$

and subsequently

$$\frac{Q_\lambda}{A_T} = \int_{-\frac{\pi}{2}}^{\frac{\pi}{2}} \int_{-\frac{\pi}{2}}^{\frac{\pi}{2}} \frac{J_\lambda}{\beta_\lambda} (1-e^{-\beta_\lambda r_o}) \cos^2\xi \cos\zeta \, d\zeta \, d\xi \qquad \text{(III-8)}$$

The relationship defining r_o as a function of ζ and ξ is different for the bottom, sidewall and top surfaces. Along the sidewall surface the flame depth is related to the projected flame depth by

$$r_o = t_o/\cos\ \xi \qquad \text{(III-9)}$$

The projected flame depth can be obtained in terms of known parameters from the law of cosines

$$R_2^2 = t_o^2 + R_1^2 - 2t_oR_1\ \cos\ (\pi - \zeta) \qquad \text{(III-10)}$$

where R_2 = radius of flame cylinder

R_1 = radius of target cylinder

Rearranging and solving for t_o yields

$$t_o = -R_1\ \cos\zeta + \sqrt{R_1^2\ \cos^2\zeta + (R_2^2 - R_1^2)} \qquad \text{(III-11)}$$

The contribution from the sidewall surface is then

$$\left.\frac{Q_\lambda}{A_T}\right)_s = \frac{J_\lambda}{\beta_\lambda} \int_{-\frac{\pi}{2}}^{\frac{\pi}{2}} \int_{\xi_1}^{\xi_2} [1 - e^{-\beta_\lambda t_o/\cos\xi}]\cos^2\xi\ \cos\zeta\ d\xi\ d\zeta \qquad \text{(III-12)}$$

The limits on ξ are

$$\xi_1 = -\tan^{-1}(h/t_o) \qquad \text{(III-13)}$$

and

$$\xi_2 = \tan^{-1}[(H_3 - h)/t_o] \qquad \text{(III-14)}$$

where h = height of the area element on the target cylinder

H_3 = height of the flame cylinder

Both ξ_1 and ξ_2 are functions of ζ through Eq. (III-11).

Along the bottom surface of the fire cylinder the flame depth is again related to the projected fire depth by Eq. (III-9). The projected flame depth can now be expressed as a function of ξ only.

$$t_o = h/\tan \xi \qquad \text{(III-15)}$$

so that the flame depth can be expressed as

$$r_o = h/\sin \xi \qquad \text{(III-16)}$$

The contribution from the bottom surface is given by Eq. (III-12) with limits of $-\pi/2$ and ξ_1 on ξ, and r_o is given by Eq. (III-16). The equation is

$$\left.\frac{Q_\lambda}{A_T}\right)_b = \frac{J_\lambda}{\beta_\lambda} \int_{-\frac{\pi}{2}}^{\frac{\pi}{2}} \int_{-\frac{\pi}{2}}^{\xi_1} [1 - e^{-\beta_\lambda h/\sin \xi}] \cos^2\xi \cos\zeta \, d\xi \, d\zeta \qquad \text{(III-17)}$$

The equations for the top surface are the same as those for the bottom surface except h is replaced by $(H_3 - h)$ and the integration limits are ξ_2 and $\frac{\pi}{2}$. The contribution from the top surface is given by

$$\left.\frac{Q_\lambda}{A_T}\right)_t = \frac{J_\lambda}{\beta_\lambda} \int_{-\frac{\pi}{2}}^{\frac{\pi}{2}} \int_{\xi_2}^{\frac{\pi}{2}} [1 - e^{-\beta_\lambda (H_3-h)/\sin \xi}] \cos^2\xi \cos\zeta \, d\xi \, d\zeta \qquad \text{(III-18)}$$

The sum of the results for the top, bottom and sidewall surfaces gives the power striking a unit target area. To obtain the total monochromatic power over the target surface it is necessary to integrate over the height and circumference of the target surface. The equations are

$$Q_\lambda = \int_{A_T} \left[\left(\frac{Q_\lambda}{A_T} \right)_s + \left(\frac{Q_\lambda}{A_T} \right)_b + \left(\frac{Q_\lambda}{A_T} \right)_t \right] dA_T \qquad \text{(III-19)}$$

Expanding in terms of the target area yields

$$Q_\lambda = \int_{h=H_1}^{h=H_2} \int_{\psi=0}^{\psi=2\pi} \left[\left(\frac{Q_\lambda}{A_T} \right)_s + \left(\frac{Q_\lambda}{A_T} \right)_b + \left(\frac{Q_\lambda}{A_T} \right)_t \right] R_1 \, d\psi \, dh \qquad \text{(III-20)}$$

where ψ is the azimuthal angle about the center line of the target cylinder and H_1 and H_2 are the bottom and top heights of the target cylinder.

The first integration can be performed since the system is assumed to be symmetric about the center line axis

$$Q_\lambda = 2\pi R_1 \int_{H_1}^{H_2} \left[\left(\frac{Q_\lambda}{A_T} \right)_s + \left(\frac{Q_\lambda}{A_T} \right)_b + \left(\frac{Q_\lambda}{A_T} \right)_t \right] dh \qquad \text{(III-21)}$$

Finally, to obtain the total radiant power incident on the target surface the monochromatic results must be

integrated over all wavelengths or rather, over all wavelengths which contribute significantly to the heating. This integration is simply expressed as

$$Q = \int_{\lambda_1}^{\lambda_2} Q_\lambda d\lambda \qquad \text{(III-22)}$$

The several integrals were evaluated using Gauss Quadrature approximations over the angles and the trapezoidal rule over the wavelengths. The applicability of these techniques is discussed in Appendix B.

Radiant Heating of a Target External to a Cylindrical Flame

In this development the target is assumed to be a small or differential area located so it sees the cylindrical surface of a right circular cylinder of flame. As with the previous development the major angles will be horizontal and directional rather than polar and azimuthal. Figure III-2 shows the details of the system geometry.

The angle ζ is the horizontal directional angle parallel to the base of the flame cylinder.

The angle ξ is the vertical directional angle always in a plane perpendicular to the base of the flame cylinder and containing the flame thickness, r.

The angle δ is the polar angle defining the orientation of the target area with respect to the

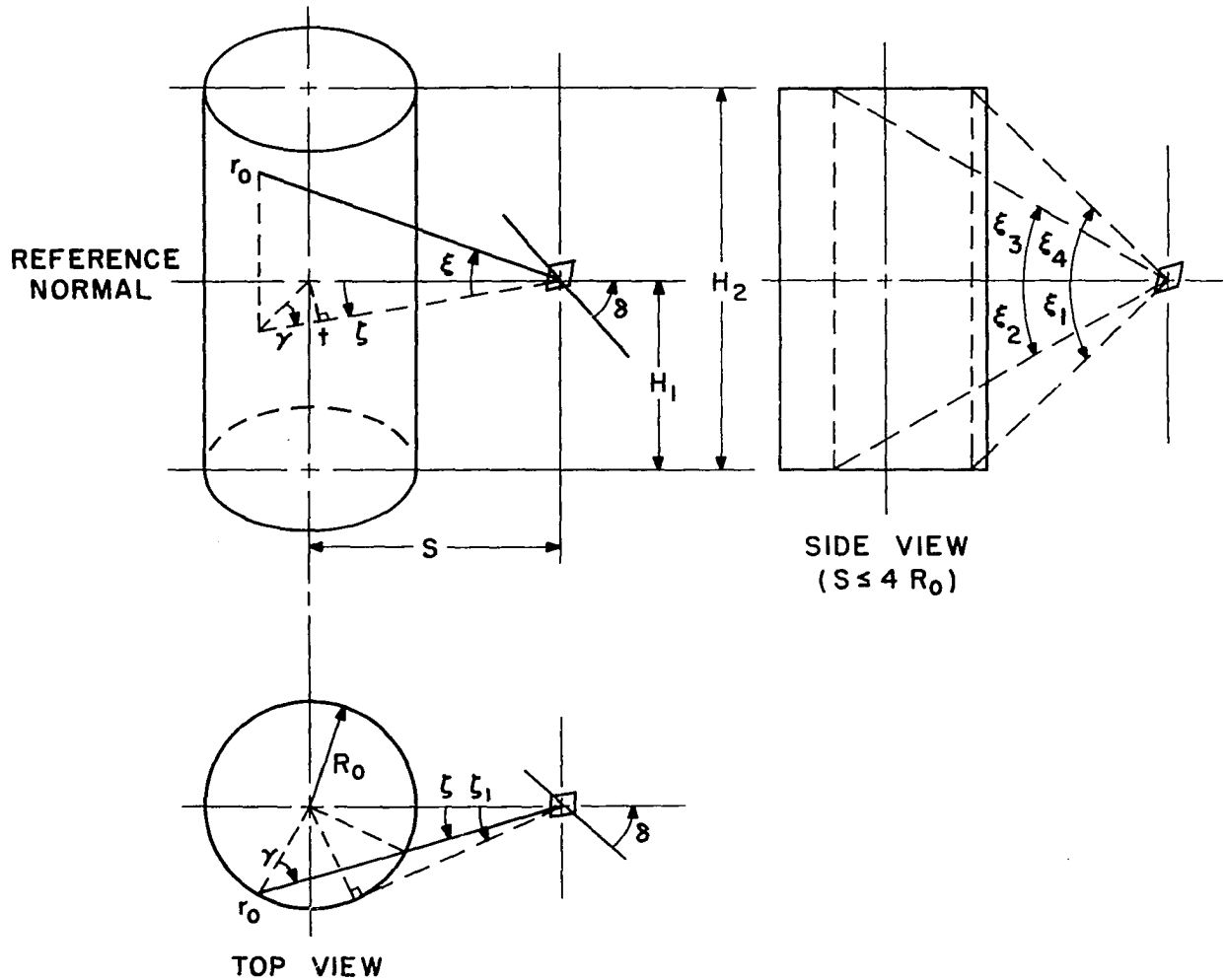

Figure III-2. System Geometry for Target External to a Cylindrical Flame.

reference normal between the fire cylinder and the target.

The monochromatic power incident on the target from a volume element along r is

$$-\Delta Q_\lambda = J_\lambda e^{-\beta_\lambda r} (t\Delta\zeta)(t\Delta\xi/\cos\xi)\Delta r\ \Delta\Omega \qquad \text{(III-23)}$$

where $\Delta\Omega$ is the solid angle to the target surface and t is the projected distance between the target and the center of the flame thickness. The radiant power term is negative with respect to the positive direction of r.

The solid angle of the element of target surface perpendicular to r is

$$\Delta\Omega = \frac{A_T \cos\delta \cos\zeta \cos\xi}{(t/\cos\xi)^2} \qquad \text{(III-24)}$$

The product $A_T \cos\delta$ is simply the target area perpendicular to the system reference normal.

An expression for the incident power per unit target area from a differential flame element results from substituting Eq. (III-24) into Eq. (III-23) and simplifying

$$-\frac{\Delta Q_\lambda}{A_T} = J_\lambda e^{-\beta_\lambda r} \cos\delta \cos^2\xi \cos\zeta\ \Delta\zeta\ \Delta\xi\ \Delta r \qquad \text{(III-25)}$$

The total power per unit target area is given by the integral of Eq. (III-25)

$$-\frac{dQ_\lambda}{A_T} = 2\int_0^{\zeta_1}\int_{\xi_1}^{\xi_4}\int_{r=0}^{r=r_o(\xi,\zeta)} J_\lambda e^{-\beta_\lambda r}\cos\delta\,\cos^2\xi\,\cos\zeta\,d\zeta\,d\xi\,dr \qquad \text{(III-26)}$$

Since ξ and ζ are constant along any given optical path the first integration can be carried out and the boundary conditions that $Q_\lambda=0$ at $r = r_o$ applied to obtain

$$-\frac{Q_\lambda}{A_T}\Bigg]_{Q_\lambda}^{0} = 2\int_0^{\zeta_1}\int_{\xi_1}^{\xi_4} -\frac{J_\lambda}{\beta_\lambda} e^{-\beta_\lambda r}\cos\delta\,\cos^2\xi\,\cos\zeta\,d\zeta\,d\xi \Bigg]_0^{r_o(\xi,\zeta)} \qquad \text{(III-27)}$$

and subsequently,

$$\frac{Q_\lambda}{A_T} = 2\int_0^{\zeta_1}\int_{\xi_1}^{\xi_4} \frac{J_\lambda}{\beta_\lambda}\left[1-e^{-\beta_\lambda r_o}\right]\cos\delta\,\cos^2\xi\,\cos\zeta\,d\zeta\,d\xi \qquad \text{(III-28)}$$

The relationship defining r_o as a function of ζ and ξ is different for the bottom, sidewall and top surfaces. For the sidewall, the projected distance between the target and the center of the flame thickness is

$$t = S\cos\zeta \qquad \text{(III-29)}$$

where S is the separation distance between the target and the flame cylinder center line. The flame thickness may be determined from

$$r_o = 2R_o \cos\gamma/\cos\xi \qquad \text{(III-30)}$$

where R_o is the radius of the flame cylinder. The angle γ is shown on Figure III-2 and may be determined from the law of sines as

$$\sin\gamma = \frac{S \sin\zeta}{R_o} \qquad \text{(III-31)}$$

The contribution from the sidewall surface is then

$$\left.\frac{Q_\lambda}{A_T}\right|_s = 2\,\frac{J_\lambda}{\beta_\lambda}\cos\delta \int_0^{\zeta_1}\int_{\xi_2}^{\xi_3} [1-\exp(-\beta_\lambda 2R_o\,\cos\gamma/\cos\xi)]\cos^2\xi\,\cos\zeta\,d\xi\,d\zeta \qquad \text{(III-32)}$$

The limits on ξ, both functions of ζ, are

$$\xi_2 = -\tan^{-1}[H_1/(t + R_o\cos\gamma)] \qquad \text{(III-33)}$$

and

$$\xi_3 = \tan^{-1}[(H_2 - H_1)/(t + R_o\cos\gamma)] \qquad \text{(III-34)}$$

where H_1 = height of the target element

H_2 = height of the flame cylinder

The limit on ζ is

$$\zeta_1 = \sin^{-1}(R_o/S) \qquad \text{(III-35)}$$

For the bottom surface of the fire cylinder the projected distance from the target to the bottom surface is dependent only on ξ, and is given by

$$t_2 = H_1/\tan \xi \qquad \text{(III-36)}$$

The projected distance from the target to the front surface of the flame cylinder is dependent on ζ and is given by

$$t_1 = t - R_o \cos\gamma \qquad \text{(III-37)}$$

where γ is defined by Eq. (III-31). The fire depth is then

$$r_o = (t_2 - t_1)/\cos\xi \qquad \text{(III-38)}$$

$$r_o = \left(\frac{H_1}{\tan \xi} - S \cos\zeta + R_o \cos\gamma \right)/\cos\xi \qquad \text{(III-39)}$$

The limits on ξ are ξ_1 and ξ_2. The latter is given by Eq. (III-33) and the former is given by

$$\xi_1 = -\tan^{-1}[H_1/(t - R_o \cos\gamma)] \qquad \text{(III-40)}$$

The contribution from the bottom surface, Eq. (III-32) with different limits on ξ and with r_o defined by Eq. (III-39), is

$$\left.\frac{Q_\lambda}{A_T}\right)_b = 2\,\frac{J_\lambda}{\beta_\lambda}\cos\delta \int_0^{\zeta_1}\int_{\xi_1}^{\xi_2} \{1 - \exp[-\beta_\lambda(\frac{H_1}{\tan\xi} - S\cos\zeta$$

$$+ R_o\cos\gamma)/\cos\xi]\}\cos^2\xi\cos\zeta\,d\zeta\,d\xi \qquad \text{(III-41)}$$

The equations for the contribution from the top surface are the same as those for the contribution from the bottom surface except H_1 is replaced by $(H_2 - H_1)$ and the integration limits are ξ_3 and ξ_4. The parameters are given by

$$t_2 = (H_2 - H_1)/\tan\xi \qquad \text{(III-42)}$$

$$r_o = \left[\frac{(H_2 - H_1)}{\tan\xi} - S\cos\zeta + R_o\cos\gamma\right] / \cos\xi \qquad \text{(III-43)}$$

$$\xi_4 = \tan^{-1}\left[(H_2 - H_1)/(t - R_o\cos\gamma)\right] \qquad \text{(III-44)}$$

The contribution from the top surface is then given by Eq. (III-32) with ξ_4 defined by Eq. (III-44) and r_o defined by Eq. (III-43).

$$\left.\frac{Q_\lambda}{A_T}\right|_t = 2\,\frac{J_\lambda}{\beta_\lambda}\cos\delta \int_0^{\zeta_1}\int_{\xi_3}^{\xi_4}\left\{1 - \exp\left[-\beta_\lambda\left(\frac{(H_2 - H_1)}{\tan\xi} - S\cos\zeta + R_o\cos\gamma\right)/\cos\xi\right]\right\}\cos^2\xi\,\cos\zeta\,d\zeta\,d\xi \qquad \text{(III-45)}$$

The limit ζ_1 is given by Eq. (III-35) and ξ_3 is given by Eq. (III-34).

The sum of the results for the top, bottom and sidewall surfaces gives the power striking a unit target area. The equation is

$$\frac{Q_\lambda}{A_T} = \left[\left(\frac{Q_\lambda}{A_T}\right)_s + \left(\frac{Q_\lambda}{A_T}\right)_b + \left(\frac{Q_\lambda}{A_T}\right)_t\right] \qquad \text{(III-46)}$$

As with all these calculations, the total power striking the target is given by integrating the monochromatic results per Eq. (III-22).

When the target to flame center line distance, S, is more than about 2 flame diameters, a reasonable approximation can be defined by using only the sidewall equation, Eq. (III-32), with slightly different limits on the vertical sweep angle, ξ. Figure III-3 is a sketch of this situation. The lower limit is determined from

$$\xi_A = \tan^{-1}(H_1/t) \qquad \text{(III-47)}$$

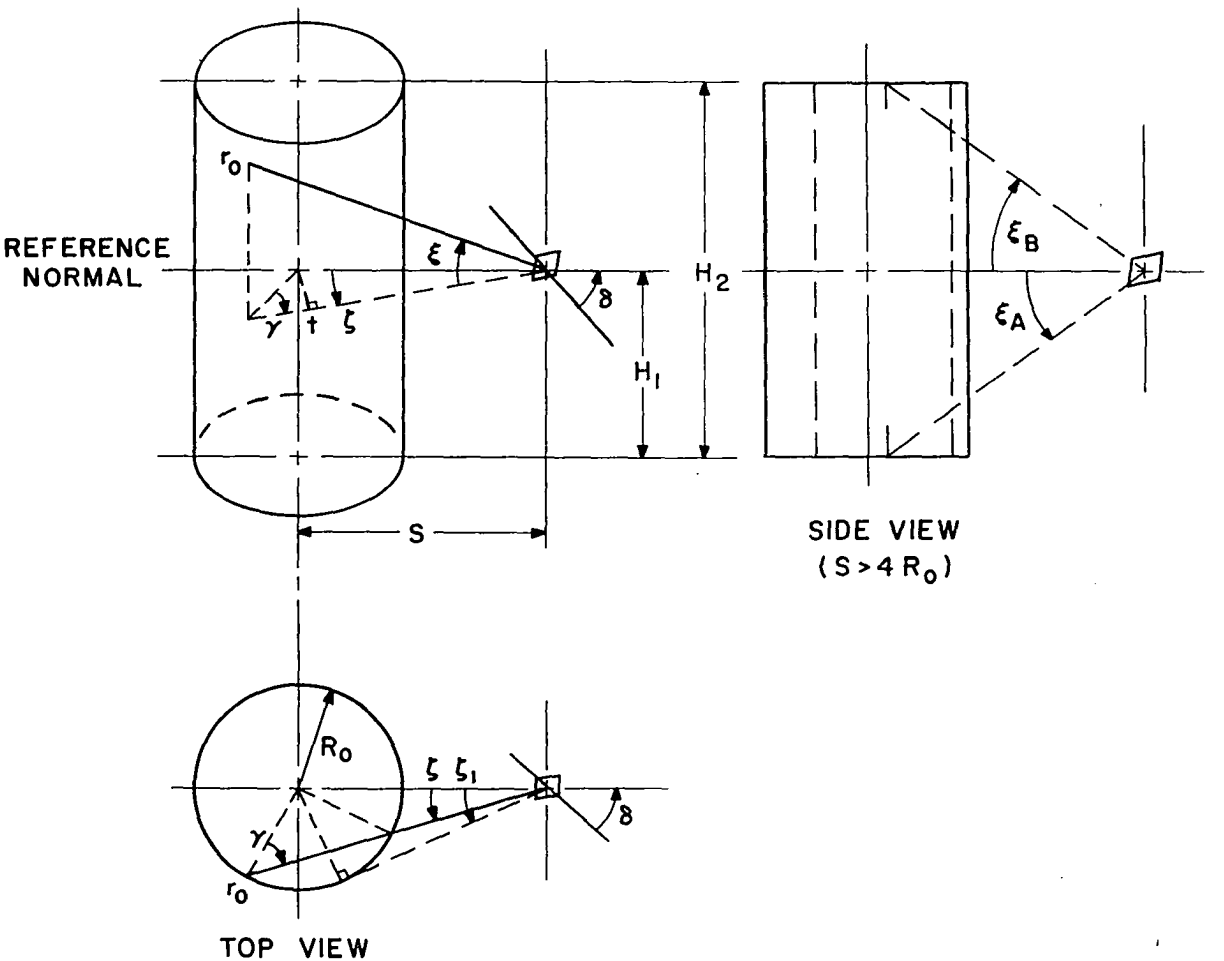

Figure III-3. Simplified Geometry for Target External to a Cylindrical Flame.

and the upper limit from

$$\xi_B = \tan^{-1} \left(\frac{H_2 - H_1}{t}\right) \qquad \text{(III-48)}$$

The projected distance between the target and center of the flame thickness, t, and the flame thickness, r_o, are given by Eq. (III-29) and (III-30), respectively. The monochromatic power striking the target is then given by

$$\frac{Q_\lambda}{A_T} = 2 \frac{J_\lambda}{\beta_\lambda} \cos\delta \int_0^{\zeta_1} \int_{\xi_A}^{\xi_B} [1-e^{-\beta_\lambda 2R_o \cos\gamma/\cos\xi}]\cos^2\xi \cos\zeta \, d\xi \, d\zeta \qquad \text{(III-49)}$$

The use of Gauss Quadrature to complete the geometric integrations and the trapezoid rule to complete the wavelength integrations are discussed in Appendix B. A 4-point Gauss Quadrature and the simple trapezoid rule were used in all the calculations.

CHAPTER IV

FACILITIES AND EQUIPMENT

Test Cylinders

The basic decision to use a water boiler design for the test probe was made in the process of preparing the research proposal (Ref. 31) for these experiments. The water boiler was chosen because it offered greater flexibility and less expensive auxiliary equipment even though its instrumentation and operation are more difficult.

A vertical cylinder was selected for the exposed or active test surface for several reasons: (1) The geometrical relationships associated with the radiation calculations are much simpler when the exposed surface is coaxial with the cylindrical shape of the fire. (2) The wetted area and liquid level changes are linear with respect to the inventory of water inside the boiler. (3) The convective heat transfer data from a small vertical cylinder is generally more applicable to all surfaces than that from a small horizontal cylinder. (4) A vertical cylinder disrupts the natural fire shape less than a horizontal cylinder.

The diameter of the cylinder (4.475 inches) was a compromise between disrupting the fire shape and providing room for a multiple thermocouple gland, inlet-outlet lines and protective insulation around these lines. The final dimensions resulted from smoothing the outside of a section of 4-inch heavy wall pipe.

Figures IV-1 and IV-2 are detail designs of the two test cylinders used. The thick wall cylinder was made from 304 stainless steel to provide a reasonably high outside surface temperature. The thin wall cylinder was made from brass. For an incident heat flux of 30,000 Btu/hr-ft^2 the ΔT across the stainless steel cylinder wall (k = 9.5 Btu/hr-ft^2°F/ft) was calculated to be 108°F and 5°F across the brass cylinder wall (k = 67. Btu/hr-ft^2°F/ft).

The bottom of each cylinder was insulated by a cap machined from grade A Lava stone purchased from the American Lava Corporation. The cap was packed with Johns-Mansville's Cerafelt high temperature insulation and attached to the cylinder by a single stainless steel screw. A small, stiff coil spring was placed between the screw head and the Lava cap to keep the cap firmly seated against the bottom of the cylinder. An additional 1/2-inch thick Lava plate was attached over the cap support screw and spring. This plate was attached to the Lava cap with two small stainless steel screws threaded into a yoke-nut placed inside the Lava cap. It should be mentioned that

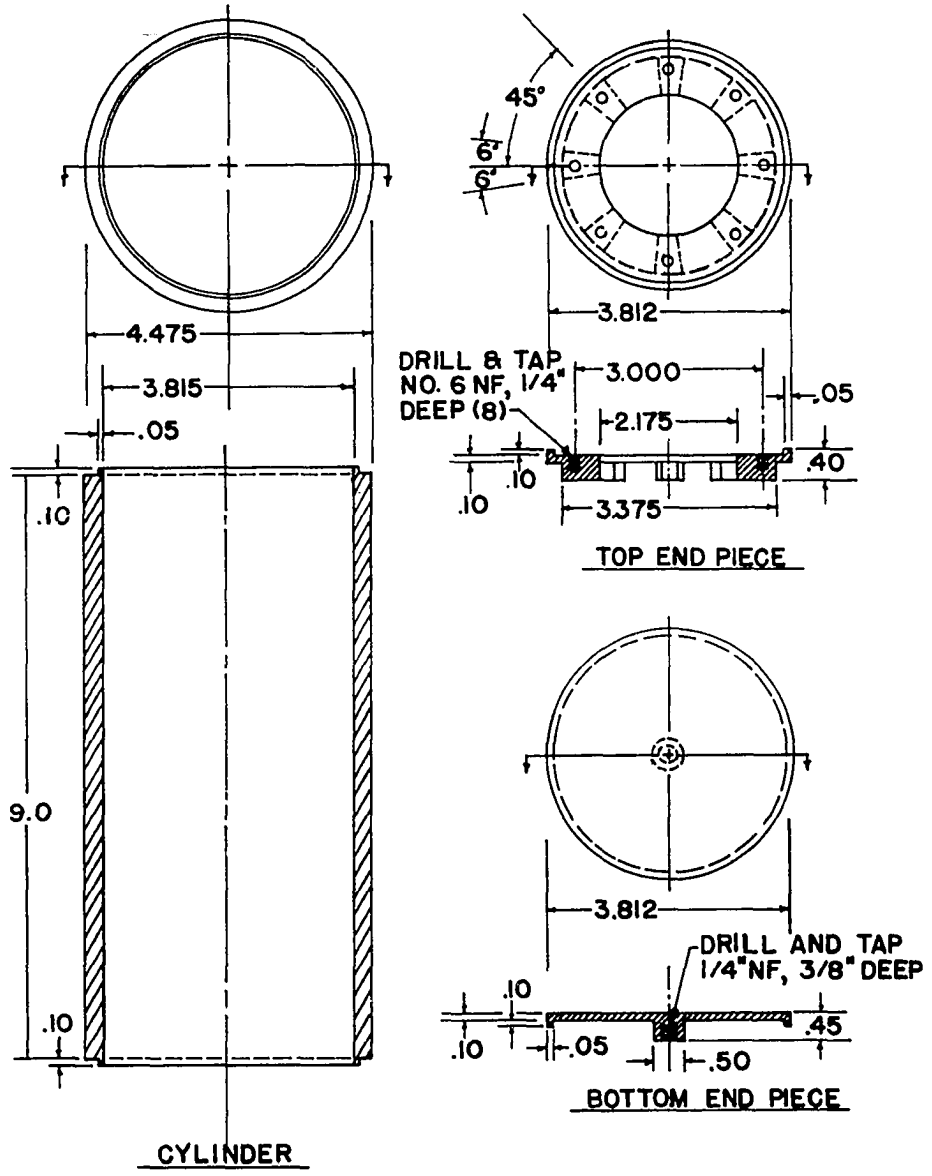

Figure IV-1. Thick-wall Test Cylinder.

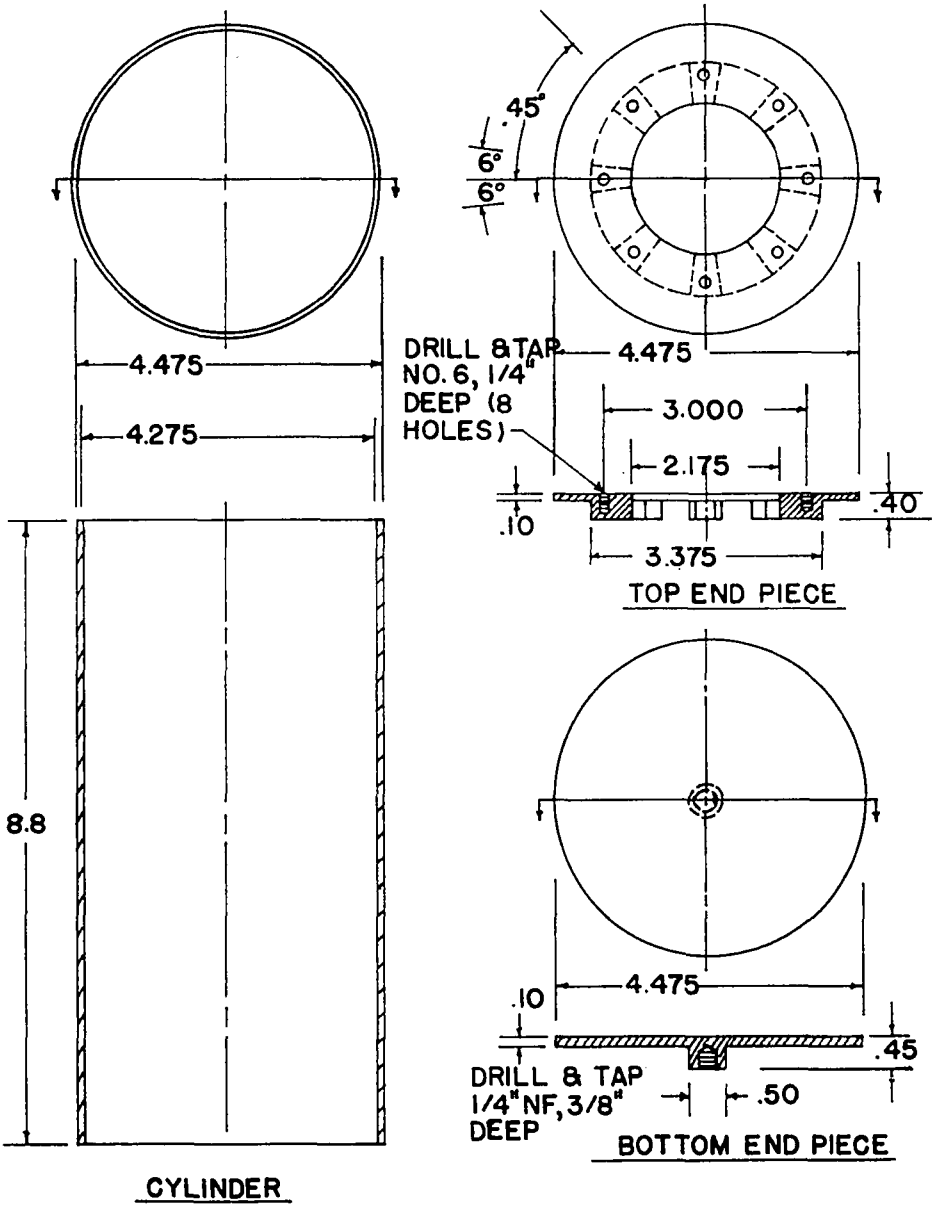

Figure IV-2. Thin-wall Test Cylinder.

in three attempts to dismantle the bottom insulator after repeated fire exposure the stainless steel screws galled and froze in the yoke nuts. These nuts were made from both carbon steel and stainless steel and liberal quantities of high temperature graphite lubricant were applied during assembly. A Lava ring was used as a transition piece between the insulated lead tube and the cylinder top. The Lava pieces are detailed on Fig. IV-3 and the metal pieces on Fig. IV-4.

Lead Tube

The lead tube assembly provided an insulated route for the coolant and instrument lines through the fire and into the test cylinder as well as primary support for the assembly. The mainstays of the lead tube were two 5-foot long pieces of 3-inch, sch. 40, 316 stainless steel pipe screwed into a 304 stainless steel pipe tee. The coolant and instrument lines were bundled in a cluster about 2 inches in diameter and routed through one branch of the support pipe. These lines made a right angle bend and extended down out the open side of the tee. The copper coolant lines (one 1/2-inch water inlet line and two 1/2-inch steam outlet lines) were soldered into a stainless steel top cap detailed on Fig. IV-5. The weight of the test cylinder and top cap were transmitted to the support pipe by a 3/8-inch diameter stainless steel rod which was threaded into a hole in the center of the top cap. This

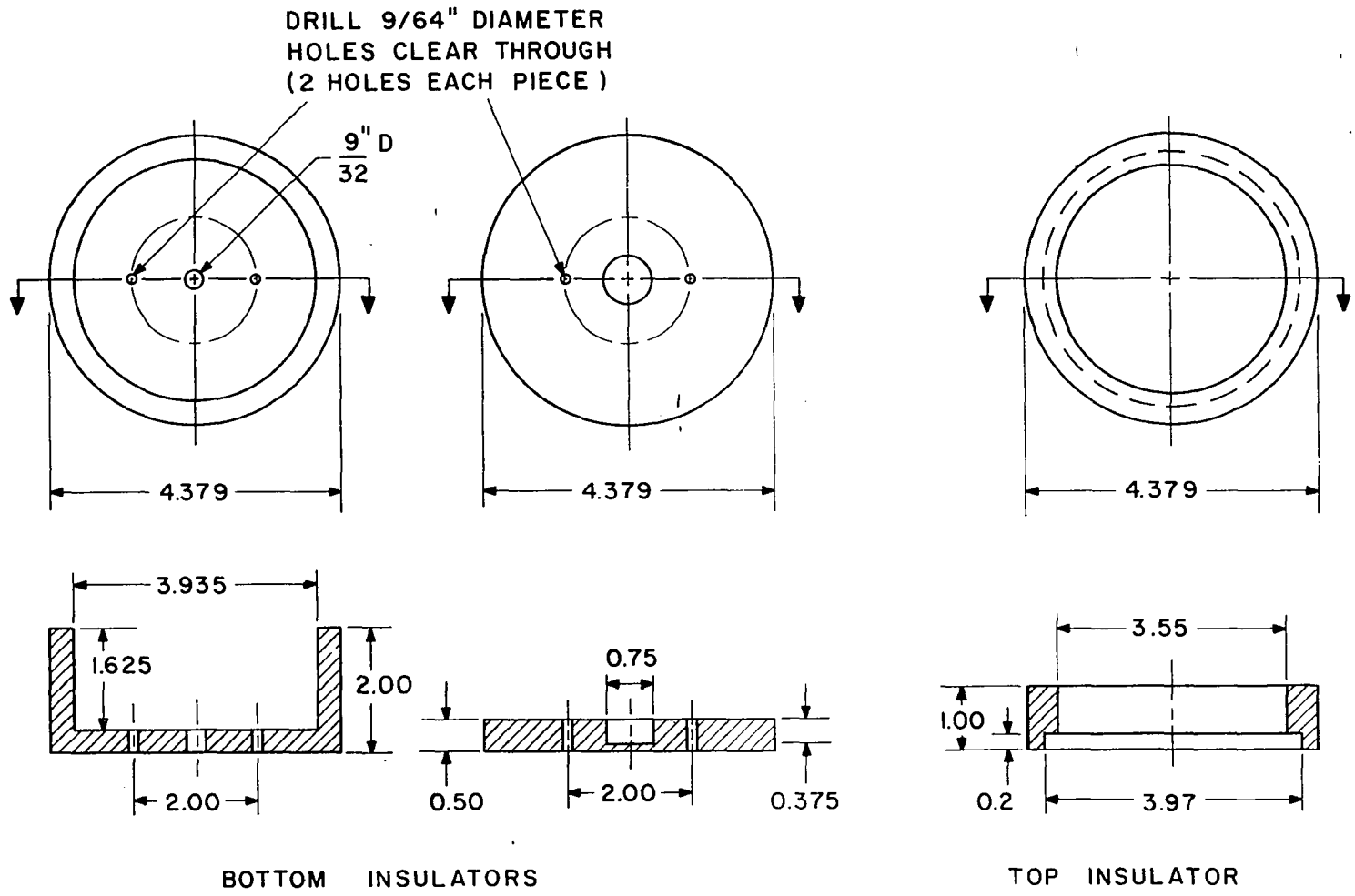

Figure IV-3. Insulating End Pieces for Test Cylinders.

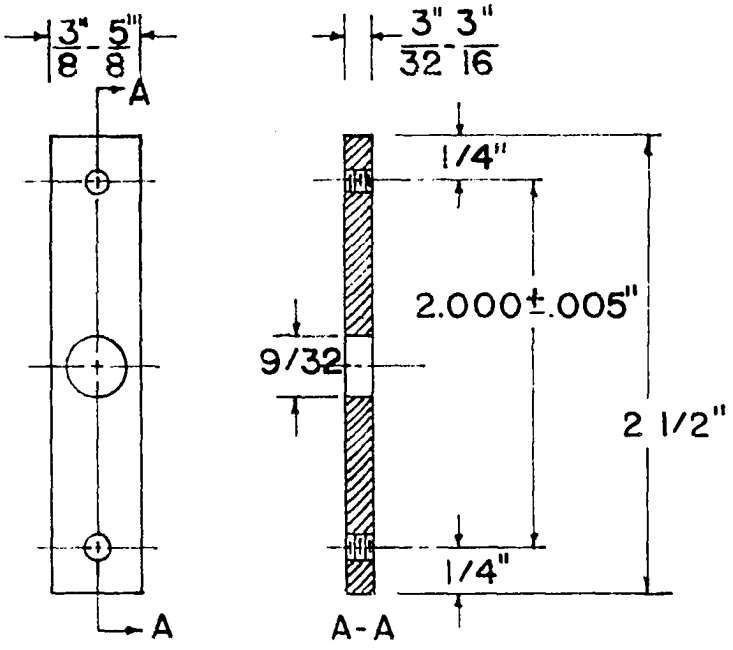

BOTTOM INSULATOR YOKE NUT

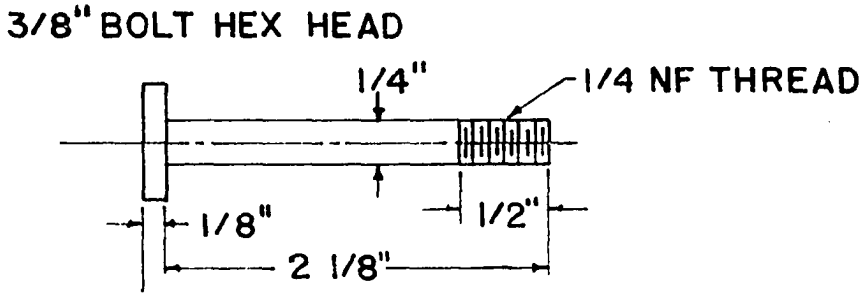

BOTTOM INSULATOR SUPPORT SCREW

Figure IV-4. Miscellaneous Metal Pieces for Test Cylinder.

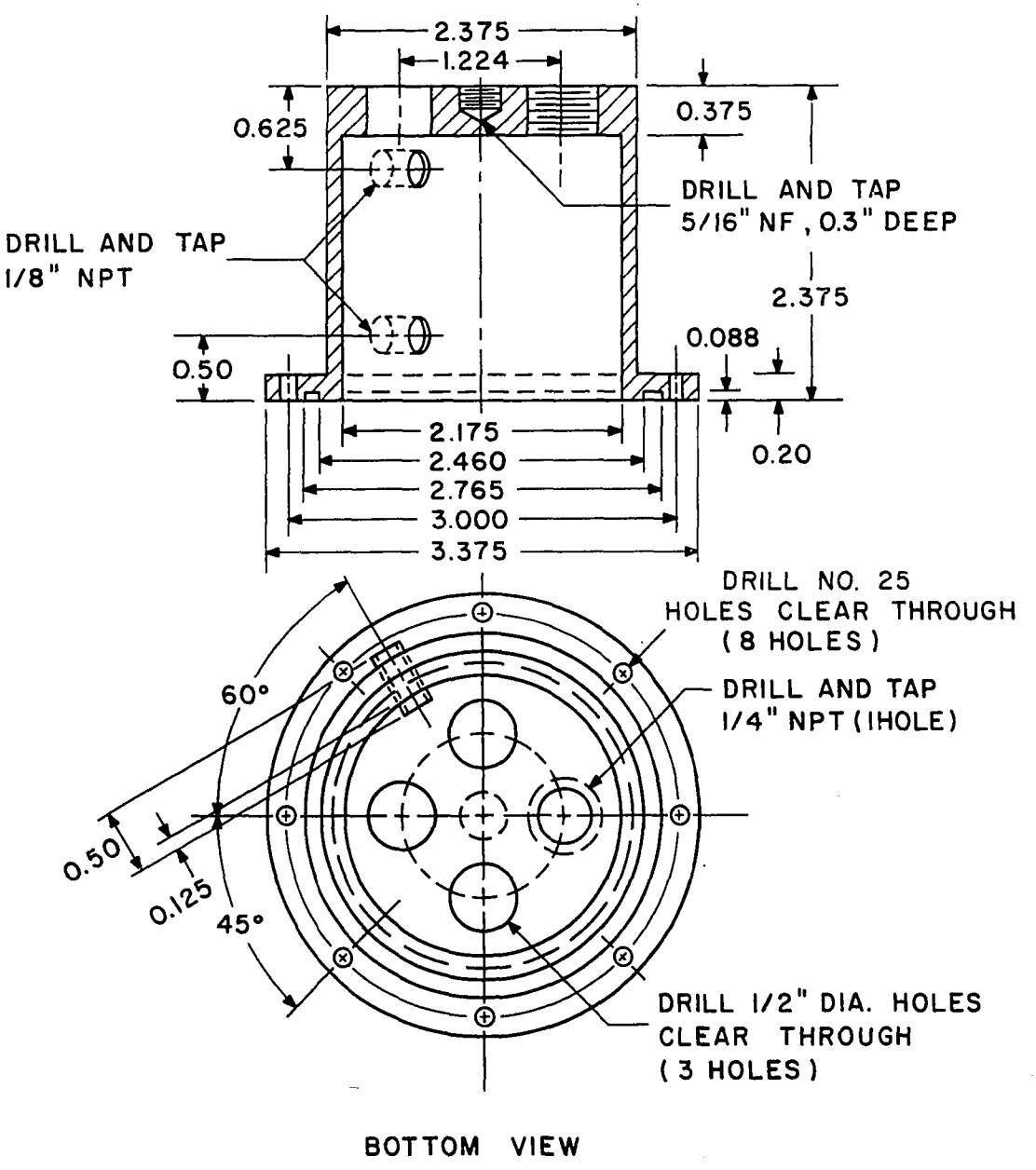

Figure IV-5. Test Cylinder Top Cap.

rod extended up through a hole drilled in the blind side of the pipe tee and was held by a heavy nut and support plate extending several inches along the length of the tee. These components are detailed on Fig. IV-6.

The test cylinder was attached to the top cap by eight 6-40 cap screws. An Inconel metal K-seal gasket, manufactured by the Haskell Engineering and Supply Co., was used between the test cylinder and top cap. A single gasket was used throughout the entire experiment without any apparent leakage. The actual operating pressure during a test was only a few inches of Hg, but the joint was tested repeatedly at city water pressure (about 40 psig) and assembled and disassembled many times.

An assembly drawing for the thin-wall test cylinder and lead tube is shown on Fig. IV-7.

The coolant lines were supported and aligned inside the lead tube by discs cut from asbestos millboard spaced about every 18 inches. The lines were held 3/8- to 1/2-inch apart and Cerafelt insulation was woven between them. The tubing bundle was wrapped with additional Cerafelt and the whole assembly was inserted inside the support pipe. Additional Cerafelt was wrapped around the outside of the support pipe and covered by 6-inch diameter galvanized stove pipe. This outside cover extended about 4 feet each side of the center tee. The outside of the pipe tee was covered by 1/2-inch of Cerafelt and a piece of 8-inch

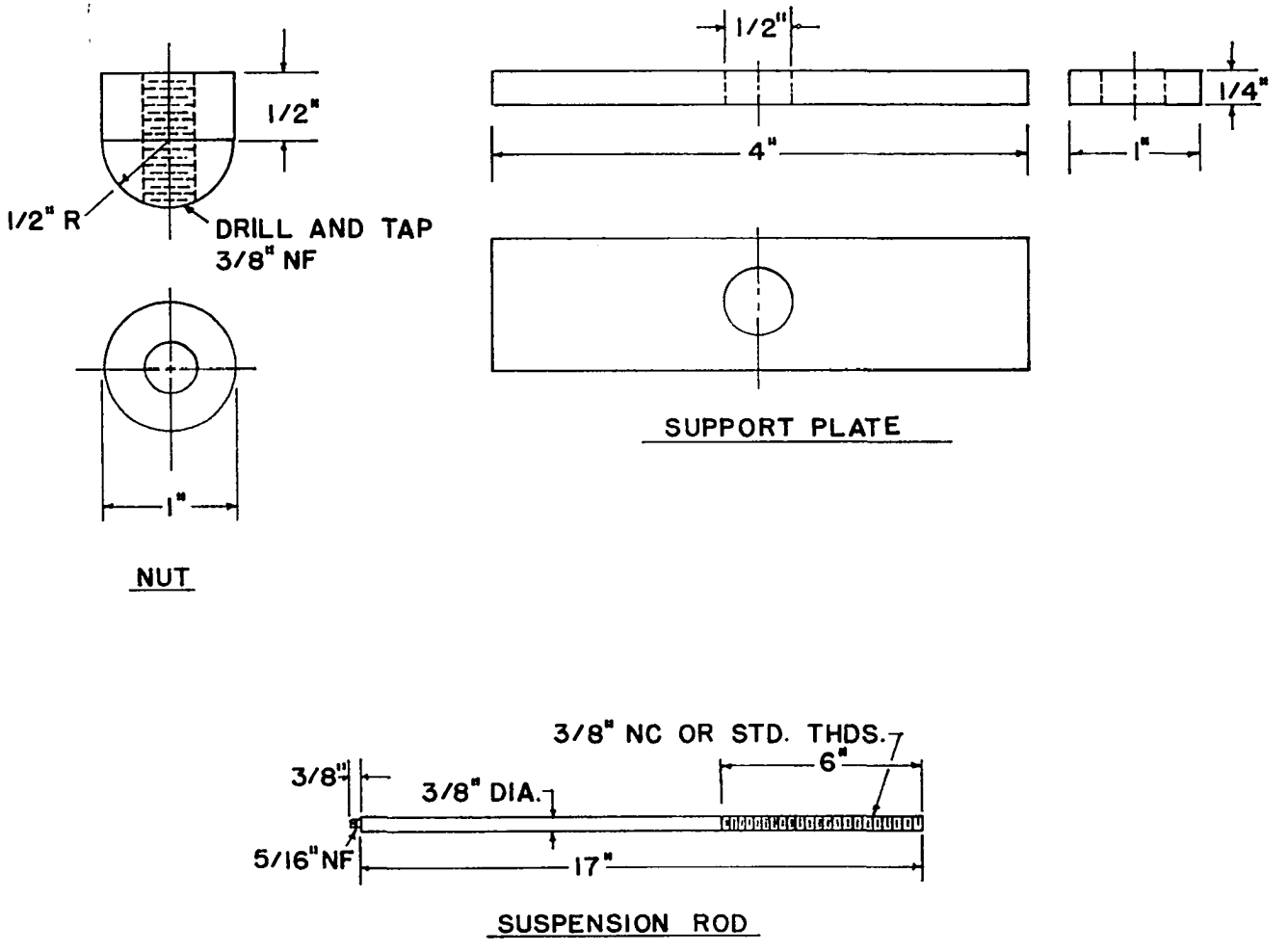

Figure IV-6. Miscellaneous Metal Pieces for Lead Tube.

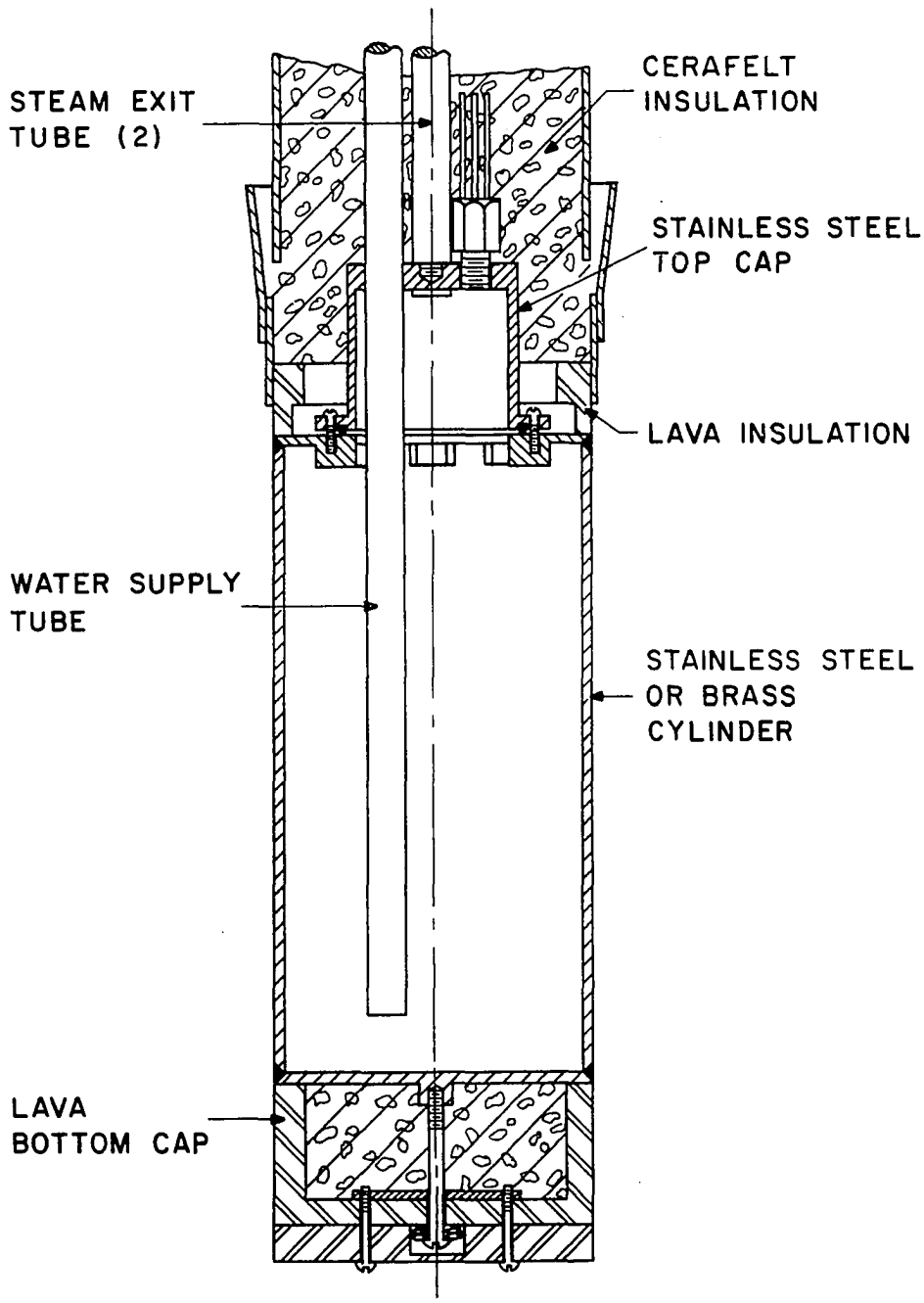

Figure IV-7. Assembly Drawing for Test Cylinder and Lead Tube.

stove pipe. The vertical section between the support pipe and the test cylinder was wrapped with Cerafelt and covered by a section of 6-inch stove pipe.

The lead tube assembly fulfilled its purpose quite satisfactorily during all the experiments. Inspection of the internals revealed no sign of heat damage to such items as Teflon insulated electrical wire and glass insulated thermocouple wire. Also, the heat pickup by the coolant while flowing to and from the test cylinder was small. Only one problem required correction. As first assembled there was a gap at the junction between the 6-inch diameter stove pipe and a piece of sheet metal which extended up from the Lava ring resting on the test cylinder top. This gap, about 1/2 inch wide, was stuffed with Cerafelt, but hot flame gases penetrated and appeared to be ruining the insulation. This situation was corrected by installing a tapered sheet metal collar between the Lava ring and the 6-inch stove pipe. The collar reduced the size of the gap and turned it up so the fire did not impinge directly on it.

Seven chromel-alumel thermocouples were attached to the lead tube. The location of these thermocouples is shown on Fig. IV-8. Thermocouples 19-22 were attached to the stainless steel pipe. The two thermocouples located along the vertical section, T-23 and T-24, were not attached to any fixed component so their location is not

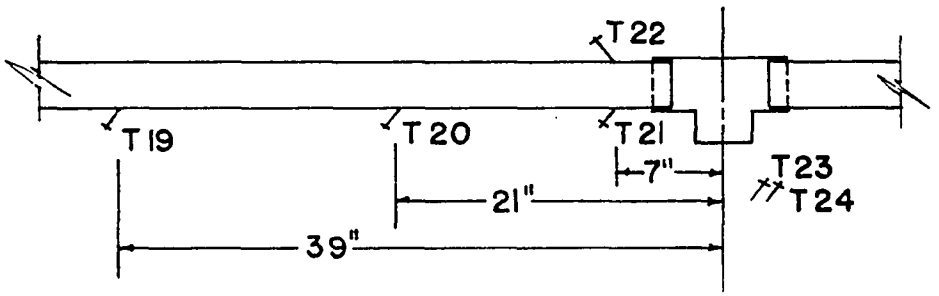

Figure IV-8. Location of Lead Tube Thermocouples.

positive; however, T-24 was placed between the sheet metal and the outer layer of Cerafelt, and T-23 was placed between the second and outer layers of Cerafelt.

The steady state temperatures attained during the fire tests are presented in Table D-3, Appendix D, for each thermocouple.

Control Panels

Figures IV-9 and IV-10 are photographs of the control panels in the observation room and the equipment panel in the test room, respectively. The test cylinder can be seen just to the right of the panel in each picture.

The test and observation rooms are part of the Low Velocity Wind Tunnel located on the North Campus. Figure IV-11 is a drawing of the wind tunnel building showing the relative location of the rooms and major equipment.

A schematic flow diagram for the entire experiment is shown on Fig's. IV-12 and IV-13. The incoming primary water (PW) flow rate was measured by the #1 or #2 PW flowmeters mounted on the control panel in the observation room and then routed through the electrical preheater mounted on the equipment panel in the test room. From the preheater the PW flowed through an insulated line connected to the inlet coolant line in the lead tube assembly. This inlet line extended through the lead tube and the top cap penetration, and it terminated near the bottom of the test

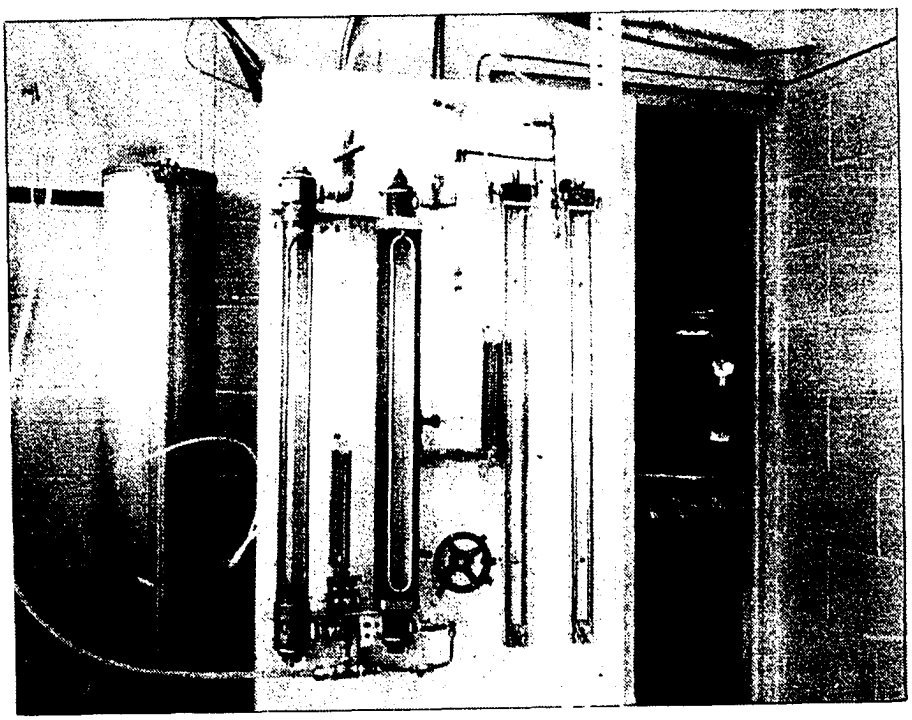

Figure IV-9. Control Panel in Observation Room.

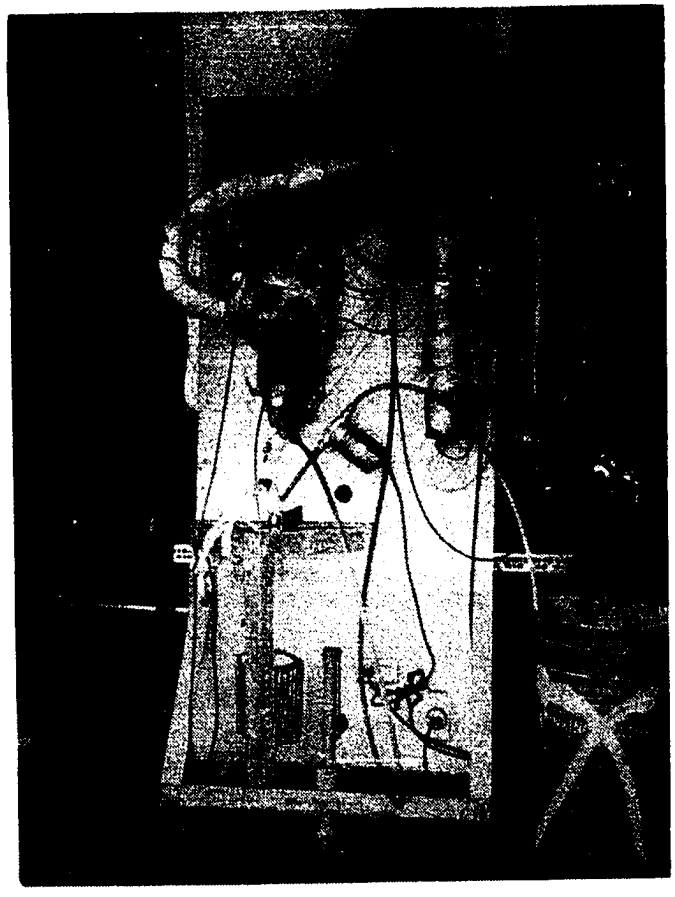

Figure IV-10. Control Panel in Test Room

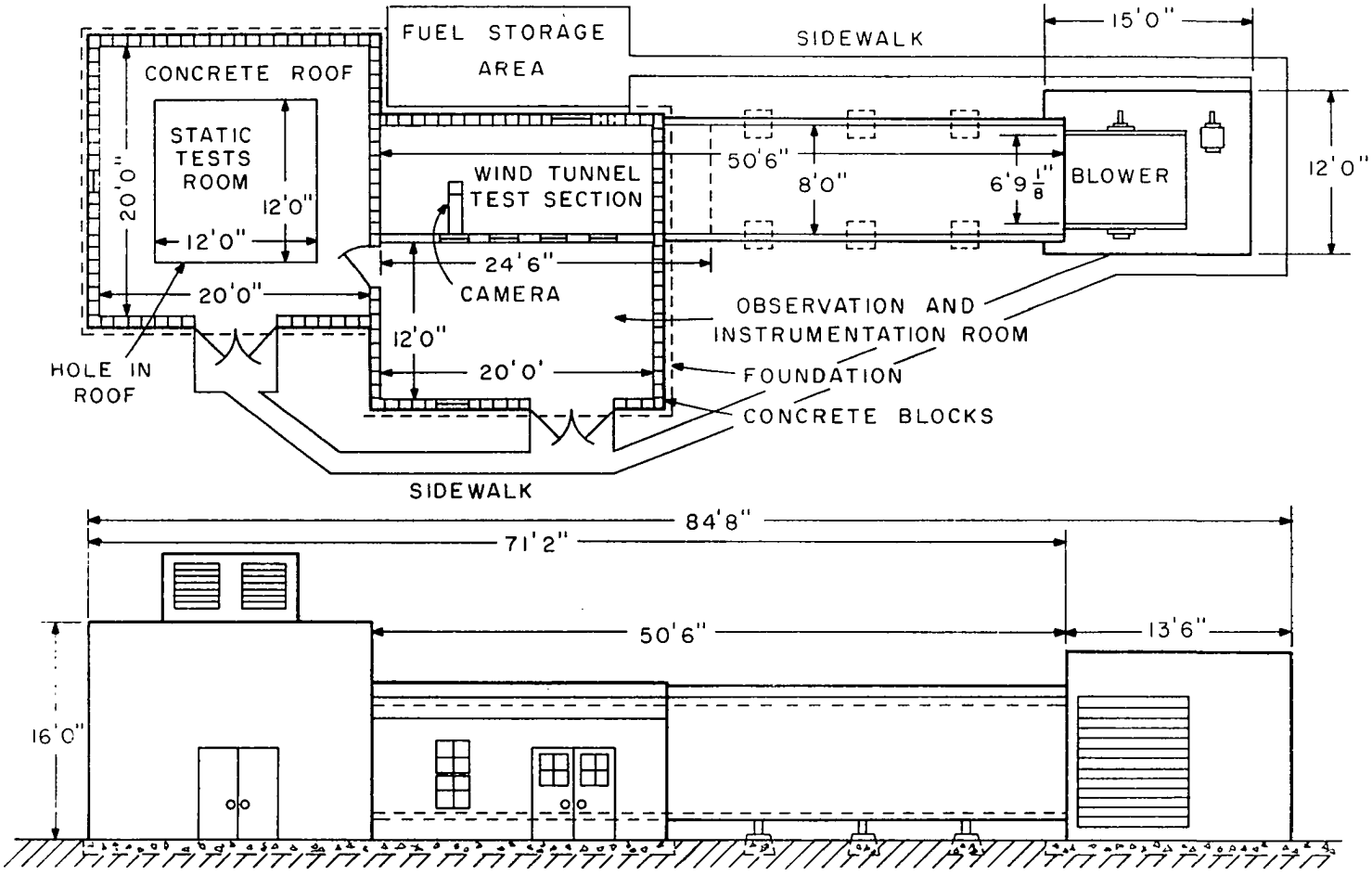

Figure IV-11. Low Velocity Wind Tunnel.

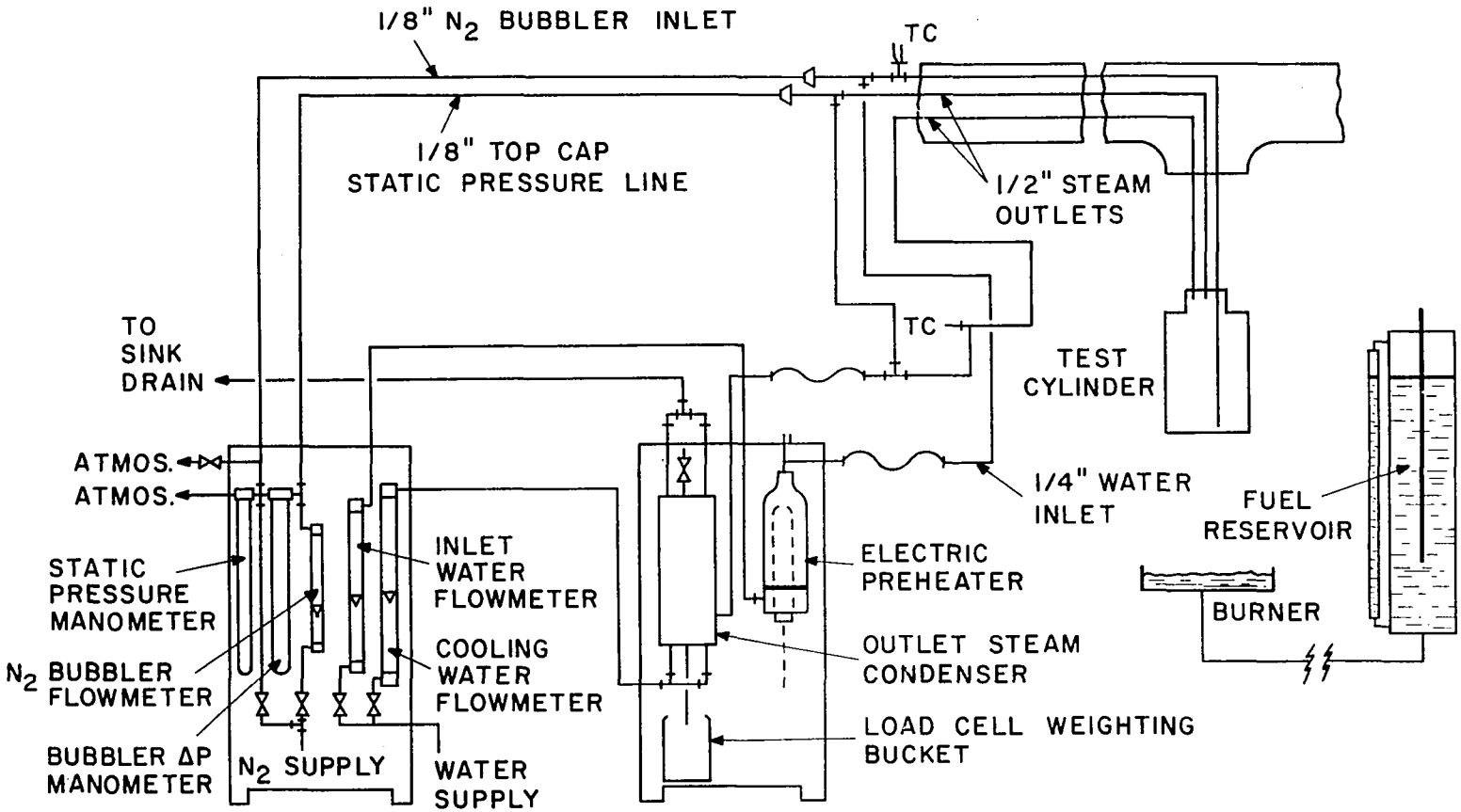

Figure IV-12. Schematic Flow Diagram for Experimental System.

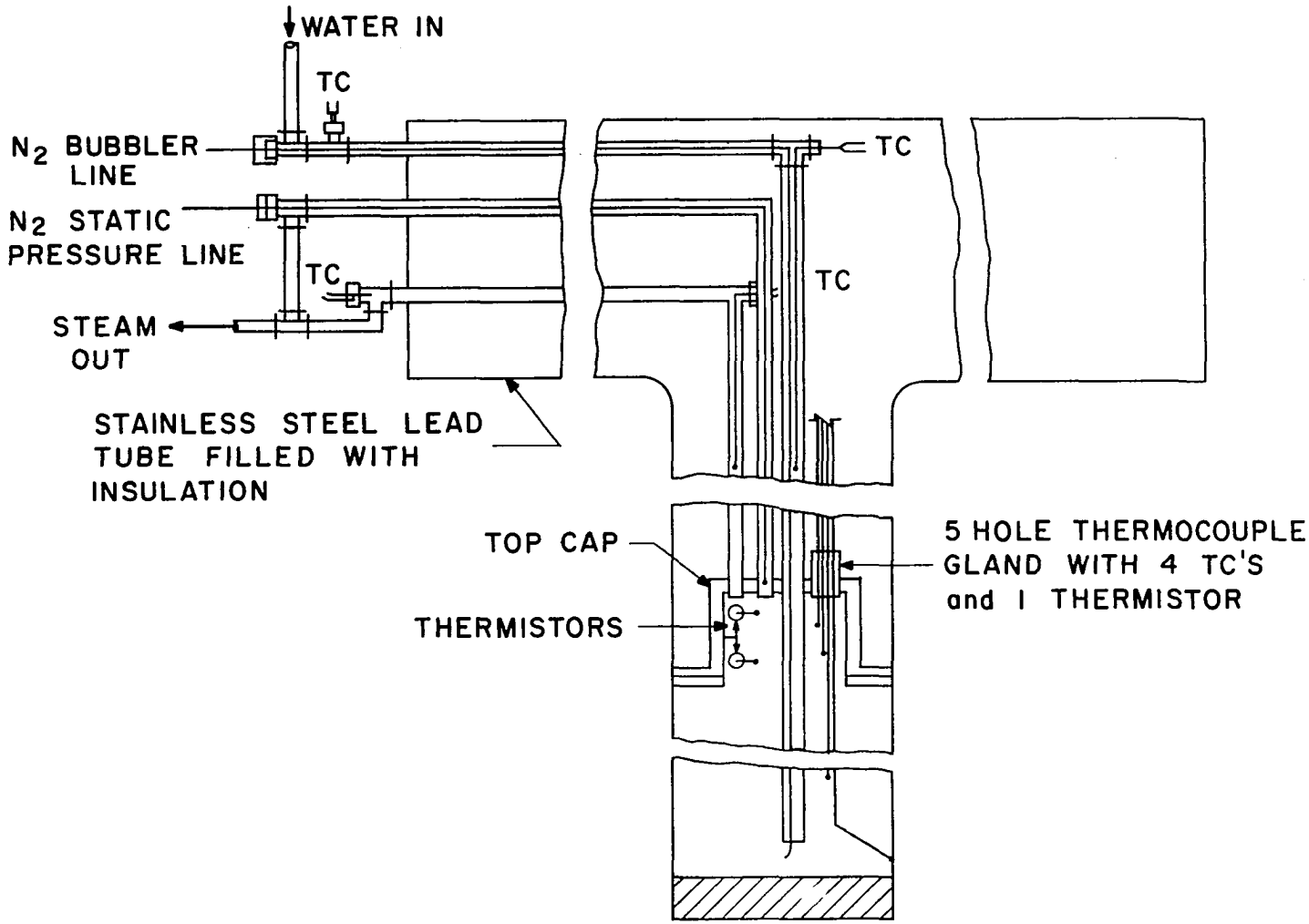

Figure IV-13. Schematic Flow Diagram for Lead Tube Assembly.

cylinder. The PW then moved up through the test cylinder to the steam-water interface at the top of the cylinder. The PW left the test cylinder as a steam-water mixture through the two outlet coolant lines which penetrated to just inside the top cap. The outlet lines paralleled the inlet line back through the lead tube to a header outside the lead tube. The PW steam-water mixture flowed to the condenser, mounted on the equipment panel, through a flexible, woven metal mesh line. The condensed PW drained by gravity into a one-gallon bucket. This bucket was supported by a load cell which provided an output signal proportional to the weight of the PW accumulated in the bucket. A manually controlled sump pump was used to empty the bucket periodically during a run. Thermocouples were located at all inlet and outlet points of the PW system.

The cooling water (CW) flow rate was measured by the CW flowmeter mounted on the control panel in the observation room. The CW was then routed into the test room, through the tube side of the condenser and back to a sink drain in the control room.

The liquid level inside the test cylinder was measured by the old-fashioned bubbler technique. The nitrogen gas used in the bubbler system flowed through a flowmeter and was then routed into the test room where it entered the lead tube assembly via an 1/8-inch diameter

Teflon tube which was run inside the 1/2-inch inlet coolant line. The Teflon tubing terminated at the bottom of the test cylinder. The N_2 gas bubbled up through the liquid in the test cylinder and flowed to the condenser with the steam. The bubbler gas and other non-condensables were vented to the atmosphere at the top of the condenser.

The high pressure side of the liquid level manometer was connected to the inlet N_2 at the control panel. The static or low pressure side of the liquid level manometer was connected to the top of the test cylinder by an 1/8-inch Teflon line which was run through one of the outlet coolant lines. The static pressure line terminated just inside the top cap. Thus the liquid level manometer measured the pressure drop of the nitrogen flowing between the control panel and the top of the test cylinder, including the head of PW inside the test cylinder.

All flow and temperature controls were manual. This arrangement was quite satisfactory for flow rates, but a fast response temperature controller on the inlet PW would have been quite helpful. In fact, a steam heater or similar system which would maintain a fixed outlet temperature during periods of variable demand would be most desirable since the major load occurs during start-up when the PW flow is initiated and usually is adjusted several times.

The condenser was designed to provide the few inches of flooding necessary to achieve reasonably low, constant outlet temperatures. However, for the larger duty services the outlet lines were too small for adequate gravity flow and excessive flooding occurred. During periods of excessive flooding the performance of the condenser was seriously impaired.

The N_2 bubbler system worked quite well for measuring the liquid level in the test cylinder. However, there is one qualification; during full boiling inside the closed system it is doubtful if the bubbler measurements can be considered very accurate. The readings were erratic, and frequent purging of the static line was necessary to maintain reasonable values. There was no evidence of this trouble during the calibration tests when an open bucket of boiling water was substituted for the test cylinder. The problem was not too serious, but it was a source of concern and demanded constant attention during most of the experiments. Part of the problem may have been due to the rather slow response to pressure changes which was apparently caused by the flow resistance in the 1/8-inch Teflon tubing (0.040 inch ID).

Thermistor actuated monitors were used as positive, fixed point checks on the liquid level. The thermistors were located at three levels inside the test cylinder, 3/4 and 1/2 inches above the top cap-cylinder interface

and 1/8 inch below the top cap-cylinder interface. The electronic circuits, described in Appendix F, were designed to actuate a light if the liquid level dropped below the thermistor location. The systems worked satisfactorily in out-of-cylinder checks, but inside the test cylinder during a test their performance was not satisfactory. As with the N_2 bubbler system the problem seemed to be due to the rather violent boiling in a restricted volume. The thermistors were also located at the wrong levels; it would have been much better if one had been placed in the middle of the top cap and one about 1/2 inch below the top cap-cylinder interface. The monitor systems did work but they required frequent adjustment of the balancing resistors and consumed a disproportionate amount of time. After establishing confidence in the N_2 bubbler system the thermistor monitors were turned off.

Support and Lifting Mechanism

The lifting mechanism used to support and position the test assembly is shown in Fig. IV-14. The static members were all 225-80 AIM slotted Dexion angle iron. Rails, or rather channels, were attached to the north and south sides of the large sheet metal hood which is a permanent part of the building. The main support frame was mounted on casters which rode in the channels so that the frame could be pushed east and west. A 1/15-horsepower motor

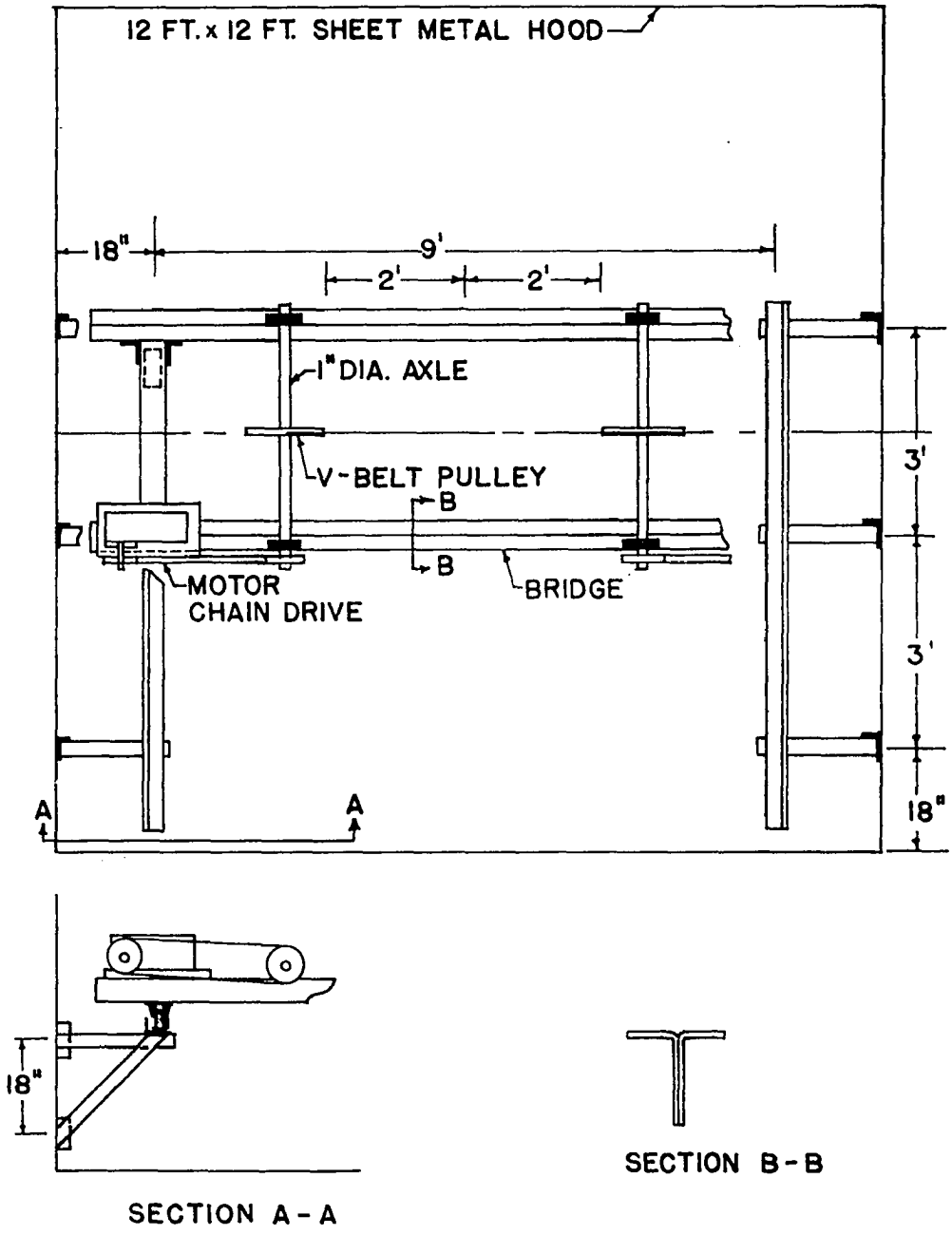

Figure IV-14. Lifting and Support Mechanism for Lead Tube Assembly.

was installed at each end of the lifting frame and connected by chain drive to the 1-inch diameter steel axles across the frame. Ten-inch, V-belt drive pulleys were keyed to the steel axles in the center of the lifting frame. The drive pulleys were connected to the stainless steel pipe of the lead tube assembly by 3/16-inch diameter stainless steel cable. These cables were looped around the stainless steel pipe about 3-1/2 feet from the center line of the test assembly. This arrangement provided a minimum bending moment at the center-line of the test assembly. The details of the mechanical design are presented in Appendix E. The electric motors were protected from direct radiant heating by wood and asbestos millboard barriers. The electric lines were rubber insulated, 300 V, cable; they were routed through flexible metal conduit wherever they were exposed to direct radiant heating from the fire.

Safety cables (3/8-inch diameter) were attached to each end of the lead tube and anchored to concrete beams in the roof of the building. These cables were adjusted so that if the lifting mechanism failed, the test cylinder could not crash down onto the fire table.

The lifting assembly was satisfactory except that the first set of lifting pulleys, which were made from some type of "pot" metal, warped during the attempts to burn hexane and cyclohexane in the 24-inch diameter burners.

Steel pulleys were installed which withstood exposure to the large fires.

Figure IV-15 is an overall photograph of the lead tube and test assembly made during Test 49. The lifting mechanism supports, lifting cable pulleys, safety cables and other equipment items can be seen on close inspection.

Burners and Fuel Supply System

Single burner pans from 12 inches to 24 inches in diameter and a cluster of nine, 6-inch diameter pans were used in these experiments. The cluster configuration consisted of one center burner with 8 burners located 45 degrees apart on 12-inch centers. The burners were all 1-1/2 to 2 inches deep. The single pans were made from brass and the 6-inch diameter pans were made from steel. Fuel flowed into the bottom of the pans from a sealed reservoir. A constant head siphon system maintained a constant fuel level in the burner pans. The system is shown schematically in Fig. IV-16 and described in detail in Ref. 43. The burners were located on a large table (about 10 feet diameter x 2 feet high) in the test room. This table, as originally used in fire merging tests (Ref. 23), was covered by blocks of insulation with the tops of the burners set flush in the insulation. During tests with large burners, vapors from the heavier fuels would flow across the table top and down through the cracks between



Figure IV-15. Photograph of Experiment Assembly During Test 49.

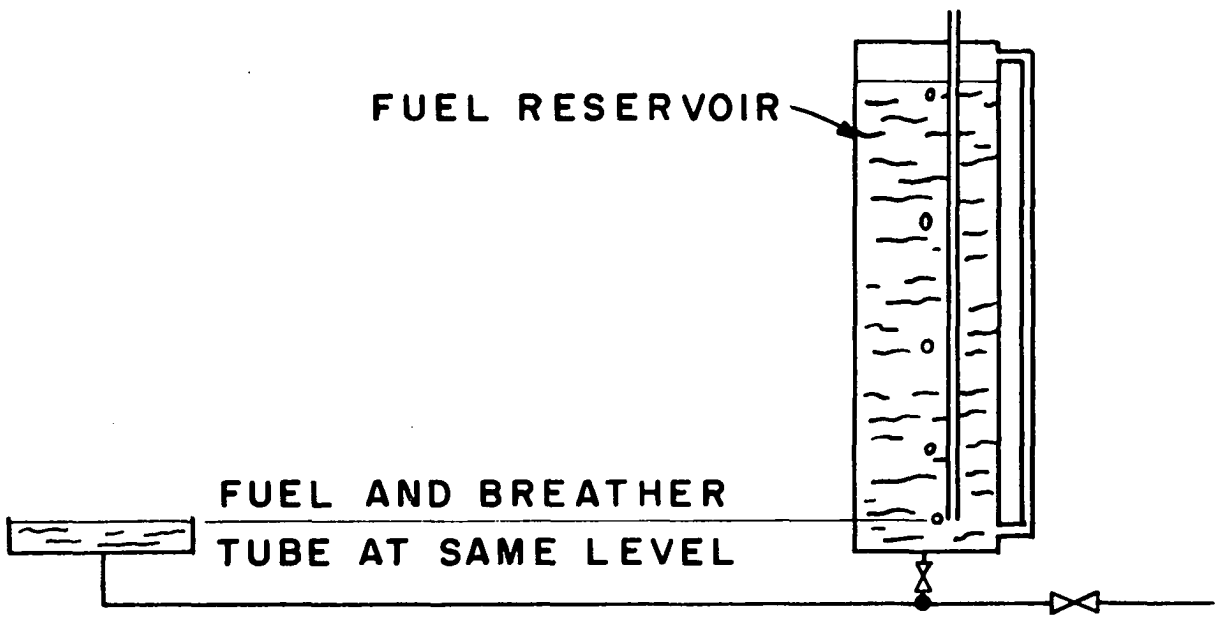

Figure IV-16. Schematic Diagram of Fuel Level Control System.

insulation blocks. These vapors would eventually ignite and burn on the underside of the table with attendant complications. The overflow problem was stopped by removing the blocks at the center of the table to make a 4-foot diameter open area around the burners. The resultant upward air flow was sufficient to lift the vapors and confine the flame spillover to the immediate vicinity of the burner. Wire screen was placed over the opening to disrupt the air turbulence, to collect large soot particles and generally to alleviate the housekeeping chores. During a test run the main air entrance into the test room was through 18-inch square, floor level openings in the three outside walls. Six inch diameter stove pipe sections were used to route most of this air flow directly under the table. Reasonably stable flames were obtained with this arrangement; however, the art of adjusting the various parts of the ventilating system was never mastered; each test seemed to present different problems. The ventilating problems are discussed further in Section V. A 48-inch diameter exhaust fan, installed in the louvered roof on top of the test room (Fig. IV-11), was in operation during many of the tests.

Instrumentation

The specifications for the recording and measuring instruments are given in Table IV-1.

TABLE IV-1

INSTRUMENT LIST

1. L&N Speedomax Multipoint Recorder, 12-point, 0-400°F, for IC thermocouples.

2. Brown Electronik Multipoint Recorder, type 153, 12-point, 0-400°F, for IC thermocouples.

3. Brown Electronik Multipoint Recorder type 153, 12-point, 0-1500°F, for CA thermocouples.

4. Honeywell Electronik 19 Laboratory Recorder, 2 pen, multiple range millivolt.

5. L&N Precision Potentiometer, model no. 8662.

6. Statham Universal Load Cell, model UC3 and 5-lb weight accessory, model UL4.

7. Pyro Optical Pyrometer, model no. 83.

8. Hy-Cal Engineering Radiometer (wide angle) model 1401-A-03, series no. 11808.

9. Barnes Engineering Industrial Radiometer (narrow angle) model R-4D1.

10. Graflex Speed Graphic Camera and Polaroid #500 film-holder.

All recorders were located in the observation room. Two large Amphenol plugs in the TC lead wire circuit were used to provide quick-disconnect convenience and wiring flexibility during the early tests. The Amphenol plugs had to be taken out of the circuits because radiant and convective heating during fire tests affected the temperature readings. Apparently the trouble was an impressed ΔT caused by unequal heating of the copper to thermocouple lead wire junctions on each side of the Amphenol plugs. The impressed ΔT caused the apparent boiling temperature to read 10°F low in some cases. The important Iron-Constantan thermocouples used in the heat balance calculation were routed through a selector switch box to facilitate checking temperatures with a potentiometer.

The wide angle radiometer was located 70 inches from the center line of the burners and 8 inches above the top of the burner pan. Monochromatic transmissivities for the radiometer for quartz window and atmospheric absorption coefficients are presented in Table G-1, Appendix G.

The narrow angle (6-mil spot) radiometer was available only for the last 8 to 10 tests. Its main purpose was to provide information on the effects of flickering and pulsing of the flame column.

The optical pyrometer temperatures were usually taken looking just below the test cylinder from a position

about 6 feet from the fire column. Whenever possible two independent readings were made. The data presented in Table D-3, Appendix D, are averages of these readings. As with previous investigators, some difficulty was experienced in getting consistent readings from the smaller fires.

Photographs of the fires were made using a 4 x 5 Polaroid film holder in a Graflex camera. The camera was mounted on a retractable platform about 15 feet from the center of the fire table as shown in Fig. IV-11. The camera was manipulated through a small window in the south observation room wall and was retracted behind a radiation shield between pictures.

Type 52 (ASA 400) or type 57 (ASA 3000) Polaroid film was used for all the fire photographs. The slow film worked best with all but the most difficult to photograph fires such as those from methanol and those which produced large quantities of smoke. Based on experience and observation, exposures of 1/5-second produced pictures which best represented the average flame size. In some cases, particularly methanol fires, periodic pulsations made it impossible to catch the average flame size with a single picture. For these cases the average fire size was determined from several photographs and recorded visual observations.

CHAPTER V

EXPERIMENTAL PROCEDURE

This chapter presents the general procedure for the experiments. Major emphasis has been put on the portions which are based on experience and will be of most help to future investigators.

After turning on the recorders and load-cell power supply, a nitrogen purge was started through both sides of the N_2-bubbler system. This purge was necessary to insure that no water remained in the lines between the liquid-level manometer and the test cylinder. The ΔP could be kept low enough to avoid over-ranging the manometer by simultaneously increasing the gas flow through each side. The purge had to be established very carefully because sudden ΔP fluctuations occurred when slugs of water were blown out of the liquid level system tubing. These ΔP fluctuations were large enough to over-range the manometer. The purge was maintained while the rest of the equipment was readied.

The block valve on the cooling water flow to the condenser was closed so the cooling water flow through the radiometer could be verified at their common outlet. Then, cooling water flow through the tube side of the condenser was established.

The primary water or shell side of the condenser was filled to its operating liquid level to avoid the delay which occurred if condensate had to accumulate to fill the condenser.

The weighing bucket was emptied and the recorder output checked at several fixed weights. The weighing system remained linear, but the zero point and the multiplication factor, which depended on the power supply voltage, changed almost daily.

The surface of the test cylinder was checked to be sure it was clean; the test cylinder and burner positions were also checked. The fuel reservoir was usually filled concurrently with most of these preliminary checks. As soon as the reservoir was full, it was sealed and fuel was turned into the burner. The system was allowed to set for several minutes while the piping was inspected for visible leaks, particularly air leaks into the top of the reservior. The latter were indicated if the fuel in the burner continued to rise above the set level of the reservoir dipstick. After the inspections were complete, final adjustments were made on the fuel level in the burner. The starting fuel level was set at least 1/2-inch below the rim of the burner to avoid overflow as the heated fuel expanded.

The fuel level in the burner pan could be adjusted during a test by simply raising or lowering the reservoir vent tube. Such adjustments were made during many tests without upsetting the system. It was also possible to refill the

fuel reservoir during operation without significantly affecting the test. The valve between the reservoir and burner was closed, then the seal plug in the top of the reservoir removed and additional fuel was pumped in. Periodically it was necessary to open the valve and permit some fuel to flow to the burner to prevent the fire size from decreasing. The siphon head level control is inoperative when the reservoir is being filled. After the reservoir was full and resealed, the valve had to be opened slowly to prevent a decrease in the fire size due to admitting excessive cold fuel to the burner.

As soon as the fuel system checks were completed, the nitrogen purge through the bubbler system was stopped and the correct N_2 flow was established through the inlet line to which the high pressure side of the ΔP manometer connects. Primary water was added to bring the water level inside the test cylinder up to the junction between the top cap and the test cylinder.

Printout was started on all recorders, and the entire system was given a final check before the fire was lighted.

The heat-up time for the test cylinder ranged from 1 to 8 minutes depending on the initial temperature, type of fuel and burner size. The bulk water temperatures and the cylinder inside-wall temperature would increase at the same constant rate, the bulk temperatures remaining 5 to 10°F below the inside-wall temperature. As full nucleate boiling was established, the inside wall temperature would rise to about 220°F and then drop back and hold a few degrees above the

bulk boiling temperature. There was always a similar hump in the bulk water temperatures, but the peak was only a degree or two above the steady state value.

During the transition into boiling the liquid level indication would fluctuate rapidly and then steady down to show that about a third of the water had evaporated or been carried out of the cylinder by entrainment. At this point primary water flow was added at a rate adequate to bring the level back to the top of the cylinder without overfilling.

It was extremely difficult to find the inlet flow rate and temperature which would provide steady state operation with the liquid level within 1/2-inch of the cylinder top. However, if the inlet flow rate was a bit too high the liquid level would vary between the top of the cylinder and the top of the top cap. Apparently when the liquid level got too high the system would eject enough water to reduce the liquid level back to the top of the cylinder where the sudden area increase would stop the action. During the ejection process the liquid level indication would fluctuate rapidly and then settle down to indicate the lower level. The liquid level would immediately start to rise and would do so rather smoothly until the ejection process started again. From 10 to 50 percent of the primary water flow rate was entrained with the steam and carried out of the test cylinder. The lag in the liquid level indication was probably due to the small size of the tubing in the level indicating system rather than a gradual reduction in level.

The outlet flow was not irregular enough to cause perceptible variations in the condenser cooling water ΔT or the flow rate out of the condenser.

If the inlet flow were further increased definite slug flow would set in. The liquid level indication would fluctuate, but it would stay above the cylinder top all the time. Slug-flow was indicated by cycles in the condenser cooling water ΔT and the flow rate out of the condenser. The data from operation in this region was not satisfactory, primarily because it was difficult to get good average values for the flow rate and cooling water ΔT.

As soon as the fire reached full size the overhead ventilating louvers and inlet air ducts were adjusted to achieve as stable a fire as possible. The best results for large fires were obtained with all the top louvers closed and the exhaust fan pulling air through the ducts under the table and up past the burner. For small fires the best resutls were obtained with the exhaust fan off and the ventilating louvers on the downwind side of the building open. At times no combination of adjustments would stabilize the fire, particularly when the wind was from the east.

Radiation and condenser cooling water ΔT were recorded on one channel of the Honeywell-19 recorder by manually switching from one to the other. This switching was unfortunate because it precluded obtaining a continuous record of the radiation history of the fires or an intelligible record of the effect of fire movement on the measured heat transfer rates.

Radiation was usually recorded during test startup. As soon as condensate began to register on the weighing system the recorder would be switched to the cooling water ΔT. The recorder was switched back to the radiometer for a minute or two every 10 or 15 minutes.

Photographs of the fire were taken at convenient times; usually several pictures were made over the course of the test. Most photographs of the bright fires were taken at f 22 for 1/5-second using type 52 (ASA 400) Polaroid film. Photographs of the methanol fires, and photographs taken through heavy smoke, were usually shot at f 6 for 1-second using type 57 (ASA 3000) Polaroid film. Opening the small (12-inch x 12-inch) window in the observation room wall to change film or camera settings usually upset the fires, therefore, it was necessary to close the window and wait a minute or so before taking the photograph. At least one long exposure (1 to 2 seconds) photograph should always be taken during fire research tests in order to record the recurring maximum fire size which appears to be the only constant with respect to the dimensions and shape of the flame column.

Data on the fuel level in the reservoir, flow rates and other constant, or slowly changing, paramenters were recorded about every ten minutes. Several times during the test the test room was entered to measure the flame temperature with the optical pyrometer and read the air temperature thermometer located behind the equipment panel.

A test was terminated by isolating the fuel reservoir and draining the fuel from the burner pan into a bucket outside the building. The fire usually burned the remaining fuel and died out within 3 minutes. Primary water flow was maintained until the temperatures inside the cylinder were below the boiling point. The soot thickness measurments were made and the cylinder was cleaned off with out removing the cylinder from the lead tube assembly; thus the next test could be started after a minimum delay.

Fire tests with hexane and cyclohexane in the 24-inch diameter burner could not be completed because the flames reached above the level of the concrete beams in the roof (12 to 14 feet above the burner). Although the normal path of the flames was between beams, these fires were large enough and moved around enough to give frequent direct contact exposure. The lifting mechanism was subjected to the same conditions. After attempting to run these two tests, it was noticed that the original "pot" metal cable pulleys had warped.

Tests using hexane and cyclohexane in the single 18-inch diameter burner and the cluster of 6-inch diameter burners were completed. These fires are about the largest that can be safely handled in the wind tunnel static test room. The flames from the single 18-inch diameter burner reached the level of the concrete roof beams but seldom made direct contact. The fires from the cluster of 6-inch burners were shorter but the total heating was just as severe.

During the large fire tests the inside surface temperature of the north wall was measured by a thermocouple pressed against the cinder block. The thermocouple was located about 1/4 of the wall length from the corner and was directly exposed to radiation from the fire. The wall temperature was allowed to reach 220°F during test No. 55 before the fire was put out. The air temperature in the shadow of the equipment panel was nearly 200°F. After this test it was decided to terminate all tests when the building wall temperature reached 200°F.

Excessive smoke in the test room was not a problem except for fires from JP-4 and benzol. Only one test, using a 12-inch diameter burner, was run with benzol; during this test the soot quickly became thick enough to preclude taking a picture of the fire as well as entering the test room to take readings. The test was terminated when the flame became invisible from the observation room. The JP-4 fires produced smoke rather than soot. The smoke level quickly discouraged entrance into the test room and fire photographs were obtained only with maximum exposure.

A 48-inch exhaust fan was running during all the large fire tests. However, the air flow into the test room was not well distributed so it is hard to judge the adequacy of the system. The ventilation was definitely better close around the fire than it was around the periphery of the test room.

Watching a fire through even a single glass window does not compare with direct, unshielded observation. Judgments concerning severity and possible damage from fires

should be made only after direct observation of the fire from a position which is exposed to the fire.

CHAPTER VI

RESULTS

General

The analysis and understanding of the experimental data were complicated by several factors which could not be fully accounted for. These factors are discussed in separate sections of this chapter. The first two sections deal with the accumulation of soot on the test cylinder and the total heat transfer rates measured in the flames. The third section covers the attempts to establish a valid technique for calculating the radiant heat transfer both within and without the flame column. The fourth section presents the convective heat transfer rates inside the flame, determined as the difference between the measured total heat transfer rate and the calculated radiant heat transfer rate. The convective heat transfer rates are expressed as heat transfer coefficients and compared to the coefficients calculated from the available correlations. Photographs of the flames obtained for each fuel and burner, and comments on the individual test results are presented in the fifth section. The sixth section discusses the measured fuel burning rates and the high heat transfer rates obtained from the cluster

burner fires. The non-uniformity of the flame column and the associated effects on the radiant and convective heat transfer are discussed in the seventh and final section.

Soot Accumulation

The effect of the accumulation of soot on the total heat transfer rate was much larger than expected. Only one of the references reviewed in preparation for these experiments mentions any effects which can be attributed to soot accumulation on the surface exposed to the flames. Reference (42) describes an increase in the heat transfer rate which occurred immediately after turning on a water deluge system. The water was sprayed directly on a large tank which had been exposed for some time to an uncontrolled, buoyant diffusion fire. It is believed that the water spray knocked off the soot which had accumulated on the tank walls, thereby causing an increase in the heat transfer rate before the cooling effect of the water set in.

The insulating effect of the soot accumulated during the experiments was high enough to obscure any heat transfer differences between the stainless steel and brass test cylinders. The thickness of the soot layer varied considerably from test to test and to a lesser extent with position on the test cylinder surface. The deposit usually formed a light, compact layer which was easily removed by scraping with a piece of cardboard. Figures VI-1, VI-2 and VI-3 are

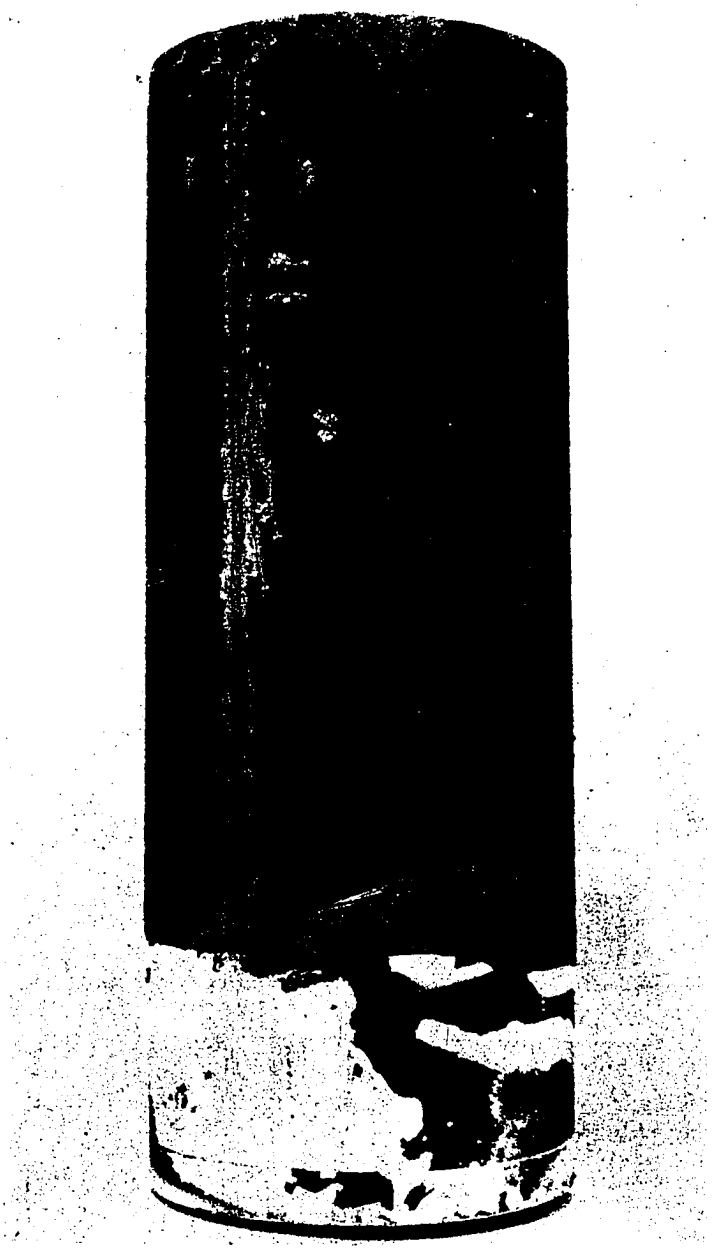

Figure VI-1. Typical Soot Deposit on Test Cylinder.

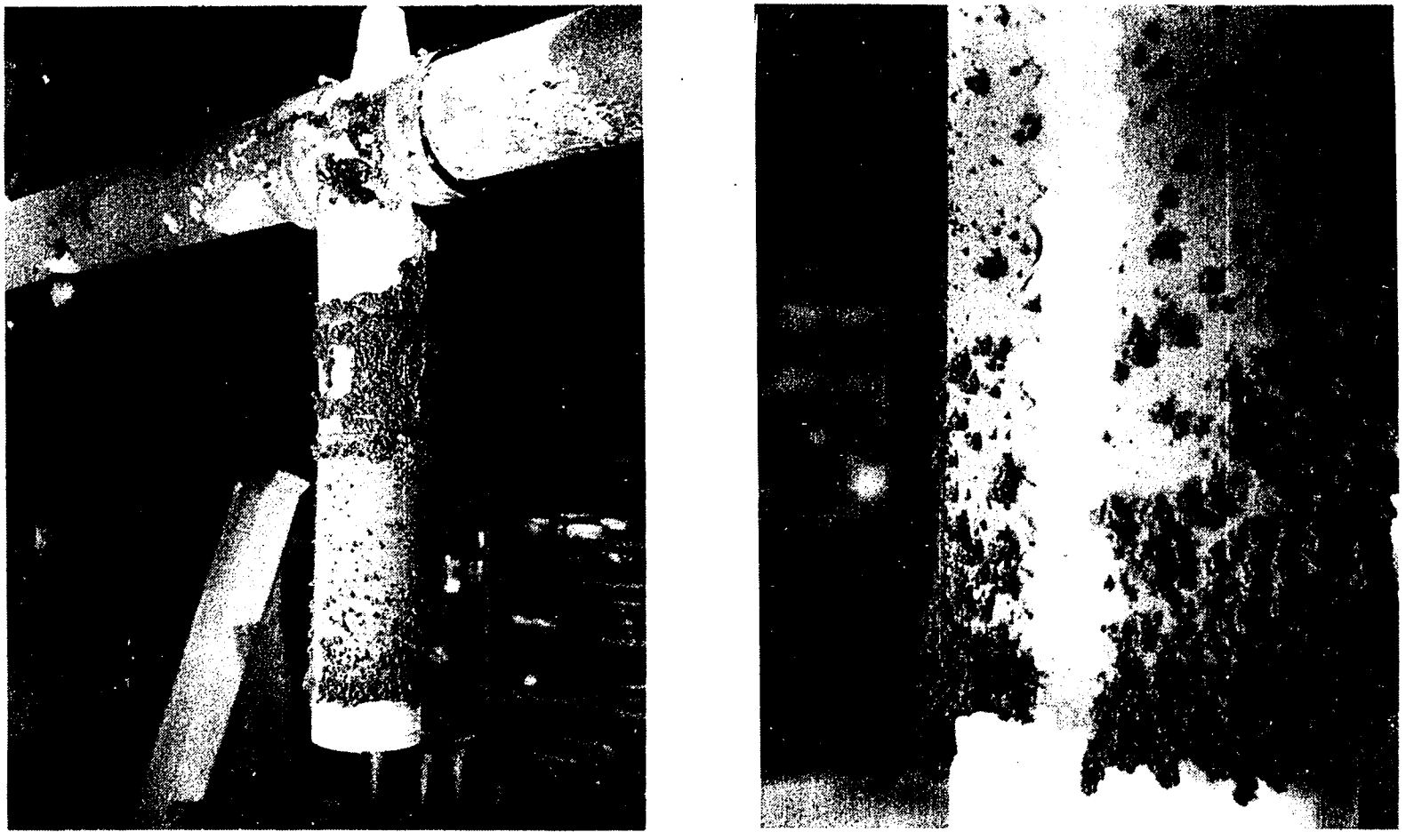

Figure VI-2. Non-typical Soot Deposit on Test Cylinder.

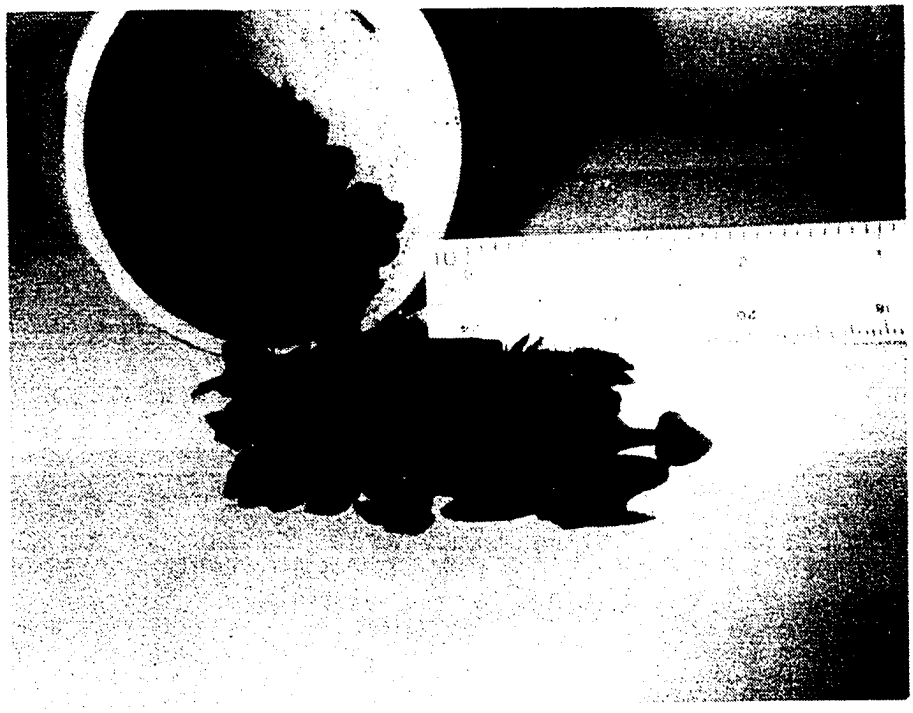

Figure VI-3. Typical Soot Deposit Removed from Test Cylinder.

photographs of the soot accumulation. The typical soot deposited on the test cylinder is shown on Fig. VI-1; the increase in soot thickness from top to bottom is apparent. As a general rule the soot was deposited uniformly and smoothly except for the top to bottom thickness difference. Several times the soot deposited from the smokier fires was quite different in appearance. Figure VI-2 shows two views of non-typical soot accumulated from JP-4 fires. The non-typical soot consisted of a very light and fluffy secondary deposit on top of a compact primary deposit which covered the entire surface of the test cylinder. Figure VI-3 shows pieces of soot which were scraped off after Test 66. These soot pieces resemble the typical soot deposited from all the fuels (except methanol which didn't deposit any soot). The test assembly was not thoroughly grounded and it has been suggested that static electrical charges may have caused the variations in the soot deposits.

The thickness of the soot deposit was measured after each test. A strip of soot was scraped off the side of the cylinder as shown on Fig. VI-1 and the thickness of the exposed edge measured with a steel ruler. The average thicknesses and test durations are reported in Table D-3, Appendix D. The accuracy of the reported soot thicknesses is probably not better than ± 50 percent. The soot thickness at the bottom of the cylindrical surface of the test cylinder was usually 1-1/2 to 2 times that at the top.

Exploratory calculations were made using a thermal conductivity of 0.04 Btu/hr-ft^2-°F/ft for the soot deposit. These calculations show that the small soot deposits can easily account for reductions in the heat transfer rate of the magnitude encountered in these experiments. The above thermal conductivity is characteristic of lampblack, not graphite or pyrolytic carbon.

Total Heat Transfer Rates

The total heat transfer rates for all fires, except those from methanol, decreased with time due to the accumulation of soot on the heat transfer surface. When the total heat transfer rate data are plotted against time on semi-log paper the points are correlated very well by a straight line. Therefore the total heat transfer rate, $Q/A)_T$, may be described by an equation of the form

$$Q/A)_T = ae^{-bt} \qquad \text{(VI-1)}$$

where t is the exposure time and a and b are coefficients dependent on factors such as fire size and fuel. The initial heat transfer rates, coefficient a, were obtained by extrapolating the straight lines through the data on the semi-log plots to zero exposure time; the time decay constants, coefficient b, were obtained from the slope of these straight lines. These coefficients may also be dependent on

other factors such as air humidity, electrical potential between the flame and target, flame turbulence or other measures of the fuel-air mixing rate, the position of the target within the flame, and the temperature of the target. In these experiments only the fuel, fire size, target temperature, and target position were controlled, measured, or accounted for. The soot accumulation obscured any effects of differences in the target temperature, and no differences due to target position within the flame could be detected. The measured data and calculated parameters associated with the total heat transfer measurements are presented in Tables D-5 through D-11, Appendix D.

Figures VI-4 through VI-13 are semi-log plots of the total heat transfer data for the several fuels and burner sizes used in these experiments. Figure VI-14 is a linear plot of the total heat transfer data from the methanol fires. Linear plots of the highest total heat transfer rates are presented on Fig. VI-15 for acetone, Fig. VI-16 for hexane, Fig. VI-17 for cyclohexane and Fig. VI-18 for the JP-4. The data on these plots are the same as those on the corresponding semi-log plots. These figures have been included to illustrate the rapid decrease in total heat transfer rate with exposure time.

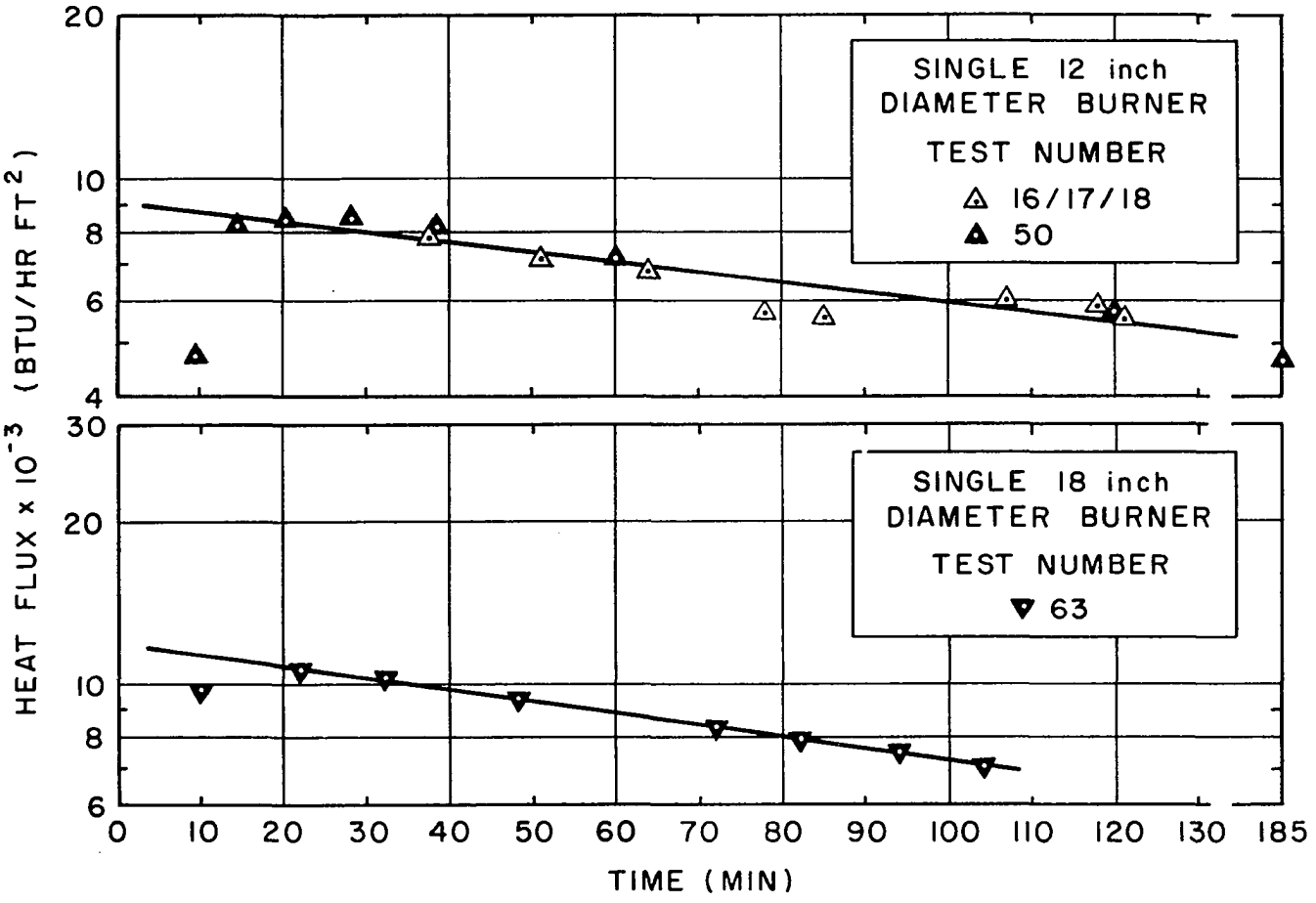

Figure VI-4. Total Heat Transfer Rates from 12- and 18-inch Diameter Single Burner Acetone Fires.

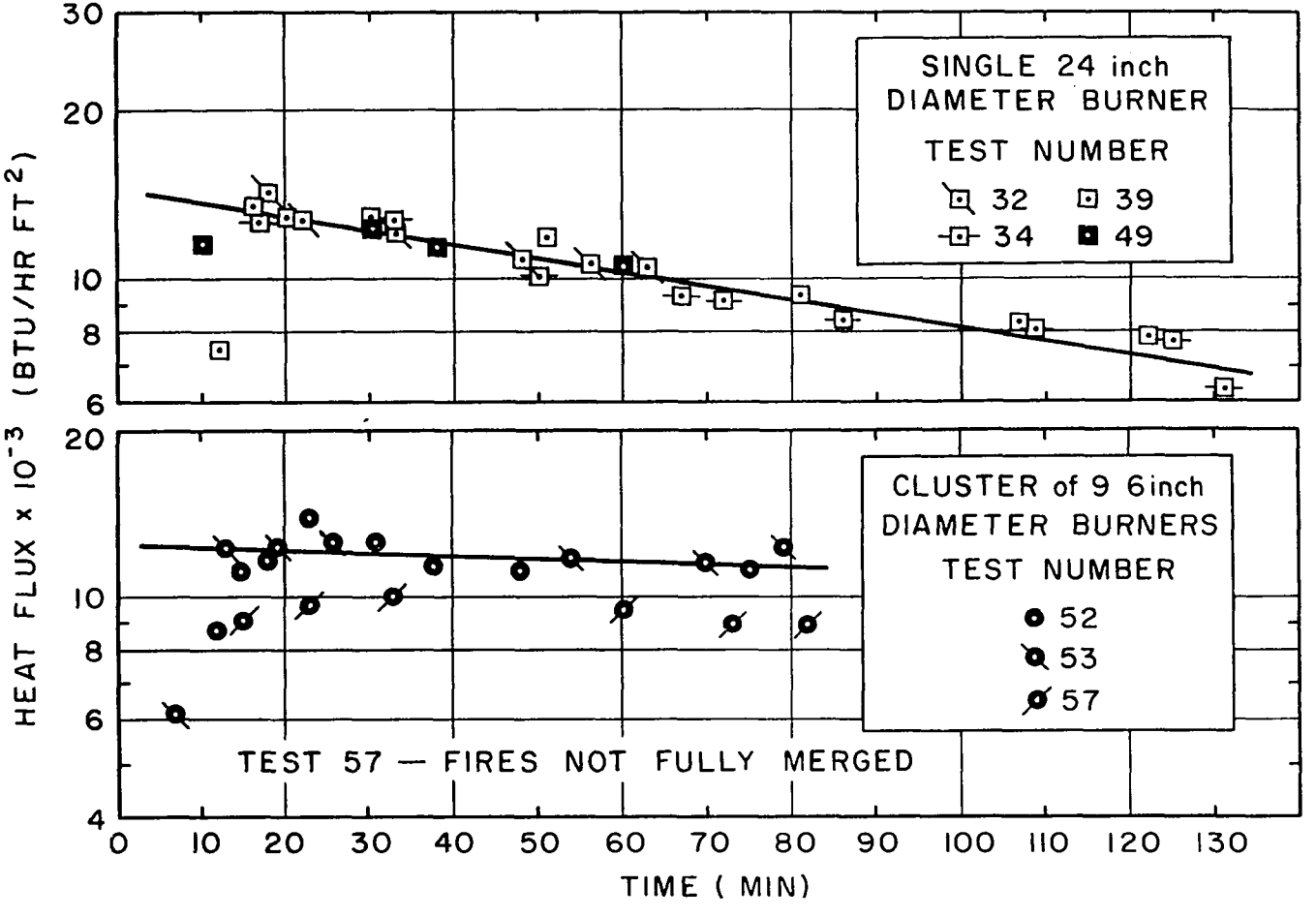

Figure VI-5. Total Heat Transfer Rates from 24-inch Diameter Single and 6-inch Diameter Cluster Burner Acetone Fires.

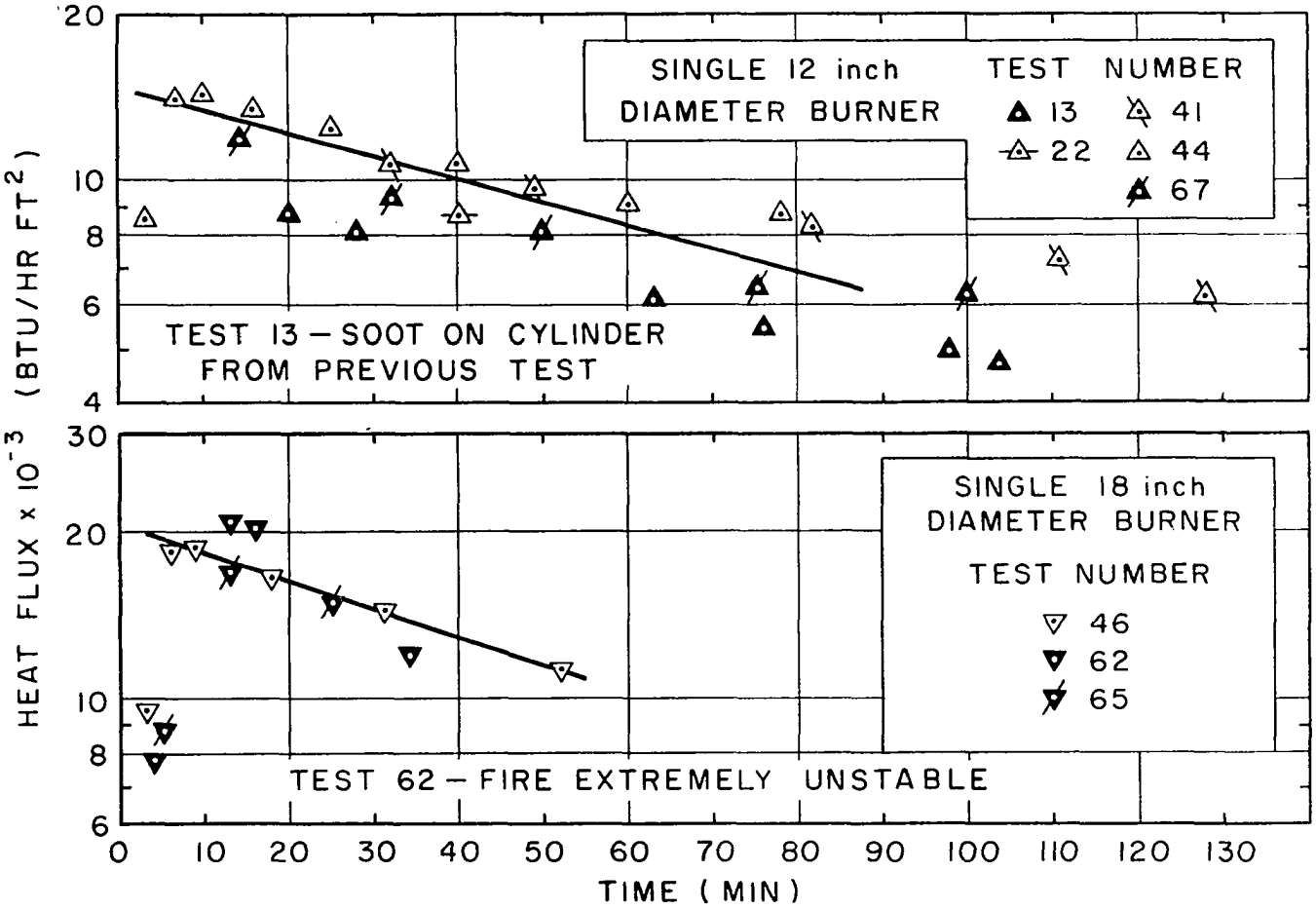

Figure VI-6. Total Heat Transfer Rates from 12- and 18-inch Diameter Single Burner Hexane Fires.

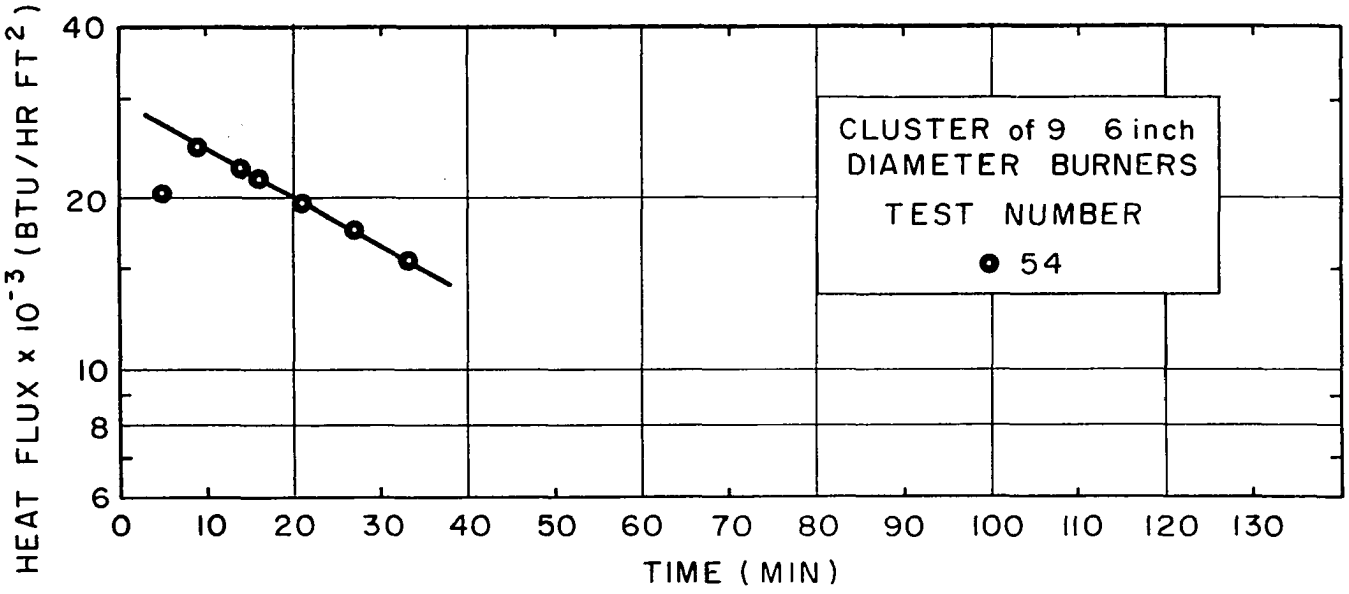

Figure VI-7. Total Heat Transfer Rates from 6-inch Diameter Cluster Burner Hexane Fires.

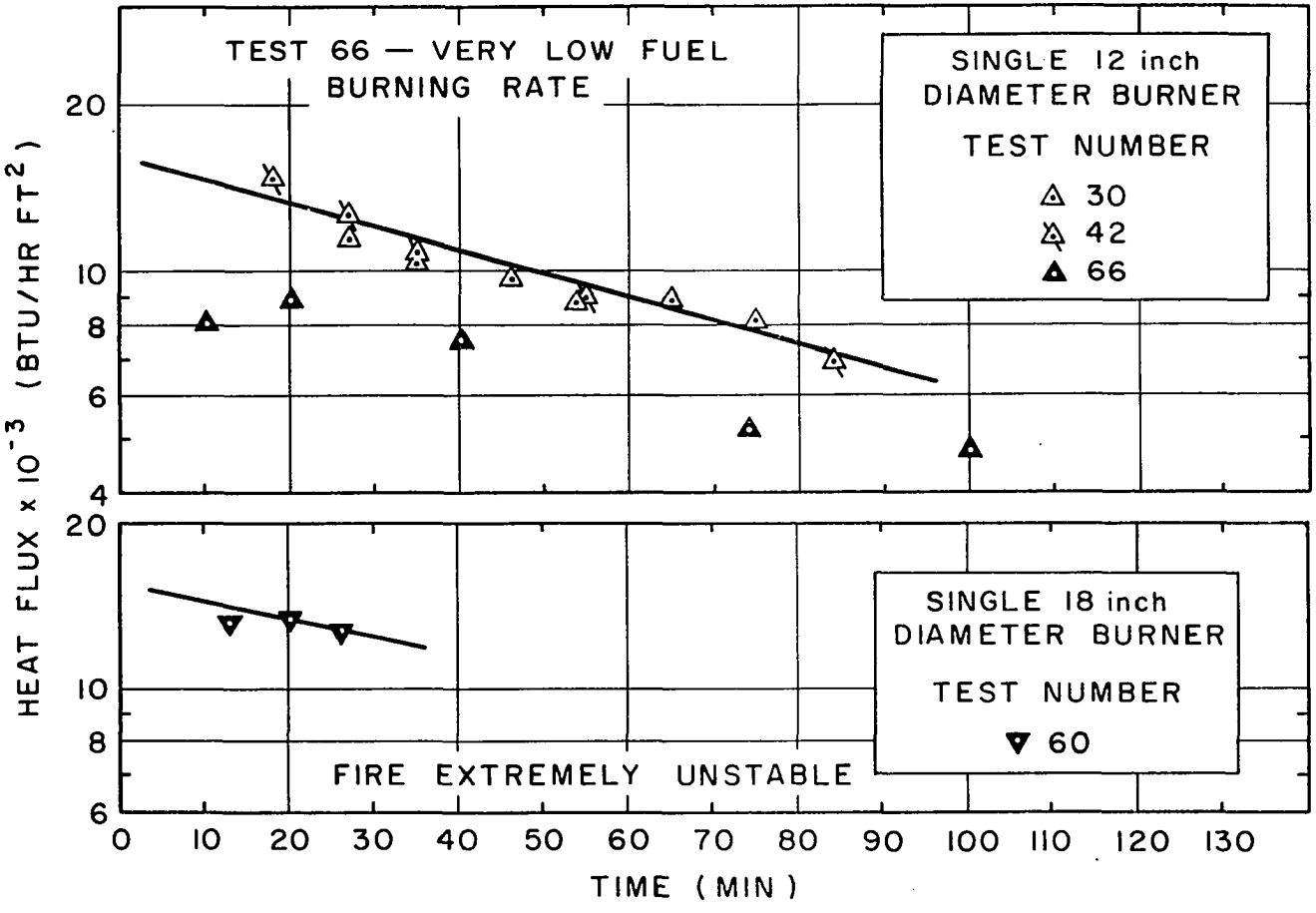

Figure VI-8. Total Heat Transfer Rates from 12-inch and 18-inch Diameter Single Burner Cyclohexane Fires.

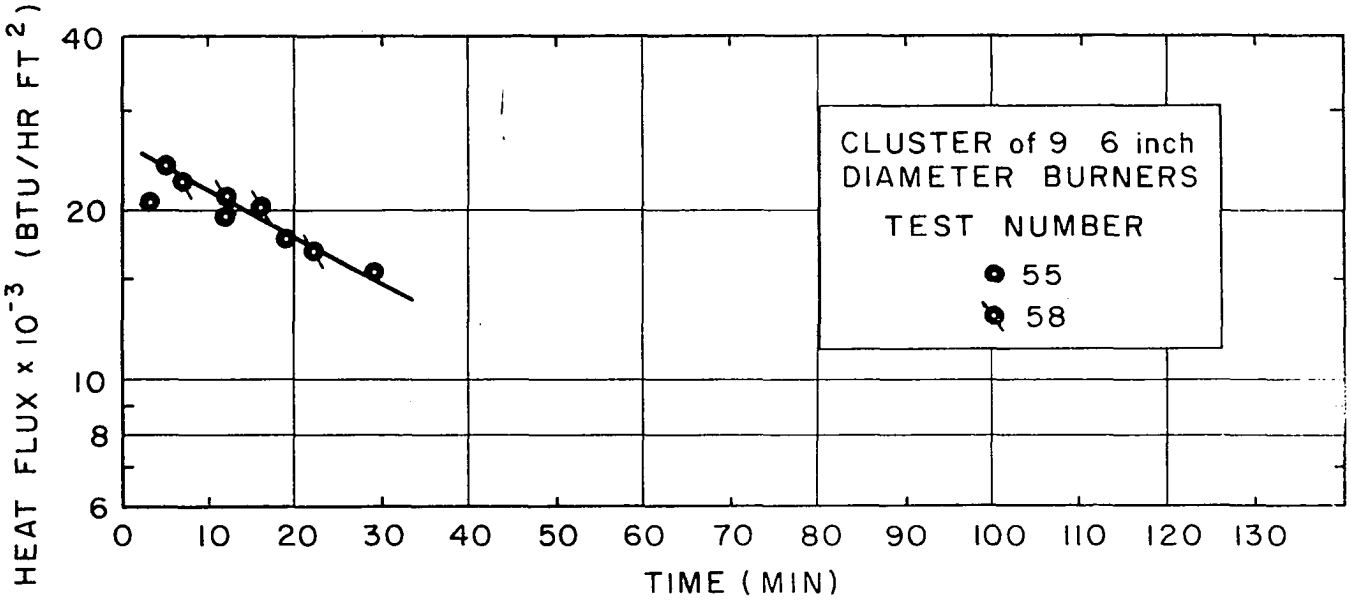

Figure VI-9. Total Heat Transfer Rates from 6-inch Diameter Cluster Burner Cyclohexane Fires.

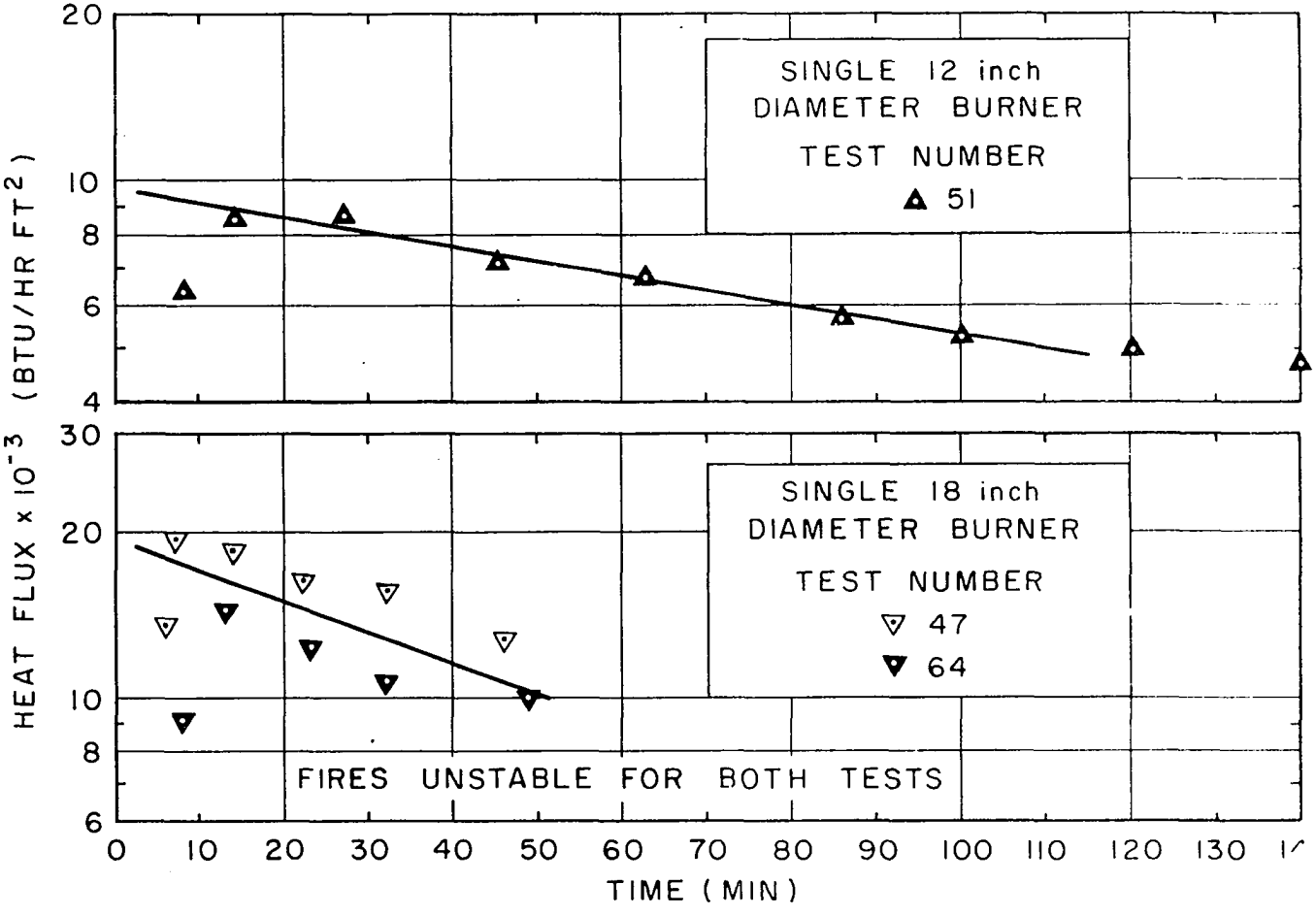

Figure VI-10. Total Heat Transfer Rates from 12- and 18-inch Diameter Single Burner JP-4 Fires.

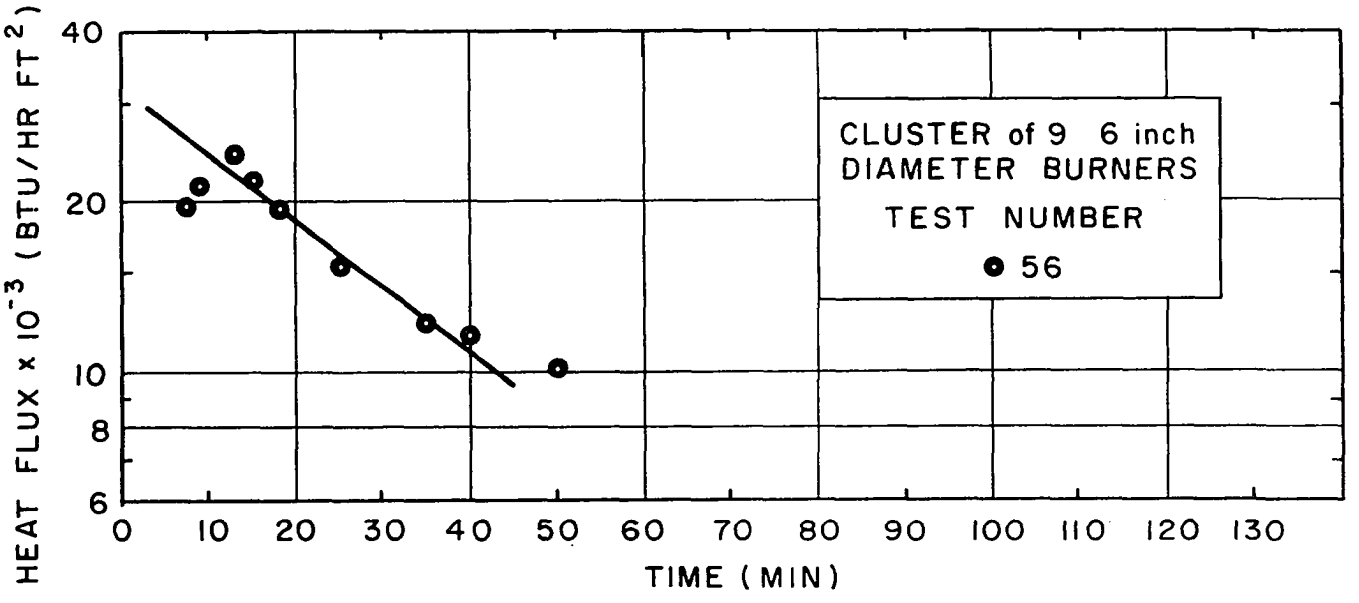

Figure VI-11. Total Heat Transfer Rates from 6-inch Diameter Cluster Burner JP-4 Fires.

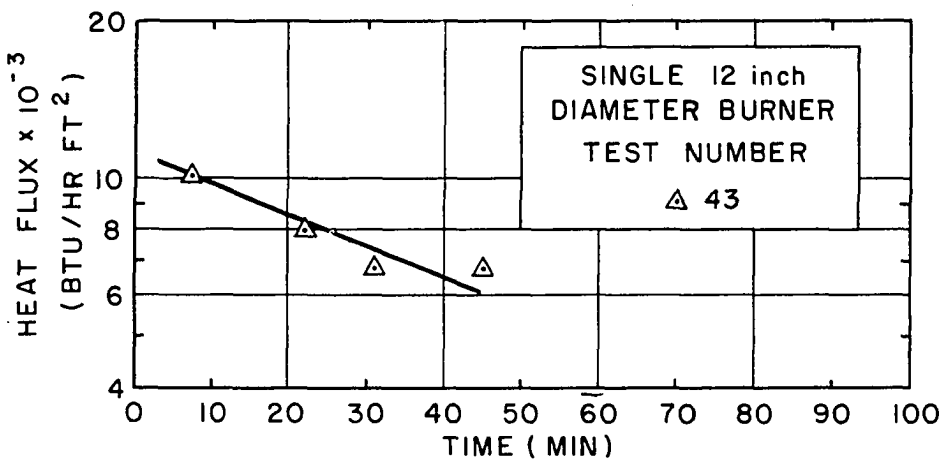

Figure VI-12. Total Heat Transfer Rates from 12-inch Diameter Single Burner Benzol Fires.

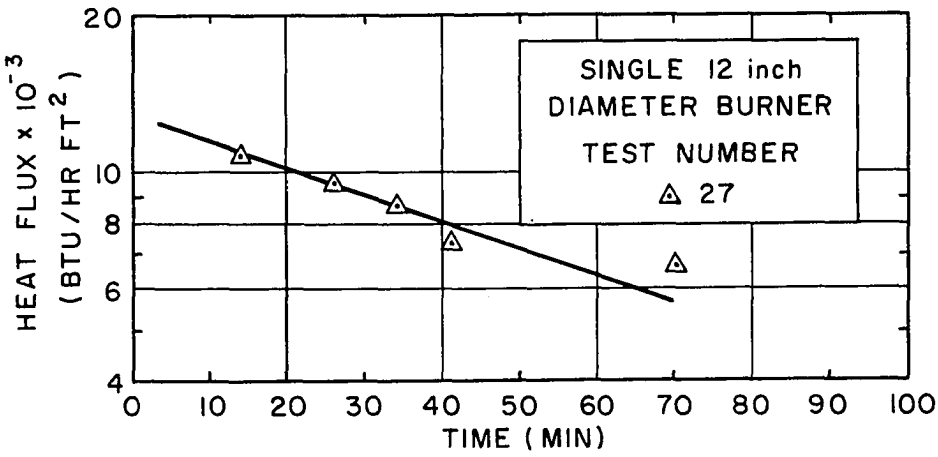

Figure VI-13. Total Heat Transfer Rates from 12-inch Diameter Single Burner Napalm Test Solvent Fires.

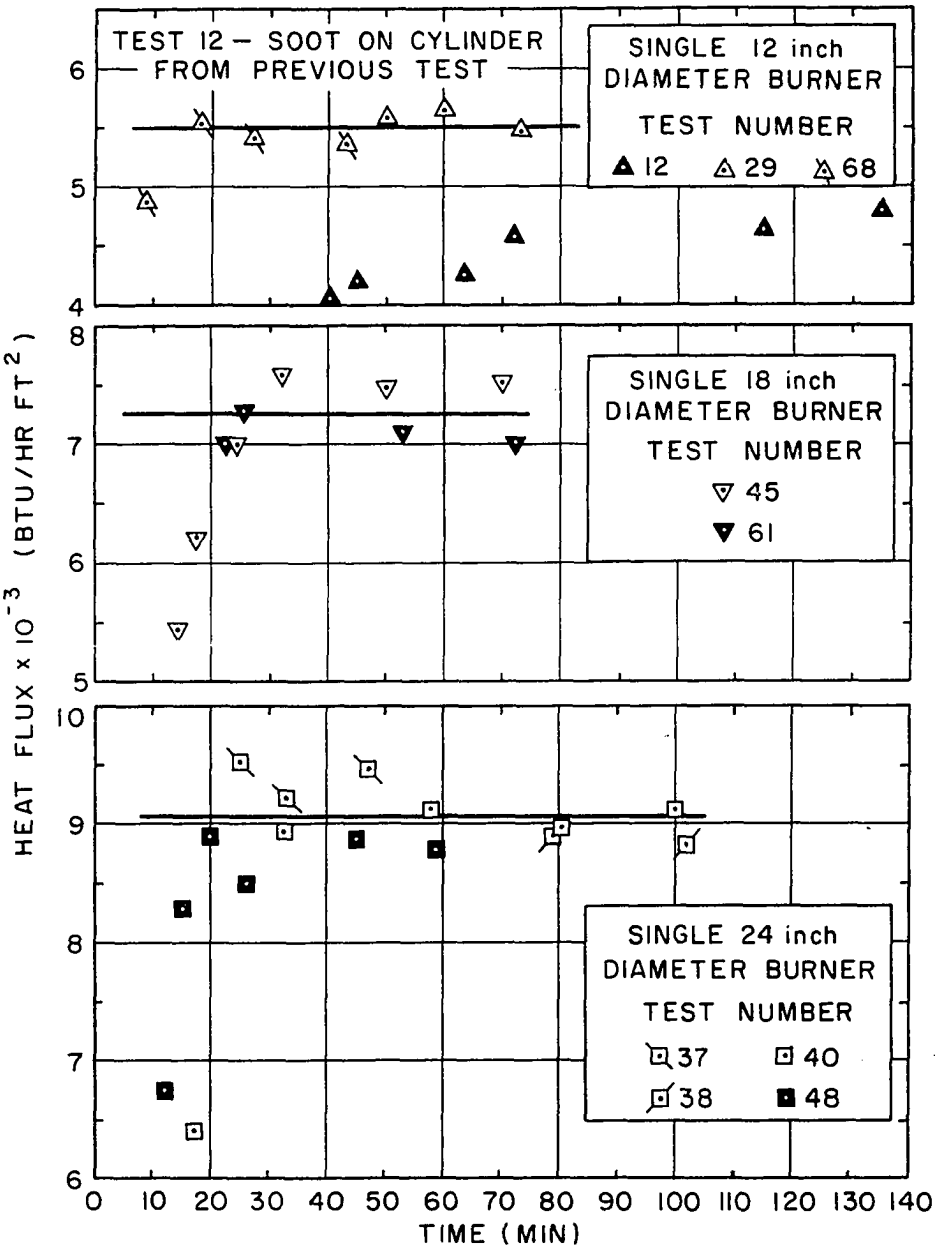

Figure VI-14. Linear Plot of Total Heat Transfer Rates from 12-, 18-, and 24-inch Diameter Single Burner Methanol Fires.

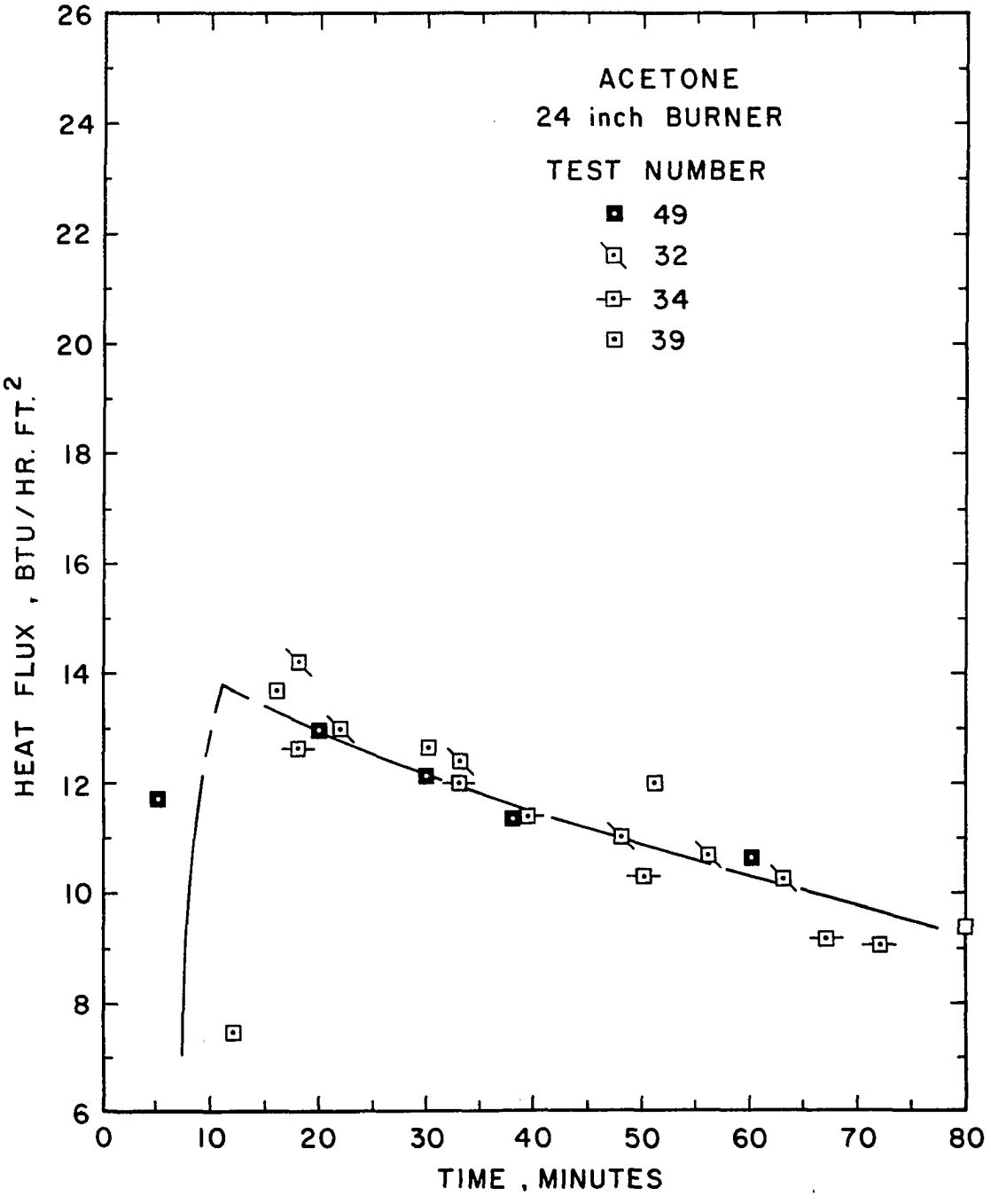

Figure VI-15. Linear Plot of Total Heat Transfer Rates from 24-inch Diameter Single Burner Acetone Fires.

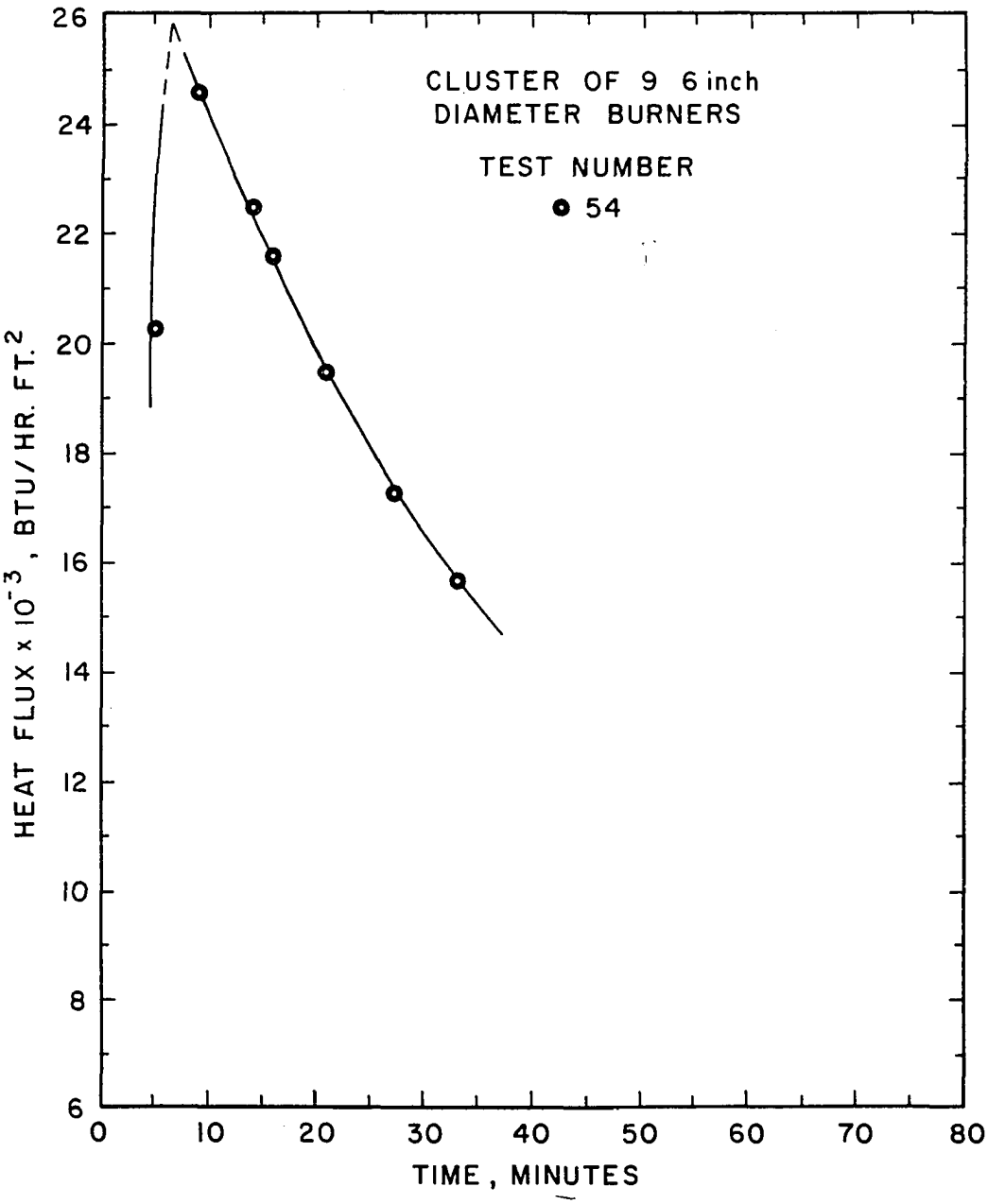

Figure VI-16. Linear Plot of Total Heat Transfer Rates from 6-inch Diameter Cluster Burner Hexane Fires.

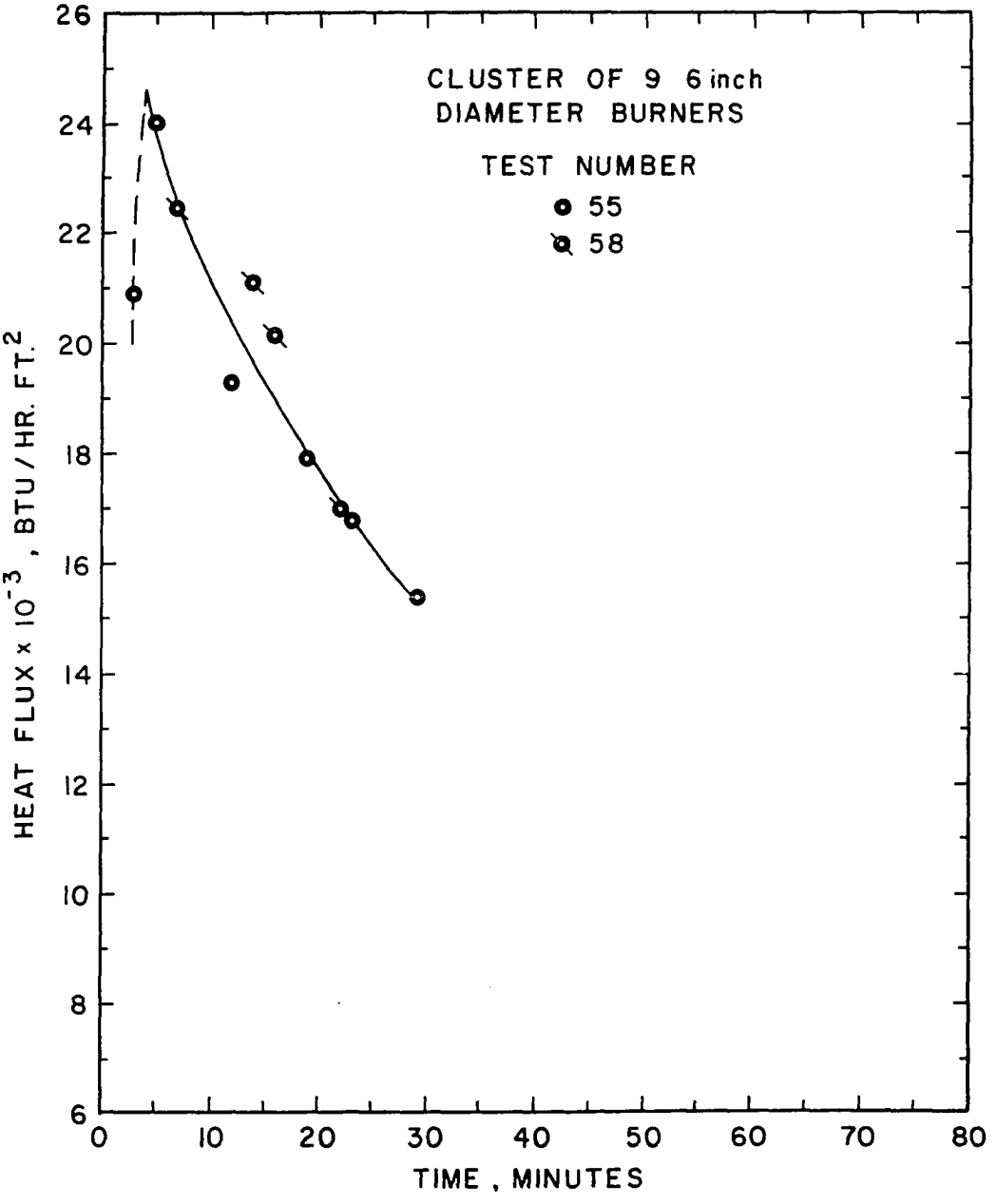

Figure VI-17. Linear Plot of Total Heat Transfer Rates from 6-inch Diameter Cluster Burner Cyclohexane Fires.

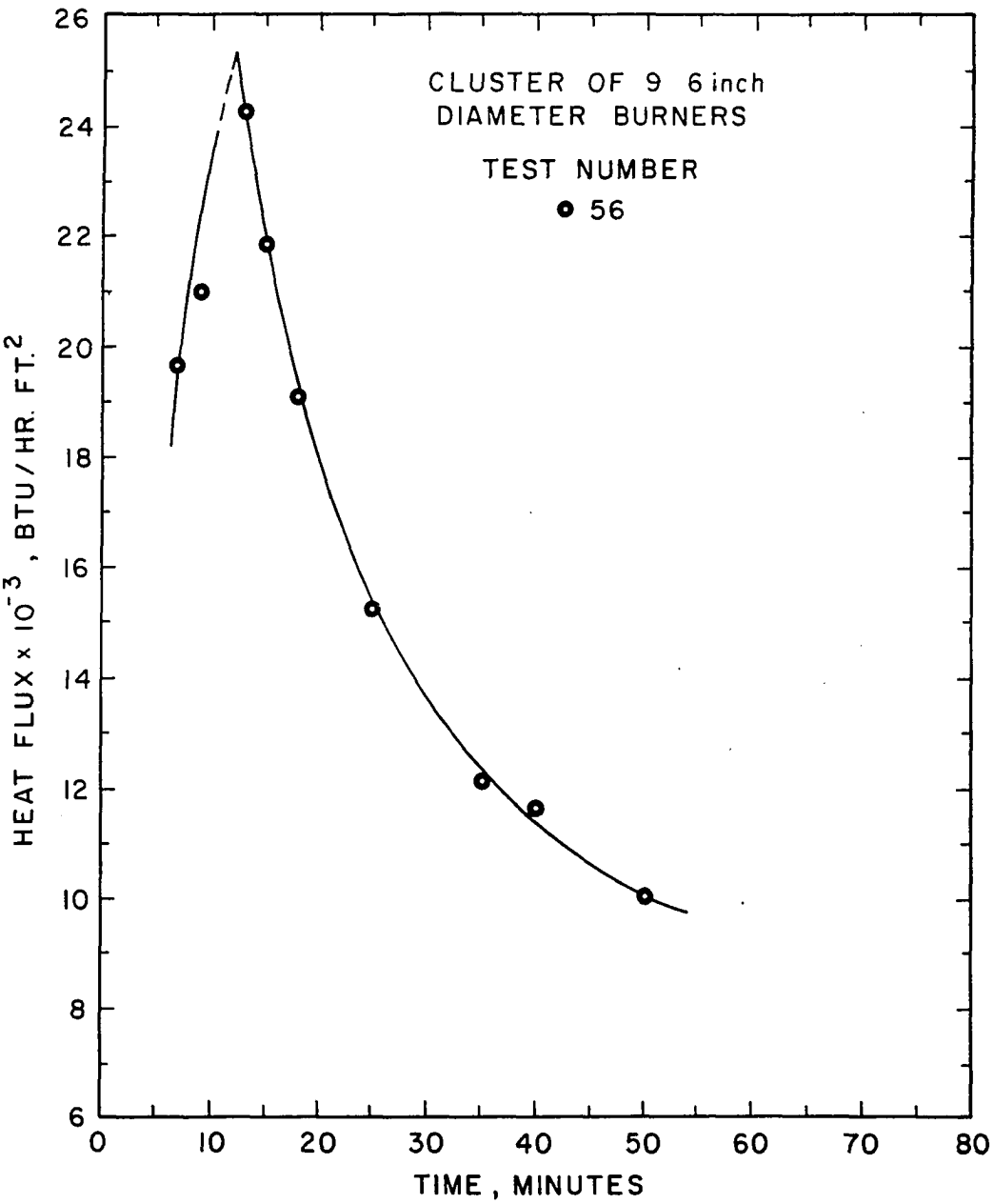

Figure VI-18. Linear Plot of Total Heat Transfer Rates from 6-inch Diameter Cluster Burner JP-4 Fires.

Values for the coefficients in Eq. (VI-1) are presented for each fuel and burner size in Table VI-1 and Table VI-2. Although the heat transfer rates from methanol fires were constant with time, the results have been included in Table VI-1 and Table VI-2 for convenience. It should be pointed out that these coefficients are strictly applicable only between the time limits included in Table VI-2. Since the values of a and b are probably valid down to zero time, the values for a have been labeled as initial heat fluxes in Table VI-1. The total heat transfer data were all taken with the test cylinder in place before the fire was lighted; therefore, the early exposure time includes the time required for the fire to reach its equilibrium size and burning rate, usually 3 to 5 minutes. Transient heating rates were evaluated from the data on the time required to heat the water and the test cylinders to 212°F. These transient heat fluxes were all from 1/2 to 2/3 of the initial heat fluxes obtained by extrapolation. If the true initial heat fluxes are significantly higher than the values reported in Table VI-1, the time period over which the higher flux is applicable is limited to a very few minutes. It should be emphasized that these values are for small to medium size fires; the initial heating rates from larger fires would be higher due to the increased radiant heating from the larger flame thickness.

TABLE VI-1

INITIAL TOTAL HEAT TRANSFER RATES

Coefficient a, Eq. (VI-1)
(Btu/hr-ft^2)

Fuel	Burner Size			
	Single 12-inch	Single 18-inch	Single 24-inch	Cluster of 9[a] 6-inch
Methanol	5,500	7,250	9,000	--
Acetone	9,100	12,000	14,500	12,500[b]
Hexane	15,000	20,500	--	30,000
Cyclohexane	16,000	15,000[c]	--	26,000
JP-4	9,600	19,500	--	31,000
Napalm Test Solvent	13,000	--	--	--
Benzol	11,500[d]	--	--	--

(a) Eight 6-inch diameter burners clustered around a single center burner, all spaced 12 inches apart.

(b) Flames probably not completely merged.

(c) Data obtained from unstable fire.

(d) Data questionable, unable to confirm fire coverage.

TABLE VI-2

EXPONENTIAL TIME DECAY CONSTANTS

Coefficient b, Eq. (VI-1)
(min^{-1})

Fuel	Burner Size			
	Single 12-inch	Single 18-inch	Single 24-inch	Cluster of 9 6-inch
Methanol	0	0	0	0
Acetone [a]	0.133 (10-180)	0.150 (15-105)	0.166 (15-105)	0.033 (10-80)
Hexane	0.266 (5-100)	0.325 (5-55)	--	0.60 (8-35)
Cyclohexane	0.20 [b] (15-25)	0.275 (15-90)	--	0.55 (5-30)
JP-4	0.175 (10-140)	0.375 (5-50)		0.80 (10-40)
Napalm Test Solvent	0.35 (15-50)	--	--	--
Benzol	0. (5-45)	--	--	--

[a] Quantities inside () are exposure time limits, minutes.

[b] Data obtained from unstable fire.

[c] Data questionable, unable to confirm fire coverage.

Radiant Heat Transfer Rates

As discussed in Chapters II and III it was originally intended to use the specular emission-absorption data obtained by Hood (Ref. 17) and Tsai (Ref. 39) to calculate the radiant heating of the test cylinder by the surrounding flames. The best of these data, available at this writing, are presented in Appendix D, Tables D-12, D-13, D-14 and D-15. It quickly became apparent that these data predicted an unrealistically small optical thickness for every fuel except methanol. For this reason, two additional methods were used to calculate the radiant heating from the experimental fires. The designation SF will be used to identify the calculation method and results using the monochromatic absorption-emission coefficients from the small laminar flames.

The second calculation method is completely non-specular; the following equation is assumed to describe the incident radiant heat transfer rate from all contributing wavelengths of a fire.

$$Q/A)_R = \alpha(1-e^{-\beta x}) \qquad \text{(VI-2)}$$

where $Q/A)_R$ = incident radiant heat transfer, Btu/hr-ft^2

α = total radiation source strength, Btu/hr-ft^2

β = average radiation absorption coefficient, in^{-1}

x = radiation path length, inches

The coefficients α and β were determined by the simultaneous

solution of Eq. (VI-2) for two different fire sizes. The radiation measurements were obtained with the narrow beam radiometer looking down the length of flames from a 2-inch wide channel burner. Since the radiation path length varied between 6 and 24 inches, the data were obtained for radiation path lengths of the same magnitude as those encountered during the experimental measurements of the heat transfer rates. The channel burner data are presented in Table D-17, Appendix D. The resulting coefficients, α and β, are presented in Table VI-3 for each fuel. The incident radiant heating rates from a hemispherical flame calculated with Eq. (VI-1) for several fuels are plotted against the flame radius on Fig. 19. It should be emphasized that the coefficient α and the calculated radiant heat flux are for a hemispherical flame with the target located at the center. To obtain the radiant heating from a solid angle it is necessary to divide α by π steradians.

These results look reasonable and the only unexpected observation is that both the methanol and acetone flames become optically thick at almost half the flame thickness of the other fuels. The non-specular calculation method utilizing the coefficients based on the channel burner data will be identified hereafter as the CB method.

The third method for calculating the radiant heating from the experimental fires was based on an adaptation of the techniques of Hottel and Thring discussed in Chapter II.

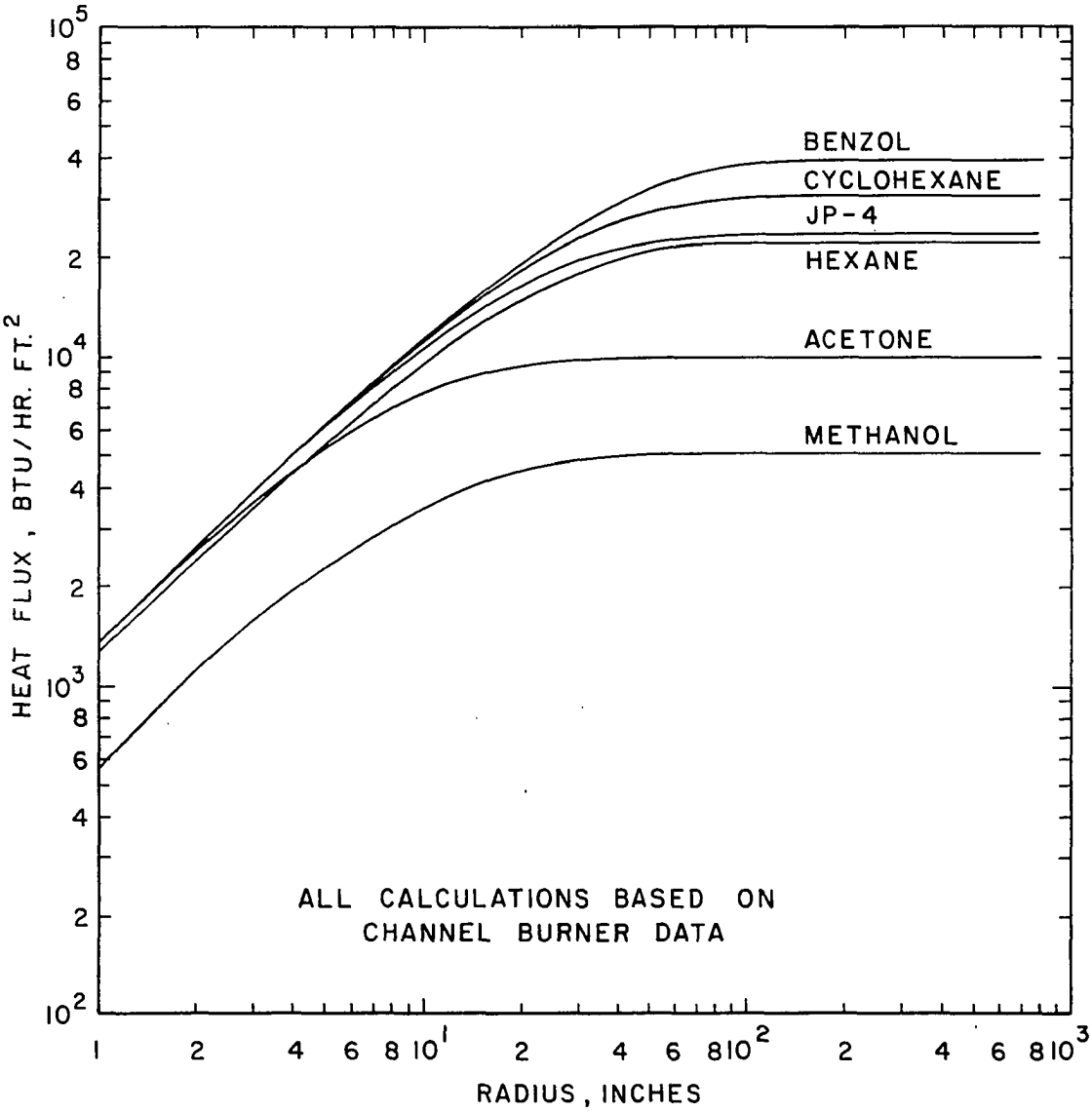

Figure VI-19. Calculated Radiant Heating from Hemispherical Flames of Several Fuels, Based on Channel Burner Data.

TABLE VI-3

COEFFICIENTS FOR CALCULATING TOTAL FLAME RADIATION BASED ON CHANNEL BURNER DATA

Fuel	$(Q/A)_R = \alpha(1-e^{-\beta x})$ α (Btu/hr-ft^2)	β (in^{-1})
Methanol	5080	0.112
Acetone	10000	0.158
Hexane	22600	0.055
Cyclohexane	30700	0.045
JP-4	23700	0.060
Benzol	38500	0.036

The radiation calculations were made for only one hypothetical flame composition corresponding to the equilibrium reaction of normal hexane with 48 mole percent of the stoichiometric air required for burning all carbon to CO_2. The air was assumed to have 50 percent relative humidity at 80°F. A 20 percent heat loss to the surroundings was also assumed. The equilibrium concentrations were calculated by Mody and Lott (Ref. 33) using the minimum free energy technique mentioned in Chapter II. The resulting equilibrium concentrations (mole percent) were:

CO - 15.9%

CO_2 - 3.7%

H_2 - 16.8%

H_2O - 7.6%

N_2 - 55.8%

C - 0.22%

The "flame" temperature from the equilibrium calculation was 1960°F and agrees with the optical pyrometer temperature measurements made on the experimental fires (see Table D-3, Appendix D). The carbon or soot concentration is equivalent to 0.225 mg/liter of flame volume and is in line with values reported by Thring (Ref. 38).

The calculation technique is that proposed by Thring and discussed in detail in Chapter II. The incident radiation heating is given as a function of flame thickness by Eq. (II-10); the contributions from the various radiating

components are added to get the total radiant heating from the flame. The correction factors for the overlap of the spectra of the non-luminous emitters and the effective emissivities of the luminous, E_L, and the non-luminous, E_n, radiators were obtained from the nomograms in McAdams (Ref. 32). The overlap of the luminous and non-luminous spectra was corrected for by using an absorption coefficient $\varkappa$ of 0.005 (cm mg/liter)$^{-1}$ in Eq. (II-10).

The incident radiant heating rate from a hemisperical flame, calculated by the above method, is plotted vs flame radius as the TH method curve on Fig. VI-20. The TH designation is used hereafter to identify the results of this calculation method.

The TH method curve does not follow a simple relationship of the form of Eq. (VI-2); however, it does follow a straight line, on the log-log plot, out to flame thicknesses of 70 to 80 inches which more than embraces the flame sizes encountered in these experiments. The incident radiant heating calculated by the TH method for flame sizes up to 70 or 80 inches may be obtained from

$$Q/A)_R = 2{,}450\ (x)^{0.565} \qquad \text{(VI-3)}$$

where $Q/A)_R$ = total radiant heat flux from the fire, Btu/hr-ft^2

x = radiation path length, inches

The maximum radiant heat predicted by the TH method is

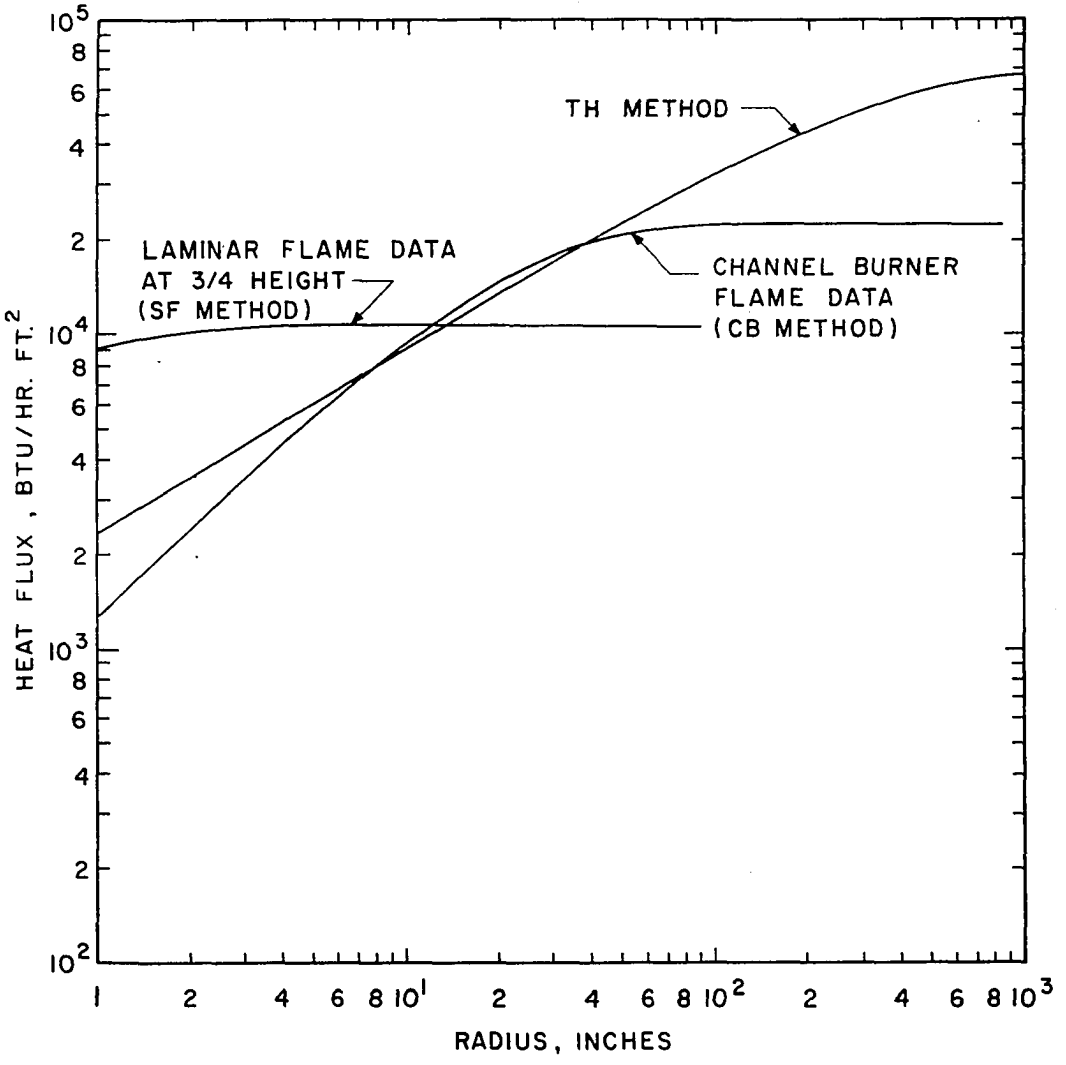

Figure VI-20. Calculated Radiant Heating from Hexane Flames Using Different Methods.

67,000 Btu/hr-ft^2, and the flame becomes optically thick at about 1000 inches. Again it should be noted that these values are for a hemisperical flame and should be divided by π steradians to get the radiant heating from a solid angle. Also it should be emphasized that the single TH method results, expressed by Eq. (VI-3) were used to make the radiation calculations for all the luminous fuels.

The radiant heating calculated for hexane fires with the three approaches outlined here are compared on Fig. VI-20. The results differ for large and small fires but agree for the medium sized fires encountered in these experiments. It is obvious that the radiant heating calculated with the small laminar flame data (SF method) are almost independent of flame thickness. The results of the SF calculations for the other fuels, except methanol, gave much the same result.

Radiation measuremtns were made with a wide angle radiometer located 70 inches from the flame column. These external measurements were intended to confirm the emission-absorption data used in the radiant heating calculations; however, the external radiation measurements continued to rise during the test due to the increasing temperature of the building walls and other visible objects. The radiation data could be extrapolated back to zero time to eliminate the increased radiation due to building heat-up; however, if sufficient cooling time was not allowed between tests the building was emitting significant radiation when

the next test was started. In short, good external radiation data could be obtained only after the building had cooled for 4 to 6 hours. Rather than limit the program to 1 or 2 tests per day, it was decided to rely in part on some of the external radiation measurements made by Huffman (Ref. 23) for a variety of merged fires from cluster burners. The radiation data obtained by Huffman are presented in Table D-16, Appendix D.

The measured and calculated external radiant heating are compared on Fig. VI-21 for methanol fires, Fig. VI-22 for acetone fires, Fig. VI-23 for hexane fires, Fig VI-24 for cyclohexane fires and Fig. VI-25 for benzol fires. The radiant heating for a measured flame size was calculated by each of the three methods, SF, CB and TH, except for methanol fires for which the TH method isn't applicable, and benzol and JP-4 fires for which specular absorption and emission coefficients for the SF method calculations were not available. For each measured radiation value there will be two or three calculated radiation values, one for each calculation method. If the measured and calculated radiation value agree the plotted point will fall on the 45 degree line on the graph.

The large differences between the calculated radiant heating rates for flames that produced the same measured radiant heating rates indicate that the dimensions of at least one of the flames were probably incorrect.

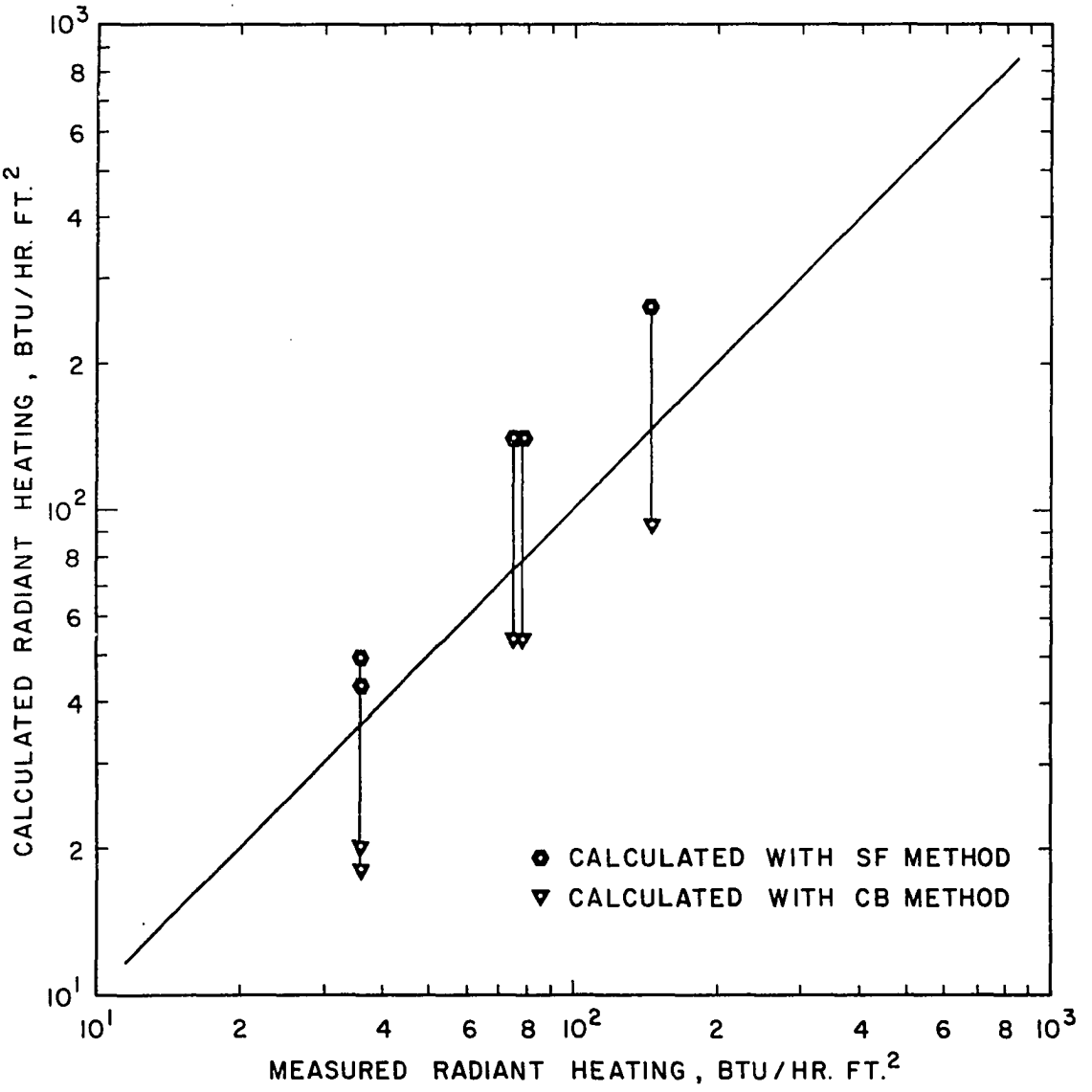

Figure VI-21. Comparison of Calculated and Measured Radiant Heating External to Methanol Fires.

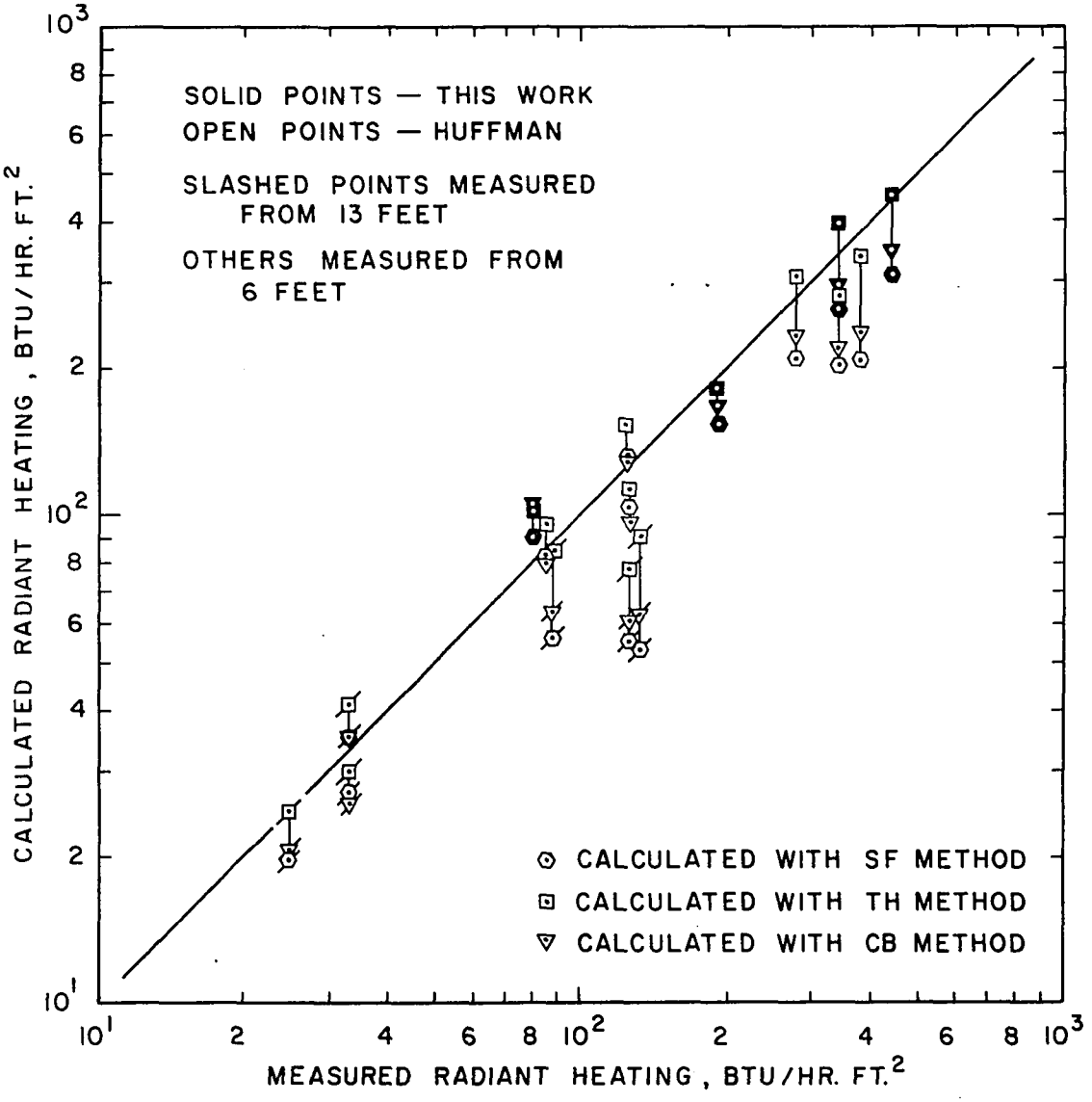

Figure VI-22. Comparison of Calculated and Measured Radiant Heating External to Acetone Fires.

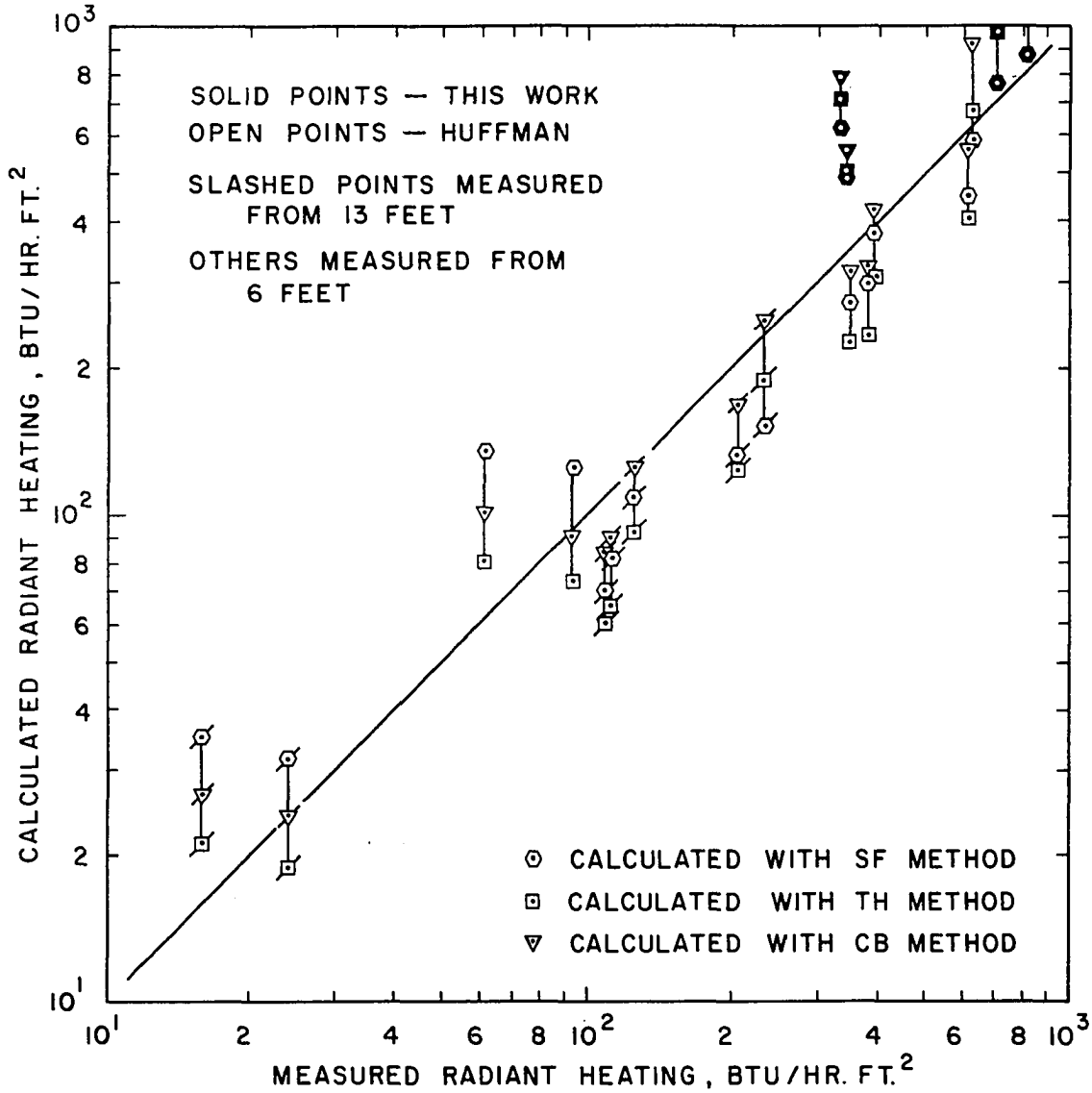

Figure VI-23. Comparison of Calculated and Measured Radiant Heating External to Hexane Fires.

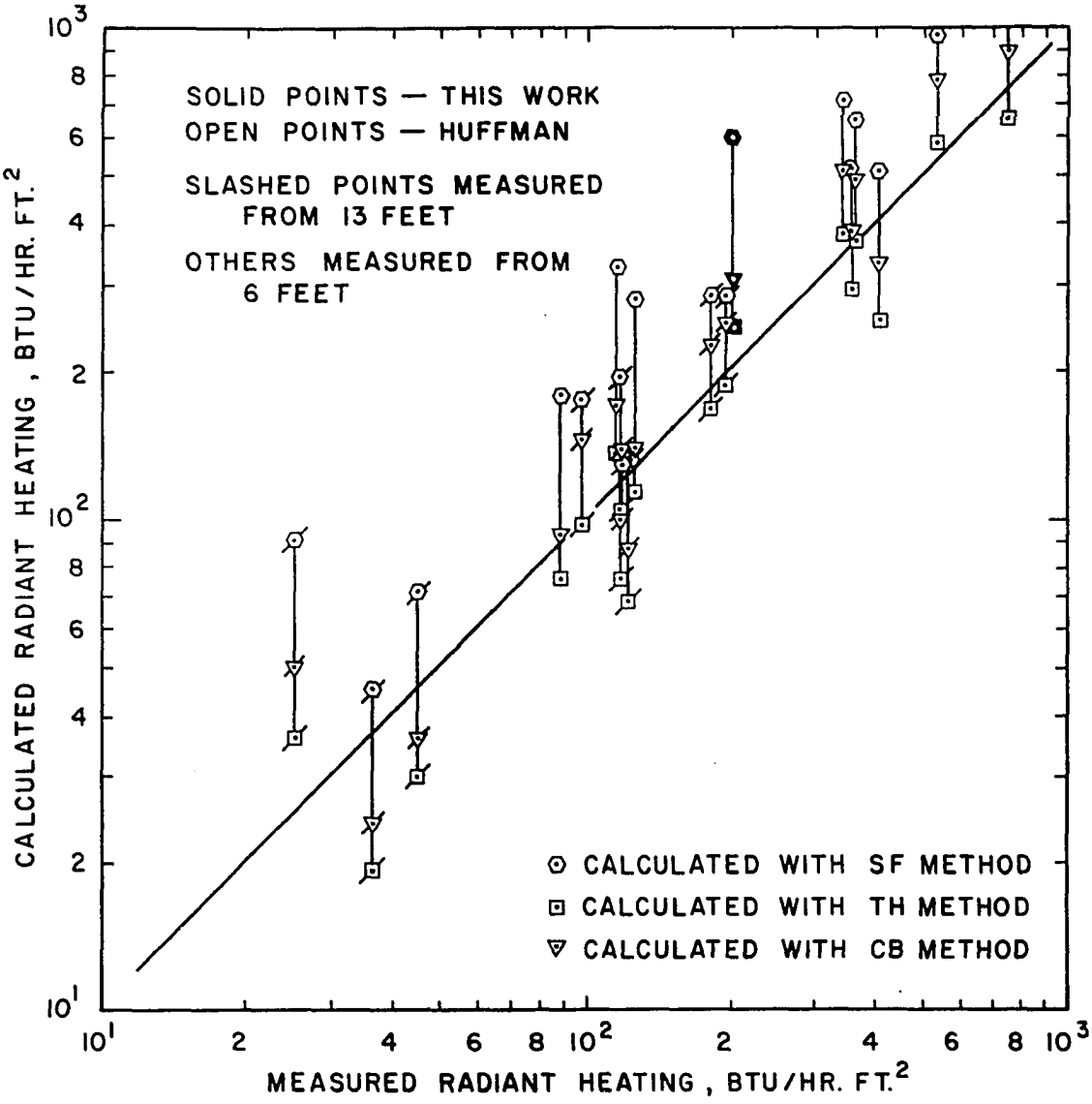

Figure VI-24. Comparison of Calculated and Measured Radiant Heating External to Cyclohexane Fires.

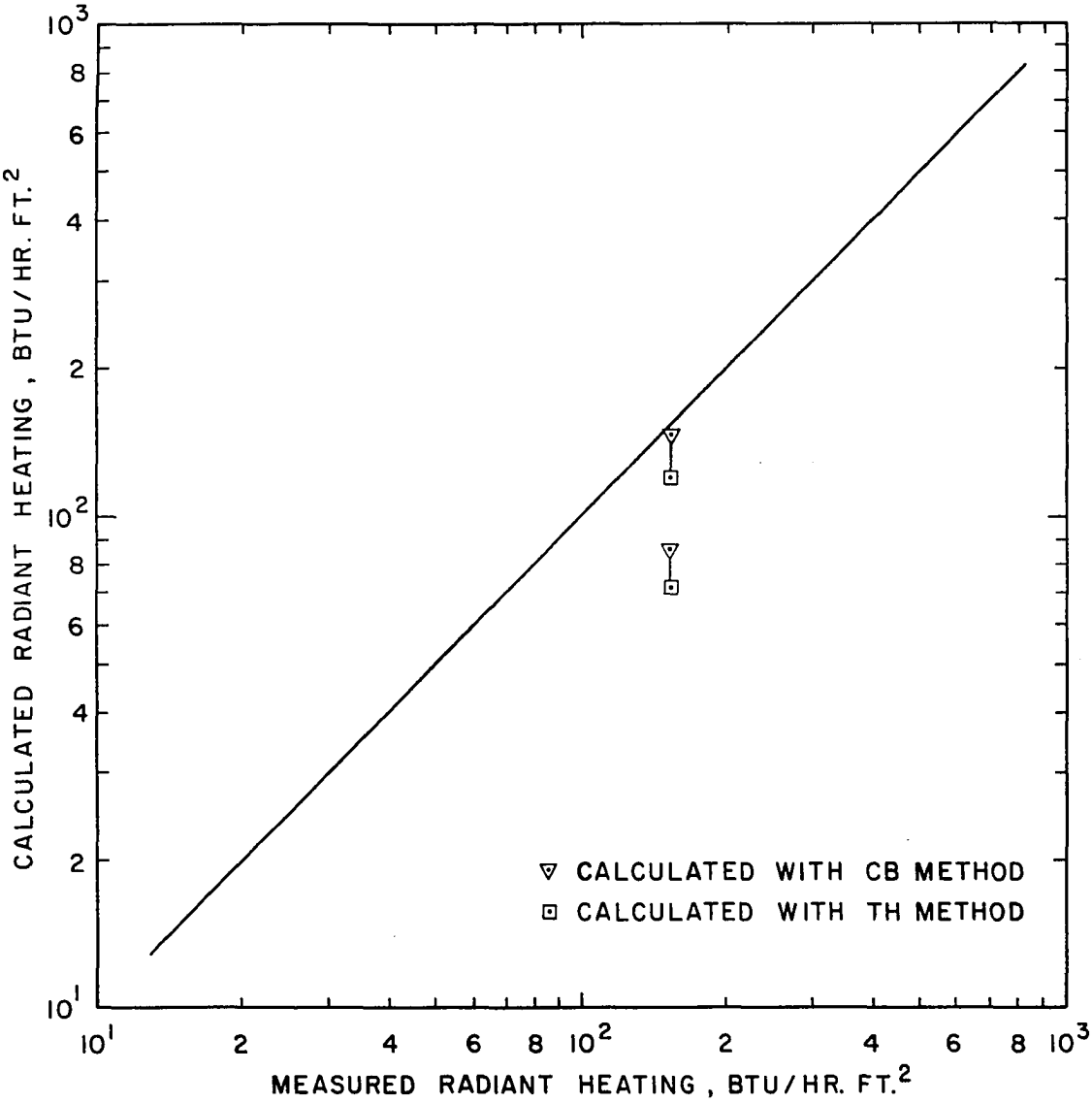

Figure VI-25. Comparison of Calculated and Measured Radiant Heating External to Benzol Fires.

This conclusion cannot be positively asserted because the radiation calculations are dependent on the flame shape as well as its size; however, the height to diameter ratio remains approximately the same for these flames so the calculated results should follow the flame size.

The external radiant heating calculations include correction factors for atmospheric absorption between the radiometer and the fire and the transmissivity of the quartz window on the radiometer. The source and magnitude of these correction factors are covered in Appendix G.

Figures VI-21 through VI-25 show that none of the radiation calculation methods provide results that are in close agreement with the measured radiation values and there is no basis for choosing one of the calculation methods over the others. The failure of the external radiation measurements to provide a basis for choosing the method results from a combination of two factors. The flame sizes are in a range where the differences between the results calculated by the various methods are small; this can be seen by comparing the calculated hemispherical flame radiation presented on Figs. VI-19 and VI-20 for radii of 6 to 60 inches. Errors in the calculated values due to inaccuracies in the flame dimensions are about the same size as the differences in the values calculated by the different methods. The lack of choice made it necessary to use all three methods for calculating the radiant heating of the test cylinder inside the flames.

The flame dimensions for all the calculations were obtained from flame photographs taken from a fixed camera position. A negative photograph, taken from the same fixed camera position, of a dimensioned grid hanging over the center of the burner location was laid over photographs of the flames. The flame dimensions (height and diameter) were read directly off this combination; the dimensions were adjusted by eye to encompass a rectangular area equivalent to the area of the flame on the photograph. The flame dimensions for the experimental fires are presented in Table D-4, Appendix D. Photographs of typical experimental fires and some discussion about the fluctuations in the physical size and structure of the flames are presented later in this chapter.

The calculated radiant heating incident on the test cylinder is presented in Table VI-4 for the methanol flames and Table VI-5 for the luminous flames. The luminous calculations were made using all three methods except where insufficient calculation parameters were available. The methanol calculations were made for only two methods, the SF method (specular data from small laminar flames) and the CB method (non-specular data from medium size channel burner flames). The methanol flame sizes changed so much due to large pulsations of the flame, that two flame sizes were used with each calculation method. One flame size was considered to be a cone shaped flame which tapered from the

TABLE VI-4

CALCULATED INCIDENT RADIANT HEATING
INSIDE METHANOL FLAMES

Test No.	Burner Diameter (inches)	Calculated Incident Radiant Heating (Btu/hr-ft^2)			
		SF Method		CB Method	(b)
		Cone	0.67 Factor	Cone	0.67 Factor
68	12	5154	4150	1090	1180
29	12	5176	4510	1130	1175
12	12	5154	4150	1000	1259
	Average =	5161	4270	1073	1205
61	18	5157	6540	1241	1800
45	18	5167	6530	1258	1800
	Average =	5162	6535	1249	1800
48	24	6531	8700	1539	2500
40	24	6815	8220	1625	2360
37/38	24	6546	7600	1550	2160
	Average =	6630	8173	1571	2340

(a) The SF method used spectral data from small laminar flames. The CB method uses non-spectral data from medium sized flames.

(b) The cone calculation uses cone shaped flame, the 0.67 factor calculation uses 0.67 of the maximum flame cylinder.

TABLE VI-5

CALCULATED INCIDENT RADIANT HEATING
INSIDE LUMINOUS FLAMES

Fuel	Test No.	Burner Diameter (inches)	Calculated Incident Radiant Heating (Btu/hr-ft^2) SF Method	CB Method	TH Method[a]
Acetone	57	6[b]	8254	8083	9607
	53	6	8232	7614	8856
	52	6	8251	8005	9486
			Avg=8245	7900	9316
	50	12	7705	4291	5163
	16/17/18	12	7515	3735	4649
			Avg=7610	4013	4906
	63	18	7941	5241	6083
	49	24	8230	7638	8940
	39	24	8230	7639	8948
	34/35/36	24	8230	7641	8963
	32/33	24	8266	8445	10330
			Avg=8239	7840	9295
Hexane	54	6	10560	11480	10410
	67	12	10530	6613	6884
	44	12	10550	9519	8958
	41	12	10560	10250	9484
	22	12	10555	8630	8323
	13/14/15	12	10555	8630	8323
			Avg=10550	8728	8394
	65	18	10560	11440	10370
	62	18	10560	11780	10630
	46	18	10560	13030	11600
			Avg=10560	12083	10866

[a] SF Method uses spectral data from small laminar flames.
CB Method uses non-spectral data from medium sized flames.
TH Method developed from techniques of Thring and Hottel.

[b] Cluster of 9, 6-inch diameter burners.

TABLE VI-5 (continued)

Fuel	Test No.	Burner Diameter (inches)	Calculated Incident Radiant Heating ($Btu/hr-ft^2$) SF Method	CB Method	TH Method[a]
Cyclo-hexane	58	6[b]	21250	13040	10090
	55	6	21123	12600	9842
			Avg=21186	12820	9966
	66	12	20460	6270	6076
	59	12	--	--	--
	42	12	21120	9960	8288
	30/31	12	21080	9329	8941
			Avg=20886	8519	8614
	60	18	21180	11080	8946
JP-4	56	6	--	12010	9842
	51	12	--	8610	7598
	47	18	--	9700	8312
	64	18	--	--	--
				Avg= 9700	8312
Benzol	43	12	--	9200	7601
Napalm	27	12	--	--	7200
	28	12	--	--	7200

[a] SF Method uses spectral data from small laminar flames.
CB Method uses non-spectral data from medium sized flames.
TH Method developed from techniques of Thring and Hottel.

[b] Cluster of 9, 6-inch burners.

burner rim to a thickness of 1- to 2-inches around the test cylinder. This cone shaped flame remained fixed and was about the minimum flame size. The other flame size calcula- were made by applying a factor of 0.67 to the radiant heating from the maximum flame diameter, i.e. the diameter of the flame pulses. The origin of the 0.67 factor is presented in the last section of this chapter. The radiant heating values were averaged for each burner size and fuel type; they are also shown in Tables VI-4 and VI-5.

Convective Heat Transfer Rates

Assuming the reflectance of the soot is negligible, all the incident radiant heat is absorbed. At the start of the tests the soot layer is thin and the radiation emitted by the test cylinder is negligible. The convective heat transfer rate at the start of the tests is then given by the difference between the initial total heat transfer rate and the absorbed radiant heat transfer rate. The initial total heat transfer rates from Table VI-1, the average calculated radiant heat transfer rates from Tables VI-4 and VI-5, and the initial convective heat transfer rates are presented in Table VI-6 for the methanol flames and Table VI-7 for the luminous flames.

The actual convective heat transfer rates should be nearly independent of flame size. This assertion can be used as a basis for selecting the best radiation calculation technique and the best convective heat transfer rates.

TABLE VI-6

SUMMARY OF HEAT TRANSFER RATES INSIDE METHANOL FLAMES

Burner Diameter (inches)	Initial Total Heat Transfer Rates ($Btu/hr-ft^2$)	Average Calculated Incident Radiant Heating Rate ($Btu/hr-ft^2$)		Initial Convective Heat Transfer Rate ($Btu/hr-ft^2$)	
		SF Method		SF Method	
		Cone	0.67 Factor	Cone	0.67 Factor
12	5500	5161	4270	339	1230
18	7250	5162	6535	2088	715
24	9000	6630	8173	2370	827
		CB Method		CB Method	
		Cone	0.67 Factor	Cone	0.67 Factor
12	5500	1073	1205	4427	4295
18	7250	1249	1800	6001	5450
24	9000	1571	2340	7429	6660

TABLE VI-7

SUMMARY OF HEAT TRANSFER RATES INSIDE LUMINOUS FLAMES

Fuel	Burner Diameter (inches)	Initial Total Transfer Rate[a] (Btu/hr-ft^2)	Average Calculated Incident Radiant Heating (Btu/hr-ft^2)			Initial Convective Heat Transfer Rate (Btu/hr-ft^2)		
			SF Method	CB Method	TH Method[b]	SF Method	CB Method	TH Method
Acetone	6[c]	12500	8245	7900	9316	4255	4600	3184
	12	9100	7610	4013	4906	1490	5087	4194
	18	12000	7941	5241	6083	4059	6759	5917
	24	14500	8239	7840	9295	6261	6660	5205
Hexane	6	30000	10560	11480	10410	19440	18520	19590
	12	15000	10550	8728	8394	4450	6272	6606
	18	20500	10560	12083	10866	9940	8417	9643
Cyclohexane	6	26000	21186	12820	9966	4814	13180	16043
	12	16000[d]	20886	8519	8619	-4886	7481	7381
	18	15500[d]	21180	11080	8946	-5680	4420	6554
JP-4	6	31000	--	12010	9842	--	18990	21158
	12	9600	--	8610	7598	--	990	2002
	18	19500	--	9700	8312	--	9800	11188
Benzol	12	11000[e]	--	9200	7601	--	1800	3399
Napalm	12	13000	--	--	7200	--	--	5800

[a] This is total heat transfer rate extrapolated to zero time, i.e. before soot buildup.

[b] SF method radiation contribution calculated using spectral data from small laminar flames, CB method radiation contribution calculated using non-spectral data from medium size flames and TH method radiation contribution calculation based on techniques of Thring and Hottel.

[c] Nine 6-inch burners run in a cluster.

[d] Data from unstable fire.

[e] Data doubtful, unable to confirm fire coverage.

Starting with the methanol flames, Table VI-6, the most consistent initial convective heat transfer rates are 4,000 to 7,500 Btu/hr-ft^2 as calculated by the CB method (non-specular data from medium sized fires). The cone fire size should yield the minimum calculated radiant heating rates for methanol; therefore the results using the 0.67 factor are preferred. If the result from the small (12-inch) burner is eliminated on the suspicion that the flame coverage of the test cylinder was not complete, the initial convective heat transfer rate lies between 5,450 and 6,660 Btu/hr-ft^2. Since there is no assurance that these convective heat transfer rates are maximum regardless of fire size a value of 7,000 Btu/hr-ft^2 is assumed to represent the average convective heat transfer rate.

The outside surface temperature of the test cylinder remained constant (no soot build-up) at about 250°F and the methanol flame temperature was probably near enough to 2250°F so that a 2000°F temperature difference can be used to back calculate a convective heating coefficient of 3.5 Btu/hr-ft^2°F. This convective coefficient is about twice the values calculated with the available correlations and presented in Table II-2, Chapter II. The maximum heat transfer from an optically thick methanol flame will consist of 5,000 Btu/hr-ft^2 from radiation plus 7,000 Btu/hr-ft^2 from convective heating, or 12,000 Btu/hr-ft^2 total heat transfer to a cold (200-300°F) target.

The convective heat transfer rates from the luminous flames, Table VI-7, are considerably more obscure than those from the non-luminous methanol flames. Ignoring for the moment the high convective heating rates calculated for most of the 6-inch cluster fires, the convective heat transfer rates based on radiant heat transfer calculations by the CB and TH method are about the same. The convective heat transfer rates based on radiant heat transfer calculations by the SF method (specular data from small laminar flames) are very inconsistent for cyclohexane fires. The radiant heat transfer rates calculated by the SF method for cyclohexane fires are considerably higher than the results calculated by the other methods. This result is not surprising since the maximum radiant heat transfer from an optically thick cyclohexane fire, based on the absorption-emission coefficients for small, laminar flames is 84,000 Btu/hr-ft^2, an extremely high value.

The convective heat transfer rates for the acetone, hexane and cyclohexane fires from single burners calculated by the CB and TH method, vary from 4,194 to 9,643 Btu/hr-ft^2. The average convective heat transfer rate is 6,913 Btu/hr-ft^2 which can be rounded to 7,000 Btu/hr-ft^2. Of course the experimental variation is ± 50 percent. The convective heat transfer rates from JP-4 single fires vary from 990 to 11,188 Btu/hr-ft^2; the average is 6,098 Btu/hr-ft^2 which is close to the average from the other fuels but the experimental variation is almost ± 100 percent. This discrepancy

for the JP-4 fires cannot be explained except to point out that the low convective heat transfer rates occur for the 12-inch burner fires which could easily have experienced poor fire coverage. The exponential time decay constant, Table VI-2, and the maximum measured total heat transfer rates (not just the initial or extrapolated values) from the 12-inch burner fires are considerably lower for JP-4 than for the similar fuels, hexane, cyclohexane, benzol and Napalm Test Solvent. The total and convective heat transfer rates from the benzol and Napalm Test Solvent data must also be suspect due to the possiblility of incomplete flame coverage. The temperature of a luminous flame is usually 200-300°F less than the temperature of a methanol flame. The outside wall temperature of the cylinder was higher during exposure to the luminous flames than during exposure to the methanol flames so a temperature difference of no more than 1750°F should be used to back calculate a convective heat transfer coefficient. The heat transfer coefficient for a convective heating rate of 7,000 Btu/hr-ft^2 is then 4.0 Btu/hr-ft^2°F. This coefficient is only slightly higher than the convective heat transfer coefficient for the methanol flames.

The discrepancy between the calculated convective heat transfer rates from the cluster burners and the large single burners is striking. The convective heat transfer rates from the acetone cluster fires are lower than those

from single fires while the convective heat transfer rates from the hexane, cyclohexane and JP-4 cluster fires are two to three times as large as those from the single burner fires. Consideration must be given to the fuel burning rates and flame sizes (volume of the flame column) before an explanation for the differences in the heat transfer rates can be offered. The next section presents photographs of the flames and briefly discusses the experiments.

Flame Photographs and Test Discussion

Figures VI-26 through VI-34 are photographs of the typical flames encountered with each fuel and burner size. Except as noted in the discussion, all the photographs were taken at exposures of 1/5- to 1/10-second from the fixed position used for determining the flame dimensions. These photographs recorded what was considered the average flame size; photographs taken at exposures of 1- to 2-seconds record a larger (by about 10 percent) flame size.

Figure IV-26 shows methanol fires from 12-, 18- and 24-inch diameter burners. The photographs were taken at f8 for 1 second using ASA 3000 Polaroid film. The fires show up well due to the glow from soot and dust particles carried into the flame with the air. Figure VI-27 is a sequence of 3 photographs showing the variation of the flame size with time, the camera was located about 5 feet from the flames and the photographs were exposed for 1/100 second. Panel (a) shows the fire pulse just even with the

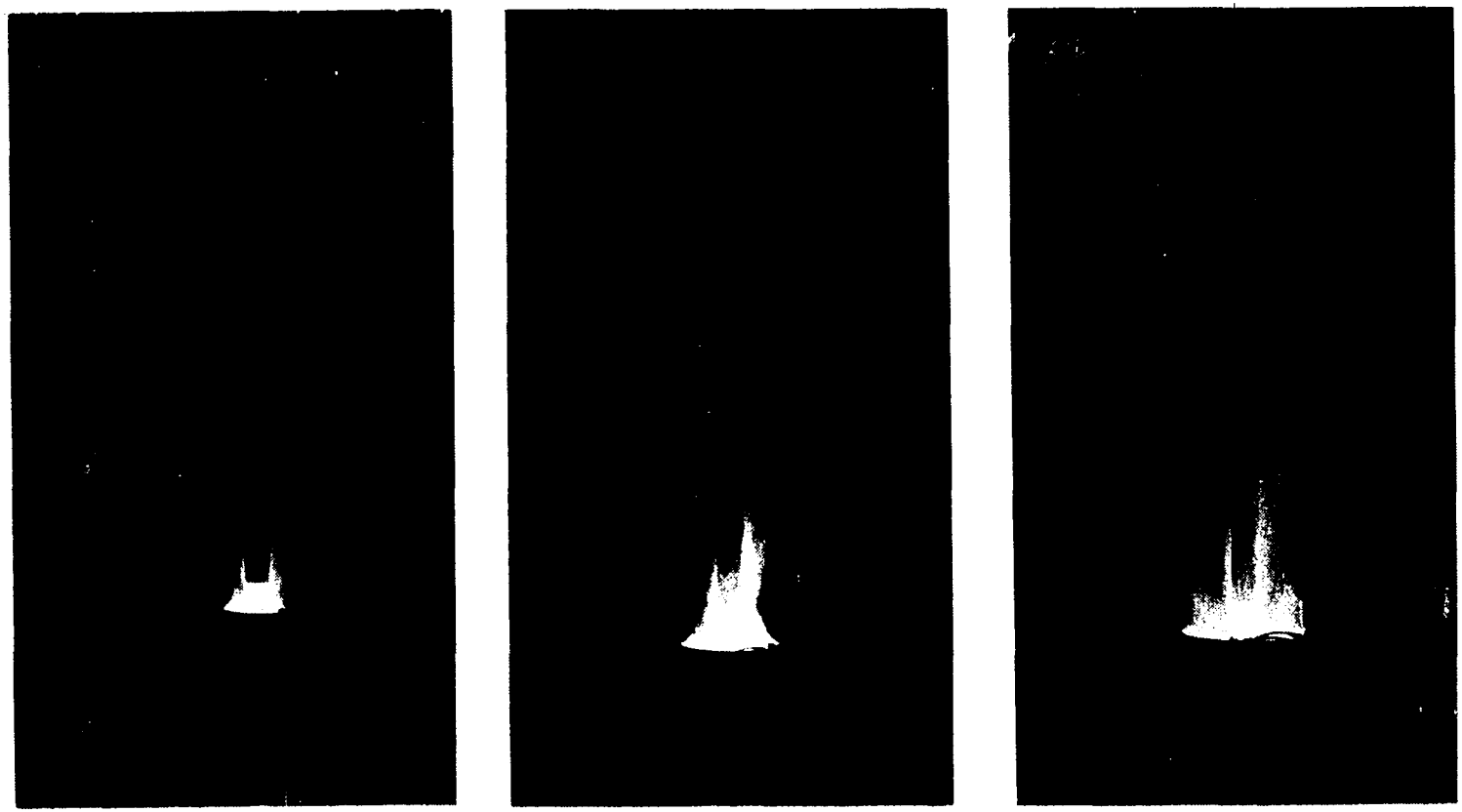

12-inch 18-inch 24-inch

Figure VI-26. Methanol Fires from 12-, 18-, and 24-inch Diameter Single Burners.

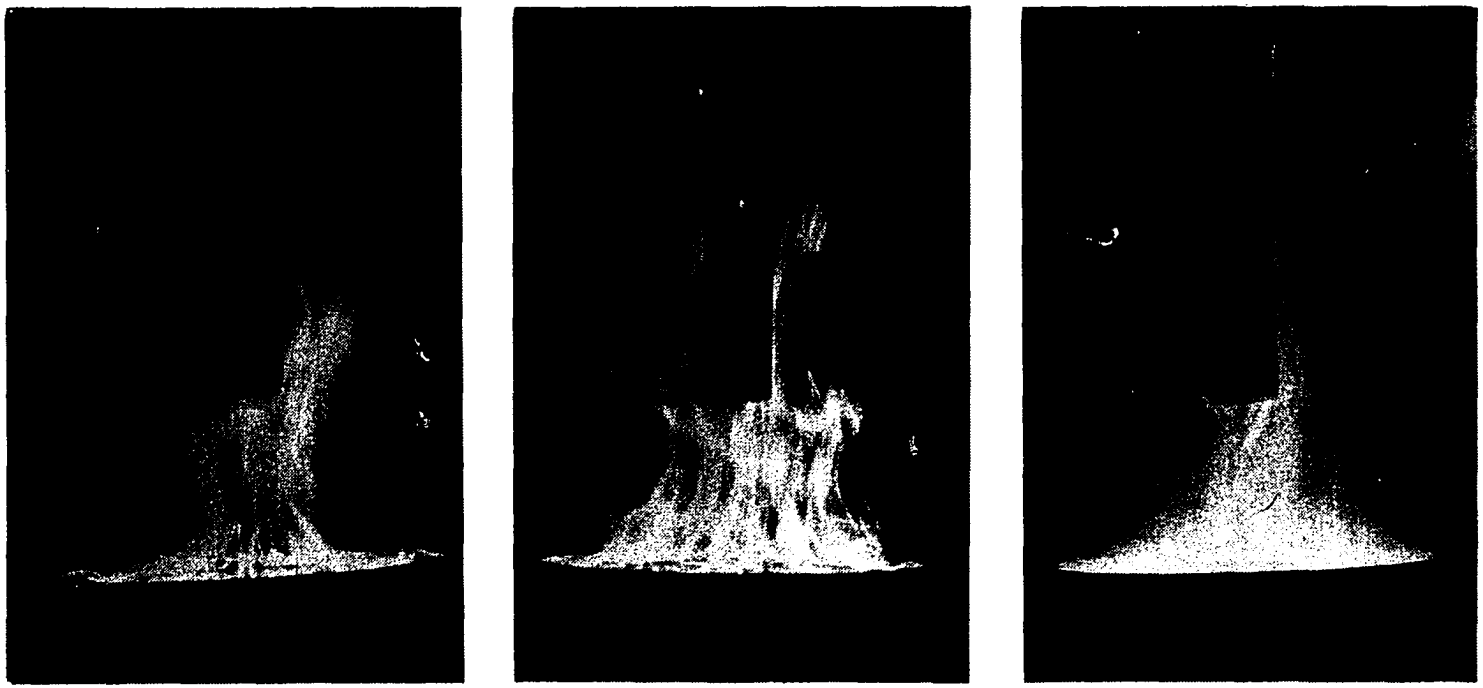

(a) (b) (c)

Figure VI-27. Variations in Methanol Flame Shape.

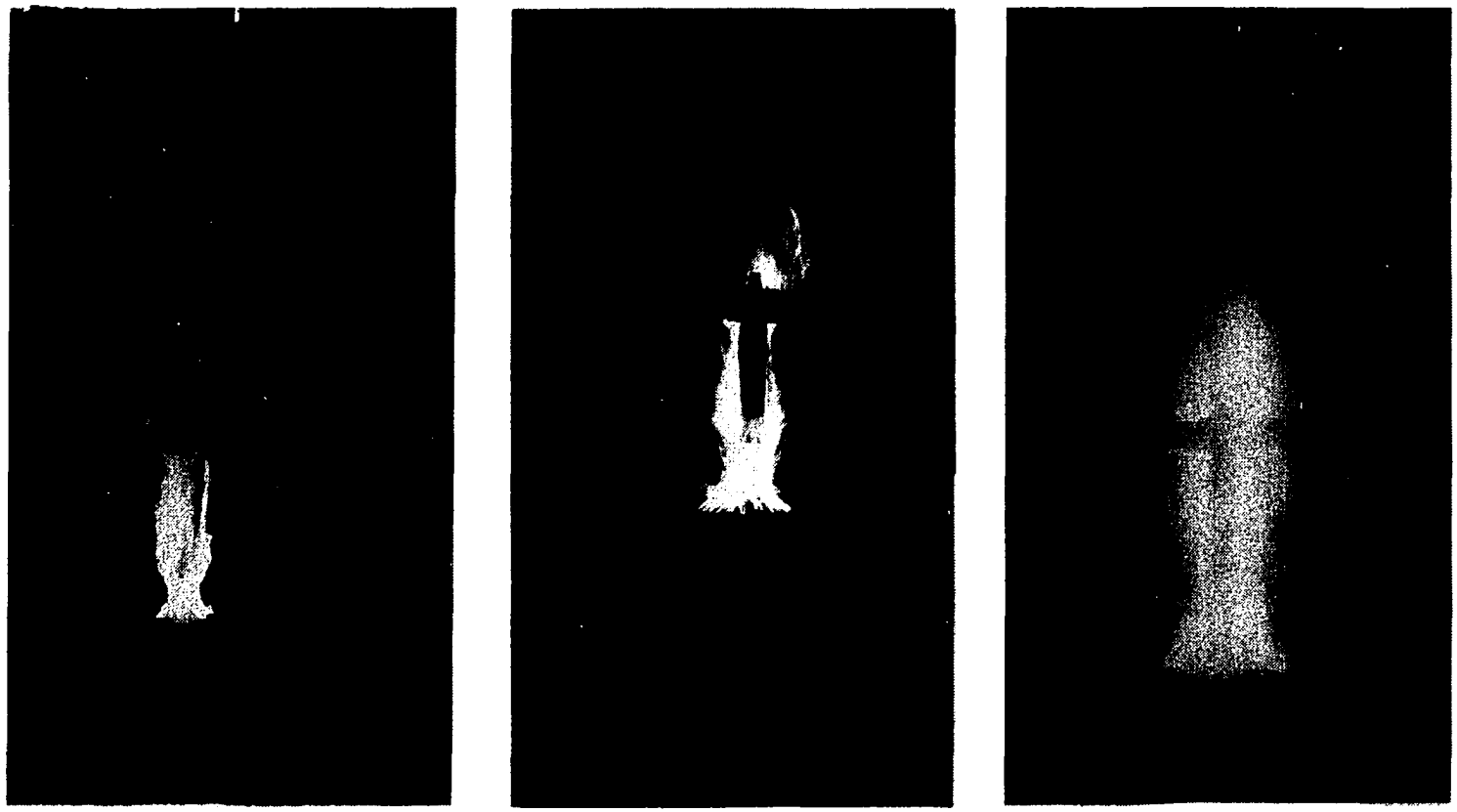

12-inch 18-inch 24-inch

Figure VI-28. Acetone Fires from 12-, 18-, and 24-inch Diameter Single Burners.

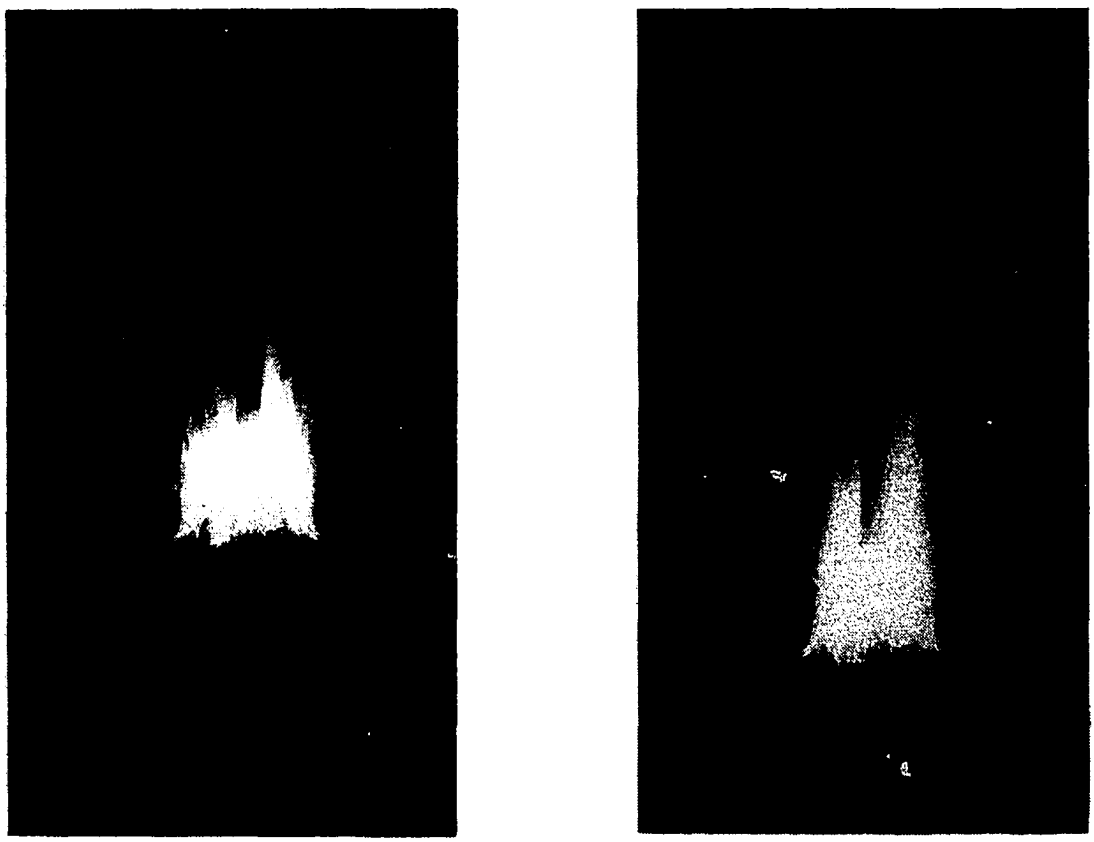

(a)
Test 57

(b)
Test 53

Figure VI-29. Acetone Fires from 6-inch Diameter Cluster Burners.

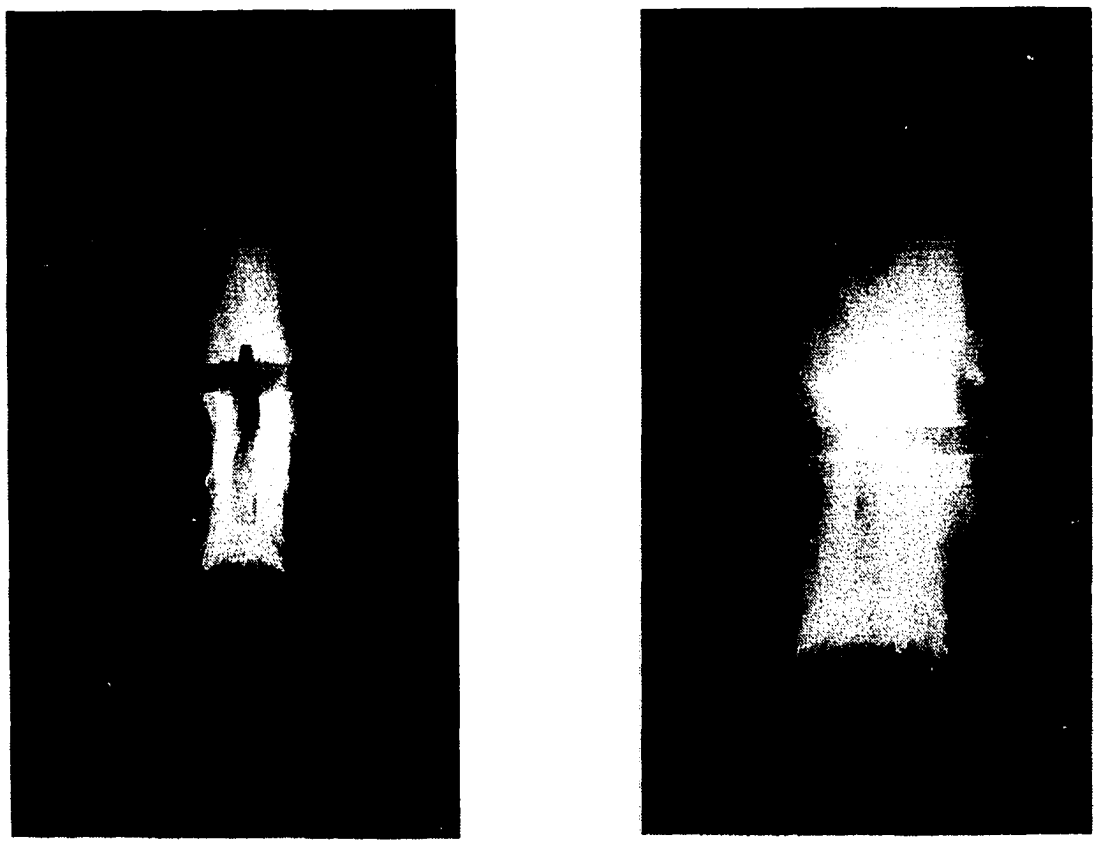

12-inch 18-inch

Figure VI-30. Hexane Fires from 12- and 18-inch Diameter Single Burners.

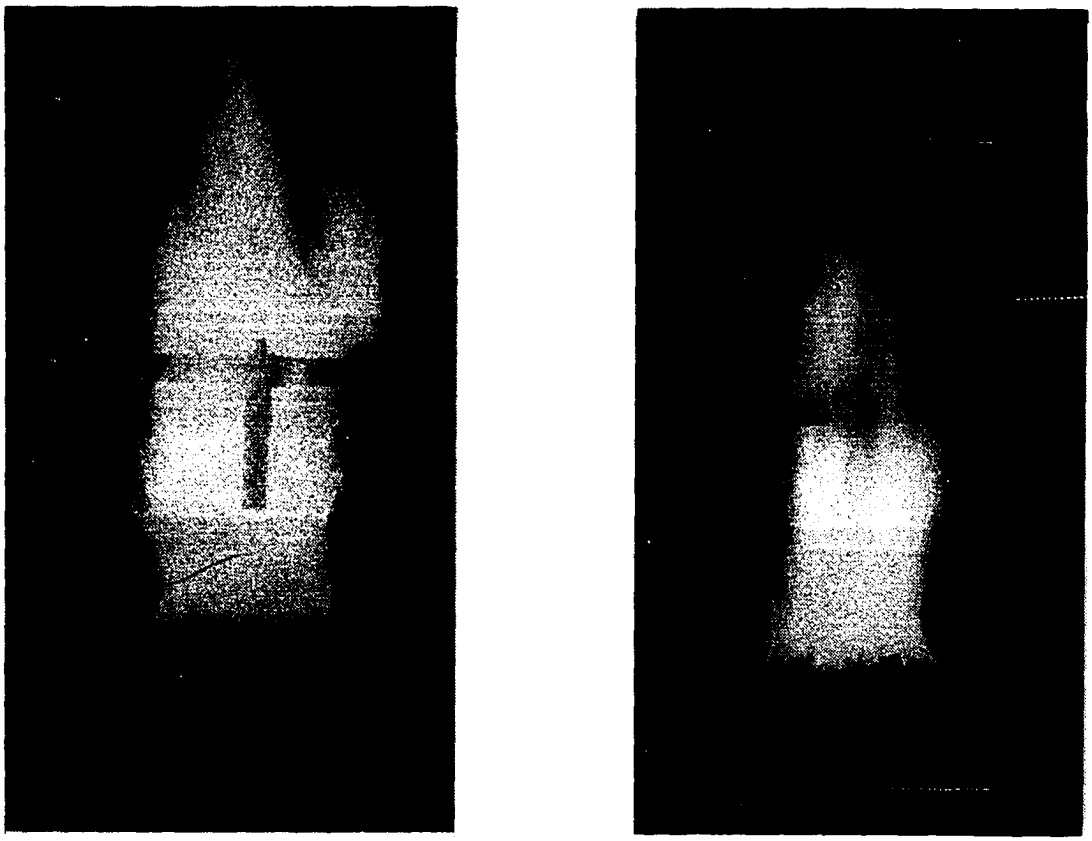

24-inch Single

6-inch Cluster

Figure VI-31. Hexane Fires from 24-inch Diameter Single and 6-inch Diameter Cluster Burners.

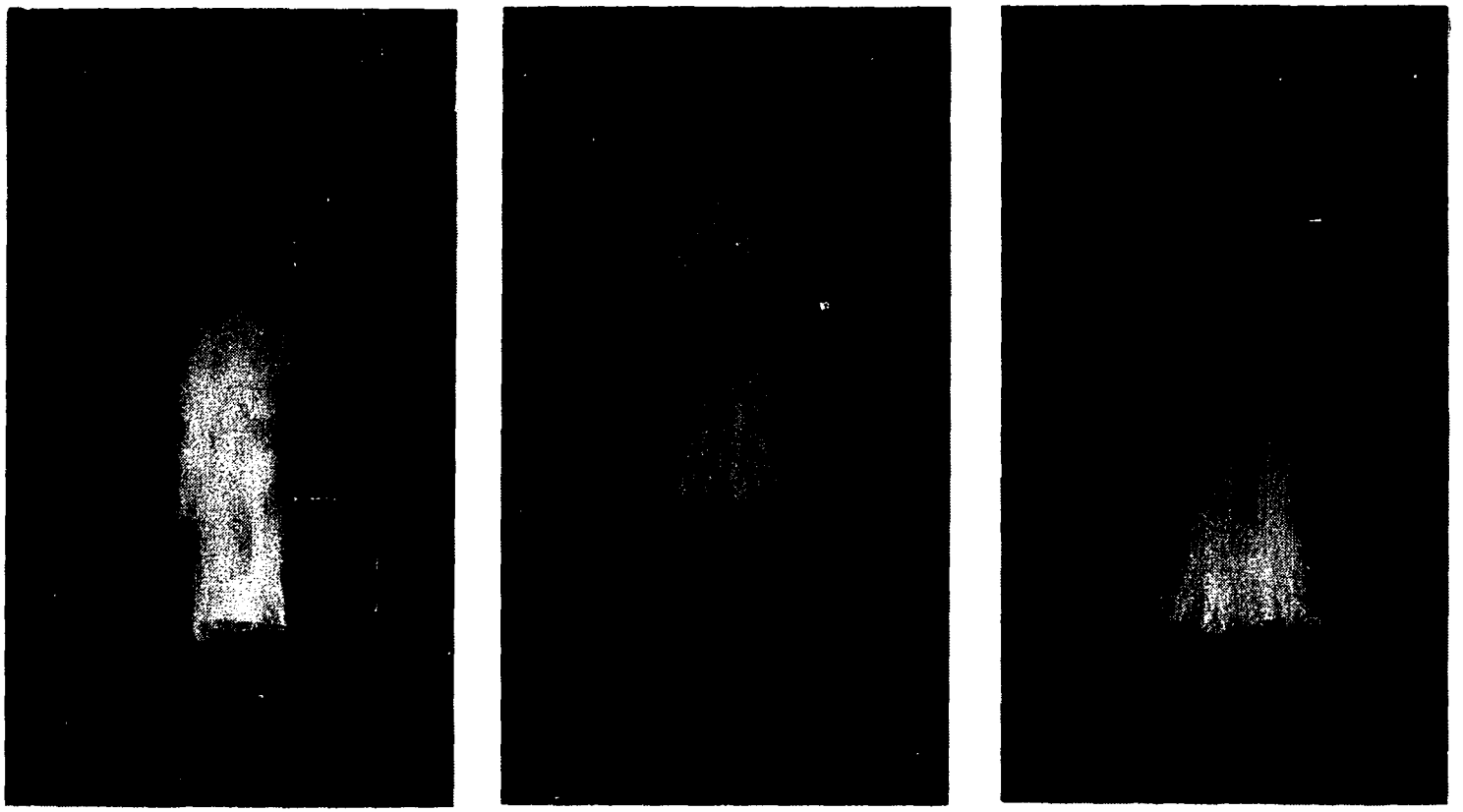

12-inch Single 18-inch Single 6-inch Cluster

Figure VI-32. Cyclohexane Fires from 12- and 18-inch Diameter Single and 6-inch Diameter Cluster Burners.

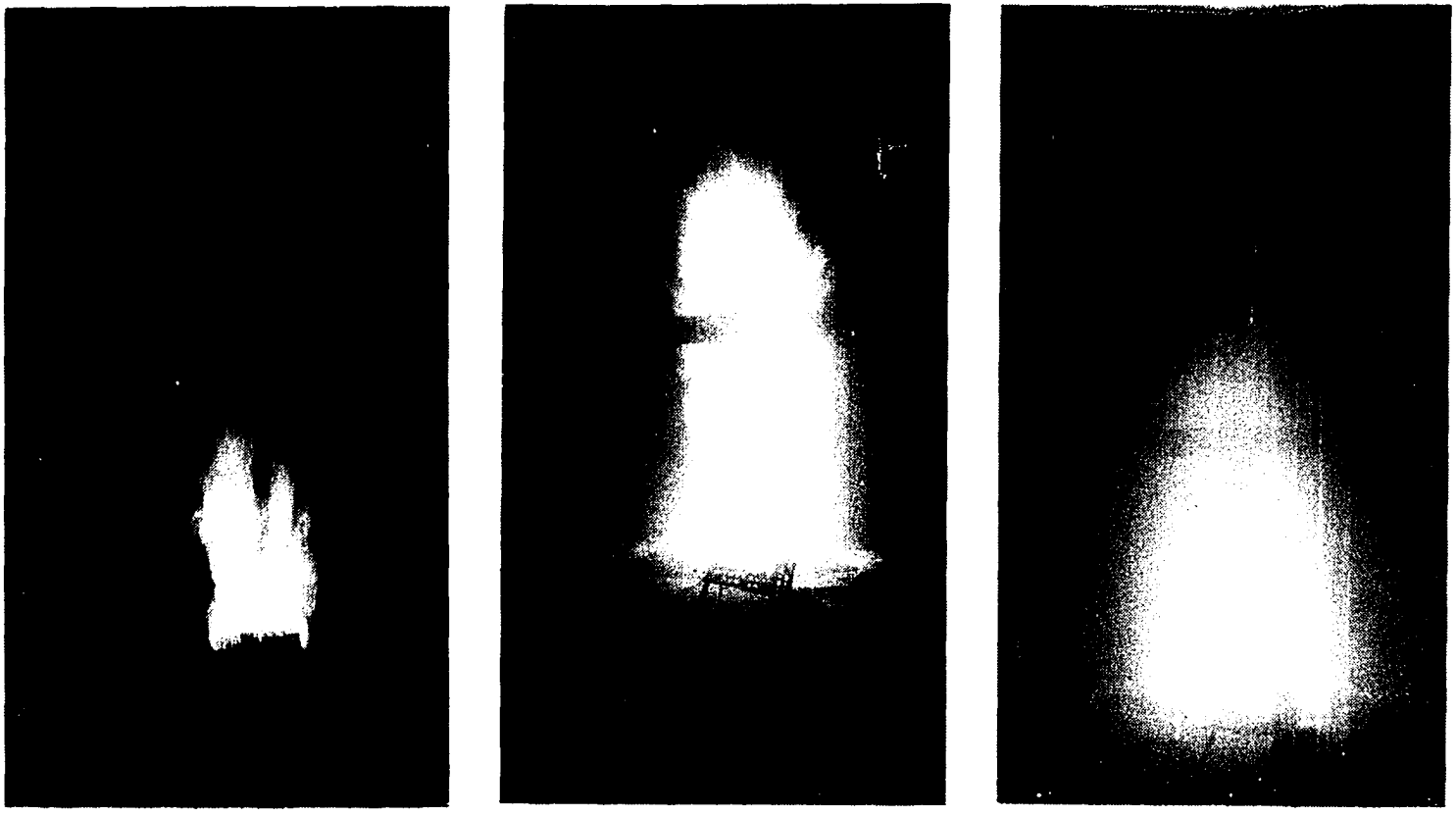

12-inch Single 18-inch Single 6-inch Cluster

Figure VI-33. JP-4 Fires from 12- and 18-inch Diameter Single and 6-inch Diameter Cluster Burners.

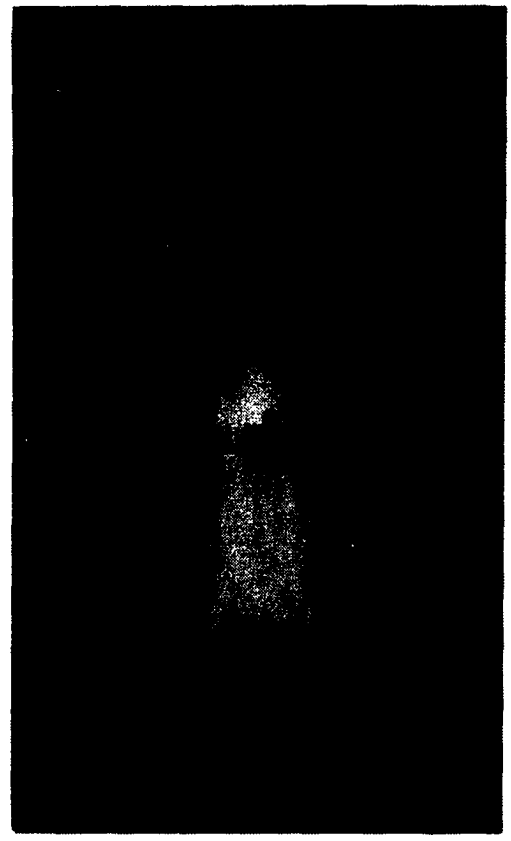

Figure VI-34. Napalm Test Solvent Fire from 12-inch Diameter Single Burner.

bottom of the test cylinder, panel (b) shows the fire pulse breaking up and panel (c) shows the flame column extended to its maximum height. These flame pulses repeated 2 to 3 times per second for all the methanol fires. A 1- to 2-inch thick layer of flame remained continuously around the entire test test cylinder, although it isn't visible in the pictures. The fires from the 12-inch diameter burner were barely high enough to cover the test cylinder so the heat transfer results are probably low. During Test 12 the cylinder was covered with a soot layer, about 1/32-inch thick, deposited during the previous tests. Figure VI-14 shows the reduced heat transfer during Test 12 and also what appears to be some small difference between the results obtained with the brass cylinder (open data points) and the stainless steel cylinder (closed data points).

Figure VI-28 shows photographs of acetone fires from 12-, 18- and 24-inch single burners. Figure VI-29 shows two photographs of acetone fires from the cluster of nine, 6-inch burners. It is not hard to see that the flames from Test 57, panel (a), are not merged as well as those from Test 53, panel (b). The difference in the flame height to diameter ratios between the single and cluster fires is quite noticeable. It is possible that none of the acetone cluster fires were fully merged. The acetone fires behaved very well and the flame coverage was good during all the tests.

Figure VI-30 shows photographs of the hexane fires from 12- and 18-inch single burners, and Fig. VI-31 shows the hexane fires from 24-inch single and 6-inch cluster burners. The flame merging is considerably better than that of the 6-inch cluster acetone fires shown on Fig. VI-29. No heat transfer data were obtained for the 24-inch hexane fire shown in Fig. VI-31; this fire was too large, endangering building and equipment, so it was allowed to burn only a few minutes. With the exception of Test 62, all the hexane fires behaved well and the flame coverage was good. The data from Test 13, Fig. VI-6, were affected by soot (about 1/32-inch thick) which remained on the cylinder from previous tests. The initial total heat transfer rate is lower for Test 13, and the additional soot accumulated during Test 13 reduces the heat transfer at the same rate as the soot deposited during tests which started with a clean cylinder.

Figure VI-32 shows photographs of the cyclohexane fires for 12- and 18-inch single and 6-inch cluster burners. Increased smoke concentration in the test room caused the photographs for the large fires to be dimmer than the photographs for the 12-inch fires. The data from Test 60, Fig. VI-8, are very poor; the flames were very unstable and persisted in spilling over the burner and onto the screen below it. Several attempts were made to obtain better flame behavior without success.

Figure VI-33 shows photographs of the JP-4 fires from 12- and 18-inch single and 6-inch cluster burners. Again the effects of the smoke concentration in the room on the photographs is quite apparent; this effect is even more pronounced since the 12-inch flame was photographed at f22 for 1/5 second, the 18-inch flame was photographed at f16 for 1/2 second and the 6-inch cluster flame was photographed at f4.7 for 1 second.

Figure VI-34 is a photograph of the Napalm Test Solvent fire; only one test was run due to the limited fuel supply. The weight composition of the Napalm Test Solvent was

20% Cyclohexane
57% n-Hexane
18% Benzene
5% iso-Octane

The soot from the benzol fire was so thick that a photograph of the flame could not be obtained. Since the visibility was so poor the relative position of the flame column and test cylinder could not be estimated.

Fuel Burning Rates

The fuel burning rates reported in Table D-4, Appendix D, were based on a number of measurements made during each test. The fuel burning rates always remained remarkably constant during a test; however, the fuel burning rates for fuels other than methanol varied quite a bit

from test to test. Figure VI-35 is a plot of the fuel level in the reservoir vs time for some of the hexane tests. The data are typical of all tests and the fit of the straight lines to the data points illustrate the constancy of the fuel burning rates during each test. Different sized fuel reservoirs were used so the slopes of the straight lines and the fuel burning rates (ml/min) do not have a single proportionality constant. The burning rate changes from test to test may have been caused by outside factors such as atmospheric conditions or the average temperature of the room air and the walls; however, the major difference is probably due to the flame spillover; some spillover was present during most of the tests as can be seen on the flame photographs in the previous section. The air flow patterns in the room were continually adjusted to minimize the movement of the flame column which accompanied the flame spillover.

For methanol the fuel burning rate per unit burner area (lb/hr-ft^2) remains nearly constant for the different burner sizes. The burning rate per unit flame volume (lb/hr-ft^3) decreases with increasing burner size; this decrease was probably due to the increasing size of a non-reacting core inside the flame.

The fuel burning rates for the luminous flames varied so much from test to test that meaningful comparisons are difficult; however, some patterns are evident. The fuel

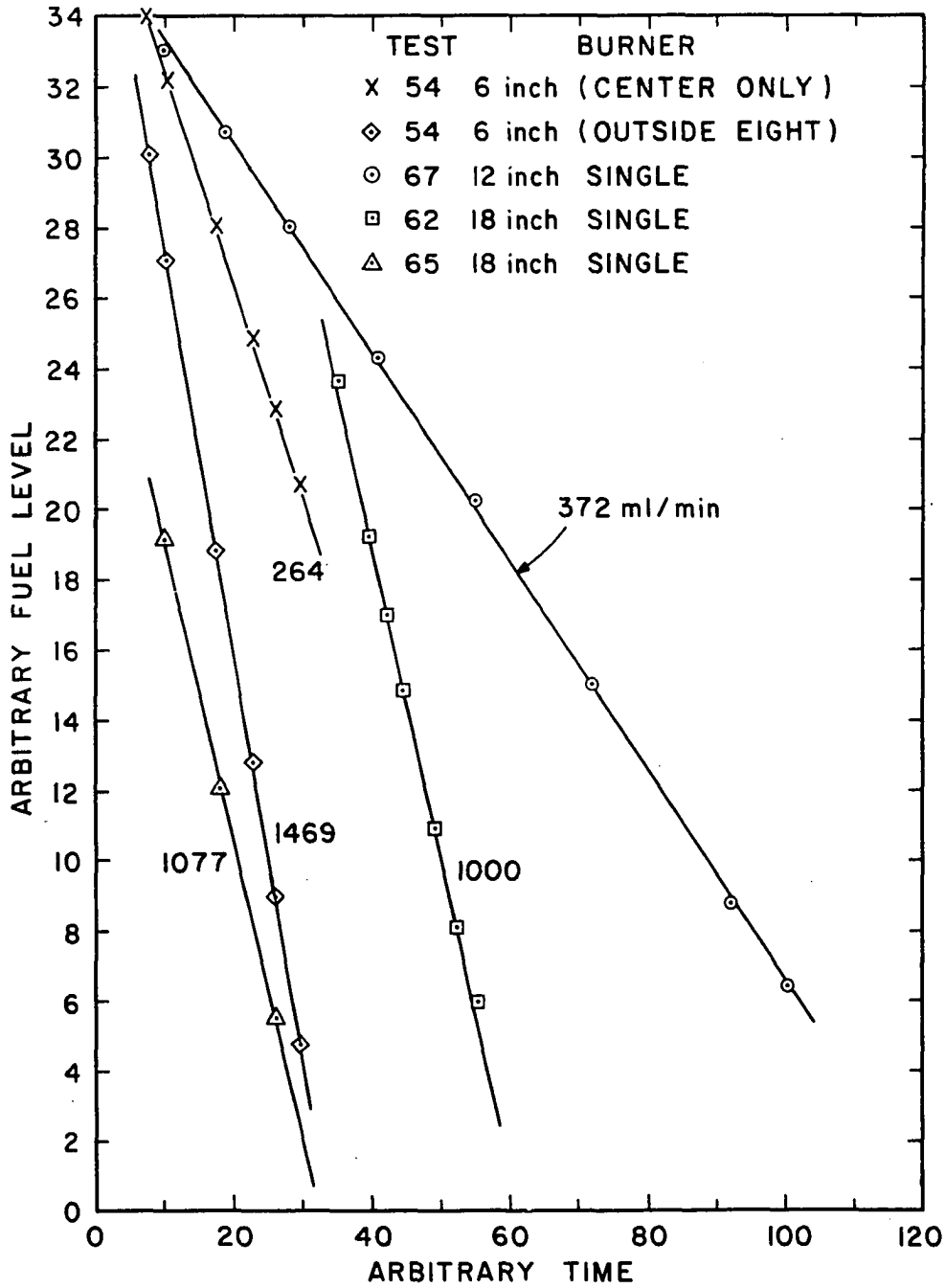

Figure VI-35. Fuel Burning Rates During Several Hexane Fire Tests.

burning rate per unit area (lb/hr-ft^2) increases with size of the single burners. The fuel burning rates (lb/hr-ft^2) from the cluster burners are higher than that from the large single burners (the surface area of an 18-inch diameter single burner equals the combined surface area of a cluster of nine, 6-inch diameter burners). The fuel burning rate per unit flame volume (lb/hr-ft^3) from the cluster burners is higher than that from the large single burners except for acetone and JP-4. The flame volume for the JP-4 fire was obtained from a photograph exposed for 1 second so the measured flame dimensions are relatively large, thus reducing the calculated fuel burning rate per unit flame volume. The acetone cluster fires were just barely merged, see Fig. VI-29, so that the flames are a cluster of small flames rather than a single, merged flame. The flame dimensions obtained from the photograph of the cluster fires may be considerably larger than the actual flame dimensions; this size error results in high calculated radiant heat transfer rates which in turn produce a low calculated convective heat transfer rate as shown in Table VI-7.

The merged cluster flames from hexane, cyclohexane and JP-4 produced much higher total heat transfer rates than similar size flames from the single burners; the increase probably occurs in both the convective and radiative heat transfer mechanisms. A plausible explanation for the differences in the total heat transfer rates between

the single and the cluster burners may be the higher fuel burning rate per unit volume (lb/hr-ft^3) of the flames from the cluster burners. This explanation is reinforced by the fact that the rate of mixing of air with the fuel is much better for the cluster burners than for the single burners.

The fuel burning rates of the cluster fires for these experiments were all 1-1/2 to 2 times higher than those measured by Huffman (Ref. 23) for the same burner arrangements. The difference was probably due to the fact that the burners were completely uninsulated in these experiments while Huffman's burners were thoroughly insulated.

Flicker Factors

Incomplete coverage of the test cylinder by the flame resulted from two different anomalies in the flame shape. The first trouble resulted from gross movement of the fire column due to the effects of air currents and other conditions which could neither be identified nor alleviated. An appreciable portion of the test cylinder surface was usually uncovered for 10 seconds or more during these upsets; however, they occurred infrequently enough so that "steady state" operation was maintained for several minutes at a time with full flame coverage of the test cylinder. The few exceptions to the steady state operation have been clearly identified in the reporting data. The irregular reporting times for the heat transfer data in Appendix D coincide with the periods of "steady state" operation.

The second mechanism was flame flicker or, to use a more descriptive term, holes in the flame column, as evidenced from photographs and radiometer measurements. Figures VI-36, VI-37 and VI-38 are a series of 16mm moving picture frames which show some of these holes. The relative time sequence is marked on each frame. The pictures on Figs. VI-36 and VI-37 were taken at 24 frames/sec (standard motion) while the pictures on Fig. VI-38 were taken at 64 frames/sec (slow motion). The physical character of the flame column changes very rapidly; only the larges disturbances are apparent to the eye. The "true" flame appears to consist of a honeycomb of flame fronts and deeply penetrated air pockets. The test cylinder at the center of the flame column provides a dark background which emphasizes the depth of the holes. It is quite apparent that the flames in this study, and probably most turbulent diffusion flames, do not approach uniformity. The flames in Fig. VI-36 were from hexane burning above a 12-inch diameter pan. The flames in Figs. VI-37 and VI-38 were from cyclohexane burning above a 12-inch diameter pan.

These major holes in the flame column exist for only a fraction of a second and generally expose only a small area on the test cylinder. Thus the time average percentage of the test cylinder area which is uncovered is small and the effect on the direct contact heat transfer by convection averages out to a constant value. These holes also

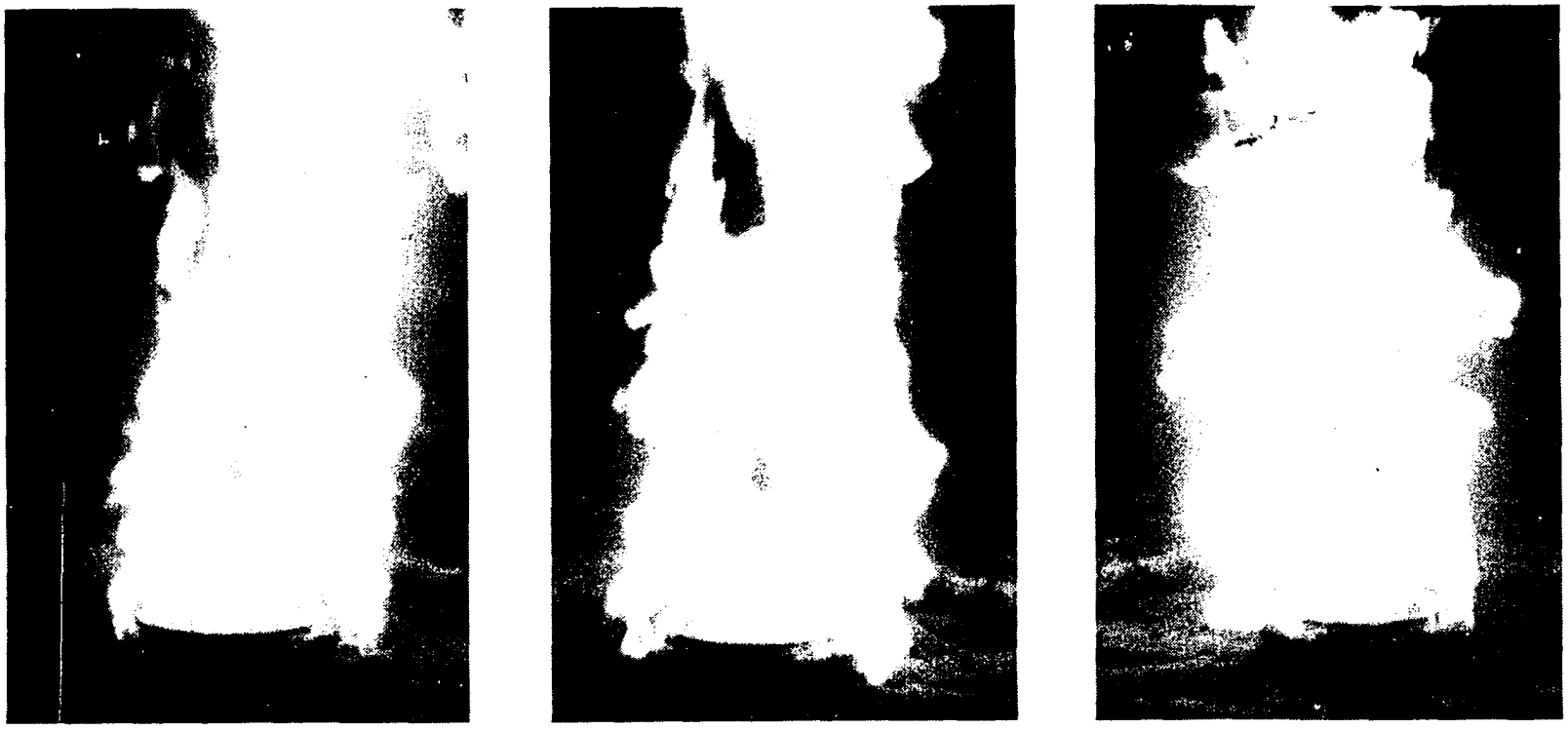

0 sec 1/2 sec 5/8 sec

Figure VI-36. Single 16 mm Movie Frames of Hexane Flames from 12-inch Diameter Single Burner (24 frames/sec).

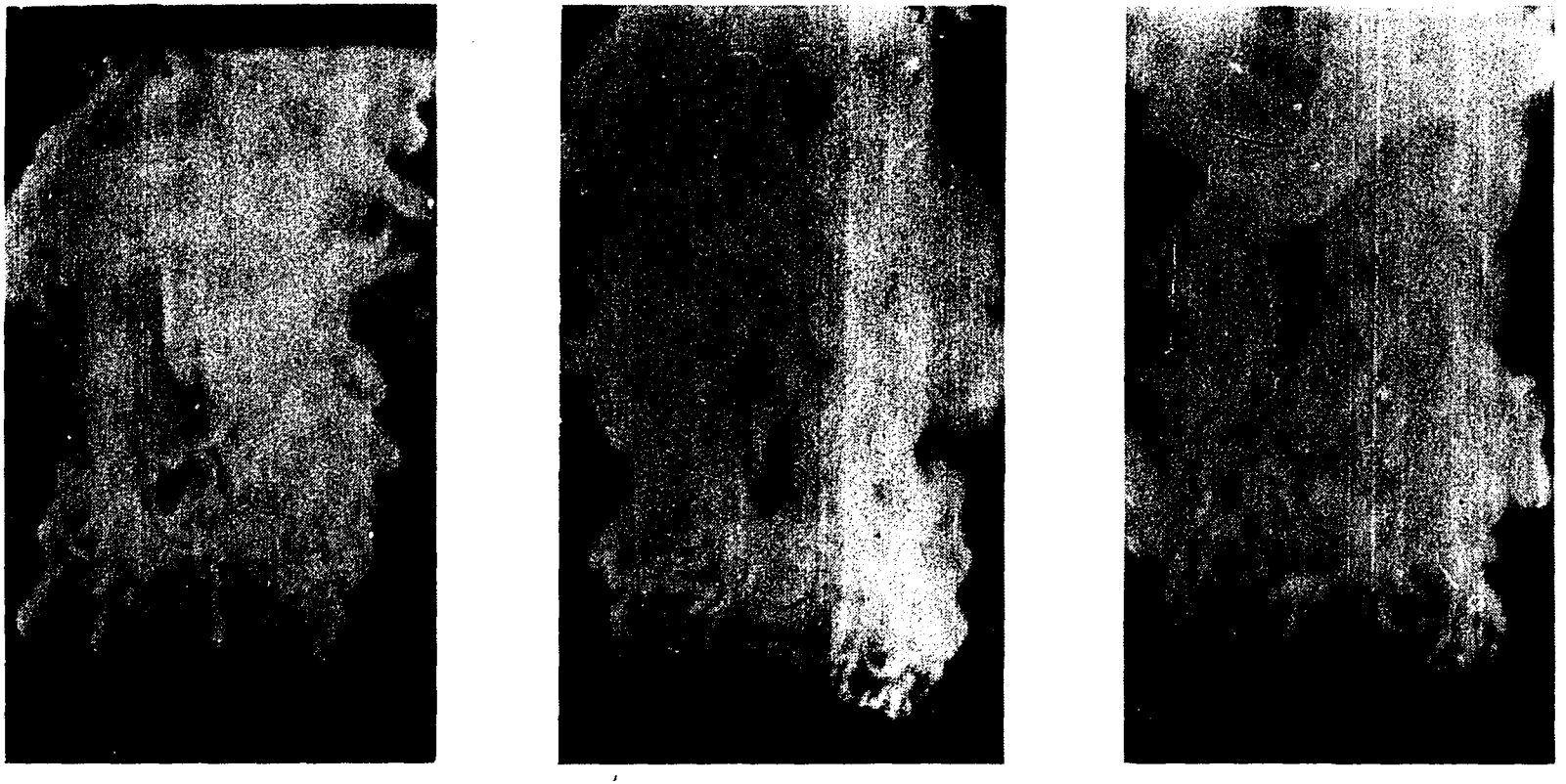

0 sec 1/8 sec 1/4 sec

Figure VI-37. Single 16 mm Movie Frames of Cyclohexane Flames from 12-inch Diameter Single Burner (24 frames/sec).

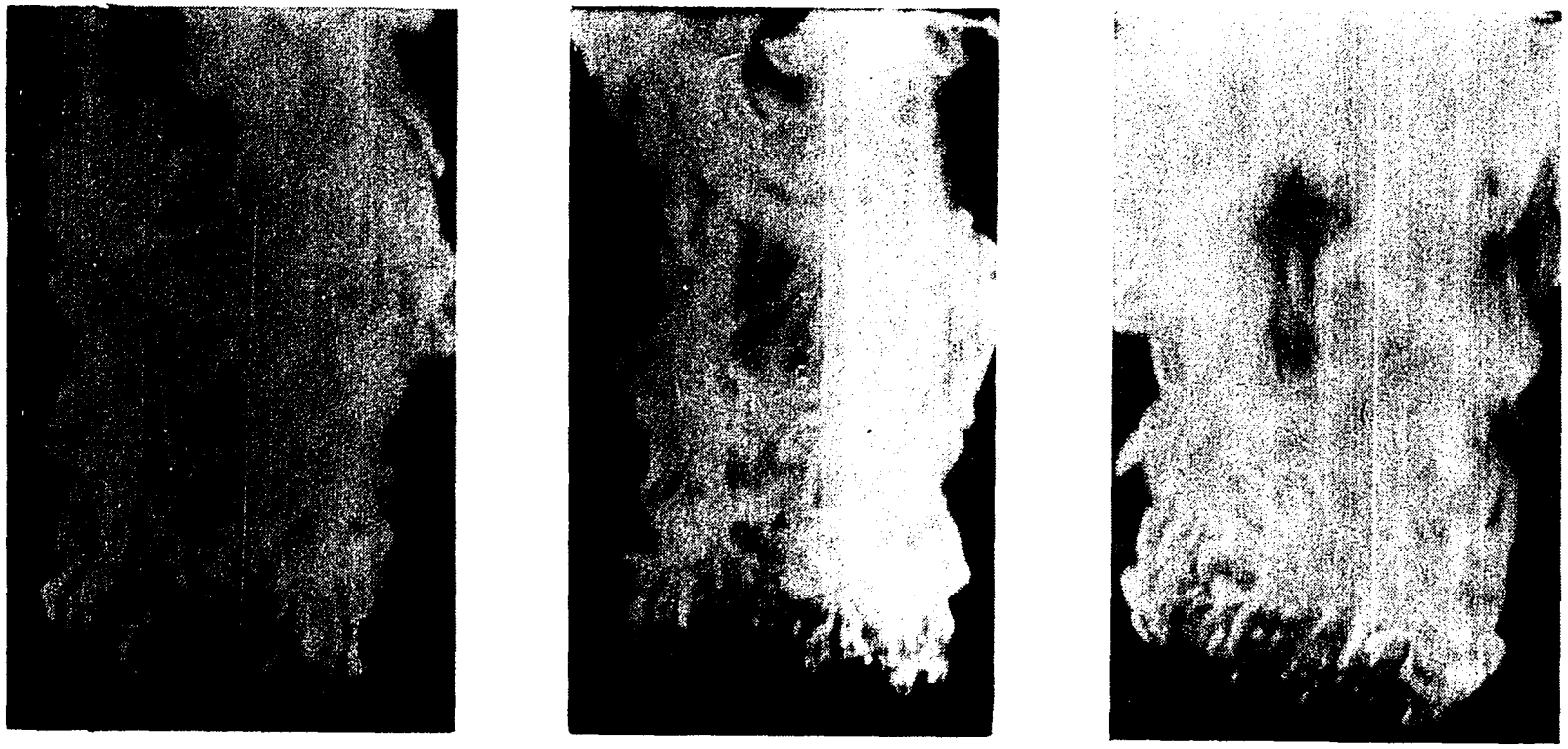

0 sec

1 1/8 sec

1 3/4 sec

Figure VI-38. Single 16 mm Movie Frames of Cyclohexane Flames from 12-inch Diameter Single Burner (64 frames/sec).

affect the effective flame size with respect to the radiation calculations. Profile photographs used here and in most other studies may not provide the correct flame size measurement. This situation is analogous to that of flame temperature measurements. Figure VI-39 shows 3 records of the recorded output from the narrow beam radiometer aimed horizontally through three experimental flame columns, 1 to 2 feet above the burner. The chart speed was 10 div/sec and radiation levels are marked on the figure. The recorder time constant was rather slow, about 1/2-second, so that these recordings may not represent the magnitude of the variation with time of the radiation from the flame.

A comparison of the radiation predicted by the CB method, Fig. VI-19, with the radiation measured by the narrow beam radiometer from flames from circular burners as shown on Fig. VI-39 is interesting. Radiation measurements on fires from the circular burners are in all cases appreciably lower than predicted by the CB method. The CB method was based on radiation measurements on flames from a 2-inch wide channel burner. These flames are quite turbulent and well mixed with air since their ratio of flame surface area to volume was much higher than that from a circular burner. The radiation from circular burner fires may be low due to a core of non-radiation gas inside the flame column at the level where the radiometer was pointed. If a non-radiating core exists, the flame column is not homogeneous as assumed

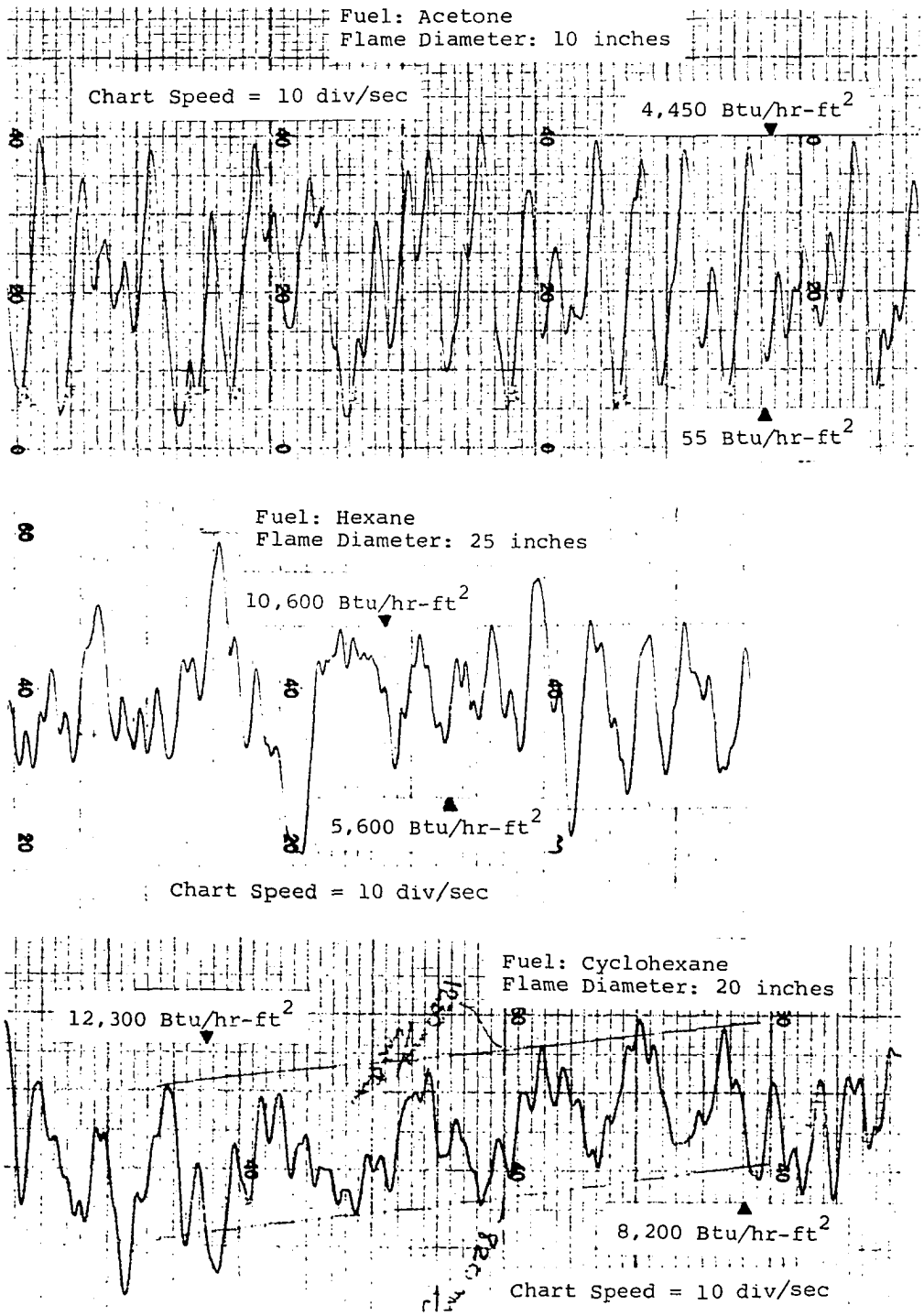

Figure VI-39. Measured Radiation Intensity from Cylindrical Flames.

by all the calculation methods. This problem is in addition to the holes previously discussed. Since enough data were not available to reconcile this problem, the calculations were completed assuming the flames were homogeneous. This assumption may be realistic when the target is inside the flames since it "sees" the outside thickness of the flame.

The profile photographs made during these experiments were usually taken with exposures of 1/5- or 1/10-second in order to photograph an average size flame column. These exposure times were based on visual estimates of the average flame size. If the narrow beam radiometer had been available at the start of the experiments it could have been used to determine a flicker factor correction for application to the large flame sizes obtained from photographs taken with exposures of 1-second or more. Since the narrow beam radiometer was available only during the last few experimental runs, the average flame size obtained from the short exposure photographs was used in the radiation calculations. One exception to this was the 0.67 factor applied to the maximum sized methanol flames; the methanol flame pulses were so large that it was almost impossible to capture the average flame size on a photograph. Flicker factors, defined as the ratio of the average to maximum radiation measured by the narrow beam radiometer, are presented in Table VI-8. These factors were obtained from the limited data, Table D-2, Appendix D, obtained during the last few experimental runs so they are only approximate at best.

TABLE VI-8

FLICKER FACTORS FOR VARIOUS FUELS
AND FLAME THICKNESSES

Fuel	Flame Thickness (inches)	Flicker Factor (average/maximum)
Methanol	10	0.66
	16	0.68
Acetone	10	0.68
	25	0.65
Hexane	14	0.75
	25	0.75
Cyclohexane	11	0.79
	25	0.68
JP-4	18	0.76

The holes in the flame column certainly introduce another factor into the problem of calculating the radiation from turbulent flames. It should be pointed out that this problem exists for any of the calculation techniques which utilize flame thickness or radiation path length. A thorough study of the effects of these holes on the effective flame size to use with radiation calculations and the related problem of how to determine consistent flame dimensions is needed.

CHAPTER VII

CONCLUSIONS

The accumulation of soot from luminous uncontrolled buoyant diffusion fires on cool targets will materially reduce the total heat transfer rate from the fire. The decrease in the heat transfer rate is exponential with time according to the equation and coefficients presented in Chapter II.

None of the radiation calculation methods and data presently available provide much more than a rough estimate of the radiant heat transfer rates from flames. The older, established techniques of Thring and Hottel (TH method) are as good as the newer techniques based on a more fundamental approach, i.e. integration of the monochromatic radiation transport equations over all contributing wavelengths (SF method).

The limited success of the calculation method based on the non-specular measurements from medium sized flames (CB method) holds some promise. The data used to develop the coefficients for the CB method were determined from medium sized flames (6-inches to 2-feet thick) and may not be applicable to large fires. However, the radiant

heating from optically thick flames calculated with this data (see Fig. VI-19) are about right when compared with the results from large fire tests reviewed in Chapter II. If the radiation data were obtained for the several major contributing wavelength bands and the calculation applied to each band the accuracy and applicability to a wider range of flame sizes would be considerably improved. If sufficiently general absorption-emission coefficients can be determined the newer techniques will offer many advantages; however, the correct coefficients may be as difficult to specify as the flame composition and temperature required by the older techniques.

All the radiation calculation techniques require knowledge of the flame shape and size. The physical structure of buoyant diffusion flames is not uniform, and the apparent or visible flame volume is probably not the effective volume with respect to radiation emission and absorption.

The relatively large measured heat transfer rates for the merged flames from cluster burners are associated with higher burning rates due to improved mixing of air into the flame collumn. A correlation of the fuel burning rate per unit flame volume, or other measure of the rate at which air is mixed into the flame column, along with the radiant and convective heat transfer coefficients, is required for a generalized heat transfer calculation technique applicable to both single and merged flames. Indeed, this type

parameter may be required for a calculation technique applicable to a wide range of single burner fire sizes.

The medium sized flames encountered in this study are not well suited to distinguishing between radiation calculation methods and coefficients. Differences between the calculated results are at a minimum for medium size flames so the ability to distinguish between calculation methods is minimized. Inaccuracies in the calculated radiation due to the inaccuracies in the effective flame size, changes in the rate of mixing of air into the flame column and other variables are as large as the differences between the results calculated by the different methods.

The maximum heat transfer rates expected from optically thick flames and the minimum optically thick flame depth are summarized in Table VII-1. The radiant heat transfer rates are based on the non-specular data from the channel burners and the convective heat transfer rate is based on the results of this investigation. It should be emphasized that the values in Table VII-1 are, in the authors opinion, the best available values.

TABLE VII-1

MAXIMUM HEAT TRANSFER RATES FOR OPTICALLY THICK FLAMES FROM SINGLE BURNERS [a]

Fuel	Optically Thick Flame Depth (inches)	Maximum Heat Transfer Rates to a Cold (200-300°F) Target ($Btu/hr-ft^2$) Radiant	Convective	Total
Methanol	35	5000	7000	12000
Acetone	35	10000	7000	17000
Hexane	70	22500	7000	29500
Cyclohexane	100	31000	7000	38000
JP-4	80	23700	7000	30700
Benzol	80	39000	7000	46000

[a] Best available values, see last paragraph on p. 171.

NOMENCLATURE

A = area

A_i, A_j = Gauss Quadrature coefficients

a = flame shape parameter or numerical coefficient

b = flame shape parameter or numerical coefficient

c = flame shape parameter or numerical coefficient

C_p = heat capacity

D = burner diameter

E_L = effective emissivity of luminous radiator

E_n = effective emissivity of non-luminous radiator

F = geometric view factor

Gr = Grashof number

g = acceleration due to gravity

H = enthalpy or height dimensions for flames and targets

ΔH = enthalpy changes

h = convective heat transfer coefficient or height of differential element on target surface

I = moment of inertia

I_λ = monochromatic radiation intensity

$I_{b\lambda}(T)$ = monochromatic radiation intensity emitted by black body at temperature T

J_λ = monochromatic, volumetric emission coefficient

k = thermal conductivity or total number of monochromatic emission-absorption bands

ℓ = characteristic length in Grashof number

M = bending moment

m = order of Gauss Quadrature

Nu = Nusselt number

PWI = inlet primary water flow rate

PWO = outlet primary water flow rate

Pr = Prandtl number

Q = power

Q_λ = monochromatic radiant heat transfer rate

q = heat transfer rate per unit area (heat flux)

Re = Reynolds number

R = radius of flame and target cylinders

r_o = flame depth to outside of flame cylinder

r = flame depth

S = separation distance between external target and flame cylinder, or mechanical stress

s = soot concentration

T = temperature

$\overline{T}$ = average temperature

t = time or projected flame depth

t_o = projected depth to outside of flame cylinder

t_λ = monochromatic transmissivity

U = overall heat transfer coefficient

X = area fraction

x = radiation path length

Greek

α = numerical coefficient or total radiation source strength

β = volumetric expansion coefficient in Grashof number or average radiation absorption coefficient

β_λ = monochromatic absorption coefficient

γ = angle between radiation path and flame cylinder radius

δ = polar angle between target surface normal and system reference normal

ϵ = emissivity

ζ = horizontal directional angle

η = flame opacity coefficient

θ = polar angle or temperature difference in Grashof number

$\varkappa$ = mass absorption coefficient

λ = wavelength

$\Delta\lambda$ = wavelength increments

μ = viscosity, abbreviation for micron or cosine θ

ξ = vertical directional angle

ρ = density or reflectance

σ = Stefan-Boltzmann constant

τ = optical distance (absorption coefficient x path length)

φ = azimuthal angle

Φ_i, Φ_j = Gauss Quadrature parameters

ψ = azimuthal angle around target cylinder

$\Delta\Omega$ = solid angle (steradians)

Subscripts

1,2,3,4 = position indices

A,B = position indices

b = flame cylinder bottom or bulk fuel

CW = cooling water

F = flame

f = flame or film

I = interior

L = luminous

M = mass inventory

n = non-luminous

o = outside

R = radiation

s = sidewall of cylinder

T = top of cylinder or total

t = top of cylinder

∞ = free stream (bulk)

REFERENCES

1. "A Study of Fire Problems," National Academy of Sciences, National Research Council Publication 949 (1961).

2. Akita, K., and Yumoto, T., "Heat Transfer in Small Pools and Rates of Burning of Liquid Methanol," Tenth International Symposium on Combustion, The Combustion Institute, Pittsburgh (1965).

3. Anderson, J. E. and Stresino, E. F., "Heat Transfer from Flames Impinging on Flat and Cylindrical Surfaces," ASME Trans., Ser. C, 85, p 49-54, Feb. 1963.

4. Bird, R. B., Stewart, W. E. and Lightfoot, E. N., Transport Phenomena, John Wiley and Sons, New York (1965).

5. Blinov, V I., and Kudiakov, G. N , "Certain Laws Governing Diffusive Burning of Liquids," Acad. Nauk. USSR Doklady, 113, 1094 (1957).

6. Broida, H. P. "Experimental Temperature Measurements in Flames and Hot Gases," Temperature; Its Measurement and Control in Science and Industry, Vol. II Reinhold Publishing Corp., New York (1955).

7. Burgess, D. S., Strasser, A., and Grumer, J., "Diffusive Burning of Liquid Fuels in Open Trays," Fire Research Abstracts and Reviews, 3, 177 (1961).

8. Chemical Engineers Handbook, 3rd Edition, J. H. Perry, Editor, Page 1236, McGraw-Hill Book Co. (1950).

9. Churchill, R. V , Complex Variables and Applications, p. 191-194, McGraw-Hill Book Co., New York (1960).

10. Compressed Gas Association, Docket 595-D, Pamphlet S-1 (1961).

11. Construction Handbook for AIM Slotted Angle, F-1051, R3-63, Acme Steel.

12. Copley, J. A., "An Analytical Method for Predicting the Temperature-Time History of a Hollow Cylinder Enveloped in Flames," Technical Report No. 2073, U. S. Naval Weapons Laboratory, Dahlgren, Virginia.

13. Douglas, W. J. M., and Churchill, S. W., "Recorrelation of Data for Convective Heat Transfer Between Gases and Single Cylinders with Large Temperature Difference," Chemical Engineering Symposium Series, 18, 52 (1956).

14. Emmons, H. W., "Some Observations on Pool Burning," The Use of Models in Fire Research, NAS-NRC Pub. 786, 50(1961).

15. Gaydon, A. G., The Spectroscopy of Flames, John Wiley & Sons, New York (1957).

16. Gaydon, A. G., and Wolfhard, H. G., Flames, Their Structure, Radiation and Temperature, Chapman and Hall Ltd. London (1960).

17. Hood, J. D., "A Method for the Determination of the Radiative Properties of Flames," Ph.D. Thesis, University of Oklahoma (1966).

18. Hottel, H. C., Fire Research Abstracts and Reviews, 1, 41, 1959 (review of Reference 5).

19. Hottel, H. C., and Broughton, F. P., Ind. Engr. Chem., Anal. Ed., 4, p. 166-175 (1953).

20. Hottel, H. C., and Egbert, R. B., "Radiation from Furnace Gases," Trans. ASME, 63:297 (1941).

21. Hottel, H. C., and Manglesdorf, "Heat Transmission by Radiation from Non-luminous Flames," Trans. AIChE, 31, p. 517 (1935).

22. Hsu, S. T., Engineering Heat Transfer, D. Van Nostrand Co., New York (1963).

23. Huffman, K. G., "The Interaction and Merging of Flames from Burning Liquids," Ph. D. Thesis, University of Oklahoma (1967).

24. Ibele, Warren (Editor), Modern Developments in Heat Transfer, Academic Press, New York (1964).

25. Kays, W. M., Convective Heat and Mass Transfer, McGraw-Hill Book Co., New York (1960).

26. Kilham, J. K., Third Symposium on Combustion, Flame and Explosion Phenomena, p. 733, Williams and Wilkins, Baltimore, Maryland (1949).

27. Kutateladze, S. S., Fundamentals of Heat Transfer, Academic Press, New York (1963).

28. Laddish General Catalog No. 55, p. 271, Laddish Company, Cudahy, Wisconsin.

29. Lott, J. L., and Sliepcevich, C. M., "An Investigation of the Emergency Venting Requirements for Cargo and Portable Tanks," unpublished, 1966.

30. Love, T. J., Radiative Heat Transfer, to be published by C. E. Merrill, Inc.

31. Neill, D. T., "Direct Contact Heat Transfer from a Buoyant Diffusion Fire (A Research Proposal)," Unpublished Special Problem, Univ. of Okla.(1967).

32. McAdams, W. H., Heat Transmission, McGraw-Hill, New York (1954).

33. Mody, P. J., and Lott, J. L., "Flame Temperatures and Equilibrium Compositions for Six Fuel-Air Systems," Internal Memorandum, Project 1454, University of Oklahoma Research Institute, Dec. 1965.

34. Rasbash, D. J., Rogowski, Z. E., and Stark, G. W. V., "Properties of Fires of Liquids," Fuel, 35, 94 (1956).

35. Schlichting, H., Boundary Layer Theory, McGraw-Hill, New York (1960).

36. Shahrokhi, F., "Numerical Technique for Calculation of Radiant Energy Flux to Targets from Flames," Ph.D. Thesis, University of Oklahoma (1965).

37. Thomas, P. H., Baldwin, R., and Heselden, A. J. M., "Buoyant Diffusion Flames: Some Measurements of Air Entrainment, Heat Transfer and Flame Merging," Tenth International Symposium on Combustion, The Combustion Institute, Pittsburgh (1965).

38. Thring, M. W., "The Science of Furnaces and Flames," Chapman and Hall Ltd., London (1962).

39. Tsai, W., Unpublished Ph.D. Thesis, University of Oklahoma (1968).

40. Tsai, W., "The Prediction of Radiative Heat Transfer from Flames," Masters Thesis, University of Oklahoma (1966).

41. Vlasov, K. P., "Connection Between Flame Temperature by Optical and Other Methods," ARS J., Vol. 30, p. 83, Jan. 1960.

42. Way, D. H., "Large Scale Fire Exposure Tests to Evaluate UNOX Foam for Fire Exposure Protection," Report FRL-62, Union Carbide Chemicals Company, South Charleston, W. Virginia (1965).

43. Welker, J. R., "The Effect of Wind on Uncontrolled Buoyant Diffusion Flames from Burning Liquids," Ph.D. Thesis, University of Oklahoma (1965).

44. White, W. B., Johnson, S. M., and Dantzig, G. B., "Chemical Equilibrium in Complex Mixtures," J. Chem. Physics, 28, p. 751-755 (1958).

45. Wolfe, W. L., Editor, Handbook of Military Infrared Technology, U. S. Government Printing Office, Washington D. C. (1965).

46. Woodruff, L. W., and Giedt, W. H., "Heat Transfer Measurements from a Partially Dissociated Gas with a High Lewis Number," ASME Trans., Ser. C, 88, p. 407-414, Nov. 1966.

47. Zartman, W. N., and Churchill, S. W., "Heat Transfer from Acoustically Resonating Gas Flames in a Cylindrical Burner," AIChE Journal, Vol. 7, p. 588-592, Dec. 1961.

APPENDIX A

CALCULATION OF HEAT TRANSFER THROUGH TEST CYLINDER FROM THE EXPERIMENTAL DATA

A boiler type heat transfer probe requires a number of calculations and corrections to determine the actual heat entering the test surface. There are three independent zones of heat in addition to the test surface. The first is the combination of heat gain and loss by the primary coolant while flowing in and out of the lead tube. The second is the heat loss from the flexible line between the lead tube outlet and the condenser inlet. The third is the heat gain through the insulation on the top and bottom of the test cylinder. Figure A-1 is a schematic diagram of the experimental system illustrating the important data points and the areas of heat loss or gain. Nomenclature for the figure and the equations follows on the next page.

An overall heat balance around the primary coolant system from the initial entrance to the lead tube assembly to the condenser outlet yields

$$\text{Input} = H_1\ PWI + \Delta H_{12A} + \Delta H_{12F} + \Delta H_F + \Delta H_T + \Delta H_B + \Delta H_{34A} + \Delta H_{34F}$$

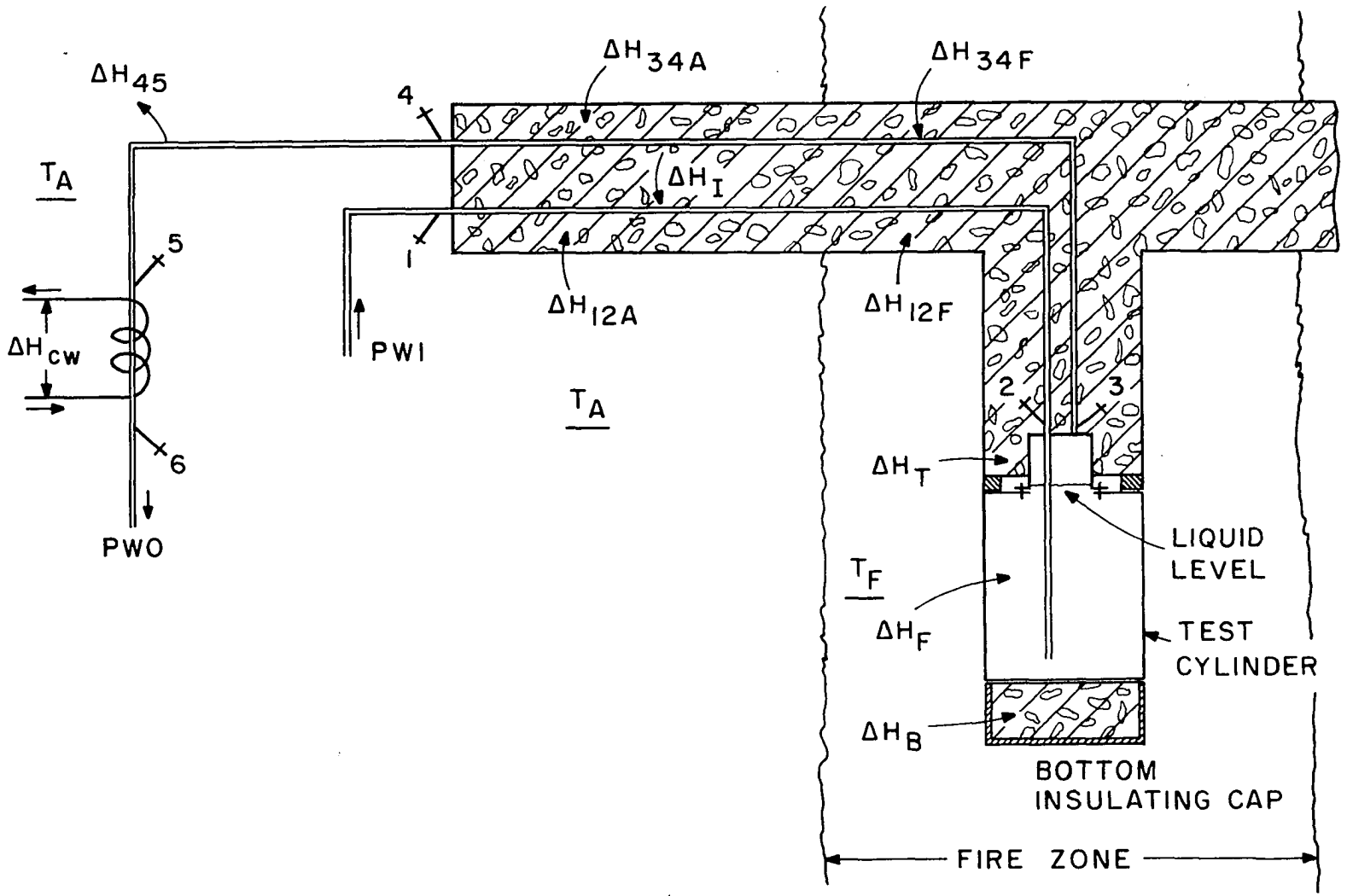

Figure A-1. Schematic of Heat Gains and Losses by Primary Coolant.

Nomenclature for Figure A-1

Primary coolant parameters are:

H_1 = primary coolant enthalpy at inlet to lead tube, Btu/lb

H_2 = primary coolant enthalpy at inlet to test cylinder, Btu/lb

H_3 = primary coolant enthalpy at outlet from test cylinder, Btu/lb

H_4 = primary coolant enthalpy at outlet from lead tube, Btu/lb

H_5 = primary coolant enthalpy at inlet to condenser, Btu/lb

H_6 = primary coolant enthalpy at outlet from the condenser, Btu/lb

PWI = primary coolant inlet flow rate, lb/hr

PWO = primary coolant outlet flow rate, lb/hr

T_A = effective air temperature, °F

T_F = effective flame temperature, °F

T_o = pseudo outside temperature, °F

Heat gains and losses by primary coolant are:

ΔH_{12A} = heat gain by PWI from zone of lead tube exposed to air, Btu/hr

ΔH_{12F} = heat gain by PWI from zone of lead tube exposed to the fire, Btu/hr

ΔH_{34A} = heat gain by PWO from zone of lead tube exposed to air, Btu/hr

ΔH_{34F} = heat gain by PWO from zone of lead tube exposed to the fire, Btu/hr

ΔH_{45} = heat loss by PWO between lead tube outlet and condenser inlet, Btu/hr

ΔH_{CW} = heat removed from PWO by cooling water inside the condenser, Btu/hr

ΔH_{I} = heat exchanged between PWO and PWI along countercurrent flow paths inside the lead tube, Btu/hr

ΔH_{M} = heat gain by primary water system due to changes in liquid level inside the test cylinder (always very small in these experiments), Btu/hr

ΔH_{T} = heat gain by primary water system through insulation on top of the test cylinder and around top cap, Btu/hr

ΔH_{B} = heat gain by primary water system through insulation on the bottom of the test cylinder, Btu/hr

ΔH_{F} = heat transferred into test cylinder through its active test surface due to direct flame contact, Btu/hr

Output = H_6 PWO + ΔH_{45} + ΔH_{CW}

Accumulation = ΔH_M

A single equation for the overall heat balance is then

$$H_1 \text{ PWI} + \Delta H_{12A} + \Delta H_{12F} + \Delta H_F + \Delta H_T + \Delta H_B + \Delta H_{34A} + \Delta H_{34F} - H_6 \text{ PWO} - \Delta H_{45} - \Delta H_{CW} = \Delta H_M \quad \text{(A-1)}$$

Separate heat balances for the inlet and outlet flow paths inside the lead tube yield respectively

$$H_1 \text{ PWI} + \Delta H_{12A} + \Delta H_{12F} + \Delta H_I - H_2 \text{ PWI} = 0 \quad \text{(A-2)}$$

and

$$H_3 \text{ PWO} + \Delta H_{34A} + \Delta H_{34F} - \Delta H_I - H_4 \text{ PWO} = 0 \quad \text{(A-3)}$$

If the experiment is operated so there is no phase change along the inlet path, the bulk water temperature at points 1 and 2 can be used to determine the enthalpies at these points

$$H_1 = C_P (T_1 - T_R) \quad \text{(A-4)}$$

$$H_2 = C_p (T_2 - T_R) \quad \text{(A-5)}$$

where T_R is an arbitrary reference temperature. If there is complete condensation inside the condenser the temperature at point 6 can be used to determine the outlet enthalpy

$$H_6 = C_p (T_6 - T_R) \quad \text{(A-6)}$$

During a fire test the outlet is a mixture of steam and water so the temperatures at points 3, 4 and 5 cannot be used to determine the enthalpies at these points.

Therefore, it is necessary to calculate the heat loss or gain for ΔH_{45}, ΔH_{34A}, ΔH_{34F} and ΔH_I, as well as the heat gain through the top and bottom insulators ΔH_T and ΔH_B, in order to determine the heat transfer through the test surface due to direct fire contact. The last two terms, ΔH_T and ΔH_B, will be developed later and are carried along without further comment for the time being.

The heat loss or gain by the primary coolant between two points can be expressed as a function of a combination heat transfer coefficient-area term and the difference between the average temperatures of the inside and the outside. The following equations are thus obtained:

$$\Delta H_{12A} = X_A (hA)_{12A} (\overline{T}_A - \overline{T}_{12}) \qquad \text{(A-7)}$$

$$\Delta H_{12F} = X_F (hA)_{12F} (\overline{T}_F - \overline{T}_{12}) \qquad \text{(A-8)}$$

$$\Delta H_{34A} = X_A (hA)_{34A} (\overline{T}_A - \overline{T}_{34}) \qquad \text{(A-9)}$$

$$\Delta H_{34F} = X_F (hA)_{34F} (\overline{T}_F - \overline{T}_{34}) \qquad \text{(A-10)}$$

$$\Delta H_I = (hA)_I (\overline{T}_{34} - \overline{T}_{12}) \qquad \text{(A-11)}$$

$$\Delta H_{45} = (hA)_{45} (\overline{T}_{45} - \overline{T}_A) \qquad \text{(A-12)}$$

The term $(hA)_{ijk}$ is the effective heat transfer coefficient (Btu/°F) between the path along ij and the k zone. The terms X_A and X_F are the area fractions exposed to the air and fire respectively. The bars above the temperatures denote that the temperature is averaged along the path in question.

The inside of the lead tube is uniformly insulated along its entire length, and since the resistance of this insulation will dominate the heat transfer coefficient, it is assumed that

$$(hA)_{12A} = (hA)_{12F} \tag{A-13}$$

$$(hA)_{34A} = (hA)_{34F} \tag{A-14}$$

and the A and F subscripts are dropped from these terms. Since there are two outlet lines and only one inlet line $(hA)_{34}$ should be one to two times as large as $(hA)_{12}$.

Rearranging the heat balance Eq. (A-2) around the inlet line yields

$$(H_2 - H_1)\ PWI - \dot{\Delta H}_I = \Delta H_{12A} + \Delta H_{12F} \tag{A-15}$$

Substituting in the right side of Eqs. (A-8) and (A-9) into Eq. (A-15) results in

$$(H_2 - H_1)PWI - \Delta H_I = X_A\ (hA)_{12}(\overline{T}_A - \overline{T}_{12}) + X_F(hA)_{12}\ (\overline{T}_F - \overline{T}_{12}) \tag{A-16}$$

Since $X_A + X_F = 1$, Eq. (A-16) can be simplified to

$$X_A\overline{T}_A + X_F\overline{T}_F = \frac{(H_2 - H_1)PWI - \Delta H_I}{(hA)_{12}} + \overline{T}_{12} \tag{A-17}$$

Adding and rearranging Eqs. (A-9) and (A-10) produces

$$\Delta H_{34A} + \Delta H_{34F} = hA_{34}(X_A\overline{T}_A + X_F\overline{T}_F) - (hA)_{34}\overline{T}_{34} \tag{A-18}$$

Substituting the right side of Eq. (A-17) into Eq. (A-18) yields

$$\Delta H_{34A} + \Delta H_{34F} = (hA)_{34}\left[\frac{(H_2 - H_1)\ PWI - \Delta H_I}{(hA)_{12}} + \bar{T}_{12}\right] - (hA)_{34}\bar{T}_{34} \qquad \text{(A-19)}$$

Defining the pseudo outside temperature as

$$\bar{T}_o = \left[\frac{(H_2 - H_1)\ PWI - \Delta H_I}{(hA)_{12}} + \bar{T}_{12}\right] \qquad \text{(A-20)}$$

allows Eq. (A-19) to be simplified to

$$\Delta H_{34A} + \Delta H_{34F} = (hA)_{34}(\bar{T}_o - \bar{T}_{34}) \qquad \text{(A-21)}$$

Substituting the left side of Eq. (A-15) and the right side of Eq. (A-21) into the overall heat balance Eq. (A-1) produces

$$H_1 PWI + (H_2 - H_1)PWI - \Delta H_I + \Delta H_F + \Delta H_T + \Delta H_B + (hA)_{34}(\bar{T}_o - \bar{T}_{34})$$

$$-H_6 PWO - \Delta H_{45} - \Delta H_{CW} = \Delta H_M \qquad \text{(A-22)}$$

The transfer coefficients $(hA)_{12}$, $(hA)_{34}$, $(hA)_I$ and $(hA)_{45}$ must be determined from special calibration tests where the measured temperature at each point can be used to determine the enthalpy at that point, i.e. there must be only one phase.

Two types of calibration tests were run: (1) Cooling tests where hot water was circulated through the system and ambient cooling produced the necessary temperature

difference between points. (2) Heating tests where heat was applied to the test cylinder by a hot water bath or wrap around electrical heaters. Direct fire heat could not be used because maximum obtainable flow rates were too low to avoid boiling inside the test cylinder. There was no superheated steam available so the coefficients for the outlet lines were determined using water flow data. However, since the lines are all heavily insulated the effect of the inside coefficient is negligible.

The heat transfer coefficients were calculated from the calibration test data as follows. The inlet and outlet heat balance, Eqs. (A-2) and (A-3), can be added to eliminate ΔH_I resulting in

$$(H_1 - H_2)\ PWI + \Delta H_{12A} + \Delta H_{12F} + (H_3 - H_4)\ PWO + \Delta H_{34A} + \Delta H_{34F} = 0 \qquad (A\text{-}23)$$

There was no fire zone in the calibration tests and the inlet flow always equaled the outlet flow so Eq. (A-23) can be simplified to

$$\left[(H_1 - H_2) + (H_3 - H_4)\right]\ PWI + \Delta H_{12} + \Delta H_{34} = 0 \qquad (A\text{-}24)$$

Equation (A-24) can be expressed in terms of measured temperatures and unknown heat transfer coefficients by substitution of equations of the form of Eqs. (A-4) and (A-7)

for the point enthalpies:

$$\left[(T_1 - T_2) + (T_3 - T_4)\right] C_p \, PWI + (hA)_{12}(\overline{T}_A - \overline{T}_{12}) + (hA)_{34}(\overline{T}_A - \overline{T}_{34}) = 0 \qquad \text{(A-25)}$$

In Eq. (A-25) everything can be measured or calculated except $(hA)_{12}$ and $(hA)_{34}$. Therefore, if two sets of data are taken the resulting simultaneous equations may be solved for $(hA)_{12}$ and $(hA)_{34}$.

After $(hA)_{12}$ and $(hA)_{34}$ are determined the interchange coefficient $(hA)_I$ can be easily determined by substituting Eq. (A-11) into Eq. (A-2) and simplifying to

$$(hA)_I = \frac{(H_2 - H_1)\ PWI - (hA)_{12}(\overline{T}_A - \overline{T}_{12})}{(\overline{T}_{34} - \overline{T}_{12})} \qquad \text{(A-26)}$$

or

$$(hA)_I = \frac{(H_4 - H_3)\ PWO - (hA)_{34}(\overline{T}_A - \overline{T}_{34})}{(\overline{T}_{34} - \overline{T}_{12})} \qquad \text{(A-27)}$$

Equation (A-12) is easily solved to obtain the heat transfer coefficient for the flexible outlet line between the lead tube and the condenser.

$$(hA)_{45} = \frac{(H_4 - H_5)\ PWO}{(\overline{T}_{45} - \overline{T}_A)} \qquad \text{(A-28)}$$

It turned out to be rather difficult to obtain reasonable values for the lead tube transfer coefficients, $(hA)_{12}$ and $(hA)_{34}$, because the substantial insulation permitted only small bulk temperature differences between

points. This difficulty was compounded by erratic readings from the thermocouple located at the cylinder outlet, point 3. In some cases it was necessary to use a temperature reading from another thermocouple located inside the top cap for point 3.

The data from some of the calibration runs is presented in Table D-1, Appendix D. The transfer coefficients obtained from these runs are

$$(hA)_{12} = 0.63 \text{ Btu/hr-°F}$$
$$(hA)_{34} = 0.89 \text{ Btu/hr-°F}$$
$$(hA)_{I} = 1.75 \text{ Btu/hr-°F}$$

Comparable values calculated from a simple model using the properties of the insualtion are 1.28, 1.86 and 1.6 respectively; however these calculated values depend rather strongly on factors such as the packed density of the insulation which cannot be specified precisely.

The worst heat balance made on the calibration runs checked within 10 percent. This error is acceptable considering that the total duty was less than 2000 Btu/hr.

The error in the transfer coefficients may be as high as ± 50 percent. However, as shown in Tables D-5 through D-11, Appendix D, the corrections for the lead tube or the flexible outlet line are always less than 10 percent of the fire heat. Thus the accuracy of the results are still acceptable. It should be pointed out that the amount of heat interchanged between the inlet and outlet lines does

not affect the final result except as part of the determination of $\overline{T}_o$.

The corrections for heat gain through the insulation at the top and bottom of the test cylinder were calculated by a combination of conformal mapping and simple linear heat transfer. Figure A-2 is a sketch illustrating the problems for both the stainless steel and brass cylinders.

The heat transferred through the bottom, Q_1, is determined by linear heat transfer between the insulator base and the bottom of the test cylinder. This term is the same for both cylinders.

$$Q_1 = (T_s - T_b) \frac{\text{Area}}{\delta} k \qquad \text{(A-29)}$$

where T_s = surface temperature of the insulator, °F

T_b = temperature of the metal bottom of the test cylinder, °F

k = thermal conductivity, Btu/hr-ft^2-°F/ft

δ = thickness, ft

Substituting values for k, δ, and the area yields

$$Q_1 = (T_s - T_b) \frac{(0.0995 \text{ ft}^2)\ (0.1 \text{ Btu/hr ft}^2\text{°F/ft})}{0.167 \text{ ft}} \qquad \text{(A-30)}$$

or

$$Q_1 = (T_s - T_b)\ (0.0595) \qquad \text{(A-31)}$$

where Q_1 is in Btu/hr and the temperatures are in °F.

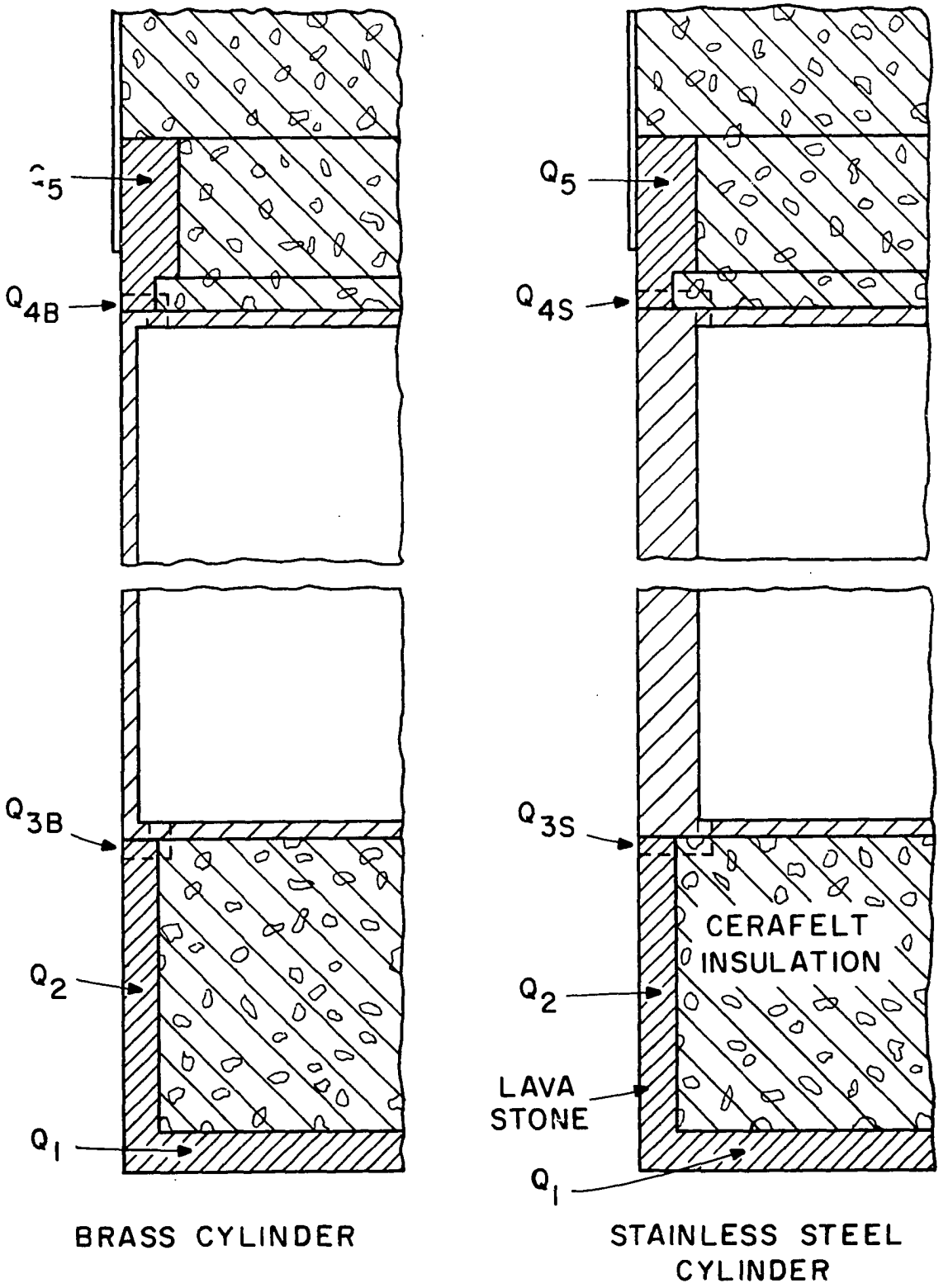

Figure A-2. Heat Gain Through Bottom and Top Insulators Around Test Cylinder.

The heat transferred through the sides of the insulating bottom cap, Q_2, is obtained by using temperature gradients from the conformal mapping solution of the infinite slab problem. Churchill (Ref. 9) develops Eq. (A-32) for the temperature gradient through the sidewall of an infinite slab as shown on Fig. A-3.

$$\left.\frac{\partial \tau}{\partial x}\right|_{x=\frac{\pi}{2}} = \frac{2}{\pi \sinh y} \qquad \text{(A-32)}$$

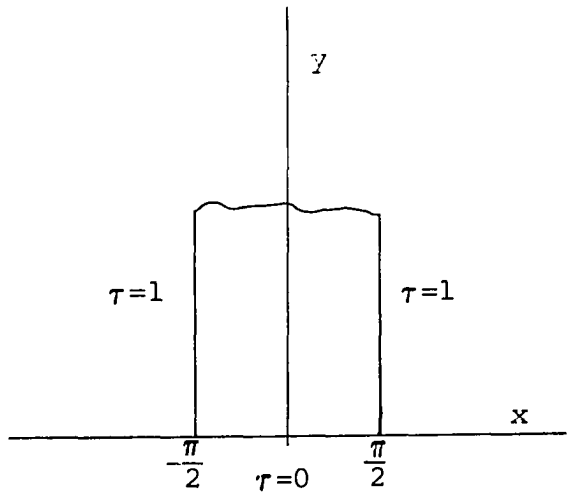

Figure A-3

Conformal Mapping Sketch for Infinite Slab

The boundary conditions for this problem are satisfied by

$$\tau = \frac{T - T_b}{T_s - T_b} \qquad \text{(A-33)}$$

Assuming the gradient through the infinite slab wall may be applied to the cylindrical wall, Q_2 can be calculated by

$$Q_2 = \int_A k\ (T_s - T_b)\ \frac{\partial T}{\partial x}\Big]_{\frac{\pi}{2}} dA \qquad \text{(A-34)}$$

where A is circumferential area of the insulator cap. This estimate is conservative since the gradient into a cylinder will be less than that into an infinite slab. Since the gradient becomes infinite at 0 height, and the heat flow path should be routed around the test cylinder wall, the lower limit of the integration is taken at 0.1 inch. The heat flow through this last 0.1 inch is treated separately as Q_3.

The surface area of the cylinder is 0.098 ft^2 per inch of height so

$$Q_2 = \int_{0.1}^{2} k(T_s - T_b)\ \left(\frac{2}{\pi \sinh y}\right) 0.098\ dy \qquad \text{(A-35)}$$

Graphical integration of Eq. (A-35) yields

$$Q_2 = 0.0267(T_s - T_b) \qquad \text{(A-36)}$$

This result is the same for both cylinders.

The path length for Q_3 is shown by dashed lines on Fig. A-2. The path length and material are quite

different for the brass and stainless steel cylinders.

For the stainless steel cylinder the conduction path is 0.1 inch wide by 0.45 inch long. Half the path is through lava stone (k = 2 Btu/hr-ft-°F/ft) and half is through Cerafelt insulation (k = 0.1 Btu/hr-ft^2-°F/ft), the effective conductivity, k_{eff}, is determined by

$$\frac{1}{k_{eff}} = \frac{0.5}{2} + \frac{0.5}{0.1} \qquad \text{(A-37)}$$

$$\frac{1}{k_{eff}} = 0.25 + 5 \qquad \text{(A-38)}$$

$$k_{eff} = 0.191 \text{ Btu/hr-ft}^2\text{-°F} \qquad \text{(A-39)}$$

Assuming an 1100°F temperature difference, which will be justified later, Q_3 for the stainless steel cylinder may be calculated from

$$Q_{3S} = k_{eff} \Delta T \frac{\text{Area}}{\delta} \qquad \text{(A-40)}$$

$$Q_{3S} = (0.191)(1100)(0.1 \times 0.098)\left(\frac{12}{0.45}\right) \qquad \text{(A-41)}$$

$$Q_{3S} = 55 \text{ Btu/hr} \qquad \text{(A-42)}$$

For the brass cylinder the conduction path is 0.1 inch wide by 0.15 inch long. The entire path is through lava stone. Assuming the same 1100°F temperature difference,

Q_{3B} will calculate out to be 1800 Btu/hr; this result is equivalent to a heat flux of 176,000 Btu/hr-ft^2, which is unreasonably high for flames. Since the applied heat flux is limited by the maximum heat transfer rate from the flames, an average value from the experimental results, 16,000 Btu/hr-ft^2, is assumed; the heat conducted through the 0.1 inch wide zone will then be

$$Q_{3B} = (Q/A)\ \text{Area} \tag{A-43}$$

$$Q_{3B} = (16{,}000)\,(0.1 \times 0.098) \tag{A-44}$$

$$Q_{3B} = 157\ \text{Btu/hr} \tag{A-45}$$

The heat flow through the Q_4 zone at the top of the cylinder, Fig. A-2, will be the same as that for the Q_3 zone.

The heat flowing into the Q_5 zone will be the sum of that flowing radially into the top cap side walls and that flowing down into the top surface of the cylinder and top cap; these heat flows are the same as previously calculated for Q_2. The radial heat flow is through 3/4 inch of Cerafelt and is calculated to be 0.141 $(T_s - T_b)$ Btu/hr. The combined heat through the Q_5 zone is

$$Q_5 = (0.141 + 0.0267)\ (T_s - T_b) \tag{A-46}$$

$$Q_5 = (0.144)\ (T_s - T_b) \tag{A-47}$$

The surface temperature of the insulator can be determined by a simple surface heat balance which neglects the small conduction away from the surface.

$$\epsilon \, Q_{Flame} = \epsilon \, \sigma \, T_s^4 \qquad \text{(A-48)}$$

Assuming an incident heat flux of 20,000 Btu/hr-ft^2 and a surface emissivity of 0.8, the surface temperature is

$$T_s = \left[\frac{16{,}000}{1470 \times 10^{-12}} \right]^{1/4} \qquad \text{(A-49)}$$

$$T_s = 1820°R = 1360°F \qquad \text{(A-50)}$$

Although this result is reasonable, it was not possible to obtain an optical pyrometer reading from the insulator surface even through methanol fires. However, the surface temperature must be above 1400°F for optical pyrometer readings to be made. Spot radiometer readings made when a methanol fire briefly moved away from the cylinder gave surface temperatures of 1020°F. Therefore, the assumed value of 1100°F for $(T_s - T_b)$ in all the calculations appears to be reasonable.

The results of these corrections for the heating through the top and bottom insulating caps are summarized in Table A-1.

TABLE A-1

SUMMARY OF HEAT GAIN THROUGH
TOP AND BOTTOM INSULATORS

Heat Gain (Btu/hr)	Brass	Stainless Steel
Q_1	$0.0595(T_s - T_b)$	$0.0595(T_s - T_b)$
Q_2	$0.0267(T_s - T_b)$	$0.0267(T_s - T_b)$
Q_3	157.	55.
Q_4	157.	55.
Q_5	$0.144\ (T_s - T_b)$	$0.144\ (T_s - T_b)$
Total	$314 + 0.230(T_s - T_b)$	$110 + 0.230(T_s - T_b)$

If $(T_s - T_b) = 1100°F$ the corrections are:

$\Delta H_T + \Delta H_B = 587$ Btu/hr for brass cylinder

$\Delta H_T + \Delta H_B = 363$ Btu/hr for stainless steel cylinder.

The ΔH_{CW} term in the overall heat balance Eq. (A-1) is simply the enthalpy change of the condenser cooling water and is determined from the measured bulk temperature difference and flow rate.

The ΔH_M term in Eq. (A-1) accounts for the change in primary coolant enthalpy due to changes in liquid level inside the test cylinder. The change of the mass of the cylinder contents is

$$PWI - PWO = \Delta M_{liq} + \Delta M_{vap} \tag{A-51}$$

and the change in the enthalpy of these contents is

$$\Delta H_M = \Delta M_{liq} \Delta H_{liq} + \Delta M_{vap} \Delta H_{vap} \tag{A-52}$$

The (PWI - PWO) term is obtained directly from the difference in the input - output flow rates. The ΔM_{liq} could be obtained directly from the measured changes in liquid level; however, these measurements are not accurate enough for such purposes. The total volume of the cylinder remains constant so a change in the liquid volume is balanced by a change in the vapor volume

$$\frac{\Delta M_{liq}}{\rho_{liq}} = \frac{\Delta M_{vap}}{\rho_{vap}} \tag{A-53}$$

$$\Delta M_{liq} = \frac{\rho_{liq}}{\rho_{liq}} (-\Delta M_{vap}) \tag{A-54}$$

Substituting Eq. (A-54) into the mass balance Eq. (A-51) yields

$$(PWI - PWO) = \frac{\rho_{liq}}{\rho_{liq}} (-\Delta M_{vap}) + \Delta M_{vap} \tag{A-55}$$

$$\Delta M_{vap} = \frac{(PWI - PWO)}{(1 - \rho_{liq}/\rho_{vap})} \tag{A-56}$$

Eq. (A-56) may be substituted into the enthalpy balance, Eq. (A-52), to obtain

$$\Delta H_M = \Delta M_{liq} \Delta H_{liq} + \frac{(PWI - PWO)\Delta H_{vap}}{(1 - \rho_{liq}/\rho_{vap})} \tag{A-57}$$

If <u>all</u> enthalpy measurements are based on saturated liquid at 212°F, Eq. (A-57) reduces to

$$\Delta H_M = \frac{(PWI - PWO)\Delta H_{vap}}{(1 - \rho_{liq}/\rho_{vap})} \tag{A-58}$$

Applying values of $\Delta H_{vap} = 970$ Btu/lb, $\rho_{liq} = 59.5$ lb/ft^3 and $\rho_{vap} = 0.037$ lb/ft^3 to Eq. (A-58) yields

$$\Delta H_M = -0.606\ (PWI - PWO)\ \text{Btu/hr} \tag{A-59}$$

The overall heat balance as given by Eq. (A-22) may now be further simplified by substitutions from Eqs. (A-11), (A-12), and (A-59) to

$$H_1\ PWI + (H_2 - H_1)\ PWI - (hA)_I(\overline{T}_{34} - \overline{T}_{12}) + \Delta H_F +$$

$$(\Delta H_T + \Delta H_B) + (hA)_{34}(\overline{T}_o - \overline{T}_{34}) - H_6\ PWO - (hA)_{45}(T_{45} - T_A)$$

$$- \Delta H_{CW} = -0.606\ (PWI - PWO) \qquad \text{(A-60)}$$

The point enthalpy terms, H_1, H_2, and H_6, must use the same reference temperature as Eq. (A-58), namely $T_R = 212°F$. The overall heat balance Eq. (A-60) can be rearranged to solve for the heat entering the active test cylinder surface

$$\Delta H_F = -(T_1 - 212)(PWI\ C_p) - (T_2 - T_1)(PWI\ C_p) +$$

$$(hA)_I\ (\overline{T}_{34} - \overline{T}_{12}) - (\Delta H_T + \Delta H_B) - (hA)_{34}(\overline{T}_o - \overline{T}_{34}) +$$

$$(T_6 - 212)(PWO\ C_p) + (hA)_{45}(\overline{T}_{45} - \overline{T}_A) +$$

$$\Delta H_{CW} - 0.606\ (PWI - PWO) \qquad \text{(A-61)}$$

where
$(hA)_{12}$ = 0.63 Btu/hr°F
$(hA)_{34}$ = 0.89 Btu/hr°F
$(hA)_{45}$ = 2.25 Btu/hr°F
$(hA)_I$ = 1.75 Btu/hr°F
$(\Delta H_T + \Delta H_B)$ = 587 Btu/hr for the brass cylinder
$(\Delta H_T + \Delta H_B)$ = 363 Btu/hr for the stainless steel cylinder

$$\overline{T}_{12} = (T_1 + T_2)/2$$

$$\overline{T}_{34} = (T_3 + T_4)/2$$

$$\overline{T}_{45} = (T_4 + T_5)/2$$

$$\overline{T}_o = \frac{(T_2 - T_1)(PWI\ C_p) - (hA)_I(\overline{T}_{34} - \overline{T}_{12})}{(hA)_{12}} + \overline{T}_{12}$$

The term ΔH_{CW} is the enthalpy change of the condenser cooling water and C_p is the heat capacity of the primary water.

There is one more consideration. The nitrogen gas used in the bubbler system and other non-condensables are vented out the top of the condenser. The maximum nitrogen gas flow was 30 cc/min. The maximum measured vent gas temperature was 150°F. Using a heat capacity of 0.25 Btu/lb°F and a density of 0.06 lb/ft^3 the net enthalpy change for a 100°F temperature change is 5 Btu/hr, which is certainly negligible.

The tabulated results in Tables D-5, D-11, and Appendix D show that the combined heat losses for the lead tube, the flexible outlet line and the top and bottom insulators seldom exceed 20 percent of the heat transfer from the fire to the test surface.

APPENDIX B

NOTES ON NUMERICAL AND ANALYTICAL INTEGRATIONS FOR CALCULATING RADIANT HEATING FROM FLAMES

Numerical Integration Over Flame Geometry

The integrations of the monochromatic power equations were made using a 4-point Gauss Quadrature for the three parameters; horizontal directional angle ζ, the vertical directional angle ξ and cylinder height. Trial problems were run to evaluate the effect on the results of using 4-point and 12-point quadratures. The results of several problems, presented in Table B-1, show that the 4-point quadrature is quite sufficient for present purposes. This result was expected since there are no radical changes in the functions between a given set of limits. Figure B-1 is a plot of the value of the integrand of Eq. (III-12) for calculating the incident radiation from the flame cylinder sidewall, evaluated at the horizontal angle ζ = 77.5 degrees, for the sweep of the vertical angle ξ from -82.5 degrees to 84.7 degrees. The plotted points are results at the 4-point and 12-point Gauss parameter locations. The curve is quite smooth, and it is not

TABLE B-1

INCIDENT RADIANT HEAT FROM SEVERAL FLAME CYLINDERS

CALCULATED WITH 4- AND 12-POINT GAUSS QUADRATURES

Integration Limits (degrees)		Fire Radius (inches)	Total Heat from Fire Cylinder Sidewall (Btu/hr-ft^2)	
Lower	Upper		4-point	12-point
-82.5	84.7	5	5391.2	5393.8
-70.6	74.9	10	7175.0	7174.6
-49.5	58.1	20	7153.2	7153.2
-28.7	37.1	40	5337.5	5337.5

Notes:

1. The target cylinder radius was 2.37 inches.
2. The integration over all wavelengths was carried out using the trapezoid rule.
3. The absorption and emission coefficients from preliminary acetone fuel data were

$$J_\lambda = 134.5 \text{ watts/cm}^3\text{-cm-steradian}$$

$$\beta_\lambda = 0.259/\text{cm}$$

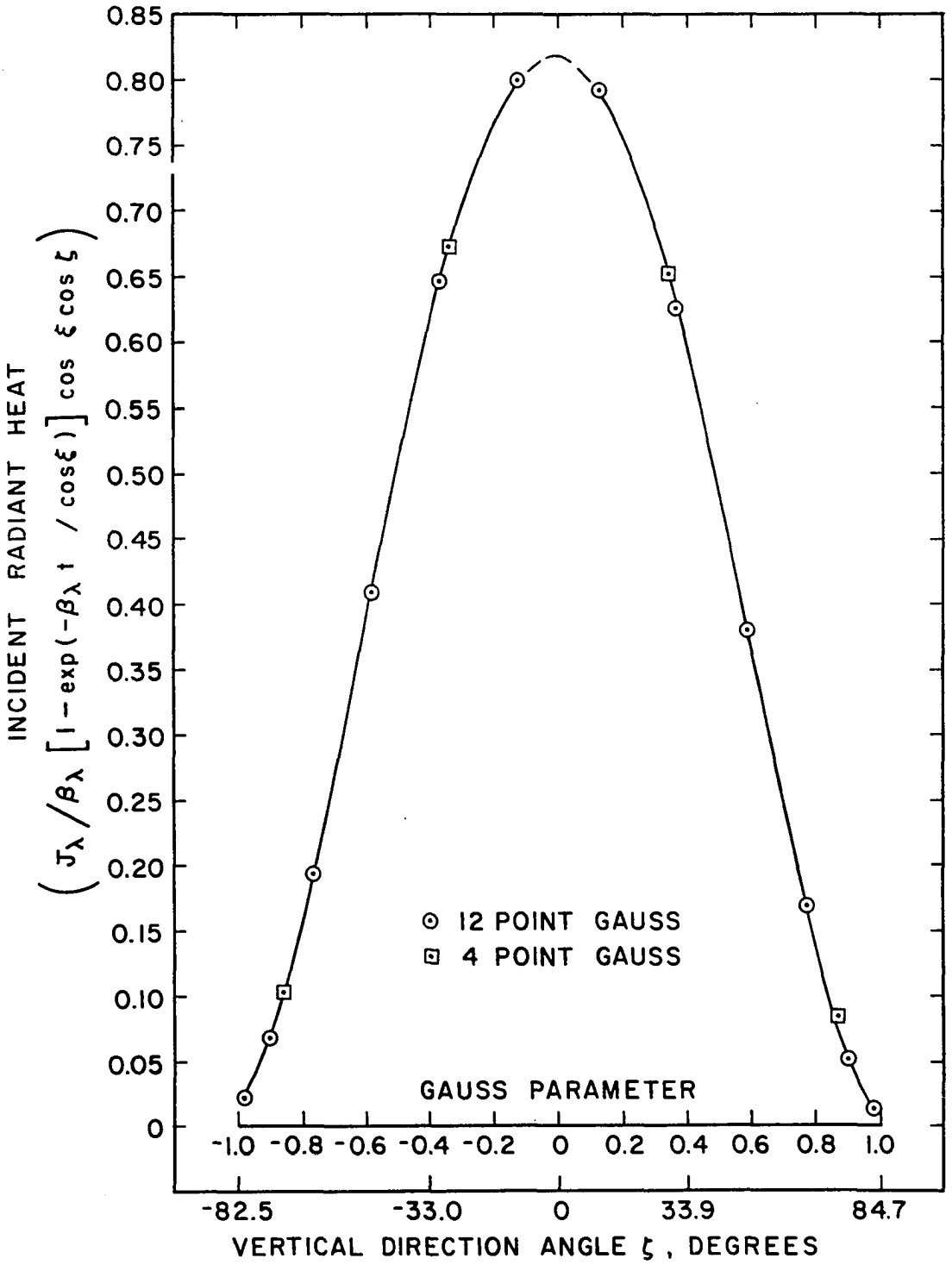

Figure B-1. Angular Distribution of Radiant Heat from Flame Cylinder.

surprising that a low order Gauss Quadrature integrates it quite well. The points are not symmetrical because the target point was off-center between the ζ limits and the slight bell shape at the bottom is due to the influence of the $(1-e^{-\beta_\lambda x})$ term.

Numerical Integration Over Wavelength Spectrum

The trapezoid rule was used to perform the integration of the flame radiation over the contributing wavelength spectrum. A word of caution is in order on the application of the trapezoid rule to the wavelength integration.

The emission and absorption data were not taken at a fixed spacing of the independent variable, i.e. $\Delta\lambda_n \neq \Delta\lambda_{n+1}$. This uneven distribution combined with little merit in calculating and storing individual values of Q_λ produces a tendency to use average values of J_λ and β_λ over each $\Delta\lambda$ interval. This procedure will give an incorrect final result which is not easily detected. If Q_λ is calculated using the point values, the trapezoid rule can then be applied using an average Q_λ over each $\Delta\lambda$ interval. The problem arises from dividing average values of J_λ by average values of β_λ. This quotient is not the same as the average of the quotient obtained from dividing point values of J_λ by point values of β_λ.

$$\frac{\left[\frac{J_{\lambda_{n-1}} + J_{\lambda_n}}{2}\right]}{\left[\frac{\beta_{\lambda_{n-1}} + \beta_{\lambda_n}}{2}\right]} \neq \left(\frac{J_{\lambda_{n-1}}}{\beta_{\lambda_{n-1}}} + \frac{J_{\lambda_n}}{\beta_{\lambda_n}}\right) \frac{1}{2} \qquad \text{(B-1)}$$

Calculating and storing individual values of Q_λ and an involved calculation of the appropriate $\Delta\lambda$ can be avoided by using point values of J_λ and β_λ with

$$\Delta\lambda_n = \frac{\lambda_{n+1} - \lambda_{n-1}}{2} \qquad \text{(B-2)}$$

The first and last calculation points require special values for $\Delta\lambda$:

$$\Delta\lambda_1 = \frac{(\lambda_2 - \lambda_1)}{2} \qquad \text{(B-3)}$$

$$\Delta\lambda_k = \frac{(\lambda_k - \lambda_{k-1})}{2} \qquad \text{(B-4)}$$

Equations for the Entire Numerical Integration

The complete statement of Eq. (III-49) using Gauss Quadrature for integrating over the directional angles and the trapezoid rule for integrating over the wavelengths is given below. Equation (III-49) was developed in Section III for calculating the radiant heating of an external target by a cylindrical flame.

$$\frac{Q}{A_T} = 2 \cos \delta \int_{\lambda_A}^{\lambda_B} \frac{J_\lambda}{\beta_\lambda} \int_0^{\zeta_A} \int_{\xi_A}^{\xi_B} [1-\exp(-\beta_\lambda 2R_o \cos\gamma/\cos\xi)]\cos^2\xi \cos\zeta \, d\xi \, d\zeta \, d\lambda \qquad \text{(B-5)}$$

$$\frac{Q}{A_T} = 2 \cos \delta \frac{\zeta_A}{2} \frac{(\zeta_B - \zeta_A)}{2} \left\{ \sum_{n=1}^{k} \frac{J_n}{\beta_n} \Delta\lambda_n \left[\sum_{i=1}^{m} A_i \sum_{j=1}^{m} A_j \right.\right.$$

$$\left.\left. (1-\exp(-\beta_\lambda 2R_o \cos\gamma_i/\cos\xi_j)) \cos^2\xi_j \cos\zeta_i \right] \right\} \qquad \text{(B-6)}$$

where ξ_j = vertical sweep angle calculated from

$$\xi_j = \left(\frac{\xi_B - \xi_A}{2}\right)\Phi_j + \frac{\xi_B + \xi_A}{2} \qquad \text{(B-7)}$$

ζ_i = horizontal sweep angle calculated from

$$\zeta_i = \left(\frac{\zeta_A}{2}\right)\Phi_i + \frac{\zeta_A}{2} \qquad \text{(B-8)}$$

γ_i = horizontal location angle calculated from

$$\gamma_i = \sin^{-1}\left(\frac{S \sin \zeta_i}{R_o}\right) \qquad \text{(B-9)}$$

Φ_i, Φ_j = Gauss Quadrature parameters

A_i, A_j = Gauss Quadrature coefficients

m = order of Gauss Quadrature

k = number of absorption-emission data points

$\Delta\lambda_n$ = wavelength increments calculated by Eqs. (B-2), (B-3), and (B-4)

The other terms are all defined for Eq. (III-48) in Section III.

The numerical integration procedure used for the radiant heat incident on a target cylinder inside a cylindrical flame required calculations from 16 locations on the flame cylinder sidewall, 16 locations on the flame cylinder top and 16 locations on the flame cylinder bottom. The calculations were repeated for 4 locations on the target cylinder and for each wavelength data point (about 62). This procedure is rather long and requires use of a digital computer. Once accurate emission-absorption coefficients are available it should be possible to average the data into some 4 to 8 absorption groups or wavelength bands which could be used for hand calculations. Of course the integration around the flame shape would still be required, but the next section provides some results which may be used to alleviate the problem.

Analytical Integrations for Hypothetical Flame Shapes

Analytical integration is possible for some hypothetical flame shapes. The solution for some flame shapes which might be useful in fire radiation calculations are presented here. Judicious application of these solutions

and the use of grouped emission-absorption coefficients should make accurate hand calculations possible.

The basic equation for the monochromatic radiant power incident on a differential area located at the origin of the coordinate system is derived in Appendix C. The well known result is

$$\frac{Q_\lambda}{A_T} = \int_{\varphi=0}^{2\pi} \int_{\theta=0}^{\pi/2} \frac{J_\lambda}{\beta_\lambda} \left[1-e^{-\beta_\lambda r}\right] \sin\theta \cos\theta \, d\theta \, d\varphi \qquad \text{(B-10)}$$

where J_λ = monochromatic emission coefficient, watts/cm^3-μ-steradian

β_λ = monochromatic absorption coefficient, cm^{-1}

θ = polar angle

φ = azimuthal angle

A_T = differential target area, cm^2

Q_λ = monochromatic radiant power, watts

The first term in Eq. (B-10) is independent of flame shape and may be easily integrated to obtain

$$\frac{Q_\lambda}{A_T} = \frac{J_\lambda}{\beta_\lambda} \left[\pi - \int_{\varphi=0}^{2\pi} \int_{\theta=0}^{\pi/2} e^{-\beta_\lambda r} \sin\theta \cos\theta \, d\theta \, d\varphi\right] \qquad \text{(B-11)}$$

Hemispherical Flame: A hemispherical flame, shown in Figure B-2 has a constant flame depth equal to the

radius of a sphere.

$$r = a \tag{B-12}$$

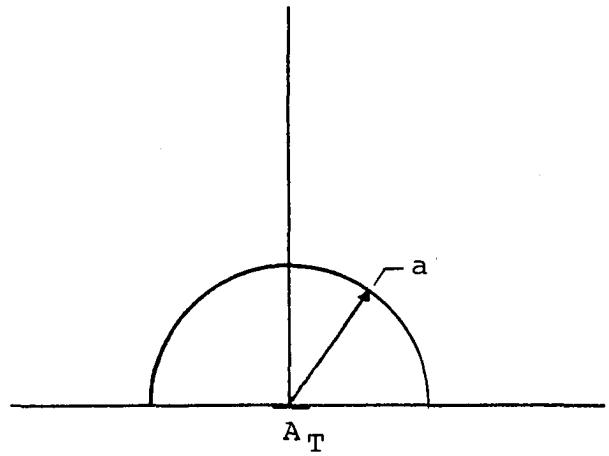

Figure B-2. Hemispherical Flame.

Substituting Eq. (B-12) into Eq. (B-11) yields

$$\frac{Q_\lambda}{A_T} = \frac{J_\lambda}{\beta_\lambda}\left[\pi - \int_{\varphi=0}^{2\pi}\int_{\theta=0}^{\pi/2} e^{-\beta_\lambda a} \sin\theta \cos\theta \, d\theta \, d\varphi\right] \tag{B-13}$$

which is easily integrated to

$$\frac{Q_\lambda}{A_T} = \pi \frac{J_\lambda}{\beta_\lambda}\left[1 - e^{-\beta_\lambda a}\right] \tag{B-14}$$

Flat Torus-shaped Flame: The flame depth of a flattened torus-shaped flame, shown on Figure B-3, is given by

$$r = b\theta \tag{B-15}$$

where b is related to the diameter of the torus as shown on Figure B 3

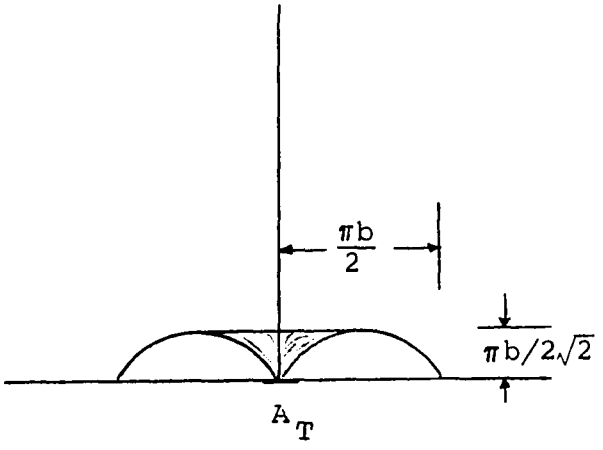

Figure B-3. Flattened Torus Flame Sketch

Substituting Eq. (B-15) into Eq. (B-11) yields

$$\frac{Q_\lambda}{A_T} = \frac{J_\lambda}{\beta_\lambda}\left[\pi - \int_{\omega=0}^{2\pi}\int_{\theta=0}^{\pi/2} e^{-\beta_\lambda b\theta}\,\sin\theta\,\cos\theta\,d\theta\,d\omega\right] \qquad \text{(B-16)}$$

which can be integrated as follows:

$$\int_{\theta=0}^{\pi/2} e^{-\beta_\lambda b\theta}\,\sin\theta\,\cos\theta\,d\theta = \frac{e^{-\beta_\lambda b\theta}\,(-b\beta_\lambda\,\sin 2\theta - 2\cos 2\theta}{2\,(b^2\beta_\lambda^2 + 4)}\Bigg]_0^{\pi/2}$$

$$= \frac{e^{-\beta\, b\pi/2} + 1}{(b^2\beta_\lambda^2 + 4)} \qquad \text{(B-17)}$$

and since

$$\int_{\varphi=0}^{2\pi} f(\theta)\, d\varphi = 2\pi\, f(\theta) \tag{B-18}$$

$$\int_{\varphi=0}^{2\pi}\int_{\theta=0}^{\pi/2} e^{-\beta_\lambda b\theta} \sin\theta \cos\theta\, d\varphi = 2\pi\left(\frac{e^{-\beta_\lambda b\pi/2} + 1}{b^2\beta_\lambda^2 + 4}\right) \tag{B-19}$$

Substituting Eq. (B-19) into Eq. (B-16) yields

$$\frac{Q_\lambda}{A_T} = \frac{\pi J_\lambda}{\beta_\lambda}\left[1 - \frac{2(e^{-\beta_\lambda b\pi/2} + 1)}{(b^2\beta_\lambda^2 + 4)}\right] \tag{B-20}$$

Torus Flame: A torus flame, shown on Figure B-4, results if the flame depth is given by

$$r = b \sin^2\theta \tag{B-21}$$

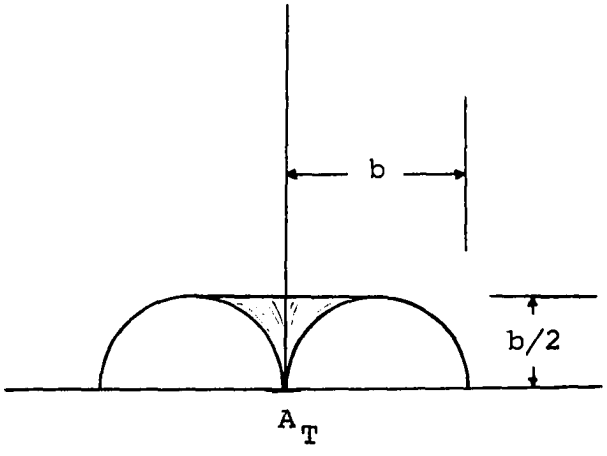

Figure B-4. Torus Flame Sketch

Substituting Eq. (B-21) into Eq. (B-11) yields

$$\frac{Q_\lambda}{A_T} = \frac{J_\lambda}{\beta_\lambda}\left\{\pi - \int_{\varphi=0}^{2\pi}\int_{\theta=0}^{\pi/2} e^{-\beta_\lambda b \sin^2\theta} \sin\theta \cos\theta \, d\theta \, d\varphi\right\} \quad \text{(B-22)}$$

which can be integrated by

$$\int_{\theta=0}^{\pi/2} e^{-\beta_\lambda b \sin^2\theta} \sin\theta \cos\theta \, d\theta = \frac{-1}{2\beta_\lambda b} e^{-\beta_\lambda b \sin^2\theta} \Bigg]_0^{\pi/2}$$

$$= \frac{1}{2\beta_\lambda b}\left[1 - e^{-\beta_\lambda b}\right] \quad \text{(B-23)}$$

and Eq. (B-18) to get

$$\int_{\varphi=0}^{2\pi}\int_{\theta=0}^{\pi/2} e^{-\beta_\lambda b \sin^2\theta} \sin\theta \cos\theta \, d\theta \, d\varphi = \frac{\pi}{\beta_\lambda b}\left[1-e^{-\beta_\lambda b}\right] \quad \text{(B-24)}$$

Substituting Eq. (B-24) into Eq. (B-22) yields

$$\frac{Q_\lambda}{A_T} = \pi \frac{J_\lambda}{\beta_\lambda}\left[1 - \frac{1}{\beta_\lambda b}\left(1-e^{-\beta_\lambda b}\right)\right] \quad \text{(B-25)}$$

Balloon Flame: A balloon-shaped flame, shown on Figure B-5, results if the flame depth is given by

$$r = b \cos^2\theta \quad \text{(B-26)}$$

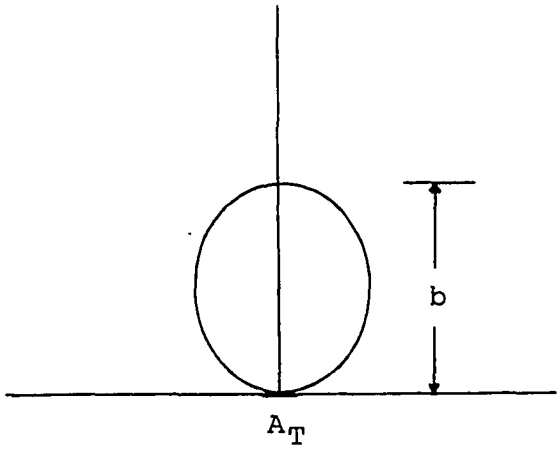

Figure B-5. Balloon Flame Sketch

Substituting Eq. (B-26) into Eq. (B-11) yields

$$\frac{Q_\lambda}{A_T} = \frac{J_\lambda}{\beta_\lambda}\left\{\pi - \int_{\omega=0}^{2\pi}\int_{\theta=0}^{\pi/2} e^{-\beta_\lambda b \cos^2\theta} \sin\theta \cos\theta \, d\theta \, d\omega\right\} \tag{B-27}$$

which can be integrated by

$$\int_{\theta=0}^{\pi/2} e^{-\beta_\lambda b \cos^2\theta} \sin\theta \cos\theta \, d\omega = \frac{1}{2\beta_\lambda b} e^{-\beta_\lambda b \cos^2\theta} \Bigg]_0^{\pi/2}$$

$$= \frac{1}{2\beta_\lambda b}\left[1-e^{-\beta_\lambda b}\right] \tag{B-28}$$

and Eq. (B-18) to get

$$\int_{\varphi=0}^{2\pi} \int_{\theta=0}^{\pi/2} e^{-\beta_\lambda b \cos^2\theta} = \frac{\pi}{\beta_\lambda b}\left[1-e^{-\beta_\lambda b}\right] \qquad \text{(B-29)}$$

Substituting Eq. (B-29) into Eq. (B-27) yields

$$\frac{Q_\lambda}{A_T} = \pi \frac{J_\lambda}{\beta_\lambda}\left[1 - \frac{1}{\beta_\lambda b}\left(1-e^{-\beta_\lambda b}\right)\right] \qquad \text{(B-30)}$$

This result is the same result as obtained for the flat torus even though the flame shapes are quite different.

Paraboloid Flame: The flame depth of a paraboloid flame, shown on Figure B-6, is given by

$$r = b \cos^2\theta + c \qquad \text{(B-31)}$$

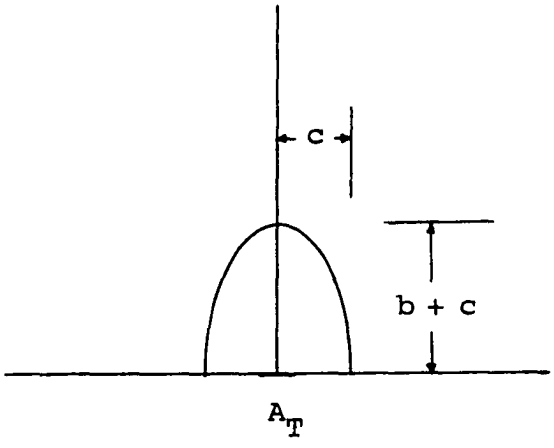

Figure B-6. Paraboloid Flame Sketch

Substituting Eq. (B-31) into Eq. (B-11) yields

$$\frac{Q_\lambda}{A_T} = \frac{J_\lambda}{\beta_\lambda}\left\{\pi - \int_{\varphi=0}^{2\pi}\int_{\theta=0}^{\pi/2} e^{-\beta_\lambda (b\cos^2\theta + c)} \sin\theta\cos\theta\, d\theta\, d\varphi\right\} \tag{B-32}$$

which can be integrated by

$$\int_{\theta=0}^{\pi/2} e^{-\beta_\lambda (b\cos^2\theta + c)} \sin\theta\cos\theta\, d\theta = \frac{e^{-\beta_\lambda (b\cos^2\theta + c)}}{2\beta_\lambda b}\Bigg]_0^{\pi/2}$$

$$= \frac{e^{-\beta_\lambda c}}{2\beta_\lambda b}\left[1-e^{-\beta_\lambda b}\right] \tag{B-33}$$

and Eq. (B-18) to get

$$\int_{\varphi=0}^{2\pi}\int_{\theta=0}^{\pi/2} e^{-\beta_\lambda (b\cos^2\theta + c)} \sin\theta\cos\theta\, d\theta\, d\varphi =$$

$$\pi\,\frac{e^{-\beta_\lambda c}}{\beta_\lambda b}\left[1-e^{-\beta_\lambda b}\right] \tag{B-34}$$

Substituting Eq. (B-34) into Eq. (B-27) yields

$$\frac{Q_\lambda}{A_T} = \pi\,\frac{J_\lambda}{\beta_\lambda}\left[1-\frac{e^{-\beta_\lambda c}}{2\beta_\lambda b}\left(1-e^{-\beta_\lambda b}\right)\right] \tag{B-35}$$

The paraboloid flame approaches a cylindrical flame when b is large compared to c.

<u>Ellipsoid Flame:</u> The ellipsoid flame, shown on Figure B-7, has a fire depth given by

$$r = b\sin^2\theta + c \tag{B-36}$$

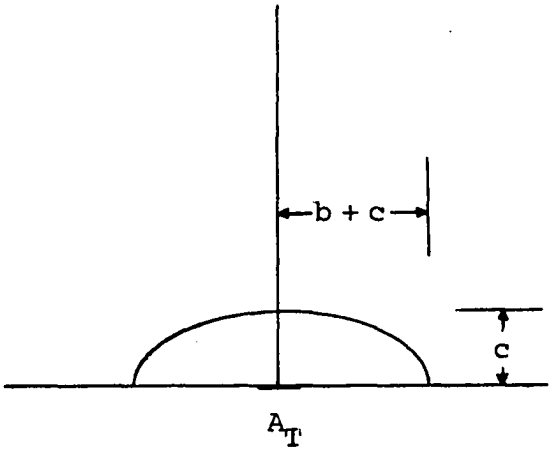

Figure B-7. Ellipsoid Flame

Substituting Eq. (B-36) into Eq. (B-11) and integrating in the same manner as before yields

$$\frac{Q_\lambda}{A_T} = \pi \frac{J_\lambda}{\beta_\lambda}\left[1 - \frac{e^{-\beta_\lambda c}}{2\beta_\lambda b}\left(1-e^{-\beta_\lambda b}\right)\right] \qquad \text{(B-37)}$$

which is the same result as obtained for the paraboloid flame.

APPENDIX C

FORMAL DEVELOPMENT OF RADIANT HEATING EQUATIONS FOR AN ABSORBING-EMITTING MEDIUM

The basic transport equation for heat transfer by radiation through an absorbing-emitting medium is

$$\frac{dI_\lambda}{dr} = -\beta_\lambda I_\lambda + J_\lambda \qquad \text{(C-1)}$$

where I_λ = monochromatic intensity of radiation, $\frac{\text{watts}}{\text{cm}^2\text{-micron-steradian}}$

J_λ = monochromatic volume emission coefficient, $\frac{\text{watts}}{\text{cm}^3\text{-micron-steradian}}$

β_λ = monochromatic absorption coefficient, cm^{-1}

r = path length over which emission and absorption occur, cm

Following the lead of previous work (Ref. 30), it is convenient to write two transport equations, one defining the intensity arriving at any point from its right, I_λ^-, and the other defining the intensity arriving at any point from its left, I_λ^+, as shown in Fig. C-1.

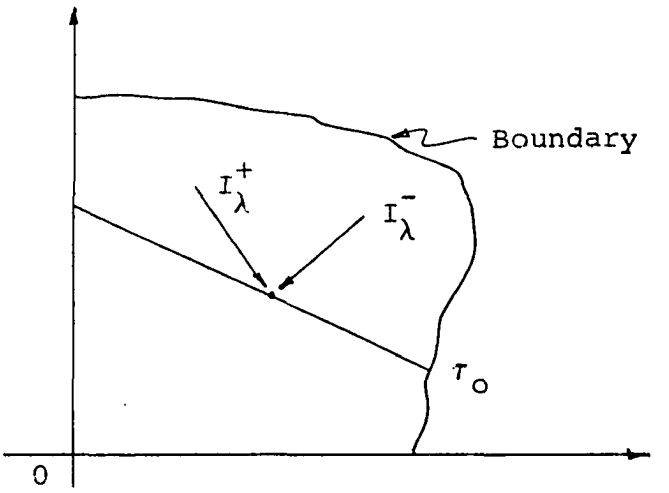

Figure C-1. Directional Intensity of Radiation

The components of the radiation intensity arriving from the left and right respectively, are then

$$\frac{dI_\lambda^+}{dr} = -\beta_\lambda I_\lambda^+ + J_\lambda \qquad \text{(C-2)}$$

$$\frac{-dI_\lambda^-}{dr} = -\beta_\lambda I_\lambda^- + J_\lambda \qquad \text{(C-3)}$$

Equations (C-2) and (C-4) are divided by β_λ to obtain the transport equations in terms of the optical distance τ, where τ is defined as

$$\tau = \int_0^r \beta_\lambda dr \qquad \text{(C-4)}$$

Both τ and r are functions of the polar and azimuthal incident angles θ and φ, measured from the normal to the target surface.

The transport equations may now be written as

$$\frac{dI_\lambda^+}{d\tau} = -I_\lambda^+ + \frac{J_\lambda}{\beta_\lambda} \tag{C-5}$$

$$\frac{-dI_\lambda^-}{d\tau} = -I_\lambda^- + \frac{J_\lambda}{\beta_\lambda} \tag{C-6}$$

The boundary conditions for a medium such as a flame are given by

$$I_\lambda^+(0) = \epsilon_t I_{b\lambda}(T_t) + \frac{\rho_t}{\pi}\int_0^{2\pi}\int_0^1 I_\lambda^-(0)\ \mu\ d\mu\ d\varphi \tag{C-7}$$

for the component from the left, and

$$I_\lambda^-(\tau_o) = 0 \tag{C-8}$$

for the component from the right.

The t subscripts refer to the properties of a target surface located at $\tau = 0$ and the o subscripts refer to the outside of the flame medium. $I_{b\lambda}(T_t)$ is the "black body" radiation intensity as defined by Planck and μ is the cosine of the polar angle θ.

The (+) transport equation can be integrated through the use of the integrating factor e^τ.

Multiplying through by the integrating factor and combining the differential terms results in

$$\frac{d(e^\tau I_\lambda^+)}{d\tau} = \frac{J_\lambda e^\tau}{\beta_\lambda} \tag{C-9}$$

Equation (C-9) is easily integrated to

$$I_\lambda^+ = \frac{J_\lambda}{\beta_\lambda} + C_1 e^{-\tau} \qquad \text{(C-10)}$$

Similarly, the (-) transport equation can be integrated through use of the integrating factor $-e^{-\tau}$ to obtain

$$I_\lambda^- = \frac{J_\lambda}{\beta_\lambda} - C_2 e^{\tau} \qquad \text{(C-11)}$$

It should be kept in mind that r, and hence τ, are functions of μ and φ.

The constants C_1 and C_2 are found through use of the boundary conditions given by Eq's. (C-7) and (C-8), respectively. Combining Eqs. (C-8) and (C-11) results in

$$C_2 = \frac{J_\lambda}{\beta_\lambda} e^{-\tau_o} \qquad \text{(C-12)}$$

The radiation component from the right then becomes

$$I_\lambda^-(\tau) = \frac{J_\lambda}{\beta_\lambda} (1-e^{\tau-\tau_o}) \qquad \text{(C-13)}$$

Combining Eq.'s (C-7) and (C-10) yields

$$\epsilon_t I_{b\lambda}(T_t) + \frac{\rho_t}{\pi} \int_0^{2\pi} \int_0^1 I_\lambda^-(0)\ \mu\ d\mu\ d\varphi = \frac{J_\lambda}{\beta_\lambda} + C_1 \qquad \text{(C-14)}$$

which can be solved for C_1 as

$$C_1 = \epsilon_t I_{b\lambda}(T_t) + \frac{\rho_t}{\pi} \int_0^{2\pi} \int_0^1 \frac{J_\lambda}{\beta_\lambda} (1-e^{-\tau_o}) \mu \, d\mu \, d\varphi - \frac{J_\lambda}{\beta_\lambda} \tag{C-15}$$

The radiation component from the left then becomes

$$I_\lambda^+(\tau) = \frac{J_\lambda}{\beta_\lambda} + \left[\epsilon_t I_{b\lambda}(T_t) + \frac{\rho_t}{\pi} \int_0^{2\pi} \int_0^1 \frac{J_\lambda}{\beta_\lambda} (1-e^{-\tau_o}) \mu \, d\mu \, d\varphi - \frac{J_\lambda}{\beta_\lambda} \right] e^{-\tau} \tag{C-16}$$

The monochromatic intensities at a point on the target surface (r=0) are

$$I_\lambda^+(0) = \epsilon_t I_{b\lambda}(T_t) + \frac{\rho_t}{\pi} \int_0^{2\pi} \int_0^1 \frac{J_\lambda}{\beta_\lambda} (1-e^{-\tau_o}) \mu \, d\mu \, d\varphi \tag{C-17}$$

and

$$I_\lambda^-(0) = \frac{J_\lambda}{\beta_\lambda} (1-e^{-\tau_o}) \tag{C-18}$$

The net monochromatic heat flow at this point is

$$\Delta Q_\lambda = \int_0^{2\pi} \int_0^1 \left[I_\lambda^+(0) - I_\lambda^-(0) \right] \mu \, d\mu \, d\varphi \tag{C-19}$$

$$\Delta Q_\lambda = \int_0^{2\pi}\int_0^{1}\left[\epsilon_t I_{b\lambda}(T_t) + \frac{\rho_t}{\pi}\int_0^{2\pi}\int_0^{1}\frac{J_\lambda}{\beta_\lambda}(1-e^{-\tau_o})\,\mu\,d\mu\,d\varphi - \frac{J_\lambda}{\beta_\lambda}(1-e^{-\tau_o})\right]\mu\,d\mu\,d\varphi \qquad \text{(C-20)}$$

$$\Delta Q_\lambda = \epsilon_t \pi\, I_{b\lambda}(T_t) + \int_0^{2\pi}\int_0^{1}\left[\frac{\rho_t}{\pi}\int_0^{2\pi}\int_0^{1}\frac{J_\lambda}{\beta_\lambda}(1-e^{-\tau_o})\,\mu\,d\mu\,d\varphi - \frac{J_\lambda}{\beta_\lambda}(1-e^{-\tau_o})\right]\mu\,d\mu\,d\varphi \qquad \text{(C-21)}$$

where Q_λ = monochromatic heat flow (watts/cm^2-micron).

An observation about the above development can be made which greatly extends the applicability of the results. If the target is not in contact with the flame, the boundary condition given by Eq. (C-7) becomes

$$I_\lambda^+(0) = \epsilon_t \pi\, I_{b\lambda}(T_t) + \frac{\rho_t}{\pi}\int_0^{2\pi}\int_0^{\mu_2(\varphi)} I_\lambda^-(0)\,\mu\,d\mu\,d\varphi \qquad \text{(C-22)}$$

where $\mu_2(\varphi)$ is the cosine of the polar angle defining the flame boundary. The solution for $I_\lambda^-(0)$ remains the same if τ_o is interpreted as being the optical distance through the flame only. The monochromatic net heat flow for a target not in contact with the flame becomes

$$\Delta Q_\lambda = \epsilon_t \pi \, I_{b\lambda}(T_t) + \int_0^{2\pi} \int_0^{1}$$

$$\left[\frac{\rho_t}{\pi} \int_0^{2\pi} \int_0^{\mu_2(\varphi)} \frac{J_\lambda}{\beta_\lambda} (1-e^{-\tau_o}) \, \mu \, d\mu \, d\varphi - \frac{J_\lambda}{\beta_\lambda} (1-e^{-\tau_o})\right] \mu \, d\mu \, d\varphi \tag{C-23}$$

Since there is no contribution from outside the integration limits, Eq. (C-23) may be further simplified to a more general form

$$\Delta Q_\lambda = \epsilon_t \pi \, I_{b\lambda}(T_t) + \int_{\varphi_1}^{\varphi_2} \int_{\mu_1(\varphi)}^{\mu_2(\varphi)}$$

$$\left[\frac{\rho_t}{\pi} \int_{\varphi_1}^{\varphi_2} \int_{\mu_1(\varphi)}^{\mu_2(\varphi)} \frac{J_\lambda}{\beta_\lambda} (1-e^{-\tau_o}) \, \mu \, d\mu \, d\varphi - \frac{J_\lambda}{\beta_\lambda} (1-e^{-\tau_o})\right] \mu \, d\mu \, d\varphi \tag{C-24}$$

The major problem in solving Eq. (C-24) is to perform the integration

$$\int_{\varphi_1}^{\varphi_2} \int_{\mu_1}^{\mu_2} \frac{J_\lambda}{\beta_\lambda} (1-e^{-\tau_o}) \, \mu \, d\mu \, d\varphi \tag{C-25}$$

Equation (C-25) can be readily simplified to a more familiar form by neglecting the contribution from the target. The equation for the radiant heat flux incident on a target inside a flame becomes

$$Q_\lambda = \int_{\varphi=0}^{2\pi} \int_{\theta=0}^{\pi/2} \frac{J_\lambda}{\beta_\lambda} [1-e^{-\tau_o}] \sin\theta \cos\theta \, d\theta \, d\varphi \qquad \text{(C-26)}$$

Of course Eq's. (C-25) and (C-26), indeed all the equations in this section, must be integrated over all contributing wavelengths to get the total radiant heating. The techniques for integrating over the geometric flame shapes and contributing wavelengths are covered in Appendix B.

APPENDIX D

TABULAR SUMMARY OF DATA

TABLE D-1

EXPERIMENTAL DATA FROM LEAD TUBE HEAT LOSS CALIBRATION TESTS

Condenser Cooling Water Flow (lb/hr)	Primary Cooling Water Flow (lb/hr)	Primary Water Temperature Differences (°F)			Primary Water Enthalpy Changes (Btu/hr)			Condenser Cooling Water ΔT (°F)	Average Primary Water Temperatures (°F)			Temperature Near Lead Tube (°F)
		$T_2 - T_1$	$T_4 - T_3$	$T_5 - T_4$	ΔH_{12}	ΔH_{34}	ΔH_{45}		$\bar{T}_{12}$	$\bar{T}_{34}$	$\bar{T}_{45}$	
205	18.3	4.44	-9.87	-12.68	-81	-180.8	2.55	6.9	122	102	91	83
219	7.8	-11.5	-2.23	-14.2	-89.6	- 17.3	111.5	1.07	175	139.5	130	80
219	7.8	-11.2	-2.77	-10.0	-87.4	- 21.6	78	0.9	160	147	135	80

TABLE D-2

MEASURED RADIATION INTENSITY FROM CIRCULAR BURNER FIRES

Fuel	Test No.	Burner Diameter (inches)	Flame Thickness in Radiometer view (inches)	Radiation[a] Maximum (watts/cm^2 steradian)	Minimum
Methanol	68	12	10	0.33	0.11
	61	18	16	0.33	0.12
Acetone	63	18[b]	10	0.56	0.18
	57	6[b]	24	2.38	0.72
Hexane	67	12	14	0.61	0.31
	62	18	25	1.14	0.56
Cyclohexane	66	12	10	0.62	0.36
	60	18[b]	11	1.23	0.82
	58	6[b]	24	1.90	0.74
JP4	64	18	16	1.00	0.52

[a] Radiation measured with narrow beam radiometer.

[b] Burner cluster consisted of 9, 6-inch diameter burners spaced 12 inches apart.

TABLE D-3

MISCELLANEOUS TEMPERATURES, SOOT ACCUMULATION AND TEST DURATION

Fuel	Test Number	Burner Diameter (inches)	Test Duration (min)	Building Wall Temperatures (°F) initial/final	Average Soot Thickness (inches)	Flame Temperatures (°F)	Lead Tube Temperatures (a) (°F) T19	T20	T21	T22	T23	T24
Methanol	68	12	50	112/108	--	--(b)	165	218	355	355	325	345
	29	12	72	--	--	--	105	110	155	145	360	480
	12	12	137	--	1/32(c)	--	115	135	220	205	--	--
	61	18	71	70/79	--	--	105	140	240	205	405	500
	45	18	103	75/85	--	--	115	135	220	205	500	505
	48	24	100	82/102	--	--	125	160	240	260	625	675
	40	24	105	114/120	--	--	150	205	350	335	610	650
	37/38(d)	24	105	--	--	--	155	215	350	335	525	575
Acetone	57	6(e)	95	57/111	1/64	2160	130	175	328	282	645	723
	53	6	81	100/148	1/64	2200	160	220	455	415	750	840
	52	6	78	65/130	1/64	2165	120	150	375	320	775	845
	50	12	185	70/90	1/16	--	130	150	250	235	590	650
	16/17/18	12	130	--	--	--	115	135	305	270	600	825
	63	18	115	72/102	1/16	2030	130	210	485	440	840	1080
	49	24	60	96/142	1/64	2150	165	235	485	435	950	1175
	39	24	125	104/130	1/32	2100	165	240	550	515	925	1060
	34/35/36	24	135	76/82	1/32	2100	165	245	670	575	930	1120
	32/33	24	65	85/88	--	2100	135	215	550	500	830	1025

(a) See Figure IV-8 for location of thermocouples on lead tube.

(b) Methanol flames too dim to read the optical pyrometer. The flame temperature was assumed to be 2200°F for use in calculations.

(c) Soot left on cylinder from two false starts with cyclohexane.

(d) Some tests include two or more cylinder positions without stopping to clean cylinder.

(e) Tests run with a cluster of 9 6-inch diameter burners spaced 12 inches apart.

TABLE D-3 (continued)

Fuel	Test Number	Burner Diameter (inches)	Test Duration (min)	Building Wall Temperatures (°F) initial/final	Average Soot Thickness (inches)	Flame Temperatures (°F)	Lead Tube Temperatures (°F) T19	T20	T21	T22	T23	(a) T24
Hexane	54	6	32	79/200	1/64	2150	150	250	625	525	1210	1370
	67	12	102	98/136	1/32	2160	180	260	550	520	950	1160
	44	12	85	123/173	--	2100	205	320	650	585	900	1075
	41	12	130	64/138	3/64	2135	155	250	635	590	1050	1200
	13/14/15	12	120	--	3/32	2110	135	200	445	400	925	850
	65	18	32	108/173	1/64	2050	195	280	525	475	1150	1370
	62	18	39	76/150	--	2000	150	220	365	340	1150	1325
	46	18	55	82/200	1/32	2000	200	320	675	625	1150	1370
Cyclohexane	58	6	25	61/143	1/32	--	125	200	450	340	1250	1425
	55	6	30	135/220	--	--	215	400	805	720	1200	1390
	66	12	125	70/120	3/32	2020	155	225	545	525	850	975
	42	12	84	109/150	--	2050	185	320	720	690	1020	1150
	30/31	12	75	90/92	1/8	--	145	250	645	550	910	1200
	60	18	32	89/132	1/64	--	135	210	385	350	850	935
JP-4	56	6	52	118/207	1/16	--	235	375	800	700	1245	1425
	51	12	145	86/132	1/16	1980	175	270	565	510	750	950
	64	18	52	86/143	1/32	--	170	255	450	405	1050	1250
	47	18	47	127/205	--	--	225	400	750	650	1215	1450
Benzol	43	12	50	120/150	1/16	--	200	315	615	560	1145	1390
Napalm	27/28	12	64	88/90	--	2080	180	320	775	700	900	1225

(a) See Figure IV-8 for location of thermocouples on lead tube.

TABLE D-4

FIRE SIZES, FUEL BURNING RATES AND EXTERNAL RADIATION

Fuel	Test Number	Burner Diameter (inches)	Cylinder Type	Fire Diameter (inches)	Fire Height (inches)	Cylinder Height[a] Bottom (inches)	Fuel Burning Rate (ml/min)	Fuel Burning Rate (lb/hr-ft^2)[i]	Fuel Burning Rate (lb/hr-ft^3)[j]	External[h] Radiation (Btu/hr-ft^2)
Methanol (ρ=49.4 lb/ft^3)	68	12	Steel[b]	10[c]	18	6	84	11.2	16.0	--
	29	12	Brass	10	17	7	94.5	12.6	19.1	36
	12	12	Steel	9	18	7	81	10.8	18.8	36
	61	18	Steel	15	25	7	193	11.4	11.8	78
	45	18	Brass	15	25	6	189	11.2	11.6	75
	48	24	Steel	24	30	12	336	11.2	6.6	145
	40	24	Brass	22	25	7	337	12.3	10.4	--
	37/38[d]	24	Brass	20	20/35	8/10	371	12.4	9.0	--
Acetone (ρ=49.4 lb/ft^3)	57	6[e]	Steel	24	30	17	419/72	27.9/36.3(29.1)[f]	6.5	--
	53	6	Steel	20	40	22	323/93.5	34.9/49.8(36.4)	8.8	--
	52	6	Steel	22	40	16	463/90	50.9/47.8(32.7)	6.6	340
	50	12	Steel	10	35	15	122	16.2	8.0	80
	16/17/18	12	Brass	10	35	12/21/16	152.6	20.2	12.3	--
	63	18	Steel	12	50	15	330.3	29.4	14.9	190
	49	24	Steel	20	60	15	802	26.3	7.7	440
	39	24	Brass	20	75	16	783	25.1	6.0	--
	34/35/36	24	Brass	20	70	27/20/16	620	20.6	5.1	--
	32/33	24	Brass	20	75	12/22	726	24.2	6.8	--

[a] Top of active cylinder surface is 9 inches above bottom.

[b] Steel cylinder made from 304 stainless steel.

[c] Methanol fire diameters are maximum values. See text for average fire size.

[d] Some tests include two or more cylinder positions without stopping to clean cylinder.

[e] Six inch diameter burners run as a cluster of 9.

[f] The fuel burning rates for the cluster reported for outer-8, center-1 and total.

[h] Radiometer located 70 inches from flame center line and 5 inches above burner top.

[i] Fuel burning rate per unit surface area of burner.

[j] Fuel burning rate per unit flame cylinder volume.

TABLE D-4 (continued)

Fuel	Test Number	Burner Diameter (inches)	Cylinder Type	Fire Diameter (inches)	Fire Height (inches)	Cylinder Height Bottom[a] (inches)	(ml/min)	Fuel Burning Rate (lb/hr-ft^2)[i]	(lb/hr-ft^3)[j]	External[h] Radiation (Btu/hr-ft^2)
Hexane (ρ=41.2 lb/ft^3)	54	6	Steel	25	80	22	1469/264	81.8/117.3(85.3)	6.6	--
	67	12	Steel	14	60	10	372	41.3	6.1	--
	44	12	Brass	20	60	25	544	60.4	4.3	--
	41	12	Brass	22	70	10	439	48.8	2.5	330
	13/14/15	12	Steel	18	65	18/10/32	290	32.2	2.6	340
	45	18	Steel	25	90	15	1077	53.9	3.8	--
	62	18	Steel	26	65	15	1000	87.2	4.4	--
	46	18	Brass	30	75	14	1152	100.5	3.3	810
Cyclohexane (ρ=48.6 lb/ft^3)	58	6	Steel	24	50	21	1060/211	69.5/110.74(74)	10.0	1700
	55	6	Steel	23	60	22	1301/246	85.5/129.1 (89.9)	11.0	--
	63	12	Steel	12	50	9	268	35.1	8.4	200
	42	12	Brass	18	55	11	477	62.6	6.1	--
	30/31	12	Brass	17	50	7/19	419	55	4.8	--
	60	18	Steel	20	65	16	825	48.1	7.2	--
JP-4 (ρ=50 lb/ft^3)	56	6	Steel	23	60	22	902/176	61.0/90.9(64.4)	7.9	--
	51	12	Steel	16	35	15	266	35.9	6.9	--
	64	18	Steel	18	60	16	79.6	45.1	9.1	--
	47	18	Steel	--	--	15	99.5	56.3	--	--
Benzol (ρ=57 lb/ft^3)	43	12	Brass	16[g]	35	11	501	71.1	14.2[g]	--
Napalm (ρ=50 lb/ft^3)	27/28	12	Brass	15	50	16/8	421.5	56.8	8.8	--

[a] Top of active cylinder surface is 9 inches above bottom.

[g] Fire size from visual estimate, too smoky to take pictures.

[h] Radiometer located 70 inches from flame center line and 5 inches above burner top.

[i] Fuel burning rate per unit surface area of burner.

[j] Fuel burning rate per unit flame cylinder volume.

TABLE D-5

TOTAL HEAT TRANSFER DATA AND CALCULATED RESULTS FOR METHANOL FIRES

TEST NUMBER - 12
FUEL - METHANOL
BURNER - 12 INCH DIAMETER, SINGLE
CYLINDER - STAINLESS STEEL

DATA

TEST TIME (MIN)	PRIMARY WATER FLOWS (LB/HR)		PRIMARY WATER TEMPERATURES (DEG F)				AIR TEMP (DEG F)	COOLING WATER FLOW (LB/HR)	TEMP DIFF (DEG F)
	PWI	PWO	T1	T2	T3	T6	TA	CW	CWDT
40	3.6	3.6	175.0	155.0	203.0	87.0	85.	214.0	17.0
45	3.6	3.6	179.0	163.0	203.0	87.0	90.	214.0	18.0
63	5.7	5.7	175.0	184.0	204.0	91.0	90.	198.0	22.0
72	5.7	4.8	167.0	173.0	204.0	94.0	100.	198.0	22.3
115	25.2	25.2	193.0	195.0	204.0	119.0	100.	198.0	30.0
135	37.0	37.0	110.0	114.0	205.0	106.0	105.	198.0	22.3

RESULTS

TEST TIME	HEAT LOSSES (BTU/HR)				FIRE HEAT ABSORBED THROUGH TEST SURFACE	
	OUTLET LINE	LEAD TUBE	CYLINDER ENDS	CONTENTS	(BTU/HR)	(BTU/HR-SQFT)
40	265.5	368.0	-380.0	0.0	3574.7	4062.1
45	254.3	302.6	-380.0	0.0	3697.6	4201.8
63	256.5	1.5	-380.0	0.0	3755.2	4267.2
72	234.0	91.3	-380.0	0.5	4044.1	4595.6
115	234.0	-70.5	-380.0	0.0	3858.7	4384.9
135	225.0	118.4	-380.0	0.0	4230.8	4807.7

TABLE D-5 (continued)

TEST NUMBER - 29
FUEL - METHANOL
BURNER - 12 INCH DIAMETER, SINGLE
CYLINDER - BRASS

DATA

TEST TIME (MIN)	PRIMARY WATER FLOWS (LB/HR)		PRIMARY WATER TEMPERATURES (DEG F)				AIR TEMP (DEG F)	COOLING WATER FLOW (LB/HR)	COOLING WATER TEMP DIFF (DEG F)
	PWI	PWO	T1	T2	T3	T6	TA	CW	CWDT
50	5.6	5.6	196.0	192.5	212.0	107.5	95.	362.0	15.5
60	5.6	5.6	182.5	190.0	212.0	105.0	95.	356.0	16.0
73	7.8	7.8	167.0	178.5	212.0	112.5	95.	356.0	15.7

RESULTS

TEST TIME	HEAT LOSSES (BTU/HR)				FIRE HEAT ABSORBED THROUGH TEST SURFACE	
	OUTLET LINE	LEAD TUBE	CYLINDER ENDS	CYLINDER CONTENTS	(BTU/HR)	(BTU/HR-SQFT)
50	263.3	138.0	-590.0	0.0	4926.7	5598.5
60	263.3	30.3	-590.0	0.0	4965.6	5642.7
73	263.3	-15.8	-590.0	0.0	4821.6	5479.1

TABLE D-5 (continued)

TEST NUMBER - 68
FUEL - METHANOL
BURNER - 12 INCH DIAMETER, SINGLE
CYLINDER - STAINLESS STEEL

DATA

TEST TIME (MIN)	PRIMARY WATER FLOWS (LB/HR)		PRIMARY WATER TEMPERATURES (DEG F)				AIR TEMP (DEG F)	COOLING WATER FLOW (LB/HR)	TEMP DIFF (DEG F)
	PWI	PWO	T1	T2	T3	T6	TA	CW	CWDT
8	12.2	11.8	130.0	138.0	212.0	104.0	80.	346.0	13.0
18	12.2	11.8	152.0	160.0	212.0	112.0	85.	346.0	15.5
27	12.2	11.5	157.5	169.5	212.0	111.5	90.	346.0	15.8
43	12.2	11.5	160.0	171.5	212.0	110.0	95.	346.0	15.8

RESULTS

TEST TIME	HEAT LOSSES (BTU/HR)				FIRE HEAT ABSORBED THROUGH TEST SURFACE	
	OUTLET LINE	LEAD TUBE	CYLINDER ENDS	CONTENTS	(BTU/HR)	(BTU/HR-SQFT)
8	297.0	163.3	-380.0	0.2	4304.5	4891.5
18	285.8	50.8	-380.0	0.2	4871.8	5536.1
27	274.5	-105.3	-380.0	0.4	4765.6	5415.4
43	263.3	-102.1	-380.0	0.4	4709.8	5352.1

TABLE D-5 (continued)

TEST NUMBER - 45
FUEL - METHANOL
BURNER - 18 INCH DIAMETER, SINGLE
CYLINDER - BRASS

DATA

TEST TIME (MIN)	PRIMARY WATER FLOWS (LB/HR)		PRIMARY WATER TEMPERATURES (DEG F)				AIR TEMP (DEG F)	COOLING WATER FLOW (LB/HR)	TEMP DIFF (DEG F)
	PWI	PWO	T1	T2	T3	T6	TA	CW	CWDT
14	16.2	16.2	113.0	92.5	212.0	98.5	80.	360.0	11.0
17	16.2	16.1	139.0	139.0	212.0	122.0	80.	360.0	16.2
22	16.2	16.1	157.5	153.0	212.0	128.0	85.	365.0	17.8
32	16.2	16.1	158.0	153.0	212.0	128.0	85.	360.0	19.4
50	16.2	15.5	167.0	174.0	212.0	126.0	90.	360.0	21.0
70	16.2	15.0	169.0	175.0	212.0	125.0	95.	365.0	20.8
100	16.2	15.0	167.5	175.0	212.0	125.0	100.	365.0	21.3

RESULTS

TEST TIME	HEAT LOSSES (BTU/HR)				FIRE HEAT ABSORBED THROUGH TEST SURFACE	
	OUTLET LINE	LEAD TUBE	CYLINDER ENDS	CYLINDER CONTENTS	(BTU/HR)	(BTU/HR-SQFT)
14	297.0	1359.8	-590.0	0.0	4791.9	5445.3
17	297.0	373.2	-590.0	0.1	5645.8	6415.7
22	285.8	466.0	-590.0	0.1	6189.3	7033.3
32	285.8	484.3	-590.0	0.1	6686.5	7598.3
50	274.5	-61.4	-590.0	0.4	6579.5	7476.7
70	263.3	-30.0	-590.0	0.7	6627.5	7531.3
100	252.0	-84.8	-590.0	0.7	6768.3	7691.2

TABLE D-5 (continued)

TEST NUMBER - 61
FUEL - METHANOL
BURNER - 18 INCH DIAMETER, SINGLE
CYLINDER - STAINLESS STEEL

DATA

TEST TIME (MIN)	PRIMARY WATER FLOWS (LB/HR)		PRIMARY WATER TEMPERATURES (DEG F)				AIR TEMP (DEG F)	COOLING WATER FLOW (LB/HR)	COOLING WATER TEMP DIFF (DEG F)
	PWI	PWO	T1	T2	T3	T6	TA	CW	CWDT
22	9.5	9.5	145.0	125.0	212.0	104.0	80.	347.0	14.5
26	3.5	3.5	160.0	154.0	212.0	104.0	80.	347.0	16.2
40	6.7	6.7	190.0	202.0	212.0	101.5	85.	347.0	17.3
52	6.7	6.7	144.0	166.0	212.0	103.0	85.	347.0	17.3
72	6.7	6.7	185.0	180.0	212.0	101.0	85.	347.0	17.0

RESULTS

TEST TIME	HEAT LOSSES (BTU/HR)				PIPE HEAT ABSORBED THROUGH TEST SURFACE	
	OUTLET LINE	LEAD TUBE	CYLINDER ENDS	CONTENTS	(BTU/HR)	(BTU/HR-SQFT)
22	297.0	852.1	-380.0	0.0	5515.1	6767.2
26	297.0	331.8	-380.0	0.0	5674.2	6448.0
40	285.8	-112.2	-380.0	0.0	5203.7	5913.3
52	285.8	-64.2	-380.0	0.0	5569.9	6329.4
72	285.8	231.6	-380.0	0.0	5473.6	6220.0

TABLE D-5 (continued)

TEST NUMBER - 37
FUEL - METHANOL
BURNER - 24 INCH DIAMETER, SINGLE
CYLINDER - BRASS

DATA

TEST TIME (MIN)	PRIMARY WATER FLOWS (LB/HR)		PRIMARY WATER TEMPERATURES (DEG F)				AIR TEMP (DEG F)	COOLING WATER FLOW (LB/HR)	TEMP DIFF (DEG F)
	PWI	PWO	T1	T2	T3	T6	TA	CW	CWDT
25	31.0	31.0	169.0	174.5	212.0	117.0	110.	349.0	30.2
33	31.0	31.0	169.5	176.0	212.0	116.0	110.	345.0	30.2
47	31.0	31.0	170.0	177.0	212.0	116.0	110.	345.0	31.0

RESULTS

TEST TIME	HEAT LOSSES (BTU/HR)				FIRE HEAT ABSORBED THROUGH TEST SURFACE	
	OUTLET LINE	LEAD TUBE	CYLINDER ENDS	CONTENTS	(BTU/HR)	(BTU/HR-SQFT)
25	229.5	-205.6	-590.0	0.0	8361.7	9501.9
33	229.5	-285.5	-590.0	0.0	8114.5	9221.0
47	229.5	-326.7	-590.0	0.0	8333.8	9470.2

TABLE D-5 (continued)

TEST NUMBER - 38
FUEL - METHANOL
BURNER - 24 INCH DIAMETER, SINGLE
CYLINDER - BRASS

DATA

TEST TIME (MIN)	PRIMARY WATER FLOWS (LB/HR)		PRIMARY WATER TEMPERATURES (DEG F)				AIR TEMP (DEG F)	COOLING WATER FLOW (LB/HR)	TEMP DIFF (DEG F)
	PWI	PWO	T1	T2	T3	T6	TA	CW	CWDT
79	28.5	28.0	175.5	182.0	212.0	122.0	120.	345.0	29.0
102	28.5	28.5	177.5	183.0	212.0	122.5	120.	345.0	28.8

RESULTS

TEST TIME	HEAT LOSSES (BTU/HR)				FIRE HEAT ABSORBED THROUGH TEST SURFACE	
	OUTLET LINE	LEAD TUBE	CYLINDER ENDS	CONTENTS	(BTU/HR)	(BTU/HR-SQFT)
79	207.0	-277.0	-590.0	0.3	7865.6	8938.2
102	207.0	-215.9	-590.0	0.0	7769.6	8829.1

TABLE D-5 (continued)

TEST NUMBER - 40
FUEL - METHANOL
BURNER - 24 INCH DIAMETER, SINGLE
CYLINDER - BRASS

DATA

TEST TIME (MIN)	PRIMARY WATER FLOWS (LB/HR)		PRIMARY WATER TEMPERATURES (DEG F)				AIR TEMP (DEG F)	COOLING WATER FLOW (LB/HR)	TEMP DIFF (DEG F)
	PWI	PWO	T1	T2	T3	T6	TA	CW	CWDT
17	26.5	26.5	147.5	141.0	212.0	121.0	100.	362.0	16.3
33	21.7	21.0	187.0	195.0	212.0	128.0	110.	367.0	26.6
59	21.7	20.9	189.0	196.0	212.0	126.0	113.	367.0	27.0
80	21.7	20.8	190.0	198.0	212.0	128.0	115.	365.0	27.0
100	21.7	20.3	194.0	202.0	212.0	129.0	115.	365.0	27.5

RESULTS

TEST TIME	HEAT LOSSES (BTU/HR)				FIRE HEAT ABSORBED THROUGH TEST SURFACE	
	OUTLET LINE	LEAD TUBE	CYLINDER ENDS	CONTENTS	(BTU/HR)	(BTU/HR-SQFT)
17	252.0	761.9	-590.0	0.0	5622.3	6389.0
33	229.5	-311.5	-590.0	0.4	7869.1	8942.2
59	222.8	-266.8	-590.0	0.5	8018.9	9112.4
80	218.3	-326.8	-590.0	0.5	7887.2	8962.7
100	218.3	-347.3	-590.0	0.8	8025.0	9119.3

TABLE D-5 (continued)

TEST NUMBER - 48
FUEL - METHANOL
BURNER - 24 INCH DIAMETER, SINGLE
CYLINDER - STAINLESS STEEL

DATA

TEST TIME (MIN)	PRIMARY WATER FLOWS (LB/HR)		PRIMARY WATER TEMPERATURES (DEG F)				AIR TEMP (DEG F)	COOLING WATER FLOW (LB/HR)	TEMP DIFF (DEG F)
	PWI	PWO	T1	T2	T3	T6	TA	CW	CWDT
12	21.8	21.8	145.0	141.0	212.0	120.0	80.	363.0	16.5
15	18.5	19.8	158.0	155.0	212.0	128.0	80.	363.0	21.0
20	18.5	19.0	169.5	170.5	212.0	129.0	90.	363.0	23.5
26	18.5	18.7	172.0	176.0	212.0	130.0	90.	363.0	23.0
45	18.5	18.7	177.0	183.5	212.0	130.0	100.	365.0	24.5
59	18.5	18.5	176.0	182.0	212.0	129.0	110.	365.0	24.2

RESULTS

TEST TIME	HEAT LOSSES (BTU/HR)				FIRE HEAT ABSORBED THROUGH TEST SURFACE	
	OUTLET LINE	LEAD TUBE	CYLINDER ENDS	CYLINDER CONTENTS	(BTU/HR)	(BTU/HR-SQFT)
12	297.0	563.1	-380.0	0.0	5924.6	6732.5
15	297.0	417.6	-380.0	-0.8	7292.6	8287.1
20	274.5	170.1	-380.0	-0.3	7804.0	8868.2
26	274.5	15.7	-380.0	-0.1	7465.7	8483.7
45	252.0	-127.8	-380.0	-0.1	7800.7	8864.4
59	229.5	-99.1	-380.0	0.0	7713.9	8765.8

TABLE D-6

TOTAL HEAT TRANSFER DATA AND CALCULATED RESULTS FROM ACETONE FIRES

TEST NUMBER - 52
FUEL - ACETONE
BURNER - 6 INCH DIAMETER, CLUSTER
CYLINDER - STAINLESS STEEL

DATA

TEST TIME (MIN)	PRIMARY WATER FLOWS (LB/HR)		PRIMARY WATER TEMPERATURES (DEG F)				AIR TEMP (DEG F)	COOLING WATER FLOW (LB/HR)	TEMP DIFF (DEG F)
	PWI	PWO	T1	T2	T3	T6	TA	CW	CWDT
11	24.2	24.2	155.0	85.0	212.0	90.5	85.	360.0	13.0
15	26.3	24.8	203.0	203.0	212.0	117.0	90.	360.0	33.0
18	26.3	24.8	151.0	169.0	212.0	124.0	90.	360.0	33.2
24	28.7	28.7	152.0	155.0	212.0	174.0	110.	360.0	32.5
31	35.7	34.4	138.0	144.0	212.0	119.0	110.	360.0	32.7
38	35.7	34.4	149.0	155.0	212.0	119.0	110.	360.0	31.7
48	35.7	35.5	152.0	158.0	212.0	120.0	115.	360.0	31.5
75	35.7	35.5	155.0	157.0	212.0	121.0	120.	360.0	31.0

RESULTS

TEST TIME	HEAT LOSSES (BTU/HR)				FIRE HEAT ABSORBED THROUGH TEST SURFACE	
	OUTLET LINE	LEAD TUBE	CYLINDER ENDS	CONTENTS	(BTU/HR)	(BTU/HR-SQFT)
11	285.8	4557.4	-380.0	0.0	7582.3	8616.2
15	274.5	46.0	-380.0	0.9	9702.1	11025.1
18	274.5	-876.3	-380.0	0.9	10393.0	11810.2
24	229.5	91.3	-380.0	0.0	12272.2	13945.7
31	229.5	-153.8	-380.0	0.8	10911.0	12398.9
38	229.5	-210.1	-380.0	0.8	10102.1	11479.7
48	218.3	-225.4	-380.0	0.1	9829.0	11169.3
75	207.0	114.0	-380.0	0.1	9905.5	11256.3

TABLE D-6 (cOntinued)

TEST NUMBER - 53
FUEL - ACETONE
BURNER - 6 INCH DIAMETER, CLUSTER
CYLINDER - STAINLESS STEEL

DATA

TEST TIME (MIN)	PRIMARY WATER FLOWS (LB/HR)		PRIMARY WATER TEMPERATURES (DEG F)				AIR TEMP (DEG F)	COOLING WATER FLOW (LB/HR)	TEMP DIFF (DEG F)
	PWI	PWO	T1	T2	T3	T6	TA	CW	CWDT
7	31.0	31.0	120.0	124.0	212.0	114.5	85.	358.0	15.5
13	31.0	30.7	140.0	144.0	212.0	121.0	90.	358.0	31.8
19	35.7	34.9	152.0	156.0	212.0	123.0	100.	358.0	33.0
26	35.7	35.5	154.0	159.5	212.0	125.0	125.	358.0	34.2
54	35.7	35.7	157.0	163.5	212.0	124.0	130.	358.0	34.0
70	40.2	40.2	149.0	155.0	212.0	130.0	130.	358.0	31.9
79	40.2	40.2	149.5	155.5	212.0	132.0	135.	358.0	33.5

RESULTS

TEST TIME	HEAT LOSSES (BTU/HR)				FIRE HEAT ABSORBED THROUGH TEST SURFACE	
	OUTLET LINE	LEAD TUBE	CYLINDER ENDS	CONTENTS	(BTU/HR)	(BTU/HR-SQFT)
7	285.8	160.9	-380.0	0.0	5445.2	6187.7
13	274.5	58.7	-380.0	0.2	10776.1	12245.5
19	252.0	-48.0	-380.0	0.5	10674.4	12129.9
26	195.8	-191.3	-380.0	0.1	10850.3	12329.9
54	184.5	-295.3	-380.0	0.0	10503.1	11935.3
70	184.5	-275.2	-380.0	0.0	10185.7	11574.6
79	173.3	-277.8	-380.0	0.0	10805.0	12278.4

TABLE D-6 (continued)

TEST NUMBER - 57
FUEL - ACETONE
BURNER - 6 INCH DIAMETER, CLUSTER
CYLINDER - STAINLESS STEEL

DATA

TEST TIME (MIN)	PRIMARY WATER FLOWS (LB/HR)		PRIMARY WATER TEMPERATURES (DEG F)				AIR TEMP (DEG F)	COOLING WATER FLOW (LB/HR)	TEMP DIFF (DEG F)
	PWI	PWO	T1	T2	T3	T6	TA	CW	CWDT
15	35.7	35.7	132.0	137.5	212.0	109.5	85.	467.0	19.4
23	35.7	35.7	127.0	132.0	212.0	107.5	90.	467.0	20.0
33	35.7	35.7	126.0	131.0	212.0	109.0	100.	467.0	20.5
60	35.7	35.7	126.0	132.0	212.0	106.0	110.	467.0	19.9
73	21.8	21.8	157.0	164.0	212.0	118.0	120.	462.0	19.4
82	21.8	21.8	160.5	169.0	212.0	120.5	130.	464.0	19.7

RESULTS

TEST TIME	HEAT LOSSES (BTU/HR)				FIRE HEAT ABSORBED THROUGH TEST SURFACE	
	OUTLET LINE	LEAD TUBE	CYLINDER ENDS	CONTENTS	(BTU/HR)	(BTU/HR-SQFT)
15	285.8	-78.8	-380.0	0.0	8083.5	9185.8
23	274.5	-8.9	-380.0	0.0	8529.4	9692.5
33	252.0	-3.8	-380.0	0.0	8834.8	10039.5
60	229.5	-92.5	-380.0	0.0	8336.3	9473.1
73	207.0	-104.9	-380.0	0.0	7834.7	8903.1
82	184.5	-205.5	-380.0	0.0	7867.8	8940.6

TABLE D-6 (continued)

TEST NUMBER - 16
FUEL - ACETONE
BURNER - 12 INCH DIAMETER, SINGLE
CYLINDER - BRASS

DATA

TEST TIME (MIN)	PRIMARY WATER FLOWS (LB/HR)		PRIMARY WATER TEMPERATURES (DEG F)				AIR TEMP (DEG F)	COOLING WATER FLOW (LB/HR)	TEMP DIFF (DEG F)
	PWI	PWO	T1	T2	T3	T6	TA	CW	CWDT
37	12.0	12.0	200.0	196.5	212.0	126.0	100.	240.0	33.5
51	17.7	17.7	199.0	201.0	212.0	126.0	100.	240.0	32.8
64	17.0	17.0	200.0	202.5	212.0	126.0	100.	240.0	31.5
79	9.8	9.8	198.0	201.0	212.0	117.5	100.	240.0	25.8
85	9.8	9.8	198.0	201.0	212.0	117.0	100.	240.0	25.2
107	15.1	15.1	201.0	203.0	212.0	126.0	100.	240.0	28.4
118	15.1	15.1	202.0	204.0	212.0	126.0	100.	239.0	27.8
121	15.1	15.1	191.0	198.0	212.0	126.0	100.	239.0	26.6

RESULTS

TEST TIME	HEAT LOSSES (BTU/HR)				FIRE HEAT ABSORBED THROUGH TEST SURFACE	
	OUTLET LINE	LEAD TUBE	CYLINDER ENDS	CONTENTS	(BTU/HR)	(BTU/HR-SQFT)
37	252.0	171.6	-590.0	0.0	6985.6	7938.2
51	252.0	-24.1	-590.0	0.0	6217.8	7065.7
64	252.0	-47.6	-590.0	0.0	5916.4	6723.2
79	252.0	-7.0	-590.0	0.0	5058.1	5747.8
85	252.0	-7.0	-590.0	0.0	4909.2	5578.6
107	252.0	-21.7	-590.0	0.0	5323.8	6049.7
118	252.0	-26.9	-590.0	0.0	5131.7	5831.5
121	252.0	-165.6	-590.0	0.0	4872.3	5536.7

TABLE D-6 (continued)

TEST NUMBER - 50
FUEL - ACETONE
BURNER - 12 INCH DIAMETER, SINGLE
CYLINDER - STAINLESS STEEL

DATA

TEST TIME (MIN)	PRIMARY WATER FLOWS (LB/HR)		PRIMARY WATER TEMPERATURES (DEG F)				AIR TEMP (DEG F)	COOLING WATER FLOW (LB/HR)	TEMP DIFF (DEG F)
	PWI	PWO	T1	T2	T3	T6	TA	CW	CWDT
9	16.5	16.5	97.0	75.0	212.0	86.0	80.	364.0	8.0
14	16.5	16.5	151.0	135.0	212.0	112.0	80.	368.0	18.8
20	16.5	16.5	173.0	173.0	212.0	125.0	85.	368.0	22.0
28	16.5	15.7	179.0	182.0	212.0	125.0	85.	368.0	22.5
38	16.5	16.5	181.0	185.5	212.0	125.5	85.	368.0	22.0
60	18.5	18.5	170.0	177.0	212.0	129.0	85.	374.0	19.5
120	18.5	18.5	173.0	180.0	212.0	126.0	90.	374.0	16.2
185	18.5	18.5	172.0	180.0	212.0	125.5	95.	373.0	14.0

RESULTS

TEST TIME	HEAT LOSSES (BTU/HR)				FIRE HEAT ABSORBED THROUGH TEST SURFACE	
	OUTLET LINE	LEAD TUBE	CYLINDER ENDS	CONTENTS	(BTU/HR)	(BTU/HR-SQFT)
9	297.0	1519.9	-380.0	0.0	4167.4	4735.7
14	297.0	989.7	-380.0	0.0	7181.6	8160.9
20	285.8	199.4	-380.0	0.0	7409.1	8419.5
28	285.8	41.6	-380.0	0.5	7406.4	8416.4
38	285.8	-32.2	-380.0	0.0	7053.8	8015.7
60	285.8	-115.6	-380.0	0.0	6324.6	7187.1
120	274.5	-131.0	-380.0	0.0	4952.8	5628.2
185	263.3	-173.0	-380.0	0.0	4072.0	4627.2

TABLE D-6 (continued)

TEST NUMBER - 63
FUEL - ACETONE
BURNER - 18 INCH DIAMETER, SINGLE
CYLINDER - STAINLESS STEEL

DATA

TEST TIME (MIN)	PRIMARY WATER FLOWS (LB/HR)		PRIMARY WATER TEMPERATURES (DEG F)				AIR TEMP (DEG F)	COOLING WATER FLOW (LB/HR)	TEMP DIFF (DEG F)
	PWI	PWO	T1	T2	T3	T6	TA	CW	CWDT
10	21.8	21.8	112.0	109.5	212.0	104.0	80.	467.0	17.5
22	31.0	31.0	133.5	139.0	212.0	117.0	90.	467.0	21.5
32	31.0	30.0	136.5	144.0	212.0	110.5	100.	467.0	21.5
48	31.0	31.0	139.0	147.0	212.0	112.0	100.	467.0	20.0
71	31.0	31.0	140.0	149.5	212.0	110.5	100.	467.0	18.8
81	17.2	17.2	133.0	150.0	212.0	116.0	100.	467.0	16.5
94	17.2	17.2	139.0	155.0	212.0	118.0	100.	467.0	16.0
104	17.2	17.2	140.0	157.0	212.0	116.5	100.	467.0	15.2

RESULTS

TEST TIME	HEAT LOSSES (BTU/HR)				FIRE HEAT ABSORBED THROUGH TEST SURFACE	
	OUTLET LINE	LEAD TUBE	CYLINDER ENDS	CONTENTS	(BTU/HR)	(BTU/HR-SQFT)
10	297.0	649.1	-380.0	0.0	8564.2	9732.0
22	274.5	-24.1	-380.0	0.0	9399.4	10681.1
32	252.0	-194.2	-380.0	0.6	9014.5	10243.7
48	252.0	-245.6	-380.0	0.0	8129.4	9237.9
71	252.0	-366.7	-380.0	0.0	7370.3	8375.4
81	252.0	-345.1	-380.0	0.0	6940.0	7886.4
94	252.0	-331.7	-380.0	0.0	6651.1	7558.1
104	252.0	-380.8	-380.0	0.0	6185.3	7028.8

TABLE D-6 (continued)

TEST NUMBER - 32
FUEL - ACETONE
BURNER - 24 INCH DIAMETER, SINGLE
CYLINDER - BRASS

DATA

TEST TIME (MIN)	PRIMARY WATER FLOWS (LB/HR)		PRIMARY WATER TEMPERATURES (DEG F)				AIR TEMP (DEG F)	COOLING WATER FLOW (LB/HR)	TEMP DIFF (DEG F)
	PWI	PWO	T1	T2	T3	T6	TA	CW	CWDT
18	40.2	40.2	160.0	170.0	212.0	130.0	110.	356.0	41.5
22	44.8	44.8	168.0	173.0	212.0	135.0	115.	356.0	38.2
33	44.8	44.8	169.0	173.0	212.0	134.0	120.	356.0	36.7
48	44.8	44.8	173.0	179.0	212.0	131.0	130.	355.0	35.0
56	44.8	44.8	172.0	178.0	212.0	130.0	130.	355.0	34.3
63	44.8	44.8	172.0	179.0	212.0	128.0	130.	355.0	33.5

RESULTS

TEST TIME	HEAT LOSSES (BTU/HR) OUTLET LINE	LEAD TUBE	CYLINDER ENDS	CONTENTS	FIRE HEAT ABSORBED THROUGH TEST SURFACE (BTU/HR)	(BTU/HR-SQFT)
18	229.5	-729.6	-590.0	0.0	12477.9	14179.4
22	218.3	-328.3	-590.0	0.0	11420.8	12978.1
33	207.0	-222.8	-590.0	0.0	10891.4	12376.6
48	184.5	-464.5	-590.0	0.0	9673.4	10992.5
56	184.5	-459.4	-590.0	0.0	9430.0	10715.9
63	184.5	-570.0	-590.0	0.0	8945.8	10165.6

TABLE D-6 (continued)

TEST NUMBER - 34
FUEL - ACETONE
BURNER - 24 INCH DIAMETER, SINGLE
CYLINDER - BRASS

DATA

TEST TIME (MIN)	PRIMARY WATER FLOWS (LB/HR)		PRIMARY WATER TEMPERATURES (DEG F)				AIR TEMP (DEG F)	COOLING WATER FLOW (LB/HR)	TEMP DIFF (DEG F)
	PWI	PWO	T1	T2	T3	T6	TA	CW	CWDT
18	47.5	47.5	158.0	163.0	212.0	132.0	110.	356.0	36.5
33	47.0	47.0	161.0	165.0	212.0	129.0	115.	356.0	35.5
39	47.0	47.0	162.0	167.0	212.0	128.0	120.	356.0	34.5
50	47.0	47.0	180.0	185.0	212.0	132.0	120.	356.0	34.0
67	40.3	40.3	157.5	166.0	212.0	126.0	125.	350.0	29.5
72	40.3	40.3	157.0	165.0	212.0	125.0	130.	350.0	29.1
86	40.3	40.3	157.0	167.5	212.0	125.0	130.	350.0	28.2
109	35.6	35.6	194.5	202.0	212.0	120.0	130.	350.0	30.5
125	35.6	35.6	195.0	203.0	212.0	120.0	130.	350.0	29.8
131	35.6	35.6	195.0	214.5	212.0	120.0	130.	350.0	29.5

RESULTS

TEST TIME	HEAT LOSSES (BTU/HR)				FIRE HEAT ABSORBED THROUGH TEST SURFACE	
	OUTLET LINE	LEAD TUBE	CYLINDER ENDS	CONTENTS	(BTU/HR)	(BTU/HR-SQFT)
18	229.5	-309.7	-590.0	0.0	11088.8	12600.9
33	218.3	-203.1	-590.0	0.0	10559.2	11999.0
39	207.0	-324.2	-590.0	0.0	9976.8	11337.3
50	207.0	-416.2	-590.0	0.0	9048.8	10282.8
67	195.8	-569.6	-590.0	0.0	8091.7	9195.1
72	184.5	-517.1	-590.0	0.0	7972.8	9059.9
86	184.5	-766.6	-590.0	0.0	7408.3	8418.5
109	184.5	-573.9	-590.0	0.0	7043.4	8003.9
125	184.5	-620.7	-590.0	0.0	6733.8	7652.1
131	184.5	-1637.8	-590.0	0.0	5611.7	6376.9

TABLE D-6 (continued)

TEST NUMBER - 39
FUEL - ACETONE
BURNER - 24 INCH DIAMETER, SINGLE
CYLINDER - BRASS

DATA

TEST TIME (MIN)	PRIMARY WATER FLOWS (LB/HR)		PRIMARY WATER TEMPERATURES (DEG F)				AIR TEMP (DEG F)	COOLING WATER FLOW (LB/HR)	TEMP DIFF (DEG F)
	PWI	PWO	T1	T2	T3	T6	TA	CW	CWDT
12	40.2	40.2	131.0	132.0	212.0	114.0	90.	358.0	20.3
16	35.6	34.9	134.0	140.0	212.0	125.0	90.	358.0	35.8
30	35.6	35.4	158.0	164.0	212.0	126.0	90.	358.0	35.8
51	38.0	37.6	157.0	164.0	212.0	130.0	100.	358.0	34.2
81	35.7	36.0	164.0	174.0	212.0	125.0	120.	348.0	30.7
107	35.7	35.7	166.0	178.0	212.0	122.0	145.	348.0	29.3
122	34.3	34.4	171.0	184.0	212.0	119.0	150.	348.0	29.2

RESULTS

TEST TIME	HEAT LOSSES (BTU/HR)				FIRE HEAT ABSORBED THROUGH TEST SURFACE	
	OUTLET LINE	LEAD TUBE	CYLINDER ENDS	CONTENTS	(BTU/HR)	(BTU/HR-SQFT)
12	274.5	314.5	-590.0	0.0	6583.0	7480.7
16	274.5	-131.9	-590.0	0.4	12109.9	13761.2
30	274.5	-254.6	-590.0	0.1	11124.4	12641.3
51	252.0	-378.5	-590.0	0.2	10534.1	11970.6
81	207.0	-641.5	-590.0	-0.2	8240.5	9364.2
107	150.8	-829.1	-590.0	0.0	7357.2	8360.5
122	139.5	-899.4	-590.0	-0.1	7018.7	7975.8

TABLE D-6 (continued)

TEST NUMBER - 49
FUEL - ACETONE
BURNER - 24 INCH DIAMETER, SINGLE
CYLINDER - STAINLESS STEEL

DATA

TEST TIME (MIN)	PRIMARY WATER FLOWS (LB/HR)		PRIMARY WATER TEMPERATURES (DEG F)				AIR TEMP (DEG F)	COOLING WATER FLOW (LB/HR)	COOLING WATER TEMP DIFF (DEG F)
	PWI	PWO	T1	T2	T3	T6	TA	CW	CWDT
5	35.5	35.5	129.0	132.0	212.0	130.5	120.	365.0	28.1
20	35.5	35.0	139.0	146.0	212.0	126.0	120.	365.0	33.5
30	35.5	35.5	170.0	177.0	212.0	127.5	130.	365.0	35.0
38	35.5	35.2	172.0	179.0	212.0	127.0	130.	365.0	33.2
60	35.5	34.5	175.0	182.5	212.0	129.0	136.	365.0	32.0

RESULTS

TEST TIME	HEAT LOSSES (BTU/HR)				FIRE HEAT ABSORBED THROUGH TEST SURFACE	
	OUTLET LINE	LEAD TUBE	CYLINDER ENDS	CONTENTS	(BTU/HR)	(BTU/HR-SQFT)
5	207.0	159.7	-380.0	0.0	10296.4	11700.5
20	207.0	-244.3	-380.0	0.3	11392.0	12945.5
30	184.5	-402.7	-380.0	0.0	10668.0	12122.7
38	184.5	-413.0	-380.0	0.2	9937.7	11292.9
60	171.0	-472.4	-380.0	0.6	9449.2	10737.7

TABLE D-7

TOTAL HEAT TRANSFER DATA AND CALCULATED RESULTS FOR HEXANE FIRES

TEST NUMBER - 54
FUEL - HEXANE
BURNER - 6 INCH DIAMETER, CLUSTER
CYLINDER - STAINLESS STEEL

DATA

TEST TIME (MIN)	PRIMARY WATER FLOWS (LB/HR)		PRIMARY WATER TEMPERATURES (DEG F)				AIR TEMP (DEG F)	COOLING WATER FLOW (LB/HR)	TEMP DIFF (DEG F)
	PWI	PWO	T1	T2	T3	T6	TA	CW	CWDT
5	63.0	63.0	148.0	152.5	212.0	127.0	145.	360.0	54.8
9	63.0	63.0	130.0	134.0	212.0	126.0	150.	698.0	32.0
14	63.0	63.0	133.5	136.0	212.0	125.0	155.	698.0	29.5
16	63.0	63.0	134.0	137.5	212.0	124.0	165.	698.0	28.8
21	63.0	63.0	136.0	140.0	212.0	122.5	175.	698.0	26.5
27	63.0	63.0	138.0	142.0	212.0	121.5	185.	698.0	24.1
33	63.0	63.0	139.0	143.5	212.0	120.0	195.	698.0	22.5

RESULTS

TEST TIME	HEAT LOSSES (BTU/HR)				FIRE HEAT ABSORBED THROUGH TEST SURFACE	
	OUTLET LINE	LEAD TUBE	CYLINDER ENDS	CONTENTS	(BTU/HR)	(BTU/HR-SQFT)
5	150.8	-368.3	-380.0	0.0	17807.4	20235.7
9	139.5	-199.0	-380.0	0.0	21644.5	24596.0
14	128.3	14.9	-380.0	0.0	19818.7	22521.2
16	105.8	-142.2	-380.0	0.0	19055.9	21654.5
21	83.3	-229.7	-380.0	0.0	17120.1	19454.6
27	60.8	-239.9	-380.0	0.0	15223.1	17299.0
33	38.3	-322.3	-380.0	0.0	13843.9	15731.7

TABLE D-7 (continued)

TEST NUMBER - 13
FUEL - HEXANE
BURNER - 12 INCH DIAMETER, SINGLE
CYLINDER - STAINLESS STEEL

DATA

TEST TIME (MIN)	PRIMARY WATER FLOWS (LB/HR)		PRIMARY WATER TEMPERATURES (DEG F)				AIR TEMP (DEG F)	COOLING WATER FLOW (LB/HR)	TEMP DIFF (DEG F)
	PWI	PWO	T1	T2	T3	T6	TA	CW	CWDT
20	16.3	15.7	154.0	156.5	204.0	121.0	100.	215.0	38.2
28	16.3	15.7	159.0	164.0	203.0	120.0	105.	215.0	36.2
63	7.8	9.1	147.0	150.0	203.0	107.0	110.	215.0	26.8
76	7.8	9.1	187.0	192.0	200.0	102.0	110.	215.0	26.8
98	5.6	6.1	141.0	152.0	191.0	89.0	120.	215.0	22.5
104	5.6	6.1	154.5	164.0	191.0	89.0	120.	215.0	22.0

RESULTS

TEST TIME	HEAT LOSSES (BTU/HR)				FIRE HEAT ABSORBED THROUGH TEST SURFACE	
	OUTLET LINE	LEAD TUBE	CYLINDER ENDS	CONTENTS	(BTU/HR)	(BTU/HR-SQFT)
20	234.0	150.9	-380.0	0.4	7730.2	8784.3
28	220.5	15.5	-380.0	0.4	7053.5	8015.3
63	209.3	222.2	-380.0	-0.8	5375.8	6108.9
76	202.5	-40.4	-380.0	-0.8	4752.9	5401.0
98	159.8	78.9	-380.0	-0.3	4353.6	4947.3
104	159.8	34.0	-380.0	-0.3	4125.6	4688.2

TABLE D-7 (continued)

TEST NUMBER - 22
FUEL - HEXANE
BURNER - 12 INCH DIAMETER, SINGLE
CYLINDER - BRASS

DATA

TEST TIME (MIN)	PRIMARY WATER FLOWS (LB/HR)		PRIMARY WATER TEMPERATURES (DEG F)				AIR TEMP (DEG F)	COOLING WATER FLOW (LB/HR)	TEMP DIFF (DEG F)
	PWI	PWO	T1	T2	T3	T6	TA	CW	CWDT
30	13.8	13.5	166.0	177.0	212.0	117.0	130.	350.0	25.2

RESULTS

TEST TIME	HEAT LOSSES (BTU/HR)				FIRE HEAT ABSORBED THROUGH TEST SURFACE	
	OUTLET LINE	LEAD TUBE	CYLINDER ENDS	CONTENTS	(BTU/HR)	(BTU/HR-SQFT)
30	184.5	-159.2	-590.0	0.2	7607.8	8645.2

TABLE D-7 (continued)

TEST NUMBER - 41
FUEL - HEXANE
BURNER - 12 INCH DIAMETER, SINGLE
CYLINDER - BRASS

DATA

TEST TIME (MIN)	PRIMARY WATER FLOWS (LB/HR)		PRIMARY WATER TEMPERATURES (DEG F)				AIR TEMP (DEG F)	COOLING WATER FLOW (LB/HR)	TEMP DIFF (DEG F)
	PWI	PWO	T1	T2	T3	T6	TA	CW	CWDT
32	16.2	15.2	188.0	194.0	212.0	130.0	100.	352.0	30.5
49	16.2	15.2	195.0	204.0	212.0	130.0	105.	348.0	29.0
82	16.2	15.8	194.0	206.0	212.0	130.0	110.	345.0	26.5
111	17.2	16.4	167.0	188.0	212.0	130.0	110.	345.0	23.0
128	17.2	16.4	189.0	210.0	212.0	125.0	120.	345.0	22.1

RESULTS

TEST TIME	HEAT LOSSES (BTU/HR)				FIRE HEAT ABSORBED THROUGH TEST SURFACE	
	OUTLET LINE	LEAD TUBE	CYLINDER ENDS	CONTENTS	(BTU/HR)	(BTU/HR-SQFT)
32	252.0	-127.2	-590.0	0.6	9413.8	10697.5
49	240.8	-287.9	-590.0	0.6	8484.5	9641.5
82	229.5	-407.7	-590.0	0.2	7370.6	8375.6
111	229.5	-695.1	-590.0	0.5	6309.1	7169.4
128	207.0	-807.6	-590.0	0.5	5403.2	6140.0

TABLE D-7 (continued)

TEST NUMBER - 44
FUEL - HEXANE
BURNER - 12 INCH DIAMETER, SINGLE
CYLINDER - BRASS

DATA

TEST TIME (MIN)	PRIMARY WATER FLOWS (LB/HR)		PRIMARY WATER TEMPERATURES (DEG F)				AIR TEMP (DEG F)	COOLING WATER FLOW (LB/HR)	TEMP DIFF (DEG F)
	PWI	PWO	T1	T2	T3	T6	TA	CW	CWDT
3	38.0	38.0	110.0	116.5	212.0	115.0	100.	362.0	21.5
7	38.0	38.0	130.0	132.0	212.0	127.0	100.	362.0	35.0
10	35.6	36.2	133.0	138.0	212.0	129.0	100.	362.0	36.5
16	35.6	36.2	160.0	164.0	212.0	131.0	110.	362.0	36.8
25	35.6	35.1	168.0	175.0	212.0	130.0	130.	362.0	36.0
40	35.6	34.2	172.0	180.0	212.0	127.0	140.	362.0	32.8
60	35.6	35.6	174.0	182.0	212.0	124.0	150.	368.0	29.0
78	35.6	34.8	180.0	188.0	212.0	122.0	155.	368.0	29.0

RESULTS

TEST TIME	HEAT LOSSES (BTU/HR)				FIRE HEAT ABSORBED THROUGH TEST SURFACE	
	OUTLET LINE	LEAD TUBE	CYLINDER ENDS	CONTENTS	(BTU/HR)	(BTU/HR-SQFT)
3	252.0	-91.1	-590.0	0.0	7543.9	8572.6
7	252.0	230.7	-590.0	0.0	12448.7	14146.3
10	252.0	-38.4	-590.0	-0.4	12644.1	14368.2
16	229.5	-88.0	-590.0	-0.4	11791.8	13399.7
25	184.5	-394.2	-590.0	0.3	10920.8	12410.0
40	162.0	-503.1	-590.0	0.8	9460.3	10750.4
60	139.5	-513.3	-590.0	0.0	7928.2	9009.3
78	128.3	-544.0	-590.0	0.5	7673.9	8720.4

TABLE D-7 (continued)

TEST NUMBER - 67
FUEL - HEXANE
BURNER - 12 INCH DIAMETER, SINGLE
CYLINDER - STAINLESS STEEL

DATA

TEST TIME (MIN)	PRIMARY WATER FLOWS (LB/HR)		PRIMARY WATER TEMPERATURES (DEG F)				AIR TEMP (DEG F)	COOLING WATER FLOW (LB/HR)	TEMP DIFF (DEG F)
	PWI	PWO	T1	T2	T3	T6	TA	CW	CWDT
14	21.8	22.9	157.5	161.0	212.0	122.0	90.	350.0	30.0
32	26.5	24.1	150.0	164.0	212.0	127.5	95.	350.0	26.6
50	26.5	24.8	151.0	166.5	212.0	123.0	110.	350.0	24.6
75	26.5	24.8	153.0	170.0	212.0	122.5	120.	350.0	21.0
100	26.5	24.9	155.0	162.0	212.0	120.5	125.	350.0	18.8

RESULTS

TEST TIME	HEAT LOSSES (BTU/HR)				FIRE HEAT ABSORBED THROUGH TEST SURFACE	
	OUTLET LINE	LEAD TUBE	CYLINDER ENDS	CONTENTS	(BTU/HR)	(BTU/HR-SQFT)
14	274.5	85.6	-380.0	-0.7	9606.5	10916.5
32	263.3	-613.9	-380.0	1.5	8187.3	9303.8
50	229.5	-718.8	-380.0	1.0	7151.0	8126.2
75	207.0	-828.8	-380.0	1.0	5693.2	6469.5
100	195.8	-174.1	-380.0	1.0	5454.8	6198.6

TABLE D-7 (continued)

TEST NUMBER - 46
FUEL - HEXANE
BURNER - 18 INCH DIAMETER, SINGLE
CYLINDER - BRASS

DATA

TEST TIME (MIN)	PRIMARY WATER FLOWS (LB/HR) PWI	PWO	PRIMARY WATER TEMPERATURES (DEG F) T1	T2	T3	T6	AIR TEMP (DEG F) TA	COOLING WATER FLOW (LB/HR) CW	TEMP DIFF (DEG F) CWDT
3	35.7	35.7	97.5	135.0	212.0	113.5	140.	362.0	30.4
6	35.7	35.7	120.0	125.0	212.0	140.0	140.	362.0	43.8
9	35.7	36.7	132.0	136.0	212.0	143.0	140.	362.0	45.5
18	40.2	37.0	140.0	145.0	212.0	140.0	150.	362.0	41.0
24	40.2	37.5	143.0	150.0	212.0	140.0	180.	362.0	39.6
31	40.2	37.9	144.5	151.5	212.0	138.0	190.	362.0	37.5
52	40.2	39.4	151.0	160.0	212.0	135.0	205.	362.0	32.2

RESULTS

TEST TIME	HEAT LOSSES (BTU/HR) OUTLET LINE	LEAD TUBE	CYLINDER ENDS	CONTENTS	FIRE HEAT ABSORBED THROUGH TEST SURFACE (BTU/HR)	(BTU/HR-SQFT)
3	162.0	-2740.5	-590.0	0.0	8407.5	9554.0
6	162.0	26.9	-590.0	0.0	16168.5	18373.3
9	162.0	54.2	-590.0	-0.6	16420.3	18659.4
18	139.5	-129.7	-590.0	1.9	14494.2	16470.7
24	72.0	-344.1	-590.0	1.6	13548.5	15396.1
31	49.5	-351.8	-590.0	1.4	12593.0	14310.3
52	15.8	-584.1	-590.0	0.5	9917.0	11269.3

TABLE D-7 (continued)

TEST NUMBER - 62
FUEL - HEXANE
BURNER - 18 INCH DIAMETER, SINGLE
CYLINDER - STAINLESS STEEL

DATA

TEST TIME (MIN)	PRIMARY WATER FLOWS (LB/HR)		PRIMARY WATER TEMPERATURES (DEG F)				AIR TEMP (DEG F)	COOLING WATER FLOW (LB/HR)	TEMP DIFF (DEG F)
	PWI	PWO	T1	T2	T3	T6	TA	CW	CWDT
4	21.8	21.8	134.0	147.5	212.0	100.5	85.	474.0	16.9
13	21.8	21.8	129.0	131.0	212.0	135.5	95.	474.0	38.0
16	31.0	31.0	140.0	147.0	212.0	135.0	100.	474.0	38.5
34	31.0	31.0	150.0	161.0	212.0	115.0	110.	474.0	24.5

RESULTS

TEST TIME	HEAT LOSSES (BTU/HR)				FIRE HEAT ABSORBED THROUGH TEST SURFACE	
	OUTLET LINE	LEAD TUBE	CYLINDER ENDS	CONTENTS	(BTU/HR)	(BTU/HR-SQFT)
4	285.8	-345.8	-380.0	0.0	6840.2	7773.0
13	263.3	314.0	-380.0	0.0	18351.0	20853.4
16	252.0	-173.4	-380.0	0.0	17792.6	20218.9
34	229.5	-533.9	-380.0	0.0	9843.6	11185.9

TABLE D-7 (continued)

TEST NUMBER - 65
FUEL - HEXANE
BURNER - 18 INCH DIAMETER, SINGLE
CYLINDER - STAINLESS STEEL

DATA

TEST TIME (MIN)	PRIMARY WATER FLOWS (LB/HR)		PRIMARY WATER TEMPERATURES (DEG F)				AIR TEMP (DEG F)	COOLING WATER FLOW (LB/HR)	TEMP DIFF (DEG F)
	PWI	PWO	T1	T2	T3	T6	TA	CW	CWDT
5	21.8	21.8	126.0	125.0	212.0	110.0	100.	363.0	21.2
13	26.5	26.5	143.0	157.5	212.0	130.5	110.	474.0	33.5
25	30.5	31.0	144.0	155.0	212.0	120.0	150.	474.0	31.0

RESULTS

TEST TIME	HEAT LOSSES (BTU/HR)				FIRE HEAT ABSORBED THROUGH TEST SURFACE	
	OUTLET LINE	LEAD TUBE	CYLINDER ENDS	CONTENTS	(BTU/HR)	(BTU/HR-SQFT)
5	252.0	494.8	-380.0	0.0	7713.6	8765.4
13	229.5	-611.4	-380.0	0.0	14785.8	16802.1
25	139.5	-489.9	-380.0	-0.3	13185.2	14983.2

TABLE D-8

TOTAL HEAT TRANSFER DATA AND CALCULATED RESULTS FOR CYCLOHEXANE FIRES

TEST NUMBER - 55
FUEL - CYCLOHEXANE
BURNER - 6 INCH DIAMETER, CLUSTER
CYLINDER - STAINLESS STEEL

DATA

TEST TIME (MIN)	PRIMARY WATER FLOWS (LB/HR)		PRIMARY WATER TEMPERATURES (DEG F)				AIR TEMP (DEG F)	COOLING WATER FLOW (LB/HR)	TEMP DIFF (DEG F)
	PWI	PWO	T1	T2	T3	T6	TA	CW	CWDT
3	65.7	65.7	144.0	151.5	212.0	141.0	190.	358.0	55.4
5	65.7	65.7	143.5	148.0	212.0	137.0	190.	358.0	58.5
12	65.7	65.7	151.5	157.5	212.0	130.0	190.	579.0	33.5
19	65.7	65.7	148.0	153.0	212.0	126.0	190.	579.0	31.1
23	65.7	65.7	150.0	155.0	212.0	124.0	190.	579.0	30.0
29	65.7	65.7	151.0	157.0	212.0	122.0	190.	579.0	28.5

RESULTS

TEST TIME	HEAT LOSSES (BTU/HR)				FIRE HEAT ABSORBED THROUGH TEST SURFACE	
	OUTLET LINE	LEAD TUBE	CYLINDER ENDS	CONTENTS	(BTU/HR)	(BTU/HR-SQFT)
3	49.5	-860.4	-380.0	0.0	18445.2	20960.4
5	49.5	-374.6	-380.0	0.0	21124.3	24005.5
12	49.5	-657.1	-380.0	0.0	16996.3	19314.0
19	49.5	-478.2	-380.0	0.0	15752.3	17900.9
23	49.5	-488.4	-380.0	0.0	14842.9	16866.9
29	49.5	-654.6	-380.0	0.0	13611.1	15467.2

TABLE D-8 (continued)

TEST NUMBER - 58
FUEL - CYCLOHEXANE
BURNER - 6 INCH DIAMETER, CLUSTER
CYLINDER - STAINLESS STEEL

DATA

TEST TIME (MIN)	PRIMARY WATER FLOWS (LB/HR)		PRIMARY WATER TEMPERATURES (DEG F)				AIR TEMP (DEG F)	COOLING WATER FLOW (LB/HR)	TEMP DIFF (DEG F)
	PWI	PWO	T1	T2	T3	T6	TA	CW	CWDT
7	58.5	58.5	117.0	117.5	212.0	130.0	90.	470.0	40.0
14	58.5	58.5	137.0	140.0	212.0	127.0	100.	470.0	43.5
16	65.3	65.3	135.5	138.5	212.0	125.0	120.	470.0	39.7
22	65.3	65.3	138.5	143.0	212.0	121.0	130.	470.0	35.4

RESULTS

TEST TIME	HEAT LOSSES (BTU/HR)				FIRE HEAT ABSORBED THROUGH TEST SURFACE	
	OUTLET LINE	LEAD TUBE	CYLINDER ENDS	CONTENTS	(BTU/HR)	(BTU/HR-SQFT)
7	274.5	413.8	-380.0	0.0	19868.8	22578.2
14	252.0	-47.7	-380.0	0.0	19684.3	22368.5
16	207.0	-89.2	-380.0	0.0	17711.1	20126.3
22	184.5	-344.7	-380.0	0.0	14955.0	16994.3

TABLE D-8 (continued)

TEST NUMBER - 30
FUEL - CYCLOHEXANE
BURNER - 12 INCH DIAMETER, SINGLE
CYLINDER - BRASS

DATA

TEST TIME (MIN)	PRIMARY WATER FLOWS (LB/HR)		PRIMARY WATER TEMPERATURES (DEG F)				AIR TEMP (DEG F)	COOLING WATER FLOW (LB/HR)	TEMP DIFF (DEG F)
	PWI	PWO	T1	T2	T3	T6	TA	CW	CWDT
27	22.5	22.5	163.0	178.0	212.0	132.5	110.	365.0	31.8
35	22.5	22.5	164.0	176.0	212.0	131.0	115.	365.0	29.5
46	22.5	22.5	165.0	177.5	212.0	130.0	120.	365.0	27.8
54	22.5	22.5	169.0	182.0	212.0	127.5	125.	365.0	26.7
65	20.5	20.5	176.0	189.0	212.0	132.0	130.	365.0	26.3
75	20.5	20.5	181.0	195.0	212.0	138.0	130.	365.0	24.5

RESULTS

TEST TIME	HEAT LOSSES (BTU/HR)				FIRE HEAT ABSORBED THROUGH TEST SURFACE	
	OUTLET LINE	LEAD TUBE	CYLINDER ENDS	CONTENTS	(BTU/HR)	(BTU/HR-SQFT)
27	229.5	-602.1	-590.0	0.0	9958.1	11316.0
35	218.3	-436.7	-590.0	0.0	9216.5	10473.3
46	207.0	-470.2	-590.0	0.0	8506.2	9666.2
54	195.8	-519.1	-590.0	0.0	7898.4	8975.4
65	184.5	-492.2	-590.0	0.0	7799.8	8863.4
75	184.5	-569.8	-590.0	0.0	7085.7	8052.0

TABLE D-8 (continued)

TEST NUMBER - 42
FUEL - CYCLOHEXANE
BURNER - 12 INCH DIAMETER, SINGLE
CYLINDER - BRASS

DATA

TEST TIME (MIN)	PRIMARY WATER FLOWS (LB/HR)		PRIMARY WATER TEMPERATURES (DEG F)				AIR TEMP (DEG F)	COOLING WATER FLOW (LB/HR)	TEMP DIFF (DEG F)
	PWI	PWO	T1	T2	T3	T6	TA	CW	CWDT
18	40.2	37.3	132.0	141.0	212.0	133.0	130.	367.0	37.0
25	40.2	40.0	148.0	157.0	212.0	133.0	130.	367.0	34.6
35	38.0	38.5	155.0	165.0	212.0	129.0	135.	367.0	31.5
55	38.0	37.5	158.0	169.5	212.0	126.0	140.	367.0	28.0
84	38.0	38.0	158.0	171.0	212.0	123.0	170.	367.0	24.2

RESULTS

TEST TIME	HEAT LOSSES (BTU/HR)				FIRE HEAT ABSORBED THROUGH TEST SURFACE	
	OUTLET LINE	LEAD TUBE	CYLINDER ENDS	CYLINDER CONTENTS	(BTU/HR)	(BTU/HR-SQFT)
18	184.5	-486.9	-590.0	1.8	12957.6	14724.6
25	184.5	-568.7	-590.0	0.1	11136.9	12655.5
35	173.3	-651.0	-590.0	-0.3	9463.0	10753.4
55	162.0	-807.7	-590.0	0.3	7867.6	8940.5
84	94.5	-949.0	-590.0	0.0	6106.9	6939.6

TABLE D-8 (continued)

TEST NUMBER - 66
FUEL - CYCLOHEXANE
BURNER - 12 INCH DIAMETER, SINGLE
CYLINDER - STAINLESS STEEL

DATA

TEST TIME (MIN)	PRIMARY WATER FLOWS (LB/HR)		PRIMARY WATER TEMPERATURES (DEG F)				AIR TEMP (DEG F)	COOLING WATER FLOW (LB/HR)	TEMP DIFF (DEG F)
	PWI	PWO	T1	T2	T3	T6	TA	CW	CWDT
10	17.2	17.2	102.0	88.0	212.0	94.5	85.	353.0	17.5
20	19.5	18.1	152.0	158.0	212.0	125.5	90.	355.0	23.4
40	19.5	17.6	169.5	178.0	212.0	124.0	100.	355.0	21.7
74	19.5	17.4	163.0	185.5	212.0	124.0	110.	353.0	17.2
100	9.2	7.8	168.0	197.5	212.0	105.0	110.	353.0	14.8
120	9.2	7.8	164.5	194.0	212.0	105.5	115.	351.5	13.5

RESULTS

TEST TIME	HEAT LOSSES (BTU/HR)				FIRE HEAT ABSORBED THROUGH TEST SURFACE	
	OUTLET LINE	LEAD TUBE	CYLINDER ENDS	CONTENTS	(BTU/HR)	(BTU/HR-SQFT)
10	285.8	1179.1	-380.0	0.0	7133.4	8106.1
20	274.5	9.1	-380.0	0.8	7815.8	8881.6
40	252.0	-204.4	-380.0	1.2	6652.2	7559.4
74	229.5	-865.6	-380.0	1.3	4481.1	5092.1
100	229.5	-505.3	-380.0	0.8	4139.7	4704.2
120	218.3	-487.4	-380.0	0.8	3703.3	4208.3

TABLE D-8 (continued)

TEST NUMBER - 60
FUEL - CYCLOHEXANE
BURNER - 18 INCH DIAMETER, SINGLE
CYLINDER - STAINLESS STEEL

DATA

TEST TIME (MIN)	PRIMARY WATER FLOWS (LB/HR)		PRIMARY WATER TEMPERATURES (DEG F)				AIR TEMP (DEG F)	COOLING WATER FLOW (LB/HR)	COOLING WATER TEMP DIFF (DEG F)
	PWI	PWO	T1	T2	T3	T6	TA	CW	CWDT
13	35.7	35.7	141.0	145.0	212.0	117.5	95.	459.0	27.0
20	35.7	35.7	153.0	159.0	212.0	116.0	110.	457.0	28.8
26	35.7	35.7	157.0	163.0	212.0	117.0	120.	457.0	28.5

RESULTS

TEST TIME	HEAT LOSSES (BTU/HR) OUTLET LINE	LEAD TUBE	CYLINDER ENDS	CONTENTS	FIRE HEAT ABSORBED THROUGH TEST SURFACE (BTU/HR)	(BTU/HR-SQFT)
13	263.3	8.2	-380.0	0.0	11445.5	13006.3
20	229.5	-230.5	-380.0	0.0	11459.7	13022.4
26	207.0	-251.0	-380.0	0.0	11172.5	12696.1

TABLE D-9

TOTAL HEAT TRANSFER DATA AND CALCULATED RESULTS FOR JP-4 FIRES

TEST NUMBER - 56
FUEL - JP-4
BURNER - 6 INCH DIAMETER, CLUSTER
CYLINDER - STAINLESS STEEL

DATA

TEST TIME (MIN)	PRIMARY WATER FLOWS (LB/HR)		PRIMARY WATER TEMPERATURES (DEG F)				AIR TEMP (DEG F)	COOLING WATER FLOW (LB/HR)	TEMP DIFF (DEG F)
	PWI	PWO	T1	T2	T3	T6	TA	CW	CWDT
7	54.0	54.0	143.0	144.5	212.0	140.0	140.	474.0	37.0
9	54.0	54.0	146.0	148.0	212.0	144.5	140.	474.0	39.5
13	54.0	49.5	150.0	150.0	212.0	138.0	140.	474.0	45.5
15	54.0	54.0	155.0	160.0	212.0	135.0	140.	474.0	44.0
18	54.0	50.8	157.5	163.5	212.0	133.0	140.	474.0	39.2
25	54.0	54.0	160.5	167.0	212.0	129.5	140.	474.0	33.5
35	54.0	52.2	162.5	170.0	212.0	126.0	140.	472.0	28.5
40	54.0	54.0	163.0	171.5	212.0	124.0	140.	472.0	28.5
50	54.0	53.5	164.0	173.5	212.0	122.0	140.	472.0	26.0

RESULTS

TEST TIME	HEAT LOSSES (BTU/HR)				FIRE HEAT ABSORBED THROUGH TEST SURFACE	
	OUTLET LINE	LEAD TUBE	CYLINDER ENDS	CONTENTS	(BTU/HR)	(BTU/HR-SQFT)
7	162.0	153.5	-380.0	0.0	17311.5	19672.1
9	162.0	71.7	-380.0	0.0	18495.7	21017.9
13	162.0	317.0	-380.0	2.7	21353.7	24265.5
15	162.0	-372.8	-380.0	0.0	19185.2	21801.3
18	162.0	-518.4	-380.0	1.9	16776.1	19063.7
25	162.0	-600.2	-380.0	0.0	13386.8	15212.3
35	162.0	-743.3	-380.0	1.1	10675.6	12131.4
40	162.0	-878.7	-380.0	0.0	10249.3	11647.0
50	162.0	-1016.6	-380.0	0.3	8814.7	10016.7

TABLE D-9 (continued)

TEST NUMBER - 51
FUEL - JP-4
BURNER - 12 INCH DIAMETER, SINGLE
CYLINDER - STAINLESS STEEL

DATA

TEST TIME (MIN)	PRIMARY WATER FLOWS (LB/HR)		PRIMARY WATER TEMPERATURES (DEG F)				AIR TEMP (DEG F)	COOLING WATER FLOW (LB/HR)	TEMP DIFF (DEG F)
	PWI	PWO	T1	T2	T3	T6	TA	CW	CWDT
8	20.8	20.8	147.0	139.0	212.0	109.0	90.	378.0	15.3
14	20.8	20.8	162.0	167.0	212.0	124.5	100.	376.0	22.5
27	20.8	21.1	163.0	171.0	212.0	125.0	100.	376.0	23.4
45	20.8	20.8	165.5	175.0	212.0	126.0	110.	378.0	20.0
63	20.8	20.8	166.0	176.0	212.0	127.0	115.	378.0	19.0
86	20.8	20.8	168.0	179.0	212.0	128.0	115.	378.0	17.0
100	20.8	20.8	169.0	180.0	212.0	126.0	120.	378.0	16.2
120	20.8	20.8	169.0	181.0	212.0	127.0	125.	382.0	15.5
140	20.8	20.8	170.0	183.0	212.0	126.0	130.	382.0	14.9

RESULTS

TEST TIME	HEAT LOSSES (BTU/HR)				FIRE HEAT ABSORBED THROUGH TEST SURFACE	
	OUTLET LINE	LEAD TUBE	CYLINDER ENDS	CONTENTS	(BTU/HR)	(BTU/HR-SQFT)
8	274.5	754.2	-380.0	0.0	5641.7	6411.0
14	252.0	-8.1	-380.0	0.0	7543.9	8572.6
27	252.0	-171.4	-380.0	-0.2	7682.3	8729.9
45	229.5	-263.3	-380.0	0.0	6324.6	7187.0
63	218.3	-292.2	-380.0	0.0	5916.8	6723.6
86	218.3	-355.2	-380.0	0.0	5077.0	5769.4
100	207.0	-360.3	-380.0	0.0	4695.9	5336.2
120	195.8	-413.1	-380.0	0.0	4450.1	5056.9
140	184.5	-470.9	-380.0	0.0	4110.2	4670.7

TABLE D-9 (continued)

TEST NUMBER - 47
FUEL - JP-4
BURNER - 18 INCH DIAMETER, SINGLE
CYLINDER - STAINLESS STEEL

DATA

TEST TIME (MIN)	PRIMARY WATER FLOWS (LB/HR)		PRIMARY WATER TEMPERATURES (DEG F)				AIR TEMP (DEG F)	COOLING WATER FLOW (LB/HR)	TEMP DIFF (DEG F)
	PWI	PWO	T1	T2	T3	T6	TA	CW	CWDT
6	35.7	35.7	142.5	148.0	212.0	134.0	90.	362.0	34.0
7	35.7	38.0	140.0	145.0	212.0	149.0	90.	362.0	47.0
14	35.7	40.6	134.5	139.0	212.0	144.5	95.	367.0	44.3
22	40.5	42.0	137.0	144.0	212.0	135.0	110.	362.0	41.0
32	40.5	39.9	146.0	154.5	212.0	142.0	120.	362.0	40.7
46	42.5	43.0	146.0	155.0	212.0	134.0	120.	362.0	35.0

RESULTS

TEST TIME	HEAT LOSSES (BTU/HR) OUTLET LINE	LEAD TUBE	CYLINDER ENDS	CYLINDER CONTENTS	FIRE HEAT ABSORBED THROUGH TEST SURFACE (BTU/HR)	(BTU/HR-SQFT)
6	274.5	-132.5	-380.0	0.0	11766.6	13371.1
7	274.5	-75.4	-380.0	-1.4	17008.1	19327.4
14	263.3	-2.9	-380.0	-3.0	16161.7	18365.6
22	229.5	-318.5	-380.0	-0.9	14175.6	16108.6
32	207.0	-514.9	-380.0	0.4	13925.9	15824.8
46	207.0	-608.5	-380.0	-0.3	11339.2	12885.5

TABLE D-9 (continued)

TEST NUMBER - 64
FUEL - JP-4
BURNER - 18 INCH DIAMETER, SINGLE
CYLINDER - STAINLESS STEEL

DATA

TEST TIME (MIN)	PRIMARY WATER FLOWS (LB/HR)		PRIMARY WATER TEMPERATURES (DEG F)				AIR TEMP (DEG F)	COOLING WATER FLOW (LB/HR)	COOLING WATER TEMP DIFF (DEG F)
	PWI	PWO	T1	T2	T3	T6	TA	CW	CWDT
8	35.7	35.7	144.0	150.0	212.0	118.0	100.	474.0	19.5
13	26.5	26.5	139.0	144.0	212.0	122.5	110.	474.0	28.0
23	31.0	31.0	138.0	146.0	212.0	120.0	115.	474.0	25.2
32	31.0	30.9	139.0	149.0	212.0	113.0	120.	474.0	23.0
49	31.0	31.0	145.5	158.0	212.0	113.0	130.	472.0	22.8

RESULTS

TEST TIME	HEAT LOSSES (BTU/HR)				FIRE HEAT ABSORBED THROUGH TEST SURFACE	
	OUTLET LINE	LEAD TUBE	CYLINDER ENDS	CONTENTS	(BTU/HR)	(BTU/HR-SQFT)
8	252.0	-184.5	-380.0	0.0	8002.3	9093.5
13	229.5	40.7	-380.0	0.0	12725.0	14460.2
23	218.3	-240.5	-380.0	0.0	10984.6	12482.4
32	207.0	-400.3	-380.0	0.1	9532.6	10832.6
49	184.5	-626.9	-380.0	0.0	8931.7	10149.6

TABLE D-10

TOTAL HEAT TRANSFER DATA AND CALCULATED
RESULTS FOR NAPALM TEST SOLVENT FIRES

TEST NUMBER - 27
FUEL - NAPALM
BURNER - 12 INCH DIAMETER, SINGLE
CYLINDER - BRASS

DATA

TEST TIME (MIN)	PRIMARY WATER FLOWS (LB/HR)		PRIMARY WATER TEMPERATURES (DEG F)				AIR TEMP (DEG F)	COOLING WATER FLOW (LB/HR)	TEMP DIFF (DEG F)
	PWI	PWO	T1	T2	T3	T6	TA	CW	CWDT
14	18.4	18.4	165.5	169.0	212.0	133.0	120.	356.0	29.5
26	22.5	20.5	170.0	185.0	212.0	132.0	130.	356.0	28.5
34	22.5	22.5	169.5	182.5	212.0	131.2	135.	356.0	26.5
41	22.5	22.5	170.5	187.0	212.0	131.5	135.	356.0	23.8
60	18.3	18.3	192.0	208.0	212.0	132.0	140.	356.0	22.5

RESULTS

TEST TIME	HEAT LOSSES (BTU/HR)				FIRE HEAT ABSORBED THROUGH TEST SURFACE	
	OUTLET LINE	LEAD TUBE	CYLINDER ENDS	CONTENTS	(BTU/HR)	(BTU/HR-SQFT)
14	207.0	73.4	-590.0	0.0	9594.4	10902.7
26	184.5	-637.9	-590.0	1.2	8408.8	9555.4
34	173.3	-521.7	-590.0	0.0	7633.8	8674.8
41	173.3	-725.7	-590.0	0.0	6452.8	7332.7
60	162.0	-645.1	-590.0	0.0	5838.9	6635.1

TABLE D-11

TOTAL HEAT TRANSFER DATA AND CALCULATED RESULTS FOR BENZOL FIRES

TEST NUMBER - 43
FUEL - BENZOL
BURNER - 12 INCH DIAMETER, SINGLE
CYLINDER - BRASS

DATA

TEST TIME (MIN)	PRIMARY WATER FLOWS (LB/HR)		PRIMARY WATER TEMPERATURES (DEG F)				AIR TEMP (DEG F)	COOLING WATER FLOW (LB/HR)	COOLING WATER TEMP DIFF (DEG F)
	PWI	PWO	T1	T2	T3	T6	TA	CW	CWDT
7	47.5	47.0	143.5	151.5	212.0	128.0	130.	363.0	29.0
22	40.3	41.4	156.0	164.0	212.0	121.0	130.	363.0	26.0
31	40.3	39.9	157.0	168.0	212.0	120.0	130.	363.0	23.8
47	35.5	35.8	168.0	180.0	212.0	121.0	130.	363.0	24.5

RESULTS

TEST TIME	HEAT LOSSES (BTU/HR)				FIRE HEAT ABSORBED THROUGH TEST SURFACE	
	OUTLET LINE	LEAD TUBE	CYLINDER ENDS	CONTENTS	(BTU/HR)	(BTU/HR-SQFT)
7	184.5	-587.1	-590.0	0.3	8840.5	10046.0
22	184.5	-512.0	-590.0	-0.7	7009.2	7965.0
31	184.5	-816.5	-590.0	0.2	5963.3	6776.5
47	184.5	-833.5	-590.0	-0.2	5958.5	6771.0

TABLE D-12

EMISSION AND ABSORPTION COEFFICIENTS
FROM SMALL METHANOL FLAMES[a]

Wavelength (microns)	Emission Coefficient (watts/cm^3-cm-steradians)	Absorption Coefficient (cm^{-1})
1.850	64.705	0.001
1.950	92.219	0.013
2.020	77.703	0.007
2.060	92.998	0.002
2.140	68.884	0.009
2.210	11.746	0.002
2.280	0.0	0.090
2.360	0.0	0.090
2.410	0.0	0.090
2.450	0.0	0.090
2.490	0.0	0.090
2.500	0.0	0.090
2.520	177.716	0.001
2.540	284.387	0.009
2.610	355.158	0.028
2.630	281.243	0.016
2.670	174.623	0.016
2.690	174.923	0.021
2.710	183.431	0.006
2.740	278.856	0.021
2.780	510.835	0.078
2.820	504.481	0.047
2.860	530.450	0.060
2.880	567.861	0.060
2.950	658.715	0.091
2.990	569.580	0.018
3.080	309.482	0.006
3.170	173.345	0.011
3.270	79.932	0.004
3.310	70.034	0.015
3.390	35.131	0.009
3.430	31.647	0.002
3.510	10.643	0.005
3.590	7.151	0.002

(a) W. Tsai, Unpublished Ph. D. Thesis, University of Oklahoma, (1968).

TABLE D-12 (continued)

Wavelength (microns)	Emission Coefficient (watts/cm^3-cm-steradians)	Absorption Coefficient (cm^{-1})
3.720	0.0	0.090
4.020	0.0	0.090
4.160	0.0	0.090
4.180	0.0	0.090
4.200	0.0	0.090
4.220	48.273	0.008
4.240	256.870	0.041
4.260	534.121	0.106
4.290	594.648	0.559
4.330	501.015	0.446
4.350	694.664	0.639
4.370	1007.231	0.518
4.390	1437.101	0.349
4.410	2456.471	0.489
4.430	3125.403	0.349
4.460	4161.394	0.264
4.500	4170.632	0.261
4.600	2309.133	0.140
4.650	1371.154	0.070
4.710	782.236	0.050
4.830	210.311	0.011
4.990	97.607	0.029
5.220	44.161	0.007

(a) W. Tsai, Unpublished Ph. D. Thesis, University of Oklahoma, (1968).

TABLE D-13

EMISSION AND ABSORPTION COEFFICIENTS
FROM SMALL ACETONE FLAMES[a]

Wavelength (microns)	Emission Coefficient (watts/cm^3-cm-steradians)	Absorption Coefficient (cm^{-1})
0.850	587.797	1.209
0.862	681.847	1.184
0.874	1,021.333	1.434
0.886	920.466	0.957
0.899	808.098	0.507
0.911	758.770	0.155
0.924	898.792	0.364
0.938	1,269.509	0.865
0.951	1,286.579	0.750
0.964	1,381.161	0.666
0.980	1,594.883	0.882
0.990	1,518.069	0.642
1.040	1,342.894	0.509
1.080	1,235.917	0.359
1.130	1,097.992	0.142
1.180	1,128.185	0.164
1.230	1,044.570	0.140
1.290	1,001.328	0.155
1.360	999.047	0.214
1.420	1,408.825	0.729
1.500	961.916	0.217
1.650	912.482	0.438
1.720	1,090.350	0.889
1.780	812.476	0.336
1.850	937.805	0.661
1.950	831.210	0.561
2.020	736.831	0.435
2.060	992.861	1.031
2.140	1,047.500	1.580
2.210	903.128	1.275
2.280	866.143	1.425
2.360	568.775	0.569
2.410	548.406	0.560
2.450	487.312	0.373

[a] W. Tsai, Unpublished Ph.D. Thesis, University of Oklahoma (1968).

TABLE D-13 (continued)

Wavelength (microns)	Emission Coefficient (watts/cm^3-cm-steradians)	Absorption Coefficient (cm^{-1})
2.490	630.931	0.879
2.500	748.076	1.197
2.520	747.615	1.025
2.540	944.971	1.405
2.610	1,890.189	2.820
2.630	1,396.587	1.788
2.670	1,508.021	2.218
2.690	1,766.658	2.971
2.710	1,508.608	2.473
2.740	1,536.900	2.062
2.780	2,930.965	2.775
2.820	4,014.946	3.540
2.860	3,161.452	3.163
2.880	3,427.194	3.687
2.950	2,388.119	2.672
2.990	2,822.025	3.591
3.080	1,162.765	1.874
3.170	887.847	2.398
3.270	440.005	1.265
3.310	421.503	1.405
3.390	294.519	0.920
3.430	265.061	0.845
3.510	214.427	0.552
3.590	190.669	0.573
3.720	157.434	0.640
4.020	116.933	0.680
4.160	88.017	0.231
4.180	88.176	0.231
4.200	163.947	1.081
4.220	438.577	1.971
4.240	1,006.823	2.384
4.260	1,777.945	1.905
4.290	3,797.342	1.509
4.330	8,704.324	1.386
4.350	9,731.047	1.177
4.370	11,056.430	1.202

(a) W. Tsai, Unpublished Ph.D. Thesis, University of Oklahoma (1968).

TABLE D-13 (continued)

Wavelengths (microns)	Emission Coefficient (watts/cm^3-cm-steradians)	Absorption Coefficient (cm^{-1})
4.390	17,048.051	2.566
4.410	19,480.844	3.321
4.430	18,849.188	3.145
4.460	19,560.238	3.379
4.450	23,036.117	4.156
4.550	13,728.086	3.052
4.600	11,227.554	3.591
4.650	8,564.566	4.020
4.710	3,791.775	2.653
4.830	6,564.129	2.487
4.990	1,177.757	0.381
5.220	755.659	0.758

(a) W. Tsai, Unpublished Ph.D. Thesis University of Oklahoma (1968).

TABLE D-14

EMISSION AND ABSORPTION COEFFICIENTS FROM SMALL HEXANE FLAMES[a]

Wavelength (microns)	Emission Coefficient (watts/cm^3-cm-steradians)	Absorption Coefficient (cm^{-1})
0.850	981.067	0.282
0.862	1528.863	0.739
0.874	1643.299	0.562
0.886	1815.377	0.484
0.899	1948.470	0.429
0.911	2777.155	0.793
0.924	2964.539	0.682
0.938	2520.914	0.209
0.951	2690.907	0.156
0.964	4431.800	0.895
0.980	5450.921	1.250
0.990	6433.074	1.446
1.040	7536.554	1.969
1.080	5930.050	1.355
1.130	5499.660	1.235
1.180	4588.644	0.825
1.230	4032.941	0.720
1.290	3806.390	0.715
1.360	3195.735	0.447
1.420	3486.814	0.427
1.500	3172.032	0.484
1.650	3981.138	1.120
1.720	3917.664	1.104
1.780	3553.433	0.903
1.850	3961.411	1.318
1.950	4650.793	1.843
2.020	3891.375	1.413
2.060	3757.908	1.367
2.140	3243.766	1.160
2.210	2918.853	1.090
2.280	2727.948	1.123
2.360	2450.765	1.045
2.410	2303.701	0.972
2.450	2301.451	1.026

[a] W. Tsai, Unpublished Ph. D. Thesis, University of Oklahoma, (1968).

TABLE D-14 (continued)

Wavelength (microns)	Emission Coefficient (watts/cm^3-cm-steradians)	Absorption Coefficient (cm^{-1})
2.490	2474.018	1.227
2.500	2487.289	1.235
2.520	2585.504	1.326
2.540	2555.378	1.285
2.610	3109.217	1.568
2.630	3142.754	1.486
2.670	2728.121	1.290
2.690	2552.804	1.278
2.710	1928.048	0.788
2.740	2220.200	1.034
2.780	3796.143	1.963
2.820	3648.970	1.890
2.860	2763.325	1.385
2.880	2516.996	1.330
2.950	2914.326	2.013
2.990	2907.362	2.138
3.080	1389.789	0.818
3.170	1227.222	0.947
3.270	1075.867	0.947
3.310	1191.087	1.363
3.390	1539.283	2.417
3.430	1562.783	2.637
3.510	1073.201	1.752
3.590	518.107	0.357
3.720	500.021	0.596
4.020	338.455	0.382
4.160	480.953	1.335
4.180	444.050	1.160
4.200	444.857	1.160
4.220	343.493	0.322
4.240	768.701	1.477
4.260	1091.969	1.275
4.290	5556.695	3.853
4.330	9184.644	3.385
4.350	12455.601	3.322
4.370	16110.875	3.910

(a) W. Tsai, Unpublished Ph. D. Thesis, University of Oklahoma, (1968).

TABLE D-14 (continued)

Wavelength (microns)	Emission Coefficient (watts/cm^3-cm-steradians)	Absorption Coefficient (cm^{-1})
4.390	14443.343	3.582
4.410	14952.964	3.935
4.430	12154.117	2.965
4.460	10341.968	2.292
4.500	10881.695	2.453
4.550	15843.425	4.786
4.600	5871.179	2.270
4.650	3460.351	1.960
4.710	2988.924	2.791
4.830	790.602	1.714
4.990	310.011	1.200
5.220	160.814	0.562

(a) W. Tsai, Unpublished Ph. D. Thesis, University of Oklahoma, (1968).

TABLE D-15

EMISSION AND ABSORPTION COEFFICIENTS
FROM SMALL CYCLOHEXANE FLAMES[a]

Wavelength (microns)	Emission Coefficient (watts/cm^3-cm-steradians)	Absorption Coefficient (cm^{-1})
0.850	2193.990	0.651
0.862	2662.193	0.820
0.874	3178.744	0.954
0.886	3485.314	0.944
0.899	3668.353	0.840
0.911	3599.569	0.593
0.924	3588.974	0.408
0.938	4071.422	0.489
0.951	4669.464	0.597
0.964	4891.390	0.485
0.980	5021.304	0.454
0.990	5248.687	0.384
1.040	5210.660	0.433
1.080	5023.429	0.381
1.130	5901.058	0.730
1.180	6745.910	0.824
1.230	6168.554	0.763
1.290	5943.312	0.837
1.360	5738.656	0.919
1.420	5106.476	0.511
1.500	3934.188	0.205
1.650	3544.200	0.171
1.720	3916.647	0.397
1.780	4093.721	0.532
1.850	4082.175	0.612
1.950	3828.423	0.684
2.020	3825.924	0.733
2.060	3905.600	0.781
2.140	3795.893	0.805
2.210	3574.117	0.770
2.280	3353.078	0.760
2.360	3452.210	0.961
2.410	3502.755	1.086
2.450	3330.783	1.066
2.490	3189.981	1.059

[a] W. Tsai, Unpublished Ph. D. Thesis, University of Oklahoma, (1968).

TABLE D-15 (continued)

Wavelength (microns)	Emission Coefficient (watts/cm^3-cm-steradians)	Absorption Coefficient (cm^{-1})
2.500	3099.155	1.034
2.520	3017.292	1.020
2.540	2894.608	0.969
2.610	4006.771	1.765
2.630	4240.687	1.749
2.670	4845.316	1.999
2.690	3644.227	1.537
2.710	2800.481	1.024
2.740	2511.621	0.718
2.780	2305.961	0.331
2.820	7450.328	3.615
2.860	4307.226	2.221
2.880	2411.824	0.899
2.950	2931.955	1.429
2.990	1870.873	0.616
3.080	1364.599	0.328
3.170	1161.932	0.379
3.270	925.920	0.166
3.310	934.808	0.264
3.390	821.762	0.208
3.430	782.838	0.196
3.510	759.866	0.259
3.590	691.981	0.221
3.720	603.478	0.173
4.020	455.970	0.218
4.160	431.403	0.312
4.180	399.692	0.152
4.200	408.834	0.200
4.220	721.121	1.201
4.240	540.784	0.176
4.260	729.787	0.251
4.290	2607.323	1.194
4.330	5907.351	1.929
4.350	6666.468	1.844
4.370	12580.718	3.478
4.390	10287.644	2.644
4.410	12608.769	3.498

(a) W. Tsai, Unpublished Ph. D. Thesis, University of Oklahoma, (1968).

TABLE D-15 (continued)

Wavelength (microns)	Emission Coefficient (watts/cm^3-cm-steradians)	Absorption Coefficient (cm^{-1})
4.430	12022.367	3.010
4.460	10475.328	2.314
4.500	11174.519	2.564
4.550	8943.293	2.520
4.600	8590.277	3.583
4.650	4393.000	2.504
4.710	1852.066	1.374
4.830	694.180	1.098
4.990	293.618	0.293
5.220	197.294	0.214

(a) W. Tsai, Unpublished Ph. D. Thesis, University of Oklahoma, (1968).

TABLE D-16

MEASURED RADIATION FROM VARIOUS MERGED FIRES[a]

Test No.	Flame Dia. x Ht. (inches)	Measured Radiation[b] (Btu/hr-ft^2) @ 73.5 in.	@ 153.5 in.
Acetone			
2210	14.4 x 21.3	85.7	24.8
2212	12.0 x 35.3	127.4	33.1
2213	13.4 x 41.4	124.5	33.1
2310	25.6 x 31.9	378.4	132.8
2312	18.4 x 47.6	340.6	127.4
2313	20.6 x 42.5	276.8	88.6
Hexane			
3110	10.0 x 29.2	93.2	24.1
3112	10.2 x 31.5	61.6	15.8
3207A	19.2 x 33.5	346.0	108.0
3210A	16.4 x 47.2	378.4	110.9
3212A	16.6 x 59.8	387.7	124.6
3307A	20.8 x 61.8	609.1	204.8
3308A	34.4 x 41.2	622.8	229.7

(a) Huffman, K. G., "The Interaction and Merging of Flames from Burning Liquids," University of Oklahoma (1967)

(b) Radiometer located 73.5 inches and 153.5 inches from flame centerline on same level as top of burners.

TABLE D-16 (continued)

Test No.	Flame Dia. x Ht. (inches)	Measured Radiation[b] (Btu/hr-ft^2) @ 73.5 in.	@ 153.5 in.
Cyclohexane			
4108	12.8 x 14.8	88.5	36.0
4109	11.8 x 25.9	124.6	44.3
4111	12.4 x 29.4	113.4	24.8
4206	21.0 x 26.4	354.2	116.3
4210	17.0 x 33.5	401.4	121.7
4213	19.0 x 44.6	340.6	116.3
4306	26.0 x 47.7	747.4	193.7
4312	22.2 x 57.2	537.1	180.0
4207	22.8 x 31.4	360.0	96.8
Benzol			
5180	9.4 x 21.7	152.3	40.3
5111	11.4 x 34.6	155.2	29.2

[a] Huffman, K. G., "The Interaction and Merging of Flames from Burning Liquids," University of Oklahoma (1967)

[b] Radiometer located 73.5 inches and 153.5 inches from flame centerline on same level as top of burners.

TABLE D-17

MEASURED RADIATION FROM VARIOUS FIRES
IN SMALL CHANNEL BURNERS

Fuel	Flame Thickness (inches)	Radiation[a] (mw/cm^2-steradian)
Methanol	6.5	255
	24	450
Acetone	7	610
	11	770
Hexane	9	840
	13	1100
Cyclohexane	10	1000
	16	1420
JP-4	10	980
	13	1400
Benzol	10	1100
	16	1600

[a] Radiometer located about 30 inches from flames. Atmospheric transmissivity approximately 0.95.

APPENDIX E

DESIGN OF THE SUPPORT AND LIFTING MECHANISM

An analysis was made to determine the bending and stress loads on the lead tube, the lifting mechanism and the static supports. The principal elements and results of the analysis are presented here; drawings of the system are presented in Chapter IV.

Lead Tube

The weight of the lead tube and internals was estimated to be

7.6 lb/ft for 3-inch, sch. 40 pipe

3.4 lb/ft for internal insulation, tubing, etc.

3.0 lb/ft for outside insulation, jacket, etc.

14.0 lb/ft Total

The maximum weight of the test cylinder and water was estimated to be

22.6 lb for 1 foot of 4-inch, sch. 160 pipe

4.4 lb of water to fill cylinder

27.0 lb Total

The vertical section of the lead tube and additional hardware located on the vertical centerline was assumed to weigh 14.0 lb.

Figure E-1 shows the resulting load, shear and moment diagrams for the lead tube assembly with suspension points 2 feet on each side of the vertical centerline.

The total weight of the lead tube assembly was 181 lb. The maximum shear, 90.5 lb, and the maximum bending moment, 63 ft-lb, occur at the suspension points. The weakest and also the hottest region of the lead tube is at the threaded tee near the vertical centerline where the shear is just over 41 lb and the bending moment is nearly zero.

The strength factor or resistance to bending moments of 3-inch, sch 40 pipe is 3,880 ft-lb for an allowable stress of 27,000 psi. (Ref. 28). The stress value of 316 stainless steel pipe is 2,350 psi. at 1400°F, the assumed maximum temperature.

The strength factor at 1400°F is then

$$3{,}880 \left(\frac{2{,}350}{27{,}000}\right) = 338 \text{ ft-lb}$$

which is well above the expected bending moment. Lead tube temperatures measured during the tests, Table D-3, Appendix D, indicate that a less expensive type of steel such as 347 or even 304 would have been satisfactory.

Lifting Mechanism

The axles for the cable sheaves were 1-inch diameter mild steel. Each axle was assumed to support a 100 lb load at the center of a 3-foot span as well as its own weight of 2.7 lb/ft.

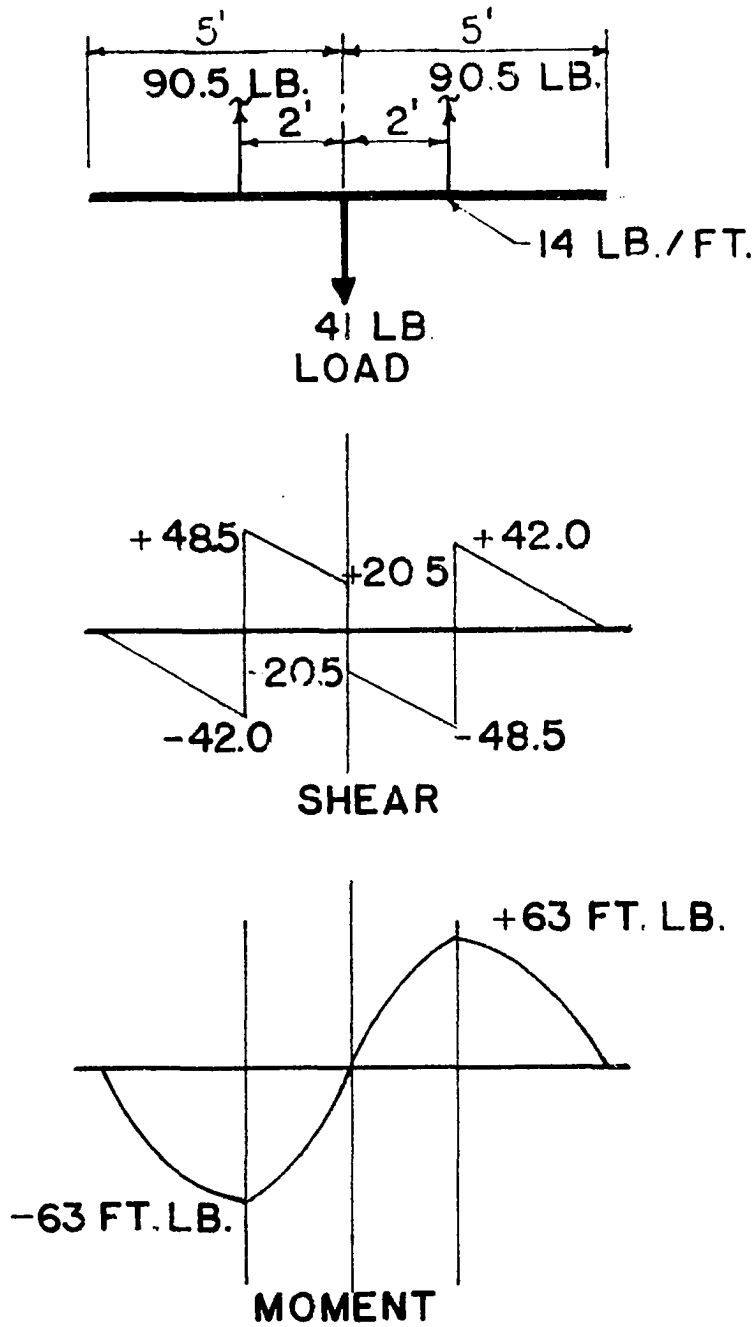

Figure E-1. Load, Shear and Bending Moment Diagrams for Lead Tube Assembly.

The maximum bending moment occurs at the center of the span and is approximately 80 ft-lb. The maximum stress, S, of the outer fibers under bending is given by the flexure formula

$$S = \frac{Mc}{I} \qquad \text{(E-1)}$$

where M is the bending moment in in-lb., c is the radius of the member in inches and I is the moment of inertia in inches to the fourth power. The maximum stress in the steel axles is then

$$S = \frac{(81 \times 12)(0.5)}{(0.0491 \times 1^4)}$$

$$S = 9,900 \text{ psi}$$

At 1000°F the yield strength of mild steel is 20,000 psi (Ref. 8) so the 1-inch diameter rods are adequate if the temperature does not exceed about 1000°F. The flames from the larger fires reached above the level of these axles and occasionally made direct contact with them.

The two 1/15-horsepower motors used to power the lifting mechanism delivered only 450 in-lb torque at 2.8 rpm. Each motor must lift 100 lbs so the 4-inch diameter chain drive prockets and 13-inch diameter V-belt pulley provided about the maximum lifting speed obtainable. The first set of 13-inch diameter V-belt pulleys were made from a "pot" metal which warped during the large fire tests. They were replaced with 10-inch steel pulleys and no additional difficulties were encountered.

Overhead Supports

The axles were mounted on a bridge constructed of T beams made from a pair of 225-80 AIM slotted steel angles. The bridge spanned 9 feet and supported 200 lbs. The design brochure (Ref. 11), supplied with the angles recommended doubling point loads to arrive at the equivalent distributed load. According to Section 6 in the brochure the bridge would support 1150 lbs if crossbraces were used at the ends of the bridge. This strength is ample provided the beams do not become too hot. Since the bridge beams were spaced 3 feet apart and are relatively close to the flames from a large fire, they were wrapped with a loose layer of asbestos cloth to provide some protection from radiation and direct contact heating. Although there were no signs of overheating, these T beams or the axles are probably the most susceptible to overheating and failure during a fire test.

The bridge was mounted on steel casters at each corner. The casters at the north and south ends of the bridge rode in a channel formed from two of the slotted steel angles. The channels were attached to the large (12 ft x 12 ft) sheet metal hood at 4-foot intervals. The channels were required to support an estimated total weight of 300 lbs including the lead tube, bridge, motors and chain drive components. A single slotted angle will support 350-lb point loads with 4-foot support spacing so the design is more than adequate.

The 12 x 12 sheet metal hood was an original part of

the wind tunnel building and is attached directly to concrete ceiling beams.

APPENDIX F

THERMISTOR ACTUATED LIQUID LEVEL MONITOR CIRCUIT

A positive independent check on the liquid level in the test cylinder was obtained by using a thermistor actuated monitor system. The electrical resistance of a thermistor is strongly temperature dependent and senses the liquid interface from the difference between the cooling capacity of the liquid or vapor phase. The N_2-bubbler system and other liquid level measuring schemes which provide continuous level indication utilize the differential pressure of the liquid head.

In most applications two thermistors are mounted one above the other and connected in parallel into a bridge circuit. The bridge voltages will change when the thermistors are heated or cooled at different rates due to immersions in different phases, i.e., liquid or vapor. It is possible to design a system which will indicate when both thermistors are in or out of the liquid although the bridge voltages are balanced in both cases. Such a system requires a rather well defined interface whose position with respect to the thermistors changes rather slowly. This requirement certainly wouldn't be met inside the test cylinder where the boiling will be violent

enough to cause surging and considerable liquid carry-over. Therefore a monitor circuit was designed which utilizes only one thermistor and which is sensitive to small changes in the thermistor temperature.

Figure F-1 is a circuit diagram of the monitor system. When the hot side of the 110 volt, 60 cycle power supply is negative, current flow through the circuit is prevented by diode D_1 and the silicone controlled rectifier SCR. When the hot side of the power supply is positive, diode D_1 conducts and the zener diode ZD_1 breaks down when the potential across it exceeds 18 volts. The large resistor ahead of D_1 limits the current flow through ZD_1. Thus far the circuit provides 18 volts half wave across points A-B.

If the bridge is balanced there is no current flow into the base of transistor Q_1 so there is no current flow from the collector side. Thus sufficient current is supplied to the base of transistor Q_2 to reduce its collector to emitter resistance and to permit a relatively large current flow. The resulting current through Q_2 overcomes the breakdown voltage of zener diode ZD_2, fires the silicone controlled rectifier SCR, and in turn permits current flow through the load resistance R_L (which was a neon glow light in this application). The 110 V power is applied across R_L only during alternate cycles; there is no current flow during the other half-cycle.

When the bridge is unbalanced sufficiently to provide about 1 volt across the bridge midpoints, Q_1 will fire and

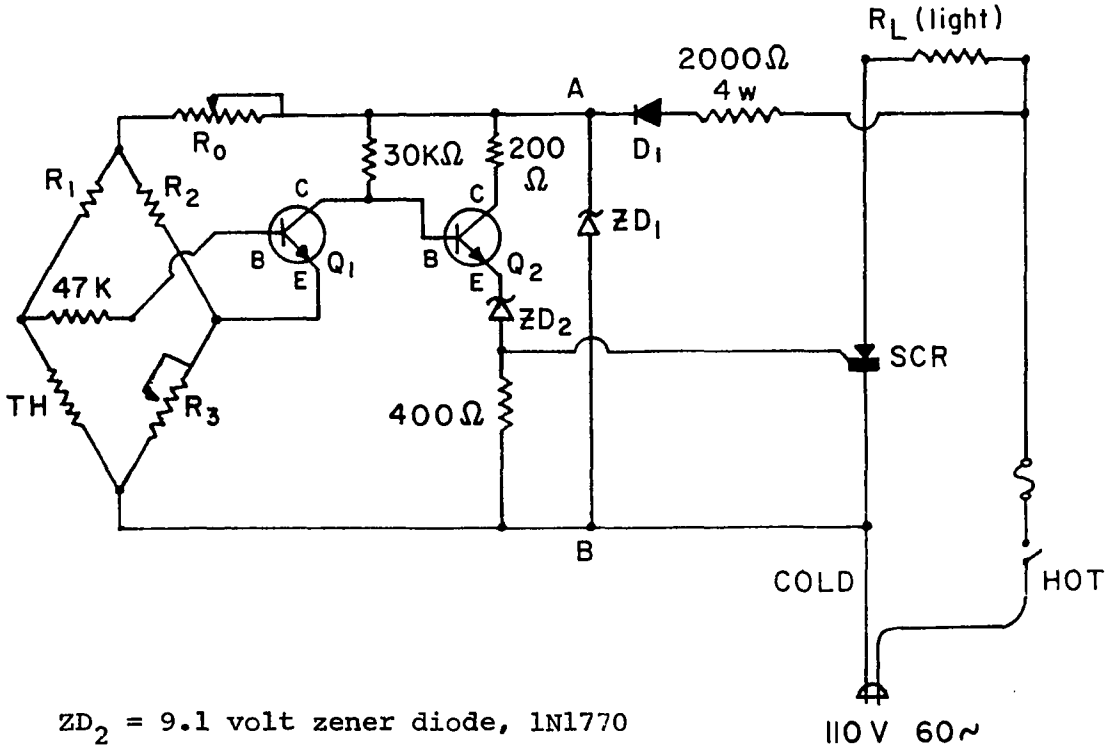

ZD_2 = 9.1 volt zener diode, 1N1770

ZD_1 = 18 volt zener diode, 1N3026

TH = thermistor, fenwal GA 51P2

SCR = silicone controlled rectifier, 2N3228

R_1, R_2 = resistors, 3000 Ω

R_3 = variable resistor, 0-5000 Ω

R_o = variable resistor, 0-25,000 Ω

R_L = load resistance (neon lamp, NE 51H)

Q_1, Q_2 = transistors, 2N 699

D_1 = diode, 2F4

Figure F-1. Thermistor Actuated Liquid Level Monitor Circuit.

shunt away the current from the base of Q_2, shutting it off. When Q_2 is off, the SCR is off and no power is supplied to the load resistance R_L.

The variable resistance R_o provides some control over the voltage applied to the bridge and subsequently the bridge midpoint voltage. This voltage must be below the breakdown voltage of zener diode ZD_2, or Q_1 will not shunt enough current away from the base of Q_2 to shut it off.

Three of these circuits were built and they worked very well in out-of cylinder tests. The entire system did not work well during actual tests as mentioned in Section VI. The circuit frequently required resetting by adjusting variable resistor R_3. The problem probably arises from the ill-defined interface between the liquid and vapor which results when vigorous boiling is confined in the test cylinder.

APPENDIX G

CORRECTION FACTORS FOR RADIATION ABSORBED BY ATMOSPHERE AND RADIOMETER QUARTZ WINDOW

Atmospheric Absorption

The CO_2 and H_2O in the atmosphere are strong absorbers of infrared radiation in three major wavelength bands. The calculation of the radiant energy incident on a target external to a flame must include the absorption of radiation by these bands to avoid serious error. The elaborate atmospheric absorption correlations reported in Ref. 45 and similar sources are oriented towards long transmission distances and are of little value in obtaining information for the 6- to 12-foot separation distances encountered in these experiments. The atmospheric absorption coefficients presented in Table G-1 were calculated from data on the absorption of radiation by 6 feet of normal, room temperature air. The monochromatic transmissivity, t_λ of the atmosphere is calculated by

$$t_\lambda = e^{-\beta_\lambda x} \qquad \text{(G-1)}$$

where x = optical path length, inches

β_λ = atmospheric absorption coefficient, $inch^{-1}$.

Quartz Window Absorption

The wide angle radiometer used to measure the external radiation was covered by a thin quartz window. Quartz absorbs considerable radiation at the longer wavelengths and the radiometer readings must be corrected to obtain the radiation incident on the outside of the quartz window. The quartz transmissivities presented in Table G-1 were based on absorption measurements, reported by Tsai (Ref.40), through the window of a radiometer identical to the one used in these experiments.

Effect on Calculated Radiation

The magnitude of the corrections for absorption by the atmosphere and the quartz window are shown on Fig. G-1 for acetone, Fig. G-2 for hexane and Fig. G-3 for cyclohexane. The calculated radiation is plotted vs the product of the flame height and diameter, referred to as the flame area. This area is that of a plane through the major diameter of the equivalent flame cylinder.

The calculated radiant heating values appear to be smooth functions of flame area, as might be expected since the height to diameter ratio is about the same for different sized, actual flames. No curve was drawn through the points since a single valued functional relationship between the flame area and the radiant heating rate exists only for a constant height to diameter ratio. The radiant

TABLE G-1

ATMOSPHERIC ABSORPTION FACTORS AND
QUARTZ WINDOW TRANSMISSIVITY

Wavelength (microns)	Quartz Window Transmissivities(1)	Atmospheric Absorption Coefficients(2) (in^{-1})
0.850	1.000	0.0
0.862	1.000	0.0
0.874	1.000	0.0
0.886	1.000	0.0
0.899	1.000	0.0
0.911	1.000	0.0
0.924	1.000	0.0
0.938	1.000	0.0
0.951	1.000	0.0
0.964	1.000	0.0
0.980	1.000	0.0
0.990	1.000	0.0
1.040	1.000	0.0
1.080	1.000	0.0
1.130	1.000	0.0
1.180	1.000	0.0
1.230	1.000	0.0
1.290	1.000	0.0
1.360	1.000	0.0
1.420	1.000	0.0
1.500	1.000	0.0
1.650	1.000	0.0
1.720	1.000	0.0
1.780	0.995	0.0
1.850	0.990	0.0
1.950	0.990	0.0
2.020	0.980	0.003
2.060	0.980	0.004
2.140	0.965	0.0
2.210	0.955	0.0
2.280	0.950	0.0
2.360	0 950	0.0

(1) Window in wide angle radiometer, No. 11808

(2) Based on measurments by W. Tsai.

TABLE G-1 (continued)

Wavelength (microns)	Quartz Window Transmissivities(1)	Atmospheric Absorption Coefficients(2) (in^{-1})
2.410	0.948	0.0
2.450	0.945	0.0
2.490	0.945	0.0
2.500	0.943	0.0
2.520	0.940	0.0
2.540	0.940	0.0
2.610	0.925	0.004
2.630	0.922	0.006
2.670	0.920	0.013
2.690	0.915	0.013
2.710	0.880	0.012
2.740	0.875	0.013
2.780	0.910	0.014
2.820	0.935	0.012
2.860	0.930	0.009
2.880	0.930	0.007
2.950	0.925	0.001
2.990	0.920	0.0
3.080	0.920	0.0
3.170	0.918	0.0
3.270	0.945	0.0
3.310	0.945	0.0
3.390	0.925	0.0
3.430	0.920	0.0
3.510	0.895	0.0
3.590	0.810	0.0
3.720	0.740	0.0
4.020	0.675	0.0
4.160	0.530	0.0
4.180	0.525	0.0
4.200	0.500	0.0
4.220	0.460	0.0
4.240	0.455	0.001
4.260	0.455	0.002
4.290	0.453	0.015
4.330	0.305	0.037

(1) Window in wide angle radiometer, No. 11808

(2) Based on measurments by W. Tsai.

TABLE G-1 (continued)

Wavelength (microns)	Quartz Window Transmissivities[1]	Atmospheric Absorption Coefficients[2] (in^{-1})
4.350	0.250	0.037
4.370	0.250	0.037
4.390	0.245	0.030
4.410	0.240	0.021
4.430	0.240	0.014
4.460	0.240	0.004
4.500	0.255	0.002
4.550	0.260	0.001
4.600	0.305	0.0
4.650	0.255	0.0
4.710	0.210	0.0
4.830	0.030	0.0
4.990	0.0	0.0
5.220	0.0	0.0

[1] Window in wide angle radiometer, No. 11808

[2] Based on measurments by W. Tsai.

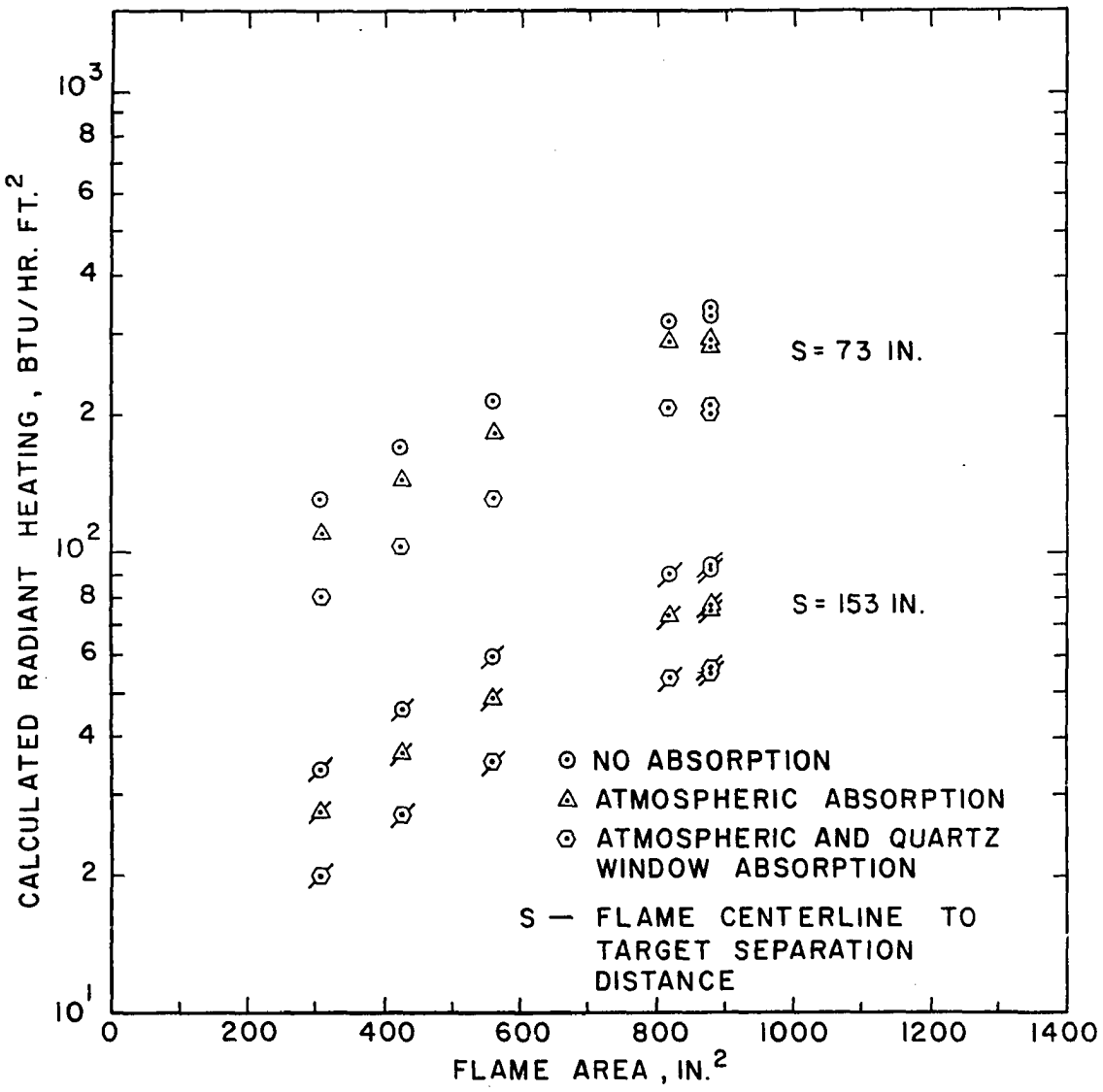

Figure G-1. Effects of Spectral Absorption Corrections on Calculated Radiant Heating from Acetone Flames.

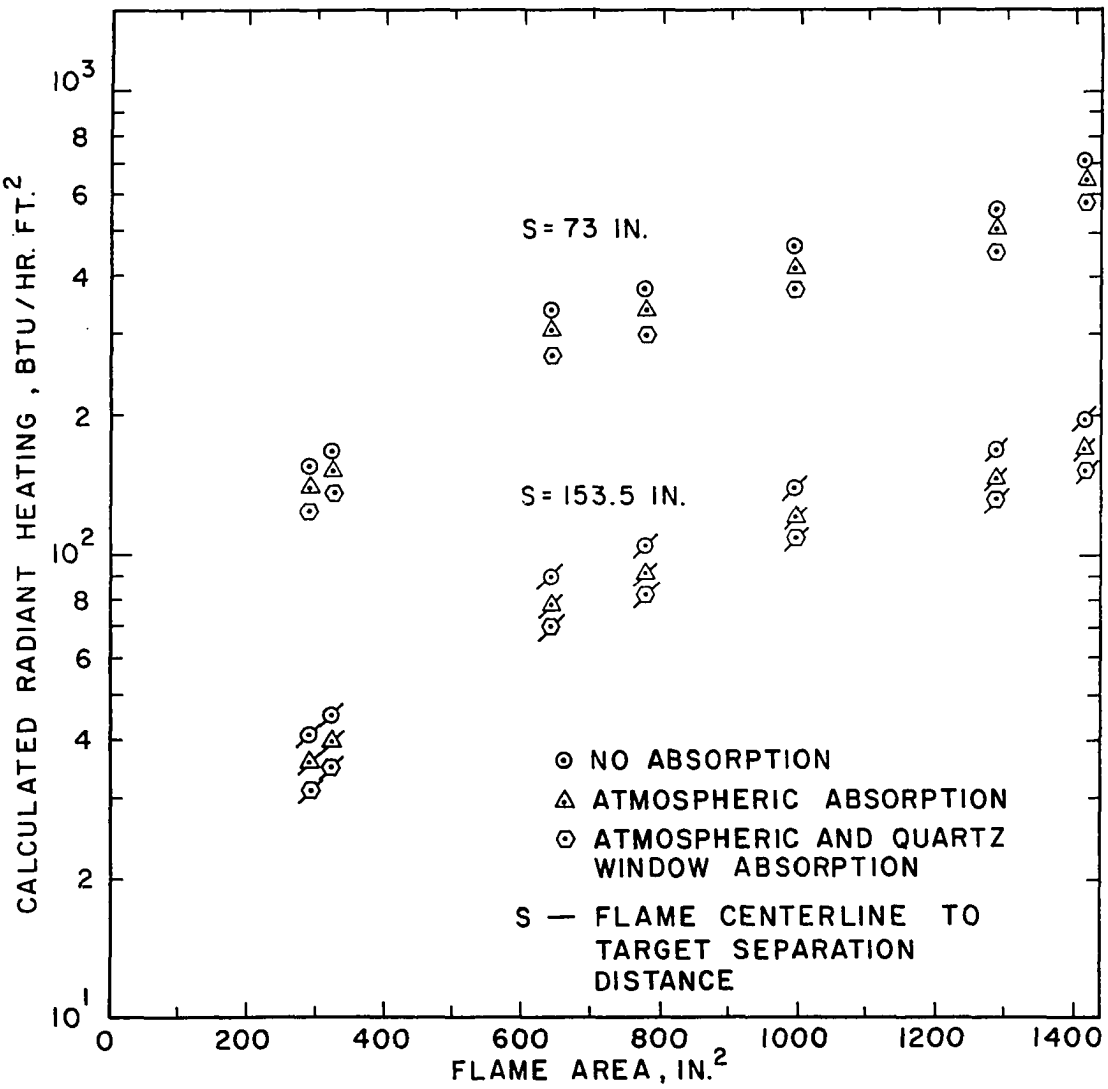

Figure G-2. Effects of Spectral Absorption Corrections on Calculated Radiant Heating from Hexane Flames.

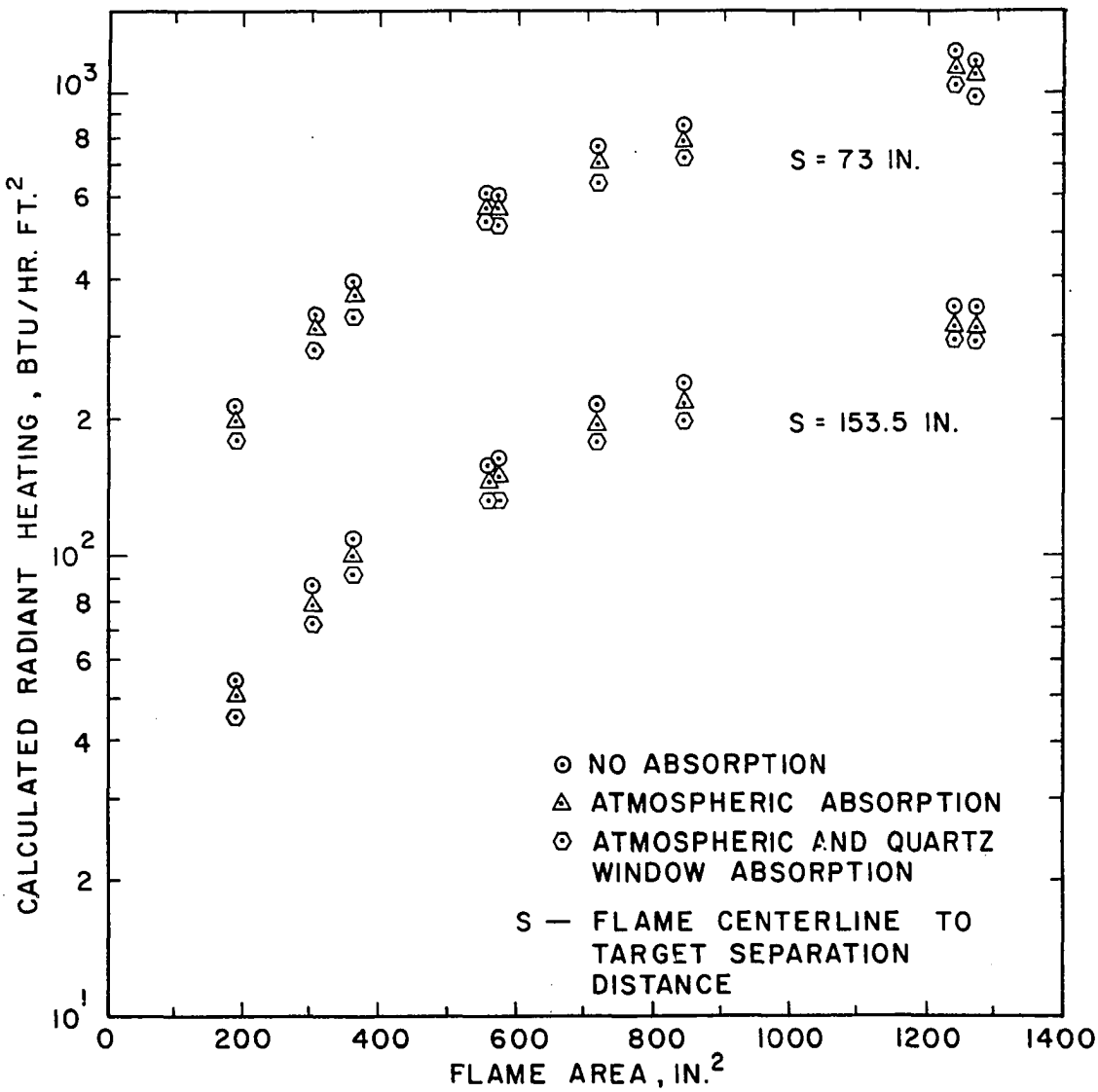

Figure G-3. Effects of Spectral Absorption Corrections on Calculated Radiant Heating from Cyclohexane Flames.

heating calculations were made using the monochromatic absorption-emission coefficients for the small, laminar flames. The effect on the magnitude of the total correction factor by the spectral distribution of the radiant energy from each fuel is apparent from the spacing between the points representing no absorption, atmospheric absorption only and combined window and atmospheric absorption.